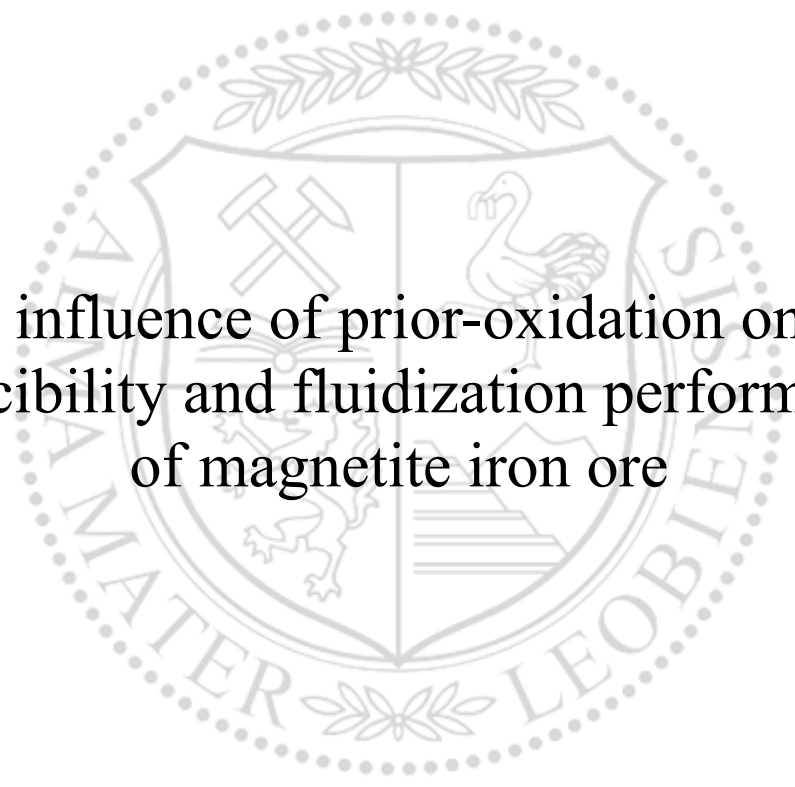




Chair of Ferrous Metallurgy

Doctoral Thesis



The influence of prior-oxidation on the
reducibility and fluidization performance
of magnetite iron ore

Heng Zheng

August 2023



AFFIDAVIT

I declare on oath that I wrote this thesis independently, did not use other than the specified sources and aids, and did not otherwise use any unauthorized aids.

I declare that I have read, understood, and complied with the guidelines of the senate of the Montanuniversität Leoben for "Good Scientific Practice".

Furthermore, I declare that the electronic and printed version of the submitted thesis are identical, both, formally and with regard to content.

Date 10.08.2023

HENG ZHENG

Signature Author
Heng Zheng

Abstract

The European Union (EU) is actively working on the goal of achieving climate neutrality by 2050. It is worth noting that, about 60 % of the crude steel is still produced through the blast furnace-basic oxygen furnace (BF–BOF) route in Europe. Although the BF-BOF route shows high production efficiency, the CO₂ emissions per ton of crude steel are higher than other alternative steelmaking routes. One promising alternative steelmaking route is using a hydrogen-based fluidized bed to produce hydrogen direct reduced iron (HDRI), followed by an electric arc furnace (EAF) process. To improve the fluidization and reduction behaviors of magnetite iron ore fines in the fluidized bed, some pretreatments of the material are investigated.

This thesis tests some pre-treatments, i.e., pre-oxidation and MgO addition, of the magnetite ore fines to maintain the fluidization state. The influence of pre-oxidation temperature, oxidation degree and the addition amount of MgO on the fluidization and reduction behaviors of the magnetite iron ore fines are analyzed. The result shows that the raw magnetite iron ore fines are de-fluidized when reduction degree reaches only around 20%. At a temperature of 600 ℃, the de-fluidization can be avoided by a prior oxidation treatment. At higher reduction temperatures, 650-800 ℃, the fluidization behavior can be further enhanced by an addition of 0.5 wt.-% MgO. The magnetite sample with higher oxidation temperature (1000 ℃) shows better fluidization behavior. While lower oxidation temperature (800 ℃) is more beneficial for the reduction rate, especially in the later reduction stage. The influence of pre-oxidation degree of the magnetite sample on its fluidization and reduction behaviors can be ignored. The primary and secondary influencing factors are oxidation temperature, pre-oxidation degree, MgO addition amount, and gas velocity. The optimum condition is that the magnetite iron ore is

deeply oxidized at 800 °C, mixed with 1.5 wt.% of MgO powder, and reduced in the fluidized bed at a gas velocity of 0.45 m/s.

As for the oxidation of magnetite samples, the oxidation rate peaks appear at around 330 °C and 550 °C, which indicates the appearance of $\gamma\text{-Fe}_2\text{O}_3$ and $\alpha\text{-Fe}_2\text{O}_3$. Theoretically, the surface energies of the hematite (104) and (110) crystal surfaces are larger than that of the (113) crystal surface. Hence, the hematite crystals may preferentially orient themselves along the (104) or (110) crystal surfaces. Therefore, the hematite phase shows a particular growth habit. The oxidation first occurs at the surface forming the grid-like hematite structures and then extends to the inside resulting in hematite needles. The specific surface area and pore volume decrease significantly during the oxidation due to the sintering effect. Based on in situ high-temperature X-ray diffraction (HT-XRD) analysis, the lattice constants of Fe_3O_4 and $\alpha\text{-Fe}_2\text{O}_3$ increase with an increase in temperature because of thermal expansion. The lattice constants can be successfully fitted with temperature by second-order polynomials. With Fe_3O_4 being oxidized into $\alpha\text{-Fe}_2\text{O}_3$, the $\alpha\text{-Fe}_2\text{O}_3$ crystallite grows.

Kurzfassung

Die Europäische Union (EU) hat das Ziel, bis 2050 Klimaneutralität (Netto-Null-Treibhausgasemissionen) zu erreichen. Derzeit wird in EU etwa 60 % des Rohstahls im Hochofen-LD Konverter Verfahren (BF-BOF) hergestellt. Obwohl das BF-BOF Verfahren eine hohe Produktionseffizienz aufweist, erzeugt es mehr CO₂ pro Tonne Rohstahl als alternative Stahlerzeugungsmethoden. Ein vielversprechendes Konzept für die zukünftige Rohstahlerzeugung ist die Verwendung einer wasserstoffbasierten Wirbelschicht zur Herstellung von wasserstoffdirektreduziertem Eisen (HDRI), gefolgt von einem Elektrolichtbogenofenprozess (EAF). Um das Fluidisierungs- und Reduktionsverhalten von Magnetit-Eisenerzfeinteilen während der wasserstoffinduzierten Wirbelschichtreduktion zu verbessern, werden verschiedene Vorbehandlungen des Materials untersucht. Darüber hinaus werden das Oxidationsverhalten und der Mechanismus von Magnetit-Eisenerzen untersucht, um die Voroxidationsbehandlung zu optimieren.

In dieser Studie werden Vorbehandlungen wie Voroxidation und MgO-Beschichtung von Magnetit-Feinerz getestet, um den gewünschten Fluidisierungszustand zu erreichen. Der Einfluss der Voroxidationstemperatur, des Oxidationsgrades und der Menge an MgO auf das Fluidisierungs- und Reduktionsverhalten der Magnetit-Eisenerzfeinstoffe wird analysiert. Die Ergebnisse zeigen, dass das unbehandelte Magnetit-Eisenerz im untersuchten Temperaturbereich zwischen 600 °C und 800 °C nicht erfolgreich fluidisiert werden kann. Bei einer Reduktionstemperatur von 600 °C kann die Entfluidisierung jedoch durch eine vorherige Oxidationsbehandlung vermieden werden. Bei höheren Reduktionstemperaturen kann das Fluidisierungsverhalten durch Zugabe von 0,5 Gew.-% MgO weiter verbessert werden. Proben mit einer höheren Oxidationstemperatur des Magnetit-Eisenerzes zeigen ein besseres Fluidisierungsverhalten, während eine niedrigere Oxidationstemperatur die Reduktionsrate begünstigt, insbesondere in der späteren Reduktionsphase. Der Oxidationsgrad der Magnetitproben zeigt keinen deutlichen Einfluss auf das Fluidisierungs- und Reduktionsverhalten. Die wichtigsten Einflussfaktoren sind die Oxidationstemperatur, der Oxidationsgrad, die Zugabemenge von MgO und die Gasgeschwindigkeit. Die optimale Bedingung besteht darin, das Magnetit-Eisenerz bei 800 °C stark zu oxidieren, mit 1,5 Gew.-% MgO-Pulver zu mischen und in der Wirbelschicht bei einer Gasgeschwindigkeit von 0,45 m/s zu reduzieren.

Bei der Oxidation der Magnetitproben zeigen sich deutliche Spitzenwerte der Oxidationsrate bei etwa 330 °C und 550 °C, was auf die Bildung von $\gamma\text{-Fe}_2\text{O}_3$ und $\alpha\text{-Fe}_2\text{O}_3$ hinweist. Besonders interessant ist die Wachstumsform der Hämatitphase. Theoretisch gesehen sind die Oberflächenenergien der (104)- und (110)-Kristallobereflächen größer als die der (113)-Kristalloberefläche. Daher neigen die Hämatitkristalle dazu, sich bevorzugt entlang der (104)- oder (110)-Kristallflächen auszurichten. Die Oxidation beginnt zunächst an der Oberfläche, wodurch gitterartige Hämatitstrukturen entstehen, und breitet sich dann im Inneren aus, was zur Bildung von Hämatitnadeln führt. Während des Oxidationsprozesses nimmt die spezifische Oberfläche und das Porenvolumen aufgrund des Sinterungseffekts erheblich ab. In-situ-Hochtemperatur-Röntgenbeugungsanalysen (HT-XRD) zeigen, dass die Gitterkonstanten von Fe_3O_4 und $\alpha\text{-Fe}_2\text{O}_3$ mit steigender Temperatur aufgrund der Wärmeausdehnung zunehmen und erfolgreich durch Polynome zweiter Ordnung an die Temperatur angepasst werden können. Beim Übergang von Fe_3O_4 zu $\alpha\text{-Fe}_2\text{O}_3$ erfolgt ein Wachstum der $\alpha\text{-Fe}_2\text{O}_3$ -Kristallite.

Acknowledgement

First of all, I would like to sincerely thank my PhD supervisor Prof. Dipl.-Ing. Dr.techn. Johannes Schenk for his guidance and helpful suggestions. I appreciate the opportunity you've given me to study and work in your group. I enjoyed every discussion I had with him. I learnt countless fruitful knowledge from him not only on scientific works but also life experiences. I am glad and proud to be his first full-time Chinese PhD student.

I am grateful to my mentor Prof. Mag. rer. nat. Dr.Frank Melcher for his generous help in the lectures about minerals. I am impressed by his extensive knowledge of worldwide ore deposits and mineral properties.

I would like to thank Dipl.-Ing. Dr.mont. Daniel Spreitzer for his kind support during my research work. He is consistently supportive and eager to share his wealth of knowledge. Without his guidance, it would have taken much longer time for me to start my research work. I extend my gratitude to my nice colleagues Dipl.-Ing. Oday daghaghele, Mr. Harald Mayrhofer, Dipl.-Ing. Andreas Pfeiffer, Dipl.-Ing. Michael Andreas Zarl, Dipl.-Ing. Thomas Wolfinger and, Dipl.-Ing. Bernd Taferner for their unwavering support and assistance in helping me acclimate to the new environment. Also, all the colleagues that I met are kind and helpful. If there is no page limitation, I would include all your names. Nevertheless, all the memories are engraved in my mind. I am also very grateful to the Chinese community in Leoben. All the Chinese friends make me feel less homesick. I will never forget the times that we went hiking, climbing, camping, celebrating and travelling together. I hope the dreams of all of us will come true one day.

I am extremely grateful to my wife Pian Lu for her support and understanding. COVID-19 came before I had a chance to get used to life in Austria. Due to the pandemic, we haven't

seen each other for more than 3 years. Her concern took away my anxieties and fears. She is my motivation to keep moving on. I am very thankful to my parents for their love, support and encouragement. I also wish to express my gratitude to my sister and her husband for taking care of our parents during my absence from home, especially during the pandemic period. In the end, I would like to thank myself for every effort that I made in the past four years.

Thesis structure

This work is a cumulative Ph.D. thesis that consists of two parts. Part I includes the background and purpose of this work, where a literature review, a theoretical consideration, experimental methodology and an executive summary of the Ph.D work are introduced. Part II of this thesis presents the comprehensive outcomes and conclusions in the form of a series of journal papers. Six published journal papers, Publication 1 - Publication 6, are included. The attached journal papers in Part II having obtained the necessary permissions from the publishers.

Table of contents

Abstract	I
Kurzfassung	III
Acknowledgement	V
Thesis structure	VII
Nomenclature	XI
Abbreviations	XII
List of Figures	XIV
List of Tables	XVIII
1 Introduction	1
1.1 Background	1
1.2 Purpose of the work.....	3
2 Literature review	4
2.1 Production routes of crude steel	4
2.1.1 Direct reduction process using iron ore fines	6
2.1.1.1 The Circored® process.....	8
2.1.1.2 The Finmet® process	9
2.1.1.3 The HyREX process	10
2.1.1.4 The HyFOR process	11
2.2 Fluidization behaviors – General considerations.....	12
2.2.1 Determination of the operating point	12

2.2.2	De-fluidization phenomena caused by the sticking iron	14
2.2.2.1	Surface iron whiskers	14
2.2.2.2	Highly active surface iron	18
2.2.3	Prevention methods to sticking problem	19
2.3	Oxidation of magnetite in particle scale.....	21
2.3.1	Stages of the oxidation process	21
2.3.2	Thermodynamics of magnetite oxidation.....	22
2.3.3	Rate-limiting analysis of oxidation reaction	23
2.3.3.1	Parabolic law	25
2.3.3.2	The nucleation and growth	28
2.3.3.3	Discussion on the kinetic models	30
2.3.4	The influence of oxidation of magnetite on its subsequent reduction	31
3	Methodology	32
3.1	Reduction experiments	32
3.1.1	Apparatus	32
3.1.2	Procedures	34
3.1.3	Determination of reduction degree (RD) and de-fluidized index (DFI)	35
3.2	Oxidation experiments	36
3.2.1	Apparatus and procedures	36
3.2.2	Determination of oxidation capacity index (OCI)	39
3.2.3	HT-XRD data treatment.....	40
3.2.3.1	Determination of lattice constants	41
3.2.3.2	Determination of crystallite size.....	41
3.2.3.3	Determination of oxidation degree.....	42
3.3	Characterization methods	43
4	Results and discussions	44
4.1	Reduction of magnetite iron ore fines in a hydrogen-induced fluidized bed	44
4.1.1	Effect of pre-oxidation.....	44
4.1.2	Effect of MgO addition	47
4.1.3	Multistep kinetic analysis	48
4.2	Parameter optimization for the hydrogen-induced fluidized bed reduction of magnetite iron ore fines	50
4.2.1	Reduction under various conditions	50
4.2.2	Orthogonal experiment analysis	53
4.3	The oxidation behavior of the magnetite iron ore fines	57

4.3.1	The oxidation capacity index	57
4.3.2	Structural evolution	59
4.3.3	Pore structure parameters based on N ₂ adsorption	61
4.3.4	Oxidation mechanism	62
4.4	Phase transition of magnetite via in situ high-temperature X-ray diffraction	64
4.4.1	Oxidation degree	64
4.4.2	Evolution of lattice constants	66
4.4.3	Evolution of crystallite size of Fe ₂ O ₃	68
5	Main conclusion.....	70
6	List of references	72

Nomenclature

d_p	Particle Diameter
D	Self-diffusion Coefficient
F_d	Drag Force
F_c	Cohesive Force
ICP - MS	Inductively Coupled Plasma-mass Spectrometry
k_p	Parabolic Rate Constant
M_g	Gravity Force
$\Delta p_{\text{measured-bed}}$	Pressure Drop across Bed Material
$\Delta p_{\text{calculated-bed}}$	Theoretical Pressure Drop over Material
$\Delta p_{\text{fixed-bed}}$	Pressure Drop when the material is in a fixed bed state
$t_{90\%}$	Time to reach RD=90%
u_{slip}	Slip Velocity
u	Superficial Velocity
ν	Kinematic Gas Viscosity
V_p	Particle Volume
V_b	Bed Volume
ρ_p	Particle Density
ρ_g	Gas Density
ε	Bed porosity

Abbreviations

AKM	Avrami kinetic model
Ave.DFI	Average De-fluidization Index
Ar	Archimedes Number
BF	Blast Furnace
BOF	Basic Oxygen Furnace
B.E.T.	Brunauer-Emmet-Teller
B.J.H.	Barrett–Joyner–Halenda
CFB	Circulating fluidized bed
DRI	Direct Reduced Iron
DFI	De-fluidization Index
DES	Energy Dispersive Spectroscopy
DOX ₁₂₅₋₂₅₀₋₁₀₀₀	Particle size with 125-250 μm and deeply oxidized at 1000 °C
POX ₁₂₅₋₂₅₀₋₈₀₀	Particle size with 125-250 μm and partly oxidized at 1000 °C
DOX ₁₂₅₋₂₅₀₋₈₀₀	Particle size with 125-250 μm and deeply oxidized at 800 °C
EU	European Union
EAF	Electric Arc Furnace
FB	Fluidized bed
Fr*	Modified Froude Number
HDRI	Hydrogen Direct Reduced Iron
HT-XRD	High-Temperature X-ray Diffraction
HBI	Hot Briquetted Iron
ICTAC	International Confederation for Thermal Analysis and Calorimetry
JMA	Johnson-Mehl-Avrami
LOI	Loss on Ignition
OCI	Oxidation Capacity Index
PAS	Positron Annihilation Spectroscopy
Re	Reynold Number
RD	Degree of Reduction
RIR	Relative Intensity Ratio
RMSD	Root-mean-square Deviation
SATP	Standard Ambient Temperature and Pressure

SEM	Scanning Electron Microscopy
TGA	Thermogravimetric Analysis
ULCOS	European Ultra Low CO ₂ Steelmaking
Ω	Liatschenko number

List of Figures

Figure 1: Different state of the art steel production route [30].	5
Figure 2: Global crude steel production by process route in 2019 [33].	6
Figure 3: Comparison of CO ₂ emissions by process route, tons CO ₂ per ton crude steel [34].	6
Figure 4: The world DRI production by year [35].	7
Figure 5: Direction reduction processes using iron ore fines [11].	7
Figure 6: The Circored [®] process flowsheet [37],[38].	8
Figure 7: Schematic flowsheet of the Finmet [®] process [39].	10
Figure 8: Schematic flowsheet of the HyREX process [40],[41].	11
Figure 9: Schematic flowsheet of the HyFOR process [13].	12
Figure 10: Reh-diagram for gas-solid systems.	13
Figure 11: Schematic of Iron activity curves and phase configuration: (a) under diffusion control; (b) under mixed control; (c) under chemical control [46].	15
Figure 12: Schematic illustration of the reduction of iron ore particle [45].	16
Figure 13: Surface morphology of reduced iron under different conditions (a) pure CO; (b) CO:H ₂ =90%:10%, (c) CO:H ₂ =70%:30%, (d) pure H ₂ ; Polished section images of the samples reduced by (e) pure CO and (f) pure H ₂ ; (g) is the mechanistic diagram of the precipitation mechanism of iron under different reducing gases.	17
Figure 14: Schematic diagram of iron formation on the surface of FeO. (Purple, red, gray and white balls represent the Fe, O, C and H atoms, respectively.) [50].	18
Figure 15: (a)-(c) Iron bridge between particles [52]–[54], (d) Sticking mechanism resulting from Fe atom diffusion [43].	19
Figure 16: Stages of magnetite during non-isothermal oxidation.	21
Figure 17: Binary Fe-O system. Reproduced with permission.	22
Figure 18: Stable region of Fe ₃ O ₄ and Fe ₂ O ₃ . (Calculated by Fact Sage 7.2, Database: FactPS, FToxid).	23

Figure 19: Schematic of oxidation facilities and sample containers	24
Figure 20: Schematic illustration of the oxidation kinetics: (a-b) in pellet scale; (c-d) in particle scale.....	25
Figure 21: The schematic of hematite sub-grains in an oxidized magnetite particle: (a) under reflected light; (b) under polarized light.....	25
Figure 22: The calculated parabolic rate constants in different temperatures and partial pressures [77].	26
Figure 23: (a) Isothermal oxidation evaluated by the solid-state diffusion: (a)different oxidation temperature; (b) different partial pressure of oxygen [81].	28
Figure 24: Isothermal oxidation evaluated by the nucleation and growth: (a) different oxidation temperature; (b) different partial pressure of oxygen [81].	29
Figure 25: Conversion curve as a function of time. Curve P ₁ is a single Avrami equation; curve P ₂ is a single diffusion equation [84].	30
Figure 26: Schematic layout of laboratory fluidized bed reactor: 1. gas mixture unit; 2. three-stage electrical furnace; 3. distributor; 4. fluidized bed reactor; 5. dust filter; 6. scale; 7. pressure regulator; 8. differential pressure monitor; 9. temperature control; 10. computer system unit.....	33
Figure 27: Laboratory fluidized bed reactor: (a) reactor, (b) gas supply system. 1. gas supply pipe; 2. gas preheating section; 3. fluidized bed reactor; 4. dust filter; 5. pressure regulator; 6. differential pressure monitor; 7. three-stage electrical furnace; 8. scale; 9. mass flow controllers; 10. evaporator.	33
Figure 28: The furnace for pre-oxidation treatment: (a) the outlook of the furnace; (b) the material being oxidized.....	35
Figure 29: STA 409 PG thermal analyzer: (a) the outlook of the device; (b) schematic layout of the device from side direction.....	37
Figure 30: Material for isothermal oxidation.....	38
Figure 31: The sample after HT-XRD measurement.....	39
Figure 32: Temperature profile for HT-XRD measurements: (a) non-isothermal HT-XRD; (b) isothermal HT-XRD.	39
Figure 33: Rietveld refinement peak profile of Ore B at different temperatures under non-isothermal condition: (a) 600 °C and (b) 800°C.	40

Figure 34: Schematic of Fe ₂ O ₃ crystal: (a) (110) plane and (b) (104) plane.	42
Figure 35: Reduction degree and de-fluidization index of raw sample and deeply oxidized sample at reducing temperature of 600 °C: (a) RD / DFI of raw sample; (b) RD / DFI of deeply oxidized sample.....	45
Figure 36: Polished section images of the raw sample and deeply oxidized sample after reduction tests at 600 °C under optical light microscope: (a), (b) raw sample; (c), (d) deeply oxidized sample.....	45
Figure 37: Fluidization and reduction behaviors of raw sample and deeply oxidized sample: (a) fluidization time; (b) reduction degree when de-fluidization starts.	46
Figure 38: Influence of MgO on reduction behavior: (a), (c) reduction degree curves; (b), (d) reduction rate.	48
Figure 39: Fitting results for deeply oxidized sample with different amount of MgO: (a) 0.25 wt.-%; (b) 0.5 wt.-%; (c) 1.0 wt.-%; (d) 1.5 wt.-%.	49
Figure 40: Effect of pre-oxidation temperature on the fluidization and reduction behaviors: (a) reduction degree and DFI; (b) reduction time to reach a specific RD.	51
Figure 41: Effect of pre-oxidation degree on the fluidization and reduction behaviors: (a) reduction degree and DFI; (b) reduction time to reach a specific RD.	51
Figure 42: The reduced samples with the particle size of 125-250 μm: (a) surface morphology of DOX ₁₂₅₋₂₅₀₋₁₀₀₀ ; (b) surface morphology of DOX ₁₂₅₋₂₅₀₋₈₀₀ ; (c) surface morphology of POX ₁₂₅₋₂₅₀₋₈₀₀ ; (d),(g) polished-section images of DOX ₁₂₅₋₂₅₀₋₁₀₀₀ ; (e),(h) polished-section images of DOX ₁₂₅₋₂₅₀₋₈₀₀ ; (f),(i) polished-section images of POX ₁₂₅₋₂₅₀₋₈₀₀ . Images of (a)-(c) were obtained by SEM; Images of (d)-(i) were obtained by optical microscope.	53
Figure 43: The fluidized reduction results of experiments No.6 and No.10: (a) reduction curve; (b) de-fluidization curve. P800-1.5%-0.45 represents that the magnetite iron ore is partly oxidized at 800 °C, mixed with 1.5 wt.% of MgO and reduced in the fluidized bed at a gas velocity of 0.45 m/s; D800-1.5%-0.45 represents that the magnetite iron ore is deeply oxidized at 800 °C, mixed with 1.5 wt.% of MgO and being reduced in the fluidized bed at a gas velocity of 0.45 m/s.	56
Figure 44: Oxidation TG-DTG curves of the samples: (a) TG curve of samples; (b) TG-DTG curve of Sample A; (c) TG-DTG curve of Sample B; (d) TG-DTG curve of Sample C.	58
Figure 45: SEM images of the oxidized products of Sample A obtained under different duration times: (a) 0 min, (b) 2 min, (c) 5 min, (d) 10 min, (e) 20 min, (f) 30 min, (g) 60 min, (h) 120 min.	59

Figure 46: SEM images of the oxidized products of Sample B obtained under different duration times: (a) 0 min, (b) 2 min, (c) 5 min, (d) 10 min, (e) 20 min, (f) 30 min, (g) 60 min, (h) 120 min.	60
Figure 47: SEM images of the oxidized products of Sample C obtained under different duration times: (a) 0 min, (b) 2 min, (c) 5 min, (d) 10 min, (e) 20 min, (f) 30 min, (g) 60 min, (h) 120 min.	60
Figure 48: Polished section images of the oxidized samples obtained under different duration times: (a)-(d) Ore A under 0, 2, 5 and 60 min; (e)-(h) Ore B under 0, 5, 30 and 120 min; (i)-(l) Ore C under 0, 2, 30 and 120 min.	61
Figure 49: Pore size distribution of the samples: (a), (d) Ore A; (b), (e) Ore B; (c), (f) Ore C.	62
Figure 50: The schematic of the oxidation mechanism of magnetite: (a) the Fe^{2+} cation turns into the Fe^{3+} cation; (b) later oxidation period.	63
Figure 51: The oxidation process of a single magnetite particle.....	64
Figure 52: In situ HT-XRD patterns at different temperatures: (a), (b) Ore B; (c), (d) Ore C.	65
Figure 53: The oxidation degrees of Ore B and C at different temperatures: (a) Ore B; (b) Ore C.	65
Figure 54: The lattice constant of Fe_3O_4 as a function of temperature measured by high-temperature X-ray diffraction during oxidation of Fe_3O_4 in air.	67
Figure 55: The relative increase in lattice parameters a and c of Fe_2O_3 at different temperatures [121],[128].	68
Figure 56: The lattice constants of Fe_2O_3 as a function of temperature: (a) lattice constant a; (b) lattice constant c.	68
Figure 57: The crystallite sizes of Ore B and Ore C along the a/b axis and the c axis of a unit cell at different temperatures: (a) Ore B; (b) Ore C.	69

List of Tables

Table 1: Important dimensionless numbers.	13
Table 2: The self-diffusion coefficients for iron in magnetite and hematite.	27
Table 3: The parabolic rate constants.....	27
Table 4: Chemical compositions of the sample, (wt.-%).....	34
Table 5: Experimental conditions of the publications 1-3.	35
Table 6: Chemical analysis of the raw magnetite samples, (wt.-%).....	36
Table 7: Particle size distributions and density of the raw magnetite samples.	37
Table 8: Fluidization state of the raw sample and the deeply oxidized sample	46
Table 9: Influence of MgO addition on the fluidization behavior and the final RD.....	48
Table 10: Kinetic analysis for Sample B with different amount of MgO	49
Table 11: Orthogonal experimental factors and levels.	54
Table 12: Orthogonal experimental plan.....	54
Table 13: The orthogonal experimental result.....	55
Table 14: The orthogonal experimental analysis regarding $t_{90\%}$	55
Table 15: The orthogonal experimental analysis regarding Ave.DFI.....	55
Table 16: The characteristic parameters of the oxidation.....	58
Table 17: The pore structure parameters of the samples within different duration times.	62

Table 18: The lattice constant and volume of the Fe_3O_4 cell measured by high-temperature X-ray diffraction during the oxidation of Fe_3O_4 in air.66

Table 19: The lattice constant and volume of the Fe_2O_3 cell67

Part I:

1 Introduction

1.1 Background

The European Union (EU) aims to reach the target of climate neutrality (net-zero greenhouse gas emissions) by 2050 [1]. It is noticed that, about 60 % of the crude steel production from Europe is based on the blast furnace-basic oxygen furnace (BF–BOF) route [2]. The BF-BOF route shows high production efficiency but produces more CO₂ than other alternative steelmaking routes. The steelmaking industry remains a significant contributor to CO₂ emissions in Europe, accounting for 4% of the total CO₂ emissions within the EU. [3]. The breakthrough technologies are required to further cut down CO₂ emissions [1,4,5]. Many different alternative steelmaking processes have already been explored under the European Ultra Low CO₂ Steelmaking (ULCOS) program [4],[5]. A promising research topic is using H₂ as a reducing agent instead of CO [6]–[10]. As a result, carbon dioxide is no longer generated during iron oxide reduction.

Numerous industrial ironmaking process employ shaft furnaces or fluidized bed reactors as the reduction units [11],[12]. Generally, the fluidized bed shows better reduction efficiency because of faster mass and heat transfer. A hydrogen-based reduction process using fine ore known as HYFOR, developed by Primetals Technologies, stands as a notable achievement [13]. However, a significant decrease in reduction efficiency will occur when the de-fluidization happens. This refers to the situation where iron ore fines are not fluidized by the gas flow. Thereafter, the process of the fluidized bed system cannot be controlled. Within a fluidized bed, the surface fresh metallic iron is sticky and shows a high probability to form iron aggregates

[14]. Therefore, how to prevent the de-fluidization in a fluidized bed reactor is of great importance.

High-grade hematite-based iron ores are not sufficient for ironmaking, which were used as the iron carrier in the blast furnace process. The price of high-grade hematite-based iron ores is going higher. Magnetite-based iron ores are abundant and occur naturally [15]. In the year 2015, the global production of iron ore derived from magnetite reached around 583 million tons, accounting for approximately 28% of the total iron ore production [16]. Typically, magnetite-based iron ore is subjected to grinding into finer particle sizes to liberate magnetite minerals from the host rock matrix. Subsequently, a process of magnetic separation is employed to enhance the iron content [15],[17]. Most of the ironmaking routes using magnetite-based iron ores as raw material still require a pelletization process [18] or sintering process [19] to achieve a suitable size range. These facilities include, for example, blast furnace [20]–[22], grate-rotary kiln [23] and Midrex shaft furnace [24],[25]. If the magnetite ore fines after beneficiation could be used in particle scale without granulation, a lot of energy and CO₂ emissions could be avoided. To achieve such a goal, a viable approach is employing a hydrogen-based fluidized bed for producing hydrogen direct reduced iron (HDRI). The HDRI can subsequently be introduced into an electric arc furnace (EAF) or smelter for subsequent processing. This strategy has the potential to decrease CO₂ emissions to a range of 25-53 kg per ton of crude steel [26],[27].

The reduction of iron oxides by H₂ is an endothermic reaction. In order to secure an adequate energy supply, it is necessary to carry out the pre-heating of iron ore in an independent heating unit. Generally, the preheating process occurs in oxidizing atmosphere, such as hot air. Consequently, the magnetite iron ore is to be oxidized. The oxidation of magnetite is an exothermic reaction which generates a lot of heat. This heat generation is advantageous in reducing the primary energy required for pre-heating. Drawing from prior research conducted by Daniel Spreitzer [28], it was observed that in an H₂-induced fluidized bed reactor, magnetite-based iron ore exhibited the poorest reducibility and least favorable fluidization behaviors. It was attributed to the formation of a dense iron shell on the particle surface. A pre-oxidation treatment could improve the reduction efficiency and fluidization behaviors significantly. Hence, it becomes important to explore the influence of distinct pre-oxidation treatments, including varying pre-oxidation temperatures and degrees, on the fluidization and reduction behaviors of magnetite ore fines. It is also of great importance to understand the oxidation mechanisms of magnetite ore fines for optimizing the process route.

1.2 Purpose of the work

This thesis deals with how to produce HDRI using magnetite ore fines without prior agglomeration. On the one hand, when pure hydrogen is used as a reducing agent, the CO₂ emissions are directly avoided. On the other hand, magnetite ore fines are used directly without prior agglomeration. For a stable process of the fluidized bed reactor, some pre-treatments of the magnetite ore fines are tested. The research conducted in this thesis can be categorized into four work packages. The first two work packages are about the fluidization and reduction behaviors of the magnetite ore fines with pre-treatments. The last two work packages focus on the pre-oxidation treatment of magnetite fines before being charged into the fluidized bed reactor.

1. The first aim of this research is to test some pre-treatments, i.e., pre-oxidation and MgO coating, of the magnetite ore fines to maintain the fluidization state. The influence of pre-oxidation temperature, pre-oxidation degree and the amount addition of MgO on the fluidization and reduction behaviors of the magnetite ore fines are tested. The kinetic analysis is conducted to understand the reduction mechanisms.
2. The ultimate goal is to confirm the optimal condition for processing the magnetite ore fines. After testing the influence of several parameters, the proper operating parameter through an orthogonal experimental method is confirmed. The primary factors influencing the fluidization and reduction behaviors of magnetite ore fines can be identified.
3. The proposed HDRI production route involves a prior oxidation treatment occurring in the preheating stage, which improves both fluidization and reduction behavior. It is, therefore, crucial to study the oxidation of magnetite ore fines to optimize the proposed process pathway. The oxidation behavior, pore structure, surface morphology and internal structure of the magnetite ore fines after pre-oxidation treatment are studied.
4. To gain a more profound understanding of the phase transformation from magnetite to hematite at a crystal level, the in situ high-temperature X-ray diffraction (HT-XRD) technique is employed to analyze the phase transition. Quantitative details regarding crystal characteristics, including lattice constants, crystallite size, and phase fractions at varying temperatures, are acquired through this approach.

2 Literature review

This chapter encompasses a comprehensive review of existing literature in accordance with the scope of this thesis. A brief description of the steel production routes is given, especially the processes involving smelting reduction and direct reduction. General considerations of fluidization phenomena, including the determination of fluidization regimes, de-fluidization mechanisms and methods to prevent sticking problems, are reviewed. In addition, the oxidation behaviors of magnetite in particle scale are introduced in both thermodynamics and kinetics aspects. The impact of magnetite oxidation on its subsequent reduction process is thoroughly examined and discussed. The discussion on the reduction of iron oxide by H_2 is not repeated here because this aspect has been systematically reviewed somewhere else. [29].

2.1 Production routes of crude steel

The production of crude steel consists of three important stages: raw material preparation, iron making and steel making. As shown in Figure 1, generally four types of production routes are available in the world [30]. The production routes are distinguished by the input material, the reducing agent, the energy source and the product state (solid or liquid) in the iron making stage. When iron ore is used as an iron carrier, three production routes are defined, namely, the integrated route, smelting reduction route and direct reduction route. If the scrap is used as metallic charge, the iron making section is not necessary. The scrap melts in the EAF and the crude steel production mainly happens in EAF.

The product in iron making stage of the integrate route and smelting production route is hot metal which is in liquid state. The hot metal is charged into BOF for further steel making. The

product from direct reduction route in iron making stage is so-called direct reduced iron (DRI) or hot briquette iron (HBI) which is in solid state. The furnace for the following steel making can also be EAF.

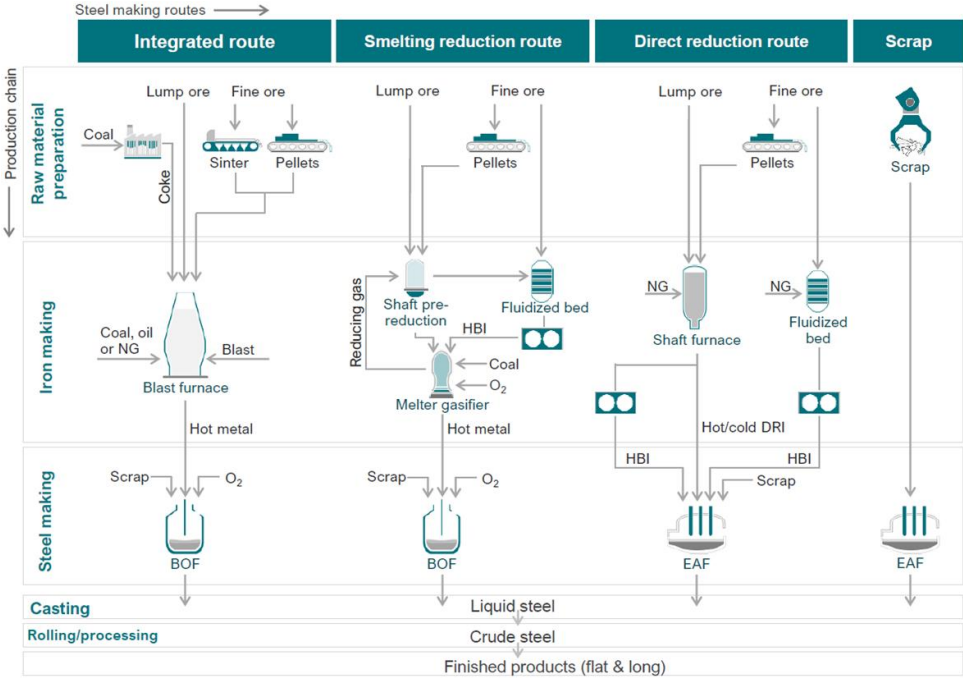


Figure 1: Different state of the art steel production route [30].

The global crude steel production was 1811 million tons in 2019 and slightly increased to 1821 and 1888 million tons in 2020 and 2021, respectively [31]. As shown in Figure 2, the dominant crude steel production route is still the integrate route, accounting for 70% [33]. The integrate route is also known as BF-BOF route, which first uses a BF to produce hot metal from iron ore and coal, and then uses a BOF to produce crude steel. However, the CO₂ emissions from this production route are enormous. Figure 3 shows the CO₂ emissions of different process route based on current technology [34]. The BF-BOF route, even with the best available technology, still emits 1.6 tons CO₂ per ton crude steel. If the CO₂ from BF-BOF route is captured, the emission can be reduced to 0.9 tons per ton crude steel. The smelting reduction route and direct reduction route emit 1.5 tons and 1.1 tons CO₂ per ton crude steel, respectively. The lowest CO₂ emission route is the scrap based EAF, which only emits 0.4 CO₂ per ton crude steel.

To reach the target of CO₂ neutral within the process, the transformation from BF-BOF to EAF is a significant trend for future steelmaking [32]. Because of the constrained availability of high-quality scrap, there exists the possibility of partial substitution with DRI. The ongoing development of HDRI-EAF route has a high potential for reducing CO₂ emission. When EAF is operated with only HDRI, CO₂ emission can be reduced to 0.025-0.053 tons per ton crude

steel [26],[27]. Therefore, how to produce HDRI properly and efficiently becomes an interesting topic. In the coming section, several commercialized and developing processes for producing HDRI using iron ore fines are introduced.

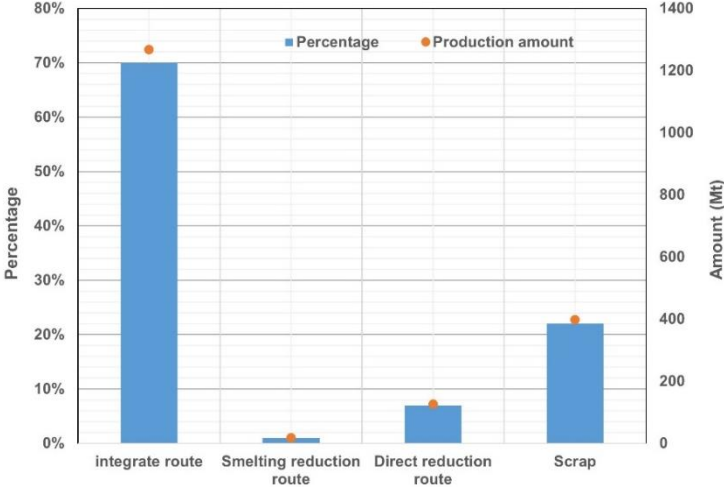


Figure 2: Global crude steel production by process route in 2019 [33].

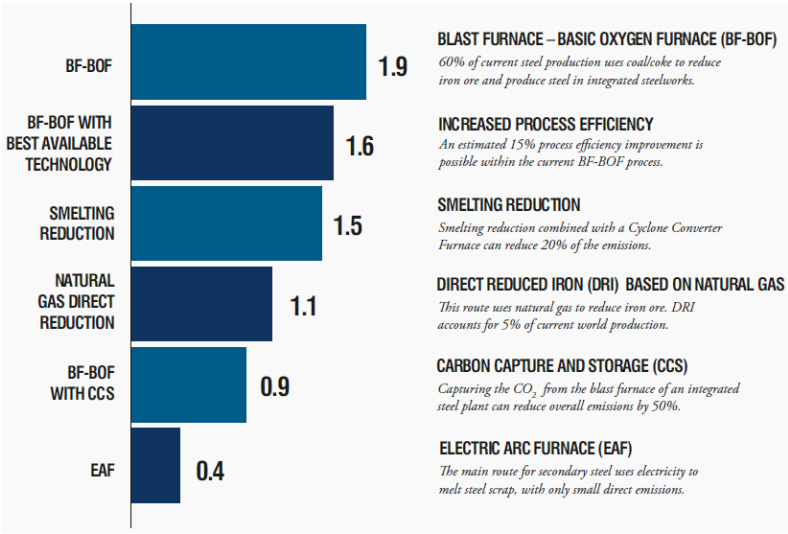


Figure 3: Comparison of CO2 emissions by process route, tons CO2 per ton crude steel [34].

2.1.1 Direct reduction process using iron ore fines

As mentioned above, the product of direct reduction route in iron making stage is in solid state. The reducing temperature is below the melting point of the input material. Conventionally, the reducing gas required for iron oxide reduction is derived from the partial oxidation of coal or the reforming of natural gas. As shown in Figure 4, the world DRI production amount is increasing yearly [35]. The two most widely used direct reduction processes are Midrex® and

HYL/Energiron, accounting for 59.5% and 12.7% of the total world production of DRI in 2021, respectively.

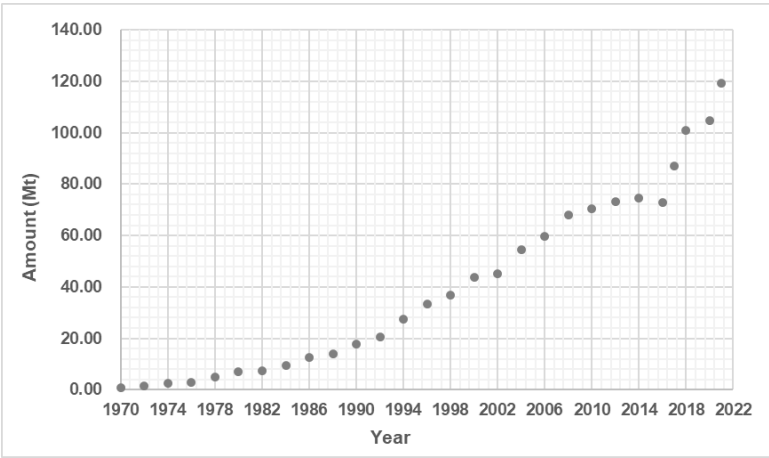


Figure 4: The world DRI production by year [35].

The above two processes are based on vertical shaft furnace, which requires iron ore pellet as the iron carrier. For the direct utilization of iron ore fines, several alternative approaches for DRI production involve the use of fluidized beds, rotary hearths, or rotary kilns. However, as shown in Figure 5, not many DR-processes are operating in industrial scale. The rotary hearth or rotary kiln-based DR process uses coal as an energy source which emits lots of CO₂ during the production [11]. When using fluidized bed as a reducing unit, it is possible to use natural gas and lower the CO₂ emissions. With the development of H₂ production technology, if natural gas is substituted by 100% green H₂, zero carbon emission can be achieved. In the following section, two commercialized and two in developing fluidized bed-based processes are introduced, namely, Circored® process, FINMET process, HyREX and HyFOR.

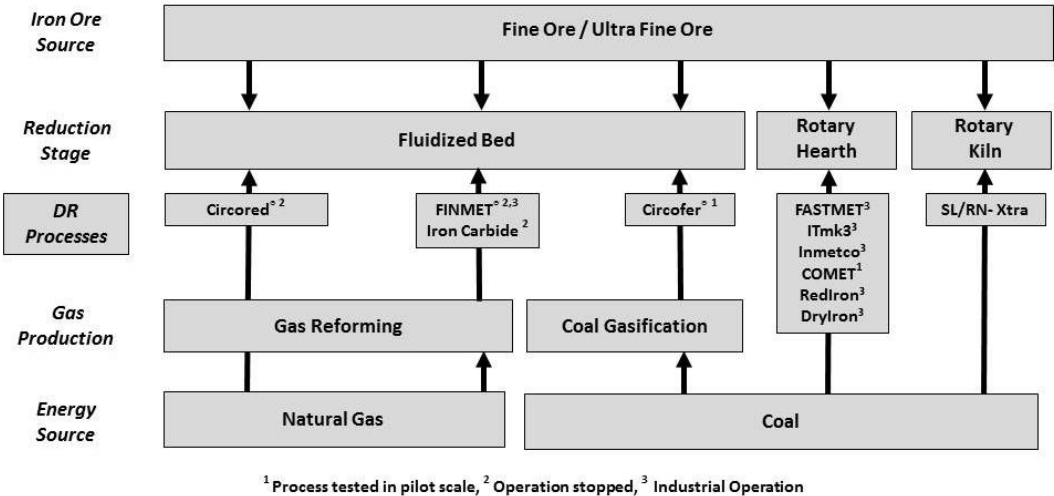


Figure 5: Direction reduction processes using iron ore fines [11].

2.1.1.1 The Circored® process

The Circored process, initially developed over 20 years ago, is currently being reintroduced as a validated method to assist the decarbonization of the ironmaking process. [36]. The Circored stands as the only 100% hydrogen-based process for iron ore reduction that has effectively showcased its operational efficacy and performance through an industrial-scale demonstration plant. The facility, initiated in 1999 in Trinidad, successfully generated more than 300,000 tons of premium-quality HBI during several months of productive functioning [37],[38].

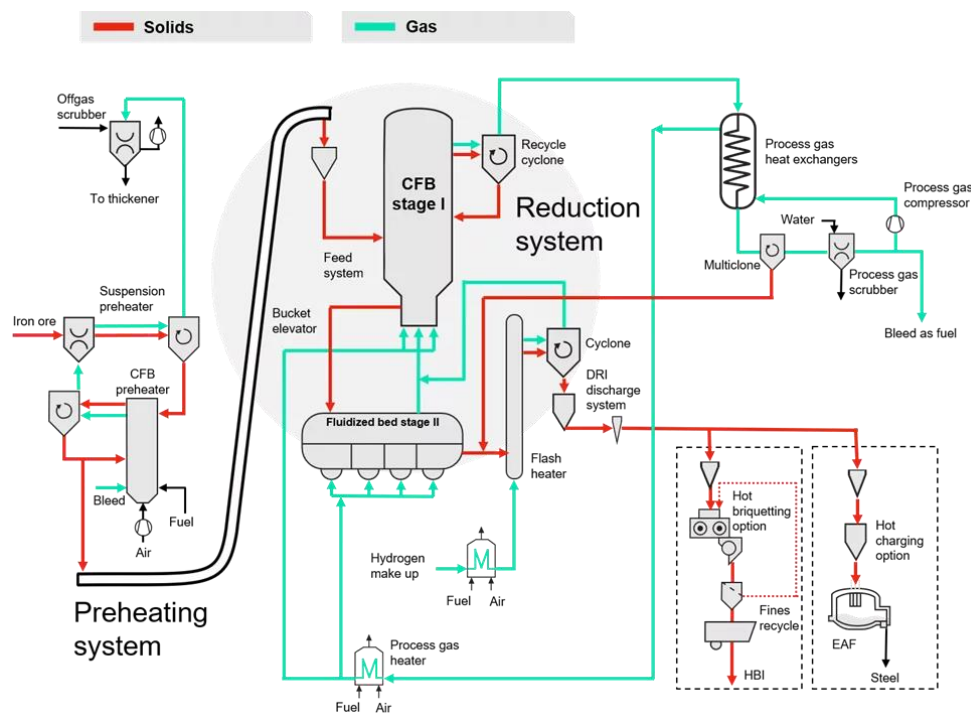


Figure 6: The Circored® process flowsheet [37],[38].

The Circored process employs a dual-stage reactor setup, beginning with a circulating fluidized bed (CFB) followed by a downstream bubbling fluidized bed (FB). In the presented flowchart, illustrated in Figure 6, the core process region for ore reduction is highlighted by the gray circle. The established plant capacity, considering technical and economic for an industrial-scale facility, is set as 1.25 million tons per year per line. Two or more lines are possible combined using joint facilities and utility areas. The main characteristics are given as follows [37],[38]:

1. The iron ore fines are preheated to 850 – 900 °C in the preheating system via a CFB reactor. For stable fluidization, the size of feeding iron ore is generally between 2 mm

and 6 mm. When ultrafines are used as raw material, a microgranulation device can be applied to assist the fluidization.

2. The duration time in the primary reduction stage is the range of 20 – 30 minutes. The iron ore burden is supposed to be reduced up a reduction degree of 65 – 80%.
3. The final reduction degree in FB reactor is 93 – 95%.
4. Hydrogen is used as the only reductant. The reducing temperature can be as low as 650 °C in the CFB and the FB. The low temperature prevents particle sticking and makes the reaction easy to control.
5. The reduced fines undergo heating in a flash heater, reaching temperatures of approximately 700 – 715 °C. During this stage, preheated make-up hydrogen is employed for both heating and transport purposes. The DRI is required to be around 680 °C for obtaining high-density HBI (> 5.0 g/cm³). To obtain the high density, the DRI should reach a temperature of approximately 680 °C.
6. The hydrogen reduction of iron oxide is an endothermic reaction, the energy must be continuously supplied during the operation. In the past, this was achieved by natural gas and process gas bleed. There is currently a plan to substitute natural gas with electric heating powered by renewable sources, often referred to as "green" power.

2.1.1.2 The Finmet® process

The Finmet process is also a fluidized bed based direct reduction process, which uses a four-stage fluidized bed reactor series [39]. The schematic flowsheet is shown in Figure 7. First of all, the gangue within the iron ore must be removed in a beneficiation plant. Initially, the iron ore fines undergo drying within a fluidized bed dryer, after which they are introduced into the reactor train through a pressurized lock hopper system. The pressure inside the reactor train is 12 bar. The feed of iron ore fines enters the upper reactor (R4), where it undergoes preheating to temperatures ranging between 550 and 570°C, facilitated by the reducing gas originating from reactor R3. The four reactors are interconnected with transfer lines for gas and solids. The solid iron ore fines flow downwards from reactor R4 to R1 under self-gravity force, while reducing gas flows counter currently upwards. Hence, the iron ore fines are reduced stepwise from hematite to magnetite, from magnetite to wüstite and finally to metallic iron. The temperature in the downmost reactor (R1) is in the range of 780-800 °C and final metallization degree is up to 93%. At this stage, some Fe is carburized to Fe₃C. The carbon content of the DRI can be flexibly altered by modifying the composition of the recycle gas introduced into R1. The hot DRI is then transported to the briquetting area where the DRI is briquetted at temperatures higher than 650 °C.

The reducing gas is sourced from a blend of recycled top gas and fresh reformer makeup gas, which is supplied through a conventional steam reformer. The recycled gas is from the top gas of R4 reactor. This top gas still contains valuable H₂ and CO gases. The top gas is initially cooled down to temperatures between 40-50 °C and subsequently subjected to wet scrubbing in a wet scrubber system. This procedure is employed to eliminate dust and water generated by the hydrogen reduction reactions. The recycled gas is split into two streams. One stream goes to a reductive gas heater burner for burning, the other one joins the fresh reformer makeup gas. In such a way, the accumulation of inert components (mainly N₂ and CH₄) can be avoided.

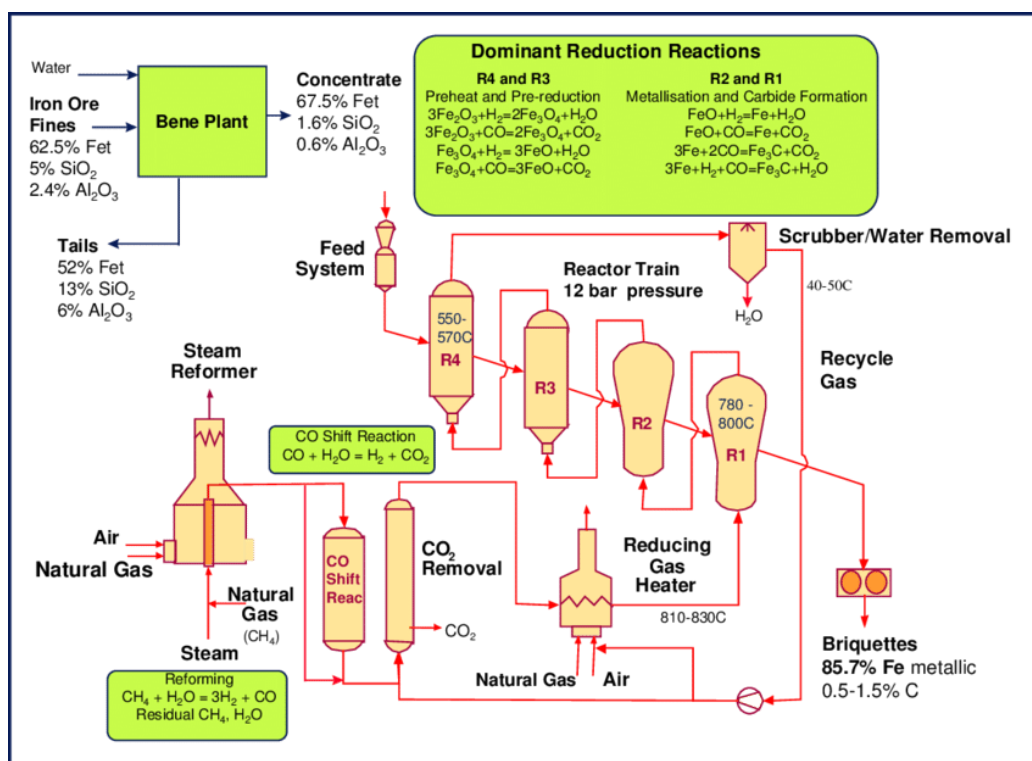


Figure 7: Schematic flowsheet of the Finmet® process [39].

2.1.1.3 The HyREX process

HyREX is a new ironmaking process based on fluidized bed reactors, which uses hydrogen as reducing agent [40],[41]. Similar to Finmet process, the core reduction unit is also a 4-stage fluidized bed reactor train. In a traditional blast furnace, the reduction and melting happen in the same furnace. However, these two reactions happen separately in HyREX, i.e., reduction in the fluidized bed reactors and melting in an electric furnace. Figure 8 shows the schematic flowsheet of the HyREX process. POSCO plans to skip the pilot stage testing and start the demonstration stage from 2025. The verification of HyREX technology shall be ready in 2030 based on the technologies and experience from FINEX process development [40],[41].

The FINEX process is a successful commercialized ironmaking process which has been operated for nearly 20 years. The HyREX process is based on fluidized reduction furnace technology applied to FINEX. The main difference is that the HyREX process uses electric smelting furnace to melt the DRI and the HyREX is able to use pure hydrogen as reducing gas and energy input. The burden of the process is sinter feed grade iron ore fines whose particle size is in a wide range. The heat for the reduction system is generated by the reaction of hydrogen and oxygen. The fluidized bed reactor train is arranged in a stair shape. The temperature of each fluidized bed reactor can be controlled by the injection of oxygen. To guarantee sufficient heat for the reduction reaction, the walls and the bottom part of the reactor can also provide additional heat.

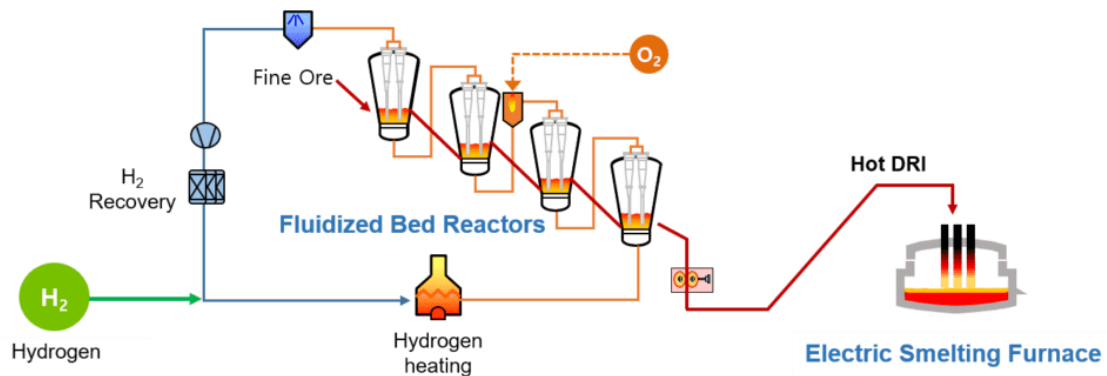


Figure 8: Schematic flowsheet of the HyREX process [40],[41].

2.1.1.4 The HyFOR process

A schematic flowsheet of the HyFOR process is shown in Figure 9. The HyFOR process also uses a four-stage fluidized bed reactor train. The difference with HyREX process is that the HyFOR process can use iron ore concentrates with particle sizes of 100% <150 μm [13]. The iron concentrates are preheated or oxidized in multistage cyclones. The energy needed for preheating is provided by the reaction of hydrogen and air. Part of the bleed gas from the recycle gas loop also goes to the heat generator. The iron concentrates are then charged into a bin that works as a buffer controlling the input of the iron concentrates to the first fluidized bed reactor. The reduction of iron oxide occurs stepwise in the fluidized bed train. Fresh reducing gas is injected in each fluidized bed reactor. The off gas of all reactors is dedusted via a dry dedusting unit. The dust is returned to the reactors. An industrial plant of HyFOR might be operational by 2025.

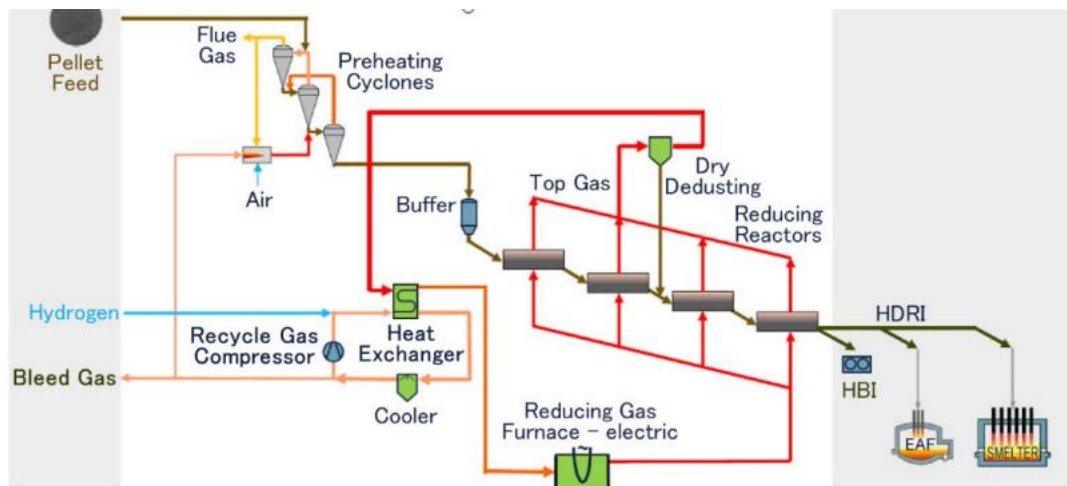


Figure 9: Schematic flowsheet of the HyFOR process [13].

2.2 Fluidization behaviors – General considerations

First of all, it is important to determine the operating point of a fluidized bed and predict the fluidization regime. The most challenging issue in fluidized bed ironmaking is the sticking problem, which can halt the fluidization process. To prevent de-fluidization, the underlying mechanisms must be understood before a solution can be identified.

2.2.1 Determination of the operating point

The so-called Reh diagram enables the visualization of some important values and helps to comprehend the fluidization patterns. For such purpose, some dimensionless numbers need to be calculated through equations (1)-(6), as shown in Table 1. The U_{slip} , U , ν , d_p , ρ_p and ρ_g are the slip velocity, superficial velocity, kinematic gas viscosity, particle diameter, particle density and gas density, respectively. V_p and V_b are particles volume and bed volume. Using the Modified Froude number (Fr^*) as vertical axis and Reynold number (Re) as horizontal axis, the Reh diagram can be plotted as shown in Figure 10. The Reh diagram also displays both the Archimedes number (Ar) and Liatschenko number (Ω), which indicate the effects of particle density and gas velocity, respectively. It provides a clue for adjusting the fluidization parameters. If the operating point locates at P1, as given in Figure 10, there are two options to move it to the fluidized bed area, i.e., decreasing the particle diameter or increasing the gas velocity. When decreasing the particle diameter, the operating point P1 can move to P2 along the Ω line. If it is still not in the fluidization area, the gas velocity can be further increased.

Thereafter, the operating point P2 is able to move to P3 along the Ar line. In summary, the fluidization state can be predicted with the assistance of Reh diagram when the particle and gas properties are available.

Table 1: Important dimensionless numbers.

Name	Equation
Reynold number	$Re = \frac{U_{slip} d_p}{\nu}$ (1)
Modified Froude number	$Fr^* = \frac{3}{4} \cdot \frac{U_{slip}^2 \rho_g}{d_p g (\rho_p - \rho_g)}$ (2)
Archimedes number	$Ar = \frac{d_p^3 g (\rho_p - \rho_g)}{\nu^2 \rho_g}$ (3)
Liatschenko number	$\Omega = \frac{U_{slip}^3 \rho_g}{\nu g (\rho_p - \rho_g)}$ (4)
Bed porosity	$\varepsilon = 1 - \frac{V_p}{V_b}$ (5)
Slip velocity	$U_{slip} = \frac{U}{\varepsilon}$ (6)

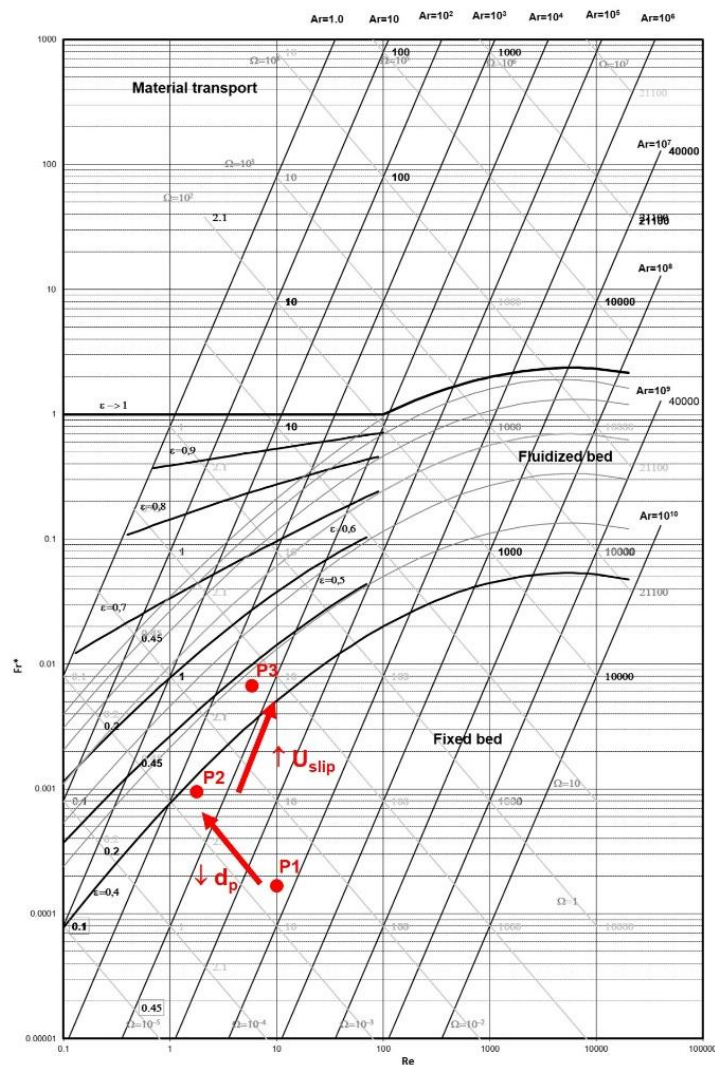


Figure 10: Reh-diagram for gas-solid systems.

2.2.2 De-fluidization phenomena caused by the sticking iron

In a fluidized bed reactor, after confirming the operating point, the fluidization is generally not a problem at the beginning of the reduction phase. However, with the reduction of the iron oxide proceeding, the de-fluidization may occur due to the newly formed iron on the particle surfaces. It is believed that the newly formed iron is sticking and increases the resistance to fluidization. The sticking problem occurs mainly during the metallization of the iron oxide at high temperatures [42]–[44]. The dominant mechanisms for the sticking can be summarized in two aspects: the generation of iron whiskers on the particle surface and the formation of highly active iron on the particle surface.

2.2.2.1 Surface iron whiskers

The iron whiskers are common formed when the iron ores are reduced in CO atmosphere [45]. If particles with whiskers on the surface collide with each other, they may stick together and result in de-fluidization. The generation of iron whiskers usually occurs during the phase transition from FeO to Fe. Nicolle et al. [46] explained the growth mechanism of iron whiskers in the reduction of wüstite based on Wagner's theory. The surface morphology showed a strong relationship to the reaction limiting step, including the removal of oxygen (chemical control) and the migration of iron ions (diffusion control). For an easy understanding, the reduction process is considered as a four-stage reaction, initial stage, supersaturation stage, nucleation stage and growth stage, in which the iron activities are varied. As shown in Figure 11, three scenarios are possible during the reduction of wüstite.

- (1) The rate at which iron ions migrate inward from the surface is notably slower than the rate at which iron ions are produced at the surface, indicating a diffusion-controlled process. As given in Figure 11(a), the iron accumulates on the surface of the particle and reaches an uncertain degree of supersaturation. The values of 1, a_c and a_0 in the vertical axis represent the iron activity of pure metallic iron, an uncertain iron activity due to supersaturation and iron activity of wüstite, respectively. When the first metal nucleation appears, the iron activity drops back to 1. Since the reaction is under diffusion control, there is no iron supply from the bulk. The growth of the nucleus requires further removal of surrounding oxygen. Therefore, the other points continue the accumulation of iron and result in many other new nucleation sites. In such way, all the nuclei grow to a lamellar shape and merge to form a metal plate on the surface.
- (2) The inward migration capacity of iron ions from the surface is similar to the production capacity of iron ions at the surface, i.e., a mixed control. As given in Figure 11(b), the

iron accumulates within part of the particle volume and reaches an uncertain degree of supersaturation. The growth of the first nucleation has two driven forces: the iron supply from local supersaturation area and the removal of surrounding oxygen. The nuclei grow very fast at the beginning and form a large foot of whisker due to adequate iron flux from supersaturation area. As iron activity decreases in supersaturation area, the growth of whisker slows down. A conical whisker on the surface is then formed.

- (3) The rate of iron ions migrating inward from the surface is notably faster than the rate of iron ions is produced at the surface, indicating a reaction control. As given in Figure 11(c), the iron accumulates within the whole particle volume and reaches an uncertain degree of supersaturation. The first nucleation occurs at the surface site by the iron supply from the supersaturation bulk wüstite. Thereafter, the cylindrical whisker is formed by the excess iron source from the bulk wüstite. Yoshiaki et al. [47] found the same situation that the iron whiskers occurred from iron-saturated wüstite by cooling without any chemical reaction.

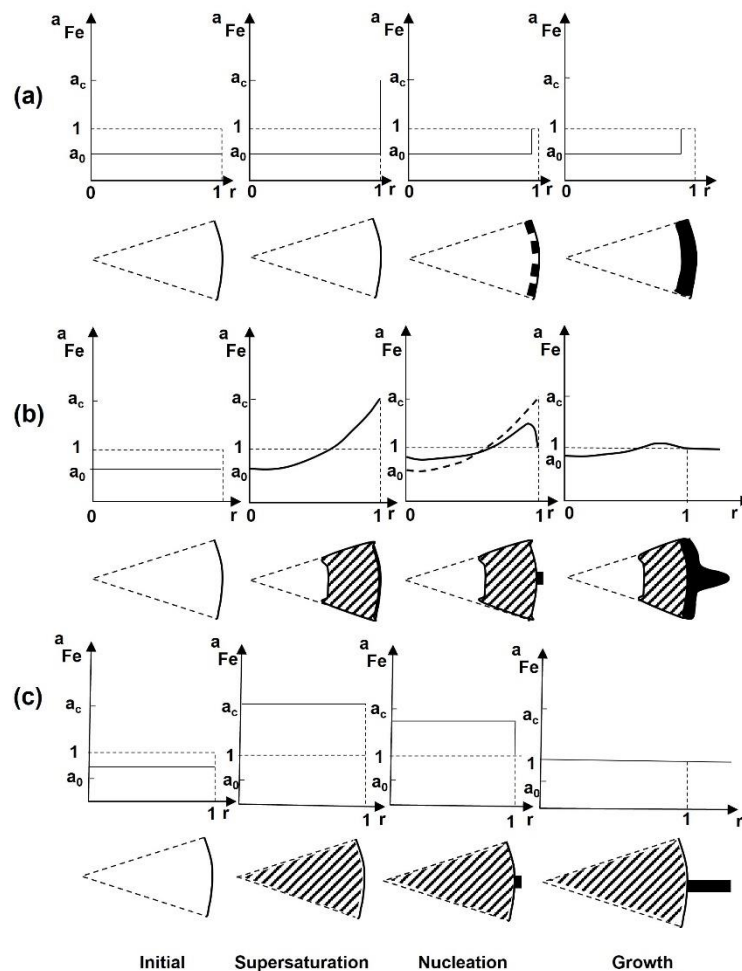


Figure 11: Schematic of Iron activity curves and phase configuration: (a) under diffusion control; (b) under mixed control; (c) under chemical control [46].

Guo et al. [45] conducted an in-situ observation analysis of the nucleation and growth of iron whiskers during the reduction of iron ore via a high-temperature confocal scanning laser microscope under CO atmosphere. The results agreed with the growth mechanism of Nicolle et al. [46]. Based on the structure's characteristics obtained in the in-situ observation, iron nucleation could also occur inside the ore particle. Figure 12 presents a schematic depiction of the structural changes occurring throughout the reduction process of an individual particle. Firstly, the Fe_2O_3 phase transforms to FeO phase. Due to crystal transformation, the volume of the particle changed and resulted in pores. The pore size gradually increased with the reaction proceeding. Afterwards, the metallic iron was formed on the surface and its shape was determined by the reaction limiting step. Some nuclei also appeared around the pores, where the lattice defects or dislocations were dense.

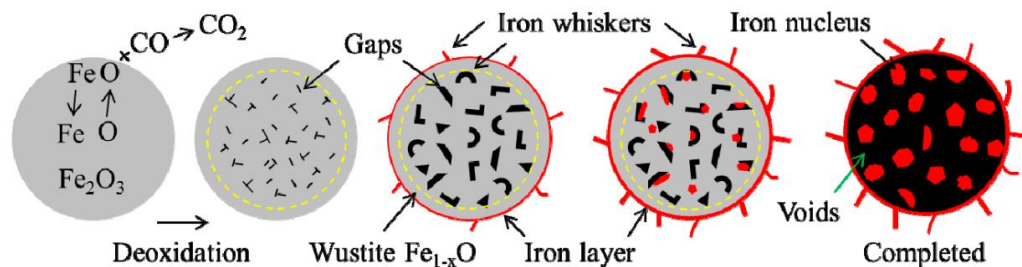


Figure 12: Schematic illustration of the reduction of iron ore particle [45].

When the reduction of iron oxide happens in H_2 atmosphere, the iron grows preferentially in plated shape on the surface. Du et al. [48] compared the morphology of reduced metallic iron obtained from H_2 and CO reducing conditions. As shown in Figure 13(a)-(d), it was found that when 10% of H_2 was applied in the CO gas flow, the surface metallic iron transferred from whisker to conical shape and lots of pores appeared on the surface. When the addition of H_2 was higher than 30%, no whiskers were observed, and the surface metallic iron was dense. It could be explained by the migration rate of reaction interface. As shown in Figure 13(e) and (f), the angle between the surface and the reaction interface was larger in the sample reduced in pure CO , resulting in a longer reaction interface. The interface was the diffusion path of Fe vacancies for further reaction. A short path was beneficial for the migration of Fe vacancies and resulted in a faster reaction. The precipitation mechanism of iron under pure H_2 and CO is shown in Figure 13(g). The white color and gray color represent Fe_{1-x}O and Fe , respectively. More iron nuclei were formed in pure H_2 and connected with each other, resulting in an iron shell on the surface. On the contrary, the iron nuclei in pure CO were sparse and resulted in the formation of whiskers.

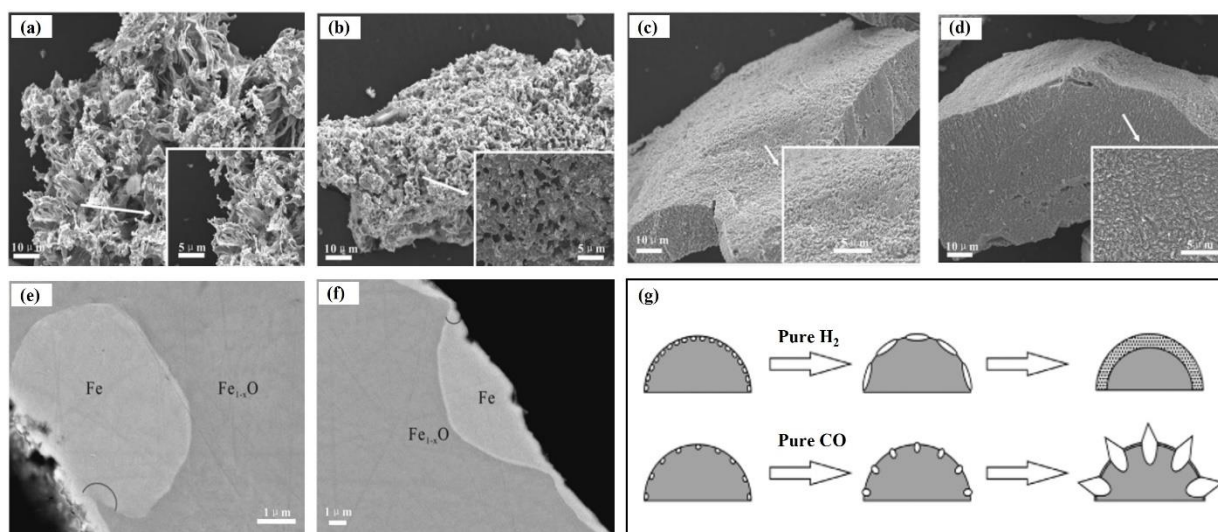


Figure 13: Surface morphology of reduced iron under different conditions (a) pure CO; (b) CO:H₂=90%:10%, (c) CO:H₂=70%:30%, (d) pure H₂; Polished section images of the samples reduced by (e) pure CO and (f) pure H₂; (g) is the mechanistic diagram of the precipitation mechanism of iron under different reducing gases.

Lu et al. [49] used phase-field method to simulate the growth of iron whiskers and found that the oxygen content in iron oxide significantly influenced the crystal lattice and the diffusion direction of Fe vacancies. The Fe ions tended to diffuse to regions with low oxygen content, while iron vacancies tended to diffuse to regions with high oxygen content. Based on density functional theory (DFT) calculations, Lu et al. [50] further illustrated that the CO molecule showed a strong force to pull iron ion of wüstite in the vertical direction, while the H₂ molecule showed no directional force. Figure 14 shows the iron formation step in atom scale. In the presence of CO, the carbon atom in CO attracted iron ions from the surface of wüstite, leading to the outgrowth of iron ions. As a consequence, the surface exhibited a vertical expansion. Furthermore, Fe vacancies were formed on the topmost layer of the surface, which iron ions could fill by using the energy released during the CO oxidation process. This energy helped overcome the diffusion energy barrier and facilitated the migration of iron ions into the Fe vacancies. As the surface expansion continued, the iron whiskers were to be formed. In contrast, in the case of H₂ reduction of wüstite, the iron ions moved in a planar direction without additional energy or attractive forces.

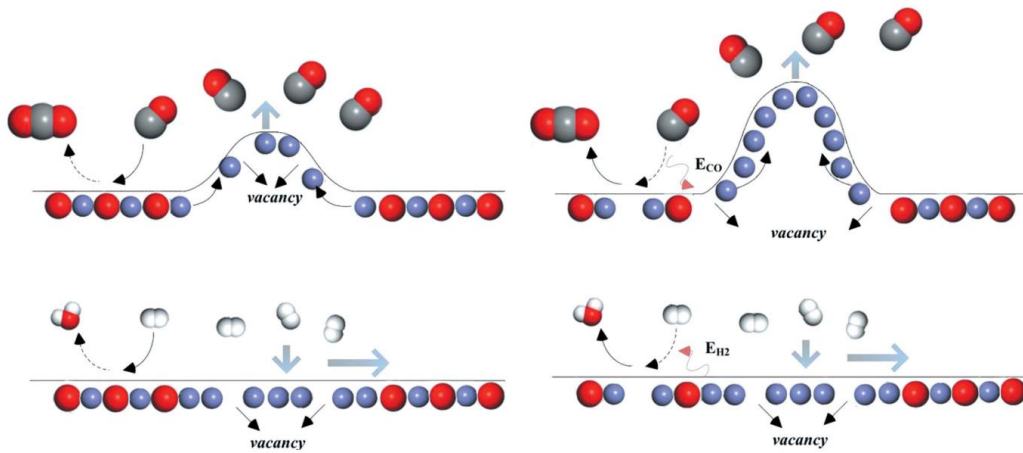


Figure 14: Schematic diagram of iron formation on the surface of FeO. (Purple, red, gray and white balls represent the Fe, O, C and H atoms, respectively.) [50]

2.2.2.2 Highly active surface iron

As mentioned above, in some cases, especially under H_2 atmosphere, no iron whiskers appear on the particle surface. Under such circumstances, the sticking problem is caused by the other mechanism, i.e., highly active surface iron. The sticking is caused by the generation of solid bridge that driven by the solid-state diffusion of iron, as shown in Figure 15(a)-(c). The solid-state diffusion of metal refers to the migration of atoms through vacancies between metal surfaces, leading to their transposition. Gong et al. [43] analyzed the crystal defect and surface vacancy of iron particle via positron annihilation spectroscopy (PAS). As given in Figure 15(d), there were many vacancy defects on the fresh iron, especially in the iron whiskers, which facilitated the diffusion of iron atoms and thus decreased its sticking temperature. The critical iron bridge of particles could be as small as 60-120 nm when the particle size was in the range of 100-200 μm , beyond which the particles became de-fluidized. Takafumi et al. [51] and Kenya et al. [52] quantitatively investigated the solid bridge of iron by numerical simulation. The de-fluidization behavior could be predicted based on the balance between the drag force and the neck strength of particles. The neck strength is also referred to as cohesive force elsewhere. Therefore, the movement of iron particles could be described by following equation (7). When $F_d \leq F_c + M_g$, the de-fluidization occurs. For detailed calculation of such forces and the prediction of iron bridge growth can be found in [43],[51],[52].

$$m \frac{dv}{dt} = F_d - F_c - M_g \quad (7)$$

Where, F_d , F_c and M_g are the drag force acting on particles, cohesive force between particles and the gravity force of particles, respectively.

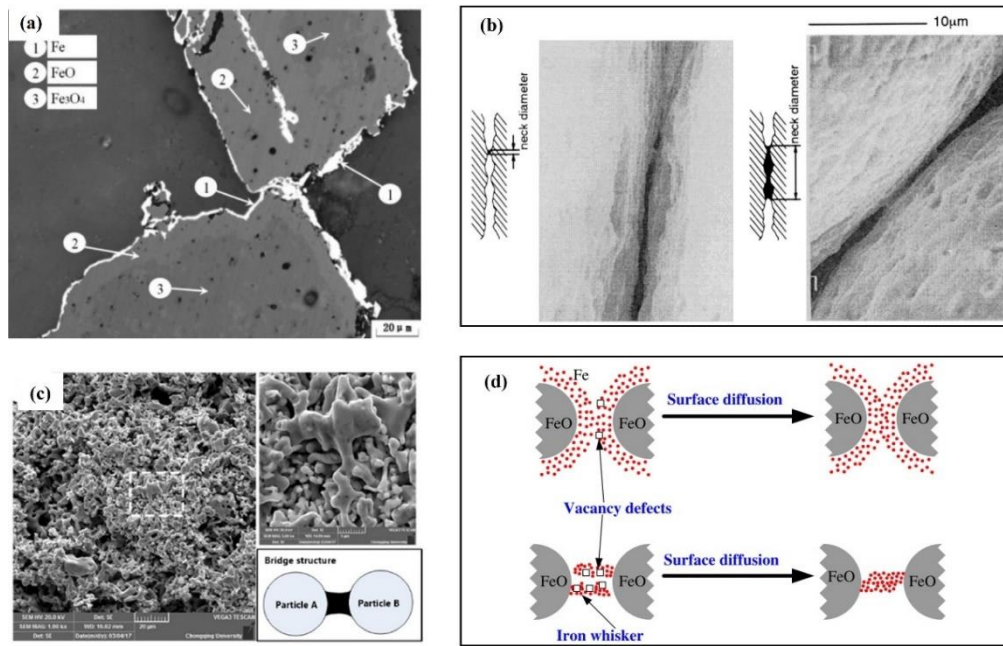


Figure 15: (a)-(c) Iron bridge between particles [52]–[54], (d) Sticking mechanism resulting from Fe atom diffusion [43].

2.2.3 Prevention methods to sticking problem

After understanding the sticking mechanism, several methods are available to prevent the sticking problem, which were also reviewed by Guo et al [55]. One of the most effective and practical ways is modifying the particle surface by coating additives. The coating treatment with additives exhibits two primary effects: modifying the surface morphology of the reduced iron particles and preventing direct contact between the reduced iron particles. The additives act as gangue elements and will remain in the product after reduction. To reach a required basicity in the subsequent steelmaking process, the amount of slag will be influenced by such coating treatment. Therefore, MgO and CaO are usually chosen as the typical additives. Both MgO and CaO are indispensable components within the melting aggregate, crucial for achieving slags with the specified basicity. Furthermore, their influence on the subsequent steelmaking process is negligible.

MgO is completely soluble in wüstite. Compared with Fe^{2+} , Mg^{2+} is easier to migrate to vacancy in wüstite. Therefore, magnesiowüstite ($\text{Fe}_x\text{Mg}_{1-x}\text{O}$) is formed, which inhibits the reduction of wüstite [56]. A comparable phenomenon was also observed in the reduction of pure hematite doped with MgO using CO [57]. The effect of MgO on the stepwise reduction of pure hematite compacts was investigated by El-Geassy [57]. The study revealed that the promotion effect occurred during the hematite-magnetite reduction stage due to an increase in

porosity and active sites resulting from the introduction of foreign cations into the Fe_2O_3 lattice. However, during the later stage, the formation of the low-reducibility phase $\text{MgO}\cdot\text{Fe}_2\text{O}_3$ hindered the reduction reaction. Reduction rate decreased during the magnetite-wüstite and wüstite-iron reduction steps, which were attributed to the formation of $\text{Fe}_x\text{Mg}_{1-x}\text{O}$. As a result, the diffusion of iron ions was affected, making it less likely to form iron whiskers. At low reducing temperature, the MgO mainly works as a physical barrier, decreasing the frequency of contact between particles [53]. Du et al. [58] found that the addition of MgO in the later reduction stages of iron ore fines (reduction of FeO) was more effective in preventing de-fluidization than adding MgO in the reduction stages of Fe_2O_3 and Fe_3O_4 . When the reduction temperature was higher than $900\text{ }^\circ\text{C}$, MgO reacted with $\text{Fe}_2\text{O}_3/\text{FeO}$ and formed $\text{Fe}_2\text{MgO}_4/\text{FeO}\cdot\text{MgO}$ on the particle surface, which served as a chemical barrier. Guo et al. [59],[60] tested four different coating method with MgO: (1) Powder method: Mixing the MgO powders and iron ores directly in solid state before charging into the reactor; (2) Briquetting method: The mixture of MgO and Fe_2O_3 powders was pressed at 40 MPa and roasted in a muffle furnace at $1000\text{ }^\circ\text{C}$ for 3 hours. Then the sintered briquettes were crushed into powders with a specific diameters range; (3) Injection method: Blew the MgO powders into the bottom of the fluidized bed reactor with a powder injector during the reaction; (4) Liquid method: The iron oxide particles were mixed in a Mg-containing solution. The particles were uniformly coated with Mg-containing compound which turned into MgO after calcination in the air. Among the coating methods, the liquid method is the most effective way. However, it is not easy to apply such a method in an industry plant. The most practical way is still the powder method. The efficacy of such method has been demonstrated experimentally, as reported by Zheng et al. [56],[61],[62].

It is widely believed that the coating of CaO is not as effective as the coating of MgO in preventing adhesion problems. Zhong et al. [63] did a comparative study of the role of MgO and CaO. Both MgO and CaO showed positive effect on improving the fluidization state. However, the intermediate product, $\text{CaO}\cdot\text{FeO}$, on the surface of CaO-coated sample could be reduced mostly to metallic iron. Therefore, the CaO only worked temporarily in preventing the de-fluidization of the materials. In order to enhance the inhibition effect of CaO, Du et al. [64] tried liquid method to coat the iron ore particles. However, the coated layer was reduced and did not adhere well to the surface of iron ore particle for inhibiting de-fluidization. After reduction, the particle surface was still covered by pure metallic iron. To further improve the coating effect, a solution containing Fe^{3+} was added during coating treatment. In this way, $2\text{CaO}\cdot\text{Fe}_2\text{O}_3$ was formed on the particle surface after calcination. The Fe_2O_3 showed a bonding effect, adhering the coated layer to the particle surface. After reduction, the surface was covered by CaO.

2.3 Oxidation of magnetite in particle scale

The oxidation of magnetite particles can take place during the preheating stage. In this chapter, a comprehensive review of magnetite oxidation is presented, including both thermodynamic and kinetic aspects. Moreover, an investigation is conducted into the impact of magnetite oxidation on its subsequent reduction behavior. In my previous review paper Publication 4 [65], a comprehensive analysis is presented regarding the exothermic impact, crystal transformation, and structural evolution that occur during the process of magnetite oxidation.

2.3.1 Stages of the oxidation process

The oxidation process of magnetite can be characterized by a minimum of two stages. Colombo et al. [66],[67] investigated the first stage of oxidation of magnetite. The results confirmed that in the first oxidation stage an intermediate phase exists, which consisted of a solid solution of $\gamma\text{-Fe}_2\text{O}_3$ in Fe_3O_4 . The impurities could stabilize the $\gamma\text{-Fe}_2\text{O}_3$ phase. However, the final oxidation product depended largely on oxidation temperature. Chen et al. [68] illustrated the main structural and chemical difference between $\gamma\text{-Fe}_2\text{O}_3$ and Fe_3O_4 . The difference is the existence of vacancies in $\gamma\text{-Fe}_2\text{O}_3$, which lowered the symmetry of $\gamma\text{-Fe}_2\text{O}_3$ (primitive Bravais lattice) with respect to Fe_3O_4 (face-centered Bravais lattice). And the Fe^{2+} in the Fe_3O_4 is completely replaced by Fe^{3+} ($\text{Fe}^{2+} \rightarrow \text{Fe}^{3+} + e^-$), so the positions that were occupied by $1/3\text{Fe}^{2+}$ in octahedron became the vacancies. $\gamma\text{-Fe}_2\text{O}_3$ showed a ferromagnetic behavior, while $\alpha\text{-Fe}_2\text{O}_3$ showed an antiferromagnetic behavior.

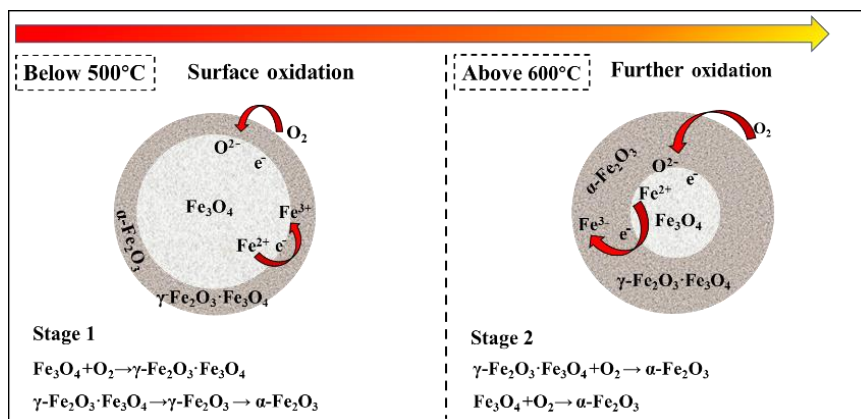


Figure 16: Stages of magnetite during non-isothermal oxidation.

The oxidation mechanism of magnetite is postulated as follows: The conversion of Fe^{2+} to Fe^{3+} initiates the diffusion of iron ions from within the Fe_3O_4 crystals towards the surface. The

occurrence of oxidation yields the formation of a solid solution of $\gamma\text{-Fe}_2\text{O}_3$ in Fe_3O_4 . As the oxidation progresses, the $\alpha\text{-Fe}_2\text{O}_3$ and the solid solution are formed at the magnetite particle surface. Subsequently, facilitated by the presence of $\alpha\text{-Fe}_2\text{O}_3$, a catalyzed reaction leads to the transformation of the solid solution into $\alpha\text{-Fe}_2\text{O}_3$ and Fe_3O_4 . The secondary Fe_3O_4 is oxidized directly to $\alpha\text{-Fe}_2\text{O}_3$ at high temperatures. Therefore, the oxidation stages of magnetite particle can be interpreted as shown in Figure 16.

2.3.2 Thermodynamics of magnetite oxidation

Daniel et al. [29] calculated the thermodynamically stable phases in the binary Fe-O system as shown in Figure 17. The ideal stoichiometry of hematite and magnetite are Fe_2O_3 and Fe_3O_4 , respectively. In theory, magnetite exists in equilibrium with hematite at lower temperatures. Additionally, two minor stable regions of magnetite phase can be observed at elevated temperatures. A closer look into the equilibrium of Fe_3O_4 and Fe_2O_3 under different temperature and O_2 partial pressure is taken in Figure 18. The diagram illustrates the stable area of a single Fe_3O_4 phase under different temperature and O_2 partial pressure. From a thermodynamic standpoint, magnetite has the potential to undergo full oxidation to hematite even under room ambient conditions. Nevertheless, due to the intricate nature of the oxidation process and the constraints imposed by kinetic factors, achieving complete oxidation of magnetite is typically impossible. Subsequent sections will delve into the analysis of oxidation kinetics.

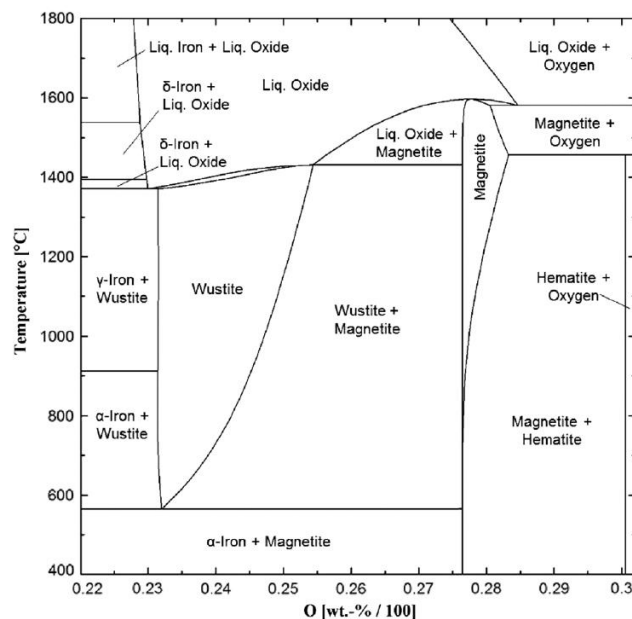


Figure 17: Binary Fe-O system. Reproduced with permission.

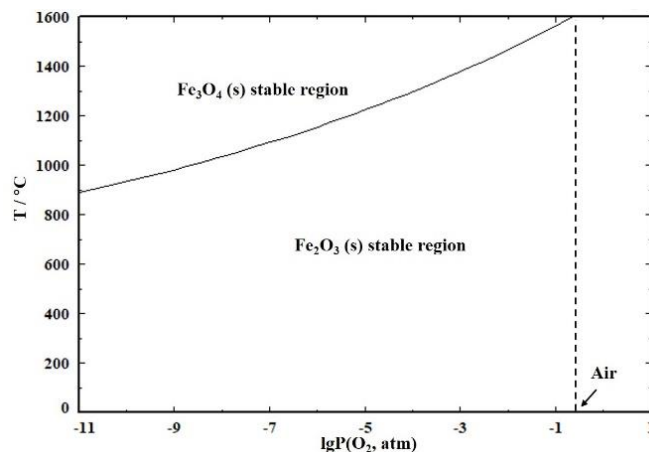


Figure 18: Stable region of Fe_3O_4 and Fe_2O_3 . (Calculated by Fact Sage 7.2, Database: FactPS, FToxid).

2.3.3 Rate-limiting analysis of oxidation reaction

The ICTAC (International Confederation for Thermal Analysis and Calorimetry) has recommended methods and guidelines for the analysis of kinetics, ensuring the dependable assessment of kinetic parameters [69],[70]. It's important to emphasize that the oxidation process is influenced not only by the oxidation conditions but also by the experimental setup, including the equipment used and even the sample containers. Figure 19 shows three typical thermogravimetric analysis (TGA) apparatuses. The differences are the direction of gas flow and the sample containers. It is difficult to decide which kind of apparatus is the best option. When a crucible serves as the container, the gas flow can solely penetrate the sample from top to bottom. This configuration may lead to the interruption of gas flow and potential disruption caused by the crucible itself and the thickness of the sample layer, potentially impacting kinetic analysis. On the other hand, when a basket is utilized, the gas flow can traverse the sample from bottom to top with minimal disturbance. In conducting oxidation TGA tests on magnetite at the particle scale, the most important consideration is to mitigate experimental errors arising from issues related to mass transfer.

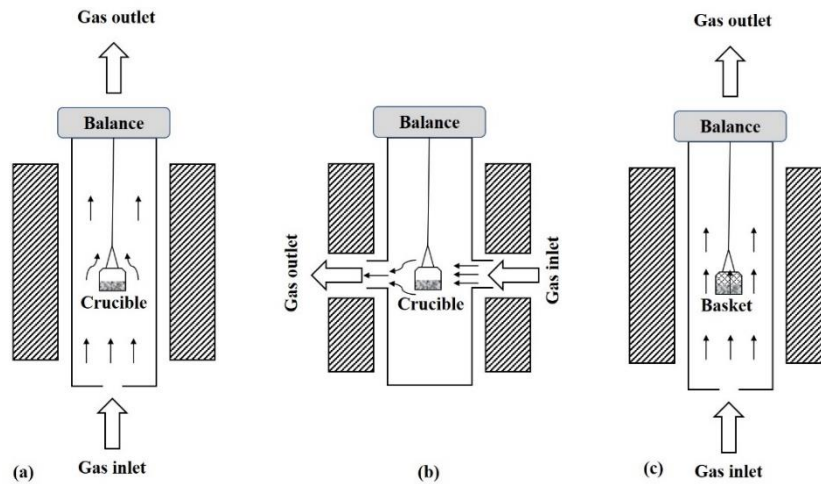


Figure 19: Schematic of oxidation apparatus and sample vessels.

Considering thermodynamics, the conversion of magnetite to hematite through oxidation is an inherently spontaneous reaction. The chemical reaction is generally not the rate-limiting step. A widely accepted understanding is that in the oxidation of pellets, the kinetics are governed by a combination of rate-limiting processes: gaseous mass transfer of molecular oxygen passing through macroscopic pores into the pellet and solid-state diffusion occurring within the oxidized particles themselves. However, when considering particle scale, the inter-particle gaseous mass transfer is typically disregarded. The diffusion of oxygen molecules into the particle becomes highly improbable due to the dense structures of both magnetite and the hematite layer. When oxidizing magnetite at the particle scale, the solid-state diffusion is widely regarded as the rate-limiting step. The solid-state diffusion can be described by parabolic law. In this case, the nature of the solid-state diffusion is the ion (Fe^{2+} , Fe^{3+} or O^{2-}) diffusion through the hematite layer. When the chemical reaction at the interface transpires significantly faster than the diffusion process, the interface is expected to progress uniformly inward, reaching the center of the particle. However, it's important to note that magnetite particles commonly are non-spherical shapes. Magnetite exhibits a preference for oxidation in specific orientations where ion diffusion transpires more rapidly compared to other orientations. This phenomenon prompts the growth of hematite needles towards the interior of the particle. The irregular shape of the particles and the inward-growth hematite may have an impact on the kinetic analysis. According to Mosen [71], it is suggested that O^{2-} ions exhibit constrained mobility within both magnetite and hematite, with diffusion primarily occurring along the boundaries between these two phases to a limited extent. In pellet oxidation, the impact of the inward growth of hematite is often disregarded due to its minor contribution to oxidation extent. Consequently, the oxidation mechanisms of magnetite at both pellet and particle scales can be represented as depicted in Figure 20.

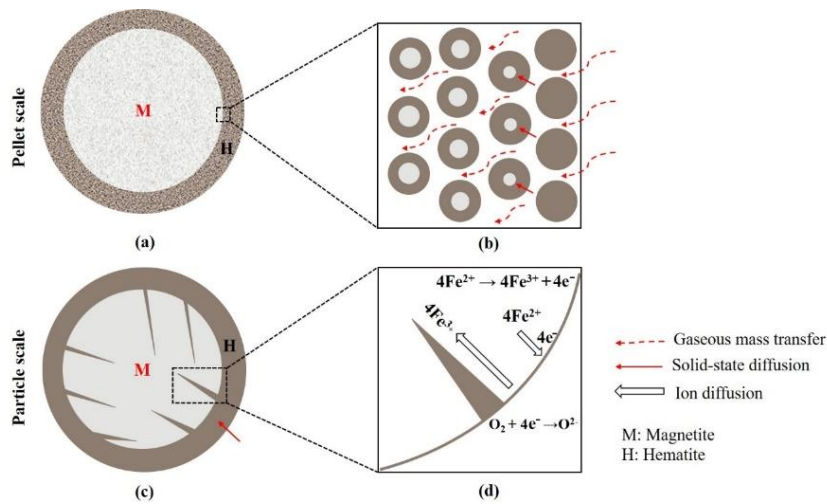


Figure 20: Schematic illustration of the oxidation kinetics: (a-b) in pellet scale; (c-d) in particle scale.

Monsen [71] found that under polarized light microscope, the hematite that oxidized from the magnetite particles were formed by several sub-grain structures. The higher the oxidation temperature, the bigger of each hematite sub grain. The Figure 21 shows the schematic of hematite sub grains in an oxidized magnetite particle. The growth of sub-grain structures can be elucidated through the mechanism of nucleation and growth. The model is known as JMA model that is developed by Johnson, Mehl, and Avrami [72]–[75]. The nucleation and growth mechanism does not contradict with the parabolic law. Both of these mechanisms inherently involve the diffusion of ions. In the following chapters, these two kinetic mechanisms are discussed.

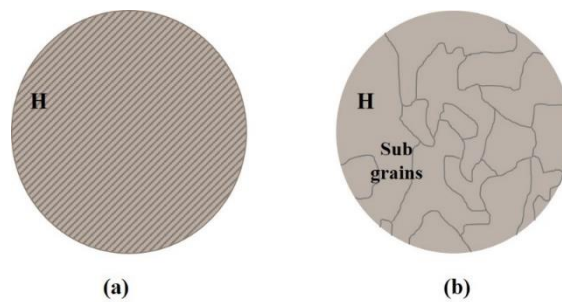


Figure 21: The schematic of hematite sub-grains in an oxidized magnetite particle: (a) under reflected light; (b) under polarized light.

2.3.3.1 Parabolic law

Cho and Pistorius [76]–[78] conducted an examination of the oxidation kinetics of magnetite concentrates employing the parabolic law. The parabolic law pertains to solid-state diffusion.

Considering particle size, the oxidation process is elucidated by equation (8). The particle size was determined through wet screening.

$$t = \left[\frac{d^2}{24k_p} \right] \times [3 - 2\alpha - 3(1 - \alpha)^{2/3}] \quad (8)$$

Where t signifies the duration of oxidation, d corresponds to the diameter of the magnetite particle, k_p represents the parabolic rate constant, and α indicates the oxidation degree.

To derive a quantitative estimate of the parabolic rate constant, a set of magnetite concentrate particles within a narrow size range from 53 μm to 63 μm were oxidized at temperatures of 500 $^\circ\text{C}$, 600 $^\circ\text{C}$ and 800 $^\circ\text{C}$, employing an 80% N_2 - 20% O_2 gas mixture. If the oxidation progress follows the parabolic law, the resulting graph will exhibit a linear pattern in accordance with equation (8). Monsen [71] analyzed the oxidation of magnetite concentrate particles with size range between 74 μm and 100 μm in air flow at the temperature range of 400 $^\circ\text{C}$ - 800 $^\circ\text{C}$ using the same model. The oxidation procedure adheres to the parabolic law in both of these investigations. The parabolic rate constant was assessed through variations in hematite thickness. In simpler terms, the measured parabolic rate constant signifies the overall movement of the reaction front on a macroscopic scale. In the study of Cho et al. [79], the determined parabolic rate constants closely resembled those computed by Monsen [71] and the oxidation rate exhibited independence from oxygen contents of 20% and higher. Pistorius [77] observed that changes in the parabolic rate constant only occur under exceedingly low partial pressure of oxygen. Figure 22 illustrates the relationships between parabolic rate constants and partial pressure, as well as temperature. It is assumed that the parabolic rate constant remains stable at the same temperature. The average parabolic rate constant calculated by Cho and Pistorius is as follows:

$$k_p = 220 \exp\left(-\frac{65100}{RT}\right) \mu\text{m}^2/\text{min} \quad (9)$$

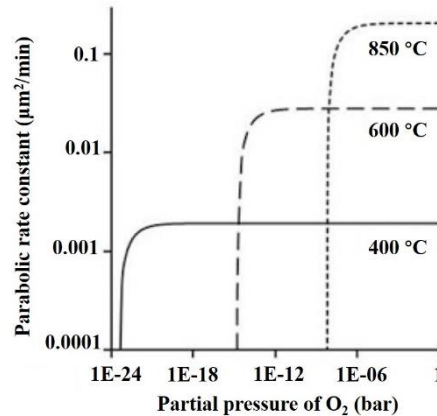


Figure 22: The calculated parabolic rate constants in different temperatures and partial pressures [77].

Himmel et al. [80] conducted measurements of the self-diffusion coefficient (D) for iron within magnetite and hematite. In order to facilitate a straightforward comparison between k_p and D , they were converted into the same unit with $\mu\text{m}^2/\text{min}$ and are presented in Table 2 and Table 3. The Table 2 reveals a substantial disparity in the self-diffusion rates of iron between magnetite and hematite, with magnetite exhibiting several orders of magnitude higher diffusion rates. Table 3 illustrates that the parabolic rate constants closely resemble the self-diffusion coefficients for iron in magnetite. As such, the mechanism of solid-state diffusion appears to be the most plausible explanation. The progression of the reaction front is likely attributed to the diffusion of iron within magnetite.

Table 2: The self-diffusion coefficients for iron in magnetite and hematite.

Specimen	Temperature, °C	D , $\mu\text{m}^2/\text{min}$
Magnetite	~ 800	5.9×10^{-2}
	~ 900	5.3×10^{-1}
Hematite	~ 1000	6.0×10^{-5}
	~ 1200	1.2×10^{-2}

Table 3: The parabolic rate constants.

Temperature, °C	k_p , $\mu\text{m}^2/\text{min}$	Average k_p , $\mu\text{m}^2/\text{min}$
400	2.5×10^{-3}	$220 \exp\left(-\frac{65100}{RT}\right)$
500	1.9×10^{-2}	
600	8.0×10^{-2}	
800	3.2×10^{-1}	

Kumar et al. [81] conducted an isothermal oxidation experiment on magnetite concentrate particles using TGA within the temperature range of 500°C to 800°C. The concentrate underwent wet sieving to obtain a narrow size distribution ranging from 38 μm to 53 μm , with an average particle diameter of 45.5 μm . The gas flow rate for oxidation was set as 200 ml/min to minimize the influence of gas diffusion. The outcomes revealed that the later stage of oxidation follows the solid-state diffusion mechanism. As elucidated earlier, the parabolic rate constant should solely be contingent upon temperature. The values of the parabolic rate constants were reflected by the slopes of the fitted lines in Figure 23. The slopes depicted in Figure 23(a) experienced an upward trend with increasing temperature, while the slopes in Figure 23(b) remained nearly constant. The gathered data provided support for the validity of the parabolic law mechanism.

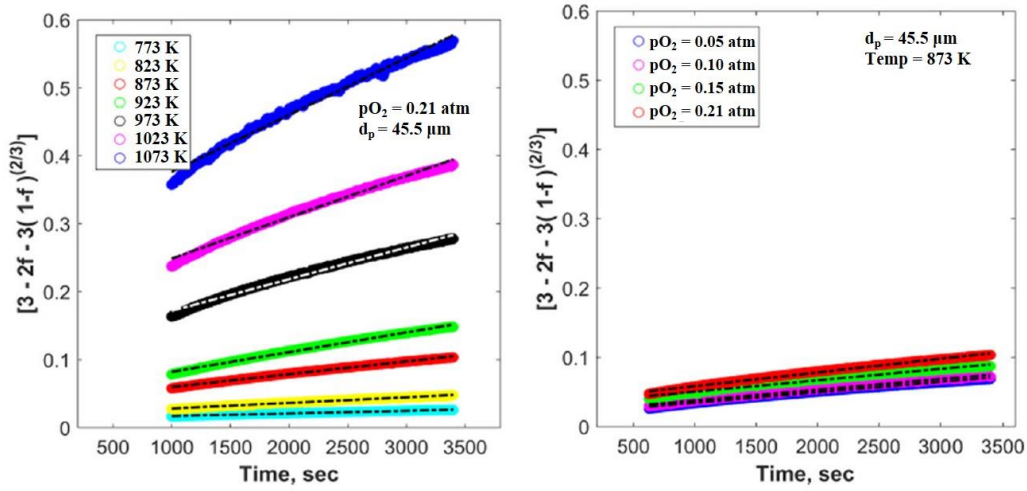


Figure 23: (a) Isothermal oxidation evaluated by the solid-state diffusion: (a) different oxidation temperature; (b) different partial pressure of oxygen [81].

2.3.3.2 The nucleation and growth

The oxidation process can also be interpreted as the nucleation and growth of hematite grains. The expansion of hematite grain occurs through the solid-state diffusion of iron ions. The JMA model is a prevalent approach for describing such reactions, defined in equation (10) or (11). This model is applicable to isothermal reactions characterized by parallel or sequential multistep kinetics. It remains relevant even when the data does not match other commonly used models [82]. This model can also be extended to non-isothermal reactions, the determination of kinetic parameters requires experimentation at varying heating rates [83]. In some literature, the JMA model is also referred to as the Avrami kinetic model (AKM) [84],[85].

$$\alpha = 1 - e^{-at^n} \quad (10)$$

or

$$\ln(-\ln(1 - \alpha)) = n \ln(t) + \ln(a) \quad (11)$$

Where α indicates the oxidation degree after a duration time t ; a corresponds to the Avrami constant, its value contingent upon the frequency of nucleation or the rate of grain growth; n represents the kinetic exponent, offering insights into the type of the nucleation and growth mechanism. Sharp and Hancock [82] condensed the correlation between the value of n and the underlying reaction mechanism. In general, if the value of n is less than 1, it indicates that the reaction is primarily controlled by solid-state diffusion. When n is approximately 1, the reaction is likely influenced by a first-order reaction mechanism. If n approaches 2, the reaction is governed by nucleation processes.

Kumar et al. [81] assumed the oxidation process of magnetite occurred in series and analyzed the same data from Figure 23 by JMA model. Due to the limited number of data points available from the weighing system in the initial stage, the subsequent analysis in his study focused exclusively on the latter stage of the oxidation process. Figure 24 presents the outcomes analyzed using the JMA model. The determined value of n is denoted as follows:

$$n = 1.76 \times 10^{-4}T + 0.1255\ln(p_{O_2}) - 2.03 \times 10^{-4}T\ln(p_{O_2}) \quad (12)$$

The values of n obtained under the experimental conditions were consistently smaller than 1, demonstrating greater sensitivity to temperature variations than changes in partial pressure of oxygen. This observation aligns with the characteristics of a solid-state diffusion mechanism.

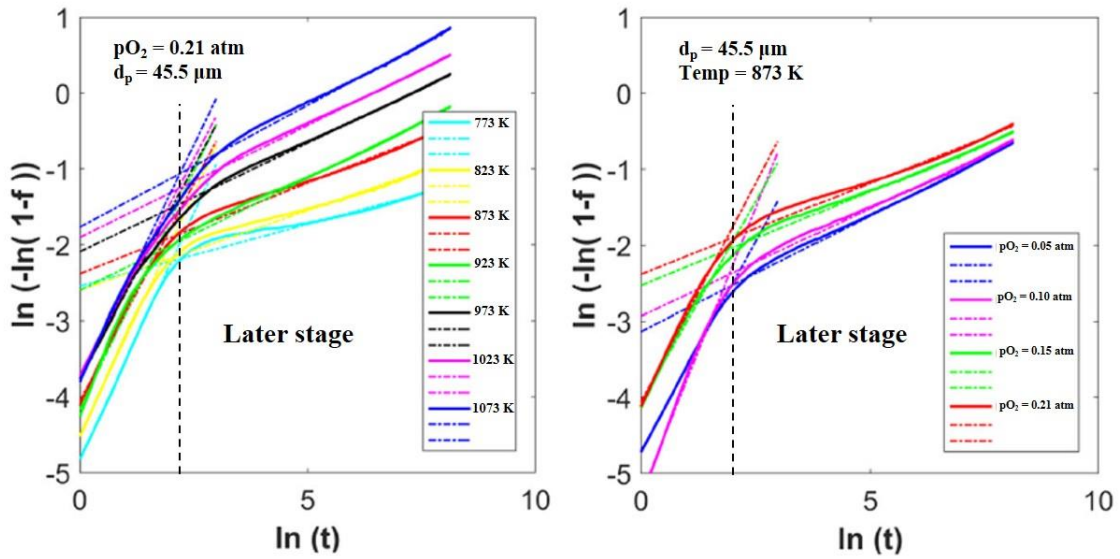


Figure 24: Isothermal oxidation evaluated by the nucleation and growth: (a) different oxidation temperature; (b) different partial pressure of oxygen [81].

Monazam et al. [84] employed this model to investigate the oxidation of magnetite particles derived from reduced hematite. However, they assumed that a parallel occurrence of two reactions during the oxidation process. In accordance with the JMA model, a parallel process of two reactions can be defined using equations (13)-(14).

$$\alpha_t = w_1(1 - e^{-a_1 n^t}) + w_2(1 - e^{-a_2 n^t}) \quad (13)$$

$$w_1 + w_2 = 1 \quad (14)$$

The model postulated that the isothermal conversion of particles occurred through parallel processes of nucleation and growth. Each process was characterized by the weight factors w_1 and w_2 . These parallel processes, denoted as P_1 and P_2 , corresponded to nucleation and diffusion, as illustrated in Figure 25. It is important to mention that the particle size range employed by the author is relatively broad, from 100 to 300 μm , which is wider compared to

other studies. This broader size range might introduce some limitations to the reliability of the fitting results.

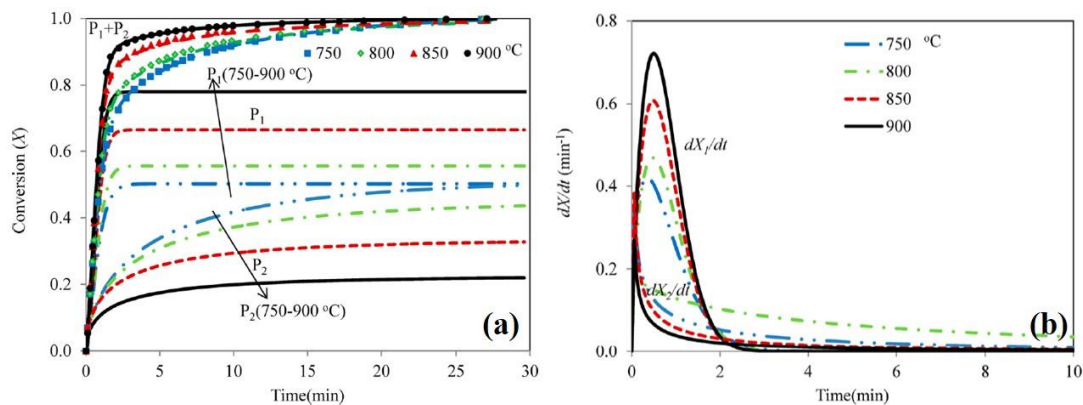


Figure 25: Conversion curve as a function of time. Curve P_1 is a single Avrami equation; curve P_2 is a single diffusion equation [84].

During the initial oxidation stage, the dominant process was P_1 , which indicated the P_1 was the rate-limiting step. As the reaction progressed, P_2 began to predominate. The P_2 process, associated with diffusion, had minimal impact on the initial stage of oxidation. In other words, the initial oxidation stage was dominated by the nucleation of hematite, whereas the later stage was governed by solid-state diffusion. Currently, no conclusive evidence is available to confirm whether the multistep kinetics of the oxidation reaction occur in parallel or in series.

2.3.3.3 Discussion on the kinetic models

The oxidation process of magnetite can be described using these two models: the parabolic law and the nucleation and growth mechanisms. Both of these models involve the diffusion of ions. The solid-state diffusion mechanism, derived from the parabolic law, is succinctly represented by equation (15). The reaction rate decreases as the thickness of the product layer increases. The equation (15) can be integrated into equation (16) which is commonly recognized as the parabolic law.

$$\frac{dl}{dt} = k \frac{1}{l} \quad (15)$$

$$l^2 = k_p t \quad (16)$$

Where l is the thickness of the product layer, k_p is the parabolic rate constant. Ginstling and Brounshtein [86] introduced a solid-state diffusion model based on the parabolic law for reactions occurring in spherical particles. This model, known as the Ginstling-Brounshtein diffusion model or D4 model, is expressed in equation (8). Khawam et al. [87] summarized various forms of solid-state diffusion models derived from one (D1), two (D2), and three (D3)

dimensional diffusion. Cho et al. [79] observed that even with the presence of inward growth of hematite ahead of the reaction interface, the fitting results were minimally affected, and the D4 model still accurately described the oxidation kinetics.

The JMA model offers the advantage of being applicable when experimental data deviate from commonly used models. It can effectively describe multistep kinetics in both parallel and series configurations. Based on the research conducted by Kumar et al. [81] and Monazam et al. [84], the later stage of magnetite oxidation primarily exhibit solid-state diffusion, regardless of whether it occurs in parallel or series. Determining whether multistep kinetics take place in parallel or series is challenging. The current approach involves fitting the data using both parallel and series methods and selecting the approach that yields the better fitting outcome.

As previously discussed, it becomes apparent that the oxidation kinetic of magnetite in particle scale predominantly follows the solid-state diffusion. In terms of determining the appropriate kinetic models, the current methodology is to choose the model with the best fit of experimental data.

2.3.4 The influence of oxidation of magnetite on its subsequent reduction

It is widely known that hematite iron ores exhibit better reducibility compared to magnetite iron ores [88],[89]. Understanding the distinction in reduction behavior between oxidized magnetite and hematite at the particle scale is of significant interest. Edström [90] conducted experiments involving the oxidation of natural single crystals of magnetite (Fe_3O_4) and subsequently compared their reduction rates with those of hematite (Fe_2O_3) under a CO atmosphere at 1000 °C. The findings revealed a slightly lower reduction rate for the oxidized Fe_3O_4 compared to Fe_2O_3 . After 120 min reduction, both Fe_2O_3 and oxidized Fe_3O_4 achieved reduction degrees more than 90%. However, the Fe_3O_4 only reached a reduction degree of 40%. Monsen [71] conducted a comprehensive study to explore the impact of oxidation temperatures of magnetite concentrates on their subsequent reduction in H_2 atmosphere within a temperature range of 700 to 800 °C. The results indicated that the magnetite samples were nearly fully oxidized at the designated temperatures (850 °C - 1250 °C). She observed that the hematite produced from magnetite oxidation at lower temperatures (850 °C - 1050 °C) exhibited enhanced reducibility compared to the hematite formed at high temperatures (1150 °C - 1250 °C). This difference in reducibility was attributed to the presence of a greater number of smaller sub-grain structures in the hematite derived at lower temperatures. These sub-grain boundaries acted as favorable sites for reduction, thereby facilitating the reduction process.

3 Methodology

The experiments in current research work can be summarized into two groups. The first group, namely reduction experiment, is to investigate the fluidization and reduction behaviors of the magnetite ore fines with some pre-treatments. The second group, namely oxidation experiment, is to study the oxidation behavior, pore structure, surface morphology and internal structure of the magnetite ore fines during pre-oxidation treatment. In this chapter, the experimental facilities, procedures and analytical methods are introduced. In addition, the characterization methods of the samples are briefly described.

3.1 Reduction experiments

3.1.1 Apparatus

The first group of experiments were carried out in a laboratory-scale fluidized bed reactor with an inner diameter of 68 mm, which was detailed introduced in Publication 1 [56] and previous PhD thesis from the Chair of Ferrous Metallurgy, Montanuniversitaet Leoben [28]. Nevertheless, the laboratory-scale fluidized bed reactor is briefly described in this section. The schematic layout of the fluidized bed reactor is shown in Figure 26 and a physical picture is given in Figure 27.

The inner diameter of the reactor is 68 mm. The upper section of the reactor was configured in a conical shape, a design choice made to decrease the superficial gas velocity and consequently minimize sample losses through entrainment during the fluidization process. H_2

and N_2 can be mixed in the gas mixing unit and preheated while passing through the supply pipe inside the furnace. The system is capable of providing a mixture of H_2 , CO , CO_2 , CH_4 and N_2 . Thermocouples (Type N) placed beneath the grid and within the specimen measure both the temperature of the reducing gas mixture and the specimen's temperature within the fluidized bed reactor. The obtained temperature data is utilized to regulate the power for the three-stage electrical resistance heating within the furnace. The fluidization characteristics are assessed through differential pressure measurements taken between the gas distributor and the material. Continuous real-time monitoring of pressure drops and changes of material weight is carried out, with the collected data being automatically recorded by the system.

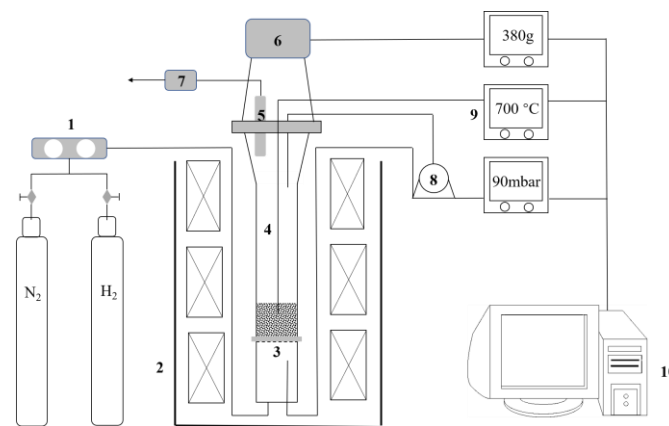


Figure 26: Schematic layout of laboratory fluidized bed reactor: 1. gas mixture unit; 2. three-stage electrical furnace; 3. distributor; 4. fluidized bed reactor; 5. dust filter; 6. scale; 7. pressure regulator; 8. differential pressure monitor; 9. temperature control; 10. computer system unit.

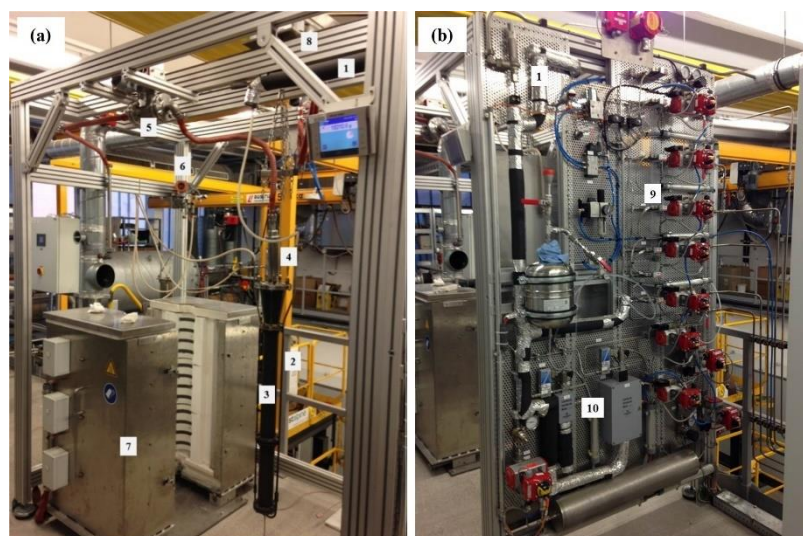


Figure 27: Laboratory fluidized bed reactor: (a) reactor, (b) gas supply system. 1. gas supply pipe; 2. gas preheating section; 3. fluidized bed reactor; 4. dust filter; 5. pressure regulator; 6. differential pressure monitor; 7. three-stage electrical furnace; 8. scale; 9. mass flow controllers; 10. evaporator.

3.1.2 Procedures

All reduction tests followed a similar procedure and introduced in publications 1-3 [56],[61],[62]. The material was charged into the reactor through a small opening at the top of reactor while preheated to 500 °C. The whole preheating stage is under N₂ atmosphere. After the material reached the desired temperature and underwent a 10-minute period of thermal stabilization, the gas atmosphere was transitioned to a reducing gas. If de-fluidization occurred, or reached the target reaction time, the reducing gas was again replaced by N₂ and sample cooling under N₂ atmosphere began. The H₂ was maintained as 15.9 l/min at standard ambient temperature and pressure (SATP). The gas velocity was controlled by changing N₂ content.

The fluidized reduction experiments utilized a low-grade magnetite iron ore as the raw material. Table 4 listed the chemical composition that was analyzed using the inductively coupled plasma-mass spectrometry (ICP-MS) method. High-purity MgO powder (>99.5 wt.-% MgO, particle size smaller than 44 μm) was utilized as an anti-sticking agent in the experiments. The MgO content was expressed as the weight percentage of MgO relative to the charged iron ore material. The raw material was segregated into three particle size ranges: 125-250 μm, 250-500 μm, and full size. The full-size fraction was achieved by blending 50 wt.-% of 125-250 μm particles with 50 wt.-% of 250-500 μm particles. The detailed experimental conditions of the publications 1-3 are listed in Table 5. The Publication 1 [56] delved into the impact of pre-oxidation treatment and the addition of MgO. The Publication 2 [61] centered its attention on the implications of various pre-oxidation treatment parameters, including distinct pre-oxidation temperatures and oxidation degrees, on fluidization behaviors, morphological characteristics, and reduction kinetics. In the end, the Publication 3 [62] tried to confirm the dominant influencing parameters and the optimal process condition.

The particle size was determined using conventional dry sieving methods. For a pre-oxidation treatment, a 250 × 350 mm steel vessel containing 1000 g of the raw material was placed into a conventional heat treatment furnace, as shown in Figure 28. The oxidation occurred at 800 °C and 1000 °C for a specified time to reach a so-called deeply oxidation and partly oxidation. The bed height of the material layer was around 2.5 mm. To ensure a uniform contact between gas and solid, the material was stirred by a steel stick every one hour.

Table 4: Chemical compositions of the sample, (wt.-%).

	Fe _{tot}	FeO	SiO ₂	Al ₂ O ₃	CaO	MgO	MnO	P
Raw magnetite	59.50	19.66	7.05	1.13	3.03	2.00	0.17	0.70

Table 5: Experimental conditions of the publications 1-3.

	Size, μm	MgO addition, wt.-%	Velocity, m/s	Reducing temp., $^{\circ}\text{C}$	Pre-oxidation temp., $^{\circ}\text{C}$	Oxidation content
Publication 1 [56]	125-500	0-1.5	0.4	600-800	1000	raw, partly, deeply
Publication 2 [61]	125-250 250-500 125-500	0.5	0.4	700	800, 1000	raw, partly, deeply
Publication 3 [62]	125-500	0.5-1.5	0.35-0.45	700	800, 900, 1000	raw, partly, deeply

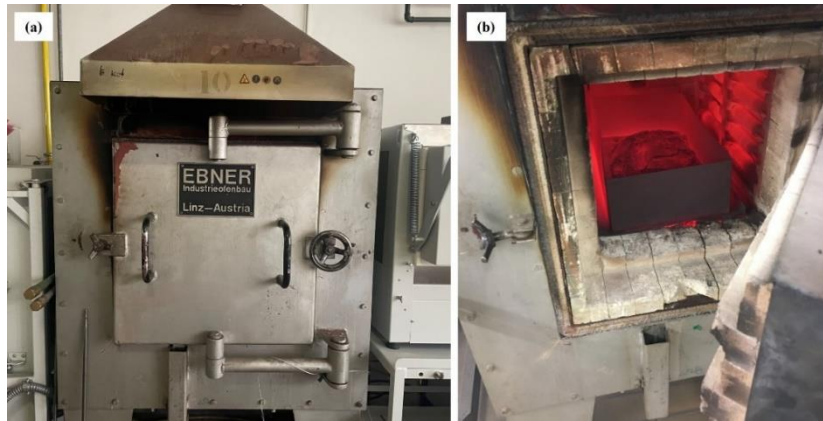


Figure 28: The furnace for pre-oxidation treatment: (a) the outlook of the furnace; (b) the material being oxidized.

3.1.3 Determination of reduction degree (RD) and de-fluidized index (DFI)

The reduction degree (RD) can be determined by the measured weight loss during reduction. The RD can be calculated using the following Equations (17) [56]:

$$\text{RD} = \left(1 - \frac{\text{O}}{1.5 \cdot \text{Fe}_{\text{tot}}}\right) \cdot 100 \% \quad (17)$$

Where O represents the amount of oxygen that is bonded to Fe in mole. The Fe_{tot} stands for the total amount of iron in the sample in mole. In such way, the phase of Fe_2O_3 , Fe_3O_4 , FeO , and Fe present a reduction degree of 0%, 11.1%, 33.3%, and 100%, respectively.

To quantify the extent of de-fluidization, a de-fluidization index (DFI) was introduced and defined by equations (18)-(20) [56],[61]. The DFI served as a real-time parameter indicating the proportion of material within the bed that were not fluidized. To facilitate a more straightforward comparison between the experiments conducted in this study, an average de-fluidization index (Ave.DFI) was also defined as presented in equation (20) [62]. The differential

pressure data were collected at intervals of two seconds. By dividing the total DFI by the amount of data, the Ave.DFI was calculated.

$$DFI = \frac{\Delta p_{\text{calculated-bed}} - \Delta p_{\text{measured-bed}}}{\Delta p_{\text{calculated-bed}} - \Delta p_{\text{Fixed-bed}}} \quad (18)$$

$$\Delta p_{\text{calculated-bed}} = \frac{m_t g}{\text{Reactor area}} \quad (19)$$

$$\text{Ave. DFI} = \frac{\sum DFI}{N_{DFI}} \quad (20)$$

where, $\Delta p_{\text{calculated-bed}}$ refers to the theoretically calculated differential pressure drop across the material, which is calculated from the initial material mass and the weight loss during the reduction if it is in a completed fluidized state; $\Delta p_{\text{measured-bed}}$ indicates the differential pressure drop actually measured for the material. $\Delta p_{\text{Fixed-bed}}$ corresponds to the differential pressure drop associated with the material in a fixed bed state, which is 2 mbar in this work; m_t is the mass of the material remaining in the fluidized bed during reduction. N_{DFI} represents the quantity of data points of DFI.

3.2 Oxidation experiments

3.2.1 Apparatus and procedures

The oxidation experiments were carried out using well-developed commercial devices. The devices and procedure were introduced in publication 5 [91]. Nevertheless, the devices and procedure are briefly described. Three brands of magnetite-based iron ore fines were used in this study. The main chemical analyses of Ore A, B and C are listed in Table 6. The particle size distributions were analyzed by CILAS 1064 particle size analyzer. The particle densities of the samples were measured by Ultra Pycnometer 1000 density analyzer. The results are listed in Table 7. The raw samples were dried at 110 °C for 6 h before all the following tests. The loss on ignition (LOI) of the magnetite samples was not taken into consideration.

Table 6: Chemical analysis of the raw magnetite samples, (wt.-%).

	Fe _{tot}	FeO	SiO ₂	Al ₂ O ₃	MgO	CaO	TiO ₂	P	S
Ore A	67.03	25.70	2.33	0.69	0.56	0.93	0.039	<0.001	0.13
Ore B	68.78	27.71	5.60	0.18	0.17	0.17	-	0.017	0.05
Ore C	65.65	27.66	3.33	1.16	1.62	1.62	0.22	0.017	0.1

Table 7: Particle size distributions and density of the raw magnetite samples.

	D10 (μm)	D50 (μm)	D90 (μm)	Density (g/cm^3)
Ore A	4.84	31.16	72.94	4.95
Ore B	4.81	28.35	62.66	4.94
Ore C	6.10	32.25	70.16	5.09

The oxidation behavior analysis, namely, oxidation capacity index (OCI), was conducted by thermogravimetric analysis (TGA). The TGA tests were conducted using STA 409 PG thermal analyzer, as shown in Figure 29. For a typical test, 50 mg of the sample was heated in an Al_2O_3 crucible ($\text{Ø}5 \times 8$ mm) to 1100 °C under air flow (100 ml/min) at a heating rate of 7.5 °C/min. Each test was conducted twice and demonstrated consistent reproducibility.

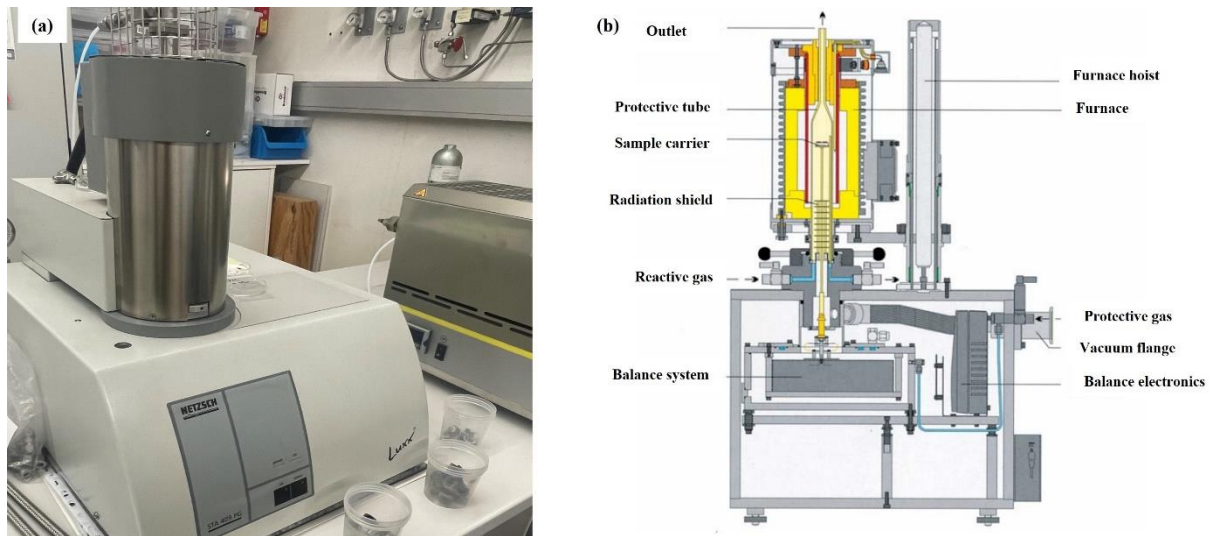


Figure 29: STA 409 PG thermal analyzer: (a) the outlook of the device; (b) schematic layout of the device from side direction.

For structural analysis, the oxidized samples were prepared using the same furnace as shown in Figure 28 under a laboratory air atmosphere. To minimize the sintering effect due to the high temperature, the material was oxidized at a relative low temperature of 700 °C. 1 g of the sample was placed in a 60×10×7 mm magnesia boat. Considering the bulk density of the sample, the estimated thickness of the material layer in the boat was approximately 0.35 mm. The oxidation process was presumed to occur uniformly throughout this material layer. As shown in Figure 30, four sets of sample boats were subjected to isothermal oxidation tests,

wherein specific controlled durations were implemented. Subsequently, after a defined period, the boats were removed from the furnace and cooled in the open air.



Figure 30: Material for isothermal oxidation.

The HT-XRD analyses were conducted using a Rigaku Ultima IV XRD diffractometer with a Cu X-ray source. The scanning was performed with a step size of 0.02 degrees and a scanning time of 0.15 seconds per step. To minimize the impact of sample area and positioning on XRD patterns, a consistent procedure was followed for each HT-XRD measurement. For the high-temperature measurements, the samples were positioned on a platinum heating strip within the HTK-16 high-temperature chamber (Anton Paar). In every test, a thin layer of approximately 0.3 g of the raw sample was employed to prevent thermal gradients along its height. The precise thickness of this layer was challenging to determine, yet it consisted of around three magnetite particles stacked together and was estimated to be under 150 μm thick. Adequate air exchange occurred between the chamber and the external environment, and due to the relatively small amount of magnetite, the change in oxygen partial pressure was negligible. The oxygen partial pressure was assumed to be the same as the ambient atmosphere. Figure 31 shows the sample after HT-XRD measurement. Two types of HT-XRD tests were carried out. (1) Non-isothermal HT-XRD: The raw sample was heated to 1000 $^{\circ}\text{C}$ at a heating rate of 100 $^{\circ}\text{C}/\text{min}$. The HT-XRD measurements were performed at various temperatures including 400 $^{\circ}\text{C}$, 600 $^{\circ}\text{C}$, 800 $^{\circ}\text{C}$, and 1000 $^{\circ}\text{C}$, as illustrated in Figure 32(a). Before and after the oxidation experiments, XRD measurements were executed at room temperature within a scanning angle range of 25 $^{\circ}$ to 65 $^{\circ}$. Notably, the temperature ramping was paused, and the material was maintained at a constant temperature during the in-situ HT-XRD measurements. The oxidation reaction continued during the HT-XRD scans. For the purpose of enhancing time resolution and minimizing the duration of the HT-XRD measurements, the scanning angle was confined to a narrow range between 32 $^{\circ}$ and 41 $^{\circ}$, where three hematite peaks and two magnetite peaks were observable. In this case, each HT-XRD measurement took around 67.5 seconds. (2) Isothermal HT-XRD: The raw sample was put on the heating strip and heated in vacuum to 400 $^{\circ}\text{C}$, 600 $^{\circ}\text{C}$, 800 $^{\circ}\text{C}$ and 1000 $^{\circ}\text{C}$,

respectively. The heating process was executed at a rate of 100 °C/min, as shown in Figure 32(b). After reaching the target temperature, the air was flushed into the chamber.

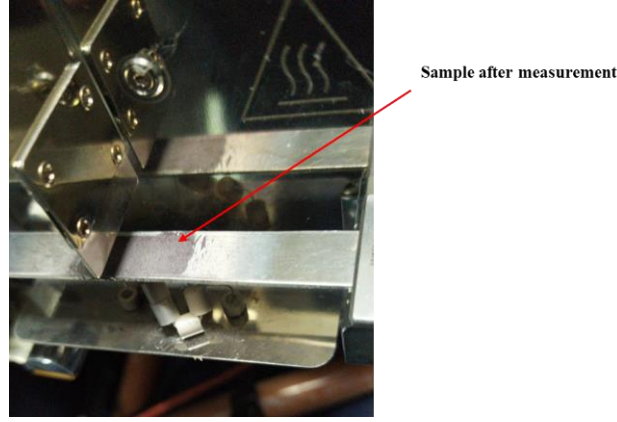


Figure 31: The sample after HT-XRD measurement.

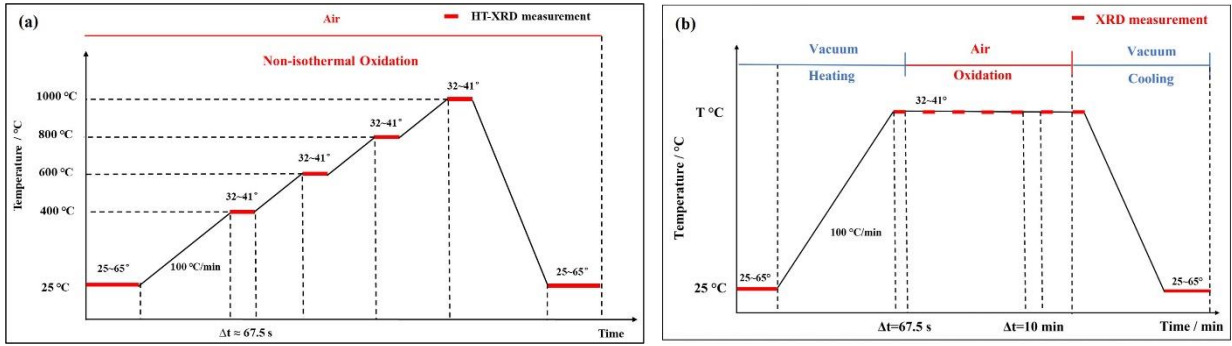


Figure 32: Temperature profile for HT-XRD measurements: (a) non-isothermal HT-XRD; (b) isothermal HT-XRD.

3.2.2 Determination of oxidation capacity index (OCI)

A TG-DTG curve of each magnetite ore could be obtained by a TGA test. In order to provide a comprehensive assessment of the oxidation behavior across various samples, the oxidation capacity index (OCI) was introduced. Analogous to the approach used for determining the comprehensive combustion property index (S) [92] of coal, the OCI of magnetite-based iron ore can be calculated according to equations (21) -(26):

$$\frac{dw}{dt} = A \cdot \exp\left(-\frac{E}{RT}\right) \quad (21)$$

$$\frac{d}{dT}\left(\frac{dw}{dt}\right) = A \cdot \exp\left(-\frac{E}{RT}\right) \cdot \frac{E}{RT^2} \quad (22)$$

Insert (22) into (21):

$$\frac{R}{E} \frac{d}{dT}\left(\frac{dw}{dt}\right) = \left(\frac{dw}{dt}\right) \frac{1}{T^2} \quad (23)$$

When oxidation starts, $T = T_i$:

$$\frac{R}{E} \frac{d}{dT} \left(\frac{dw}{dt} \right)_{T=T_i} = \left(\frac{dw}{dt} \right)_{T=T_i} \frac{1}{T_i^2} \quad (24)$$

(25) is obtained by multiplying $\frac{(dw/dt)_{\max} (dw/dt)_{\text{mean}}}{(dw/dt)_{T=T_i} T_e}$ at both sides of (24):

$$\frac{R}{E} \frac{d}{dT} \left(\frac{dw}{dt} \right)_{T=T_i} \frac{(dw/dt)_{\max} (dw/dt)_{\text{mean}}}{(dw/dt)_{T=T_i} T_e} = \frac{(dw/dt)_{\max} (dw/dt)_{\text{mean}}}{T_i^2 T_e} \quad (25)$$

Where $\frac{d}{dT} \left(\frac{dw}{dt} \right)_{T=T_i}$ indicates the oxidation rate of the magnetite at the initial oxidation temperature; $\frac{(dw/dt)_{\max}}{(dw/dt)_{T=T_i}}$ is the ratio of maximum reaction rate and the initial reaction rate; $\frac{(dw/dt)_{\text{mean}}}{T_e}$ is the ratio of mean reaction rate and the reaction finishing temperature T_e , which indicates the overall oxidation rate.

The right side of formula (25) is defined as OCI:

$$\text{OCI} = \frac{(dw/dt)_{\max} (dw/dt)_{\text{mean}}}{T_i^2 T_e} \quad (26)$$

3.2.3 HT-XRD data treatment

In this study, the Jade 6.0 software, developed by Materials Data Inc., was utilized for the identification and fitting of diffraction peaks. Through the application of refinement method in Jade 6.0, the overlapped peaks in the vicinity of 35° associated with magnetite and hematite were effectively separated. This process enabled the determination of peak location and profile of individual peaks, as shown in Figure 33. Moreover, the quantitative information of crystal information, such as lattice constants [93], crystallite size [94], and phase fraction [95], can be calculated.

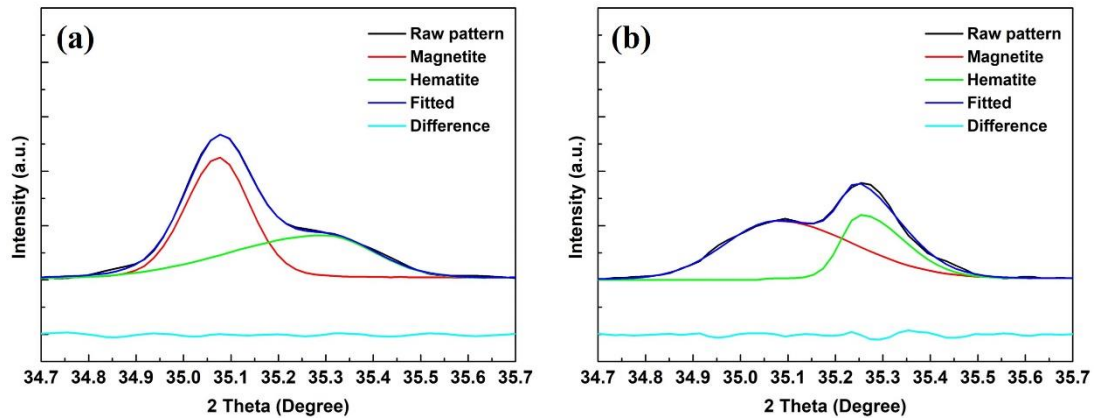


Figure 33: Rietveld refinement peak profile of Ore B at different temperatures under non-isothermal condition: (a) 600 °C and (b) 800 °C.

3.2.3.1 Determination of lattice constants

According to our previous TGA tests, the oxidation initiated at approximately 200 °C followed by the appearance of the first peak around 330 °C. The second peak occurred at around 400 °C [91]. The oxidation product was supposed to be γ -Fe₂O₃ between 200 °C and 400 °C. Above 400 °C, γ -Fe₂O₃ transformed into α -Fe₂O₃. In the current study, the oxidation temperature was higher than 400 °C, and thus only α -Fe₂O₃ was expected to be the oxidation product (hereafter, α -Fe₂O₃ is referred to as Fe₂O₃). Therefore, two crystal structures were considered: Fe₃O₄ (cubic close-packed crystal) and Fe₂O₃ (hexagonal close-packed crystal). The relationship between interplanar spacings (d), lattice constants (a), and crystal planes {hkl} are expressed in equations (27)-(29) [96]. Given a specific plane and its corresponding interplanar spacing, it is possible to calculate the lattice constants. The interplanar spacing can be obtained by Bragg's law as shown in equation (29).

$$\text{Cubic close-packed crystal:} \quad \frac{1}{d^2} = \frac{h^2+k^2+l^2}{a^2} \quad (27)$$

$$\text{Hexagonal close-packed crystal:} \quad \frac{1}{d^2} = \frac{4}{3} \frac{(h^2+k^2+hk)}{a^2} + \frac{l^2}{c^2} \quad (28)$$

$$\text{Bragg's law:} \quad d = \frac{n\lambda}{2\sin\theta} \quad (29)$$

where, d is the interplanar spacing; a and c are the lattice constants, (hkl) is the crystal plane; n is the diffraction order, and here the value is 1.

3.2.3.2 Determination of crystallite size

Crystallite size (D) can be calculated using the Scherrer equation, as shown in equation (30). It should be noted that the crystallite size refers to the average thickness perpendicular to the (hkl) planes. The (110) and (104) planes of Fe₂O₃ crystal were selected for the purpose of determining the crystallite size. These two peaks were chosen due to their relatively high intensities and the similarity in their instrumental broadening conditions, i.e., peak position [97]. As shown in Figure 34, the (110) plane is parallel to the c-axis and (104) plane is at a small angle to the a/b- axis [97]. Therefore, the crystallite size along the c-axis and a/b axis can be calculated according to equations (31)-(32).

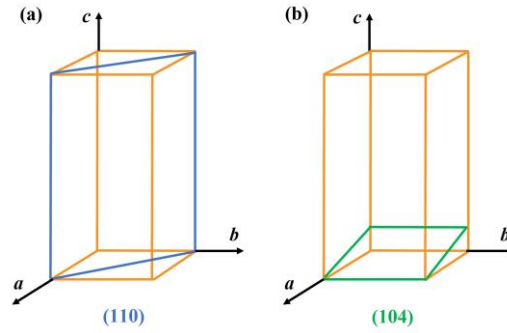


Figure 34: Schematic of Fe_2O_3 crystal: (a) (110) plane and (b) (104) plane.

$$D = \frac{K\lambda}{\beta \cos\theta} \quad (30)$$

$$D_{a/b} = D_{110} \times \cos\alpha_{110} \quad (31)$$

$$D_c = D_{104} \times \cos\alpha_{104} \quad (32)$$

where, D is crystallite size, nm; K is 0.94 (Scherrer constant); λ is 0.15406 nm (the wavelength of $K\alpha$ Cu X-ray source); β is full width at half maximum (FWHM), radians; θ is peak position, radians; $D_{a/b}$ and D_c represent the crystallite size calculated based on (110) and (104) peaks; α_{110} is the angle between [110] direction and x-y plane; α_{104} is the angle between the [104] direction and the y-z plane. Here, $\cos\alpha_{110}=1$ and $\cos\alpha_{104}=0.6192$ [97].

3.2.3.3 Determination of oxidation degree

The matrix-flushing method [98],[99] was used to obtain the content of Fe_3O_4 and Fe_2O_3 . The relative mass content of each phase is proportional to the ratio between its peak intensity and relative intensity ratio (RIR). The RIR value of each phase can be found in the PDF card database. The RIRs of the Fe_3O_4 and Fe_2O_3 phases are 4.9 and 3.2, respectively. The impurities were not considered in the calculation. The content of Fe_2O_3 and Fe_3O_4 can be calculated based on equations (33) - (34) [91].

$$x_H/x_M = \frac{I_H}{k_H} / \frac{I_M}{k_M} \quad (33)$$

$$x_H + x_M = 1 \quad (34)$$

where x_H and x_M are the relative mass content of Fe_2O_3 and Fe_3O_4 . I_H , I_M , k_H and k_M are the intensities and RIR values of Fe_2O_3 and Fe_3O_4 , respectively.

Kapelyushin et al. [100] calculated the reduction degree of Fe_3O_4 in the CO-CO_2 atmosphere based on HT-XRD analysis. The oxidation degree of Fe_3O_4 can be obtained by a similar method. The initial mass content of Fe_3O_4 was determined by the mass balance of iron. Hence,

the theoretical weight gain can be obtained as given in equations (35)-(36). The actual weight gain was calculated based on the Fe₂O₃ mass content via equation (37). Thereafter, the oxidation degree (w) can be obtained by equation (38) [101],[102].

$$m_M = x_M + \frac{x_H}{W_H} \times \frac{2}{3} \times W_M \quad (35)$$

$$\Delta m_{\text{theory}} = \frac{m_M}{W_M} \times \frac{W_O}{4} \quad (36)$$

$$\Delta m = \frac{x_H}{W_H} \times \frac{2}{3} \times \frac{W_O}{4} \quad (37)$$

$$w = \frac{\Delta m}{\Delta m_{\text{theory}}} \cdot 100 \% \quad (38)$$

where W_H , W_M , and W_O are mole masses of Fe₂O₃, Fe₃O₄, and O₂, respectively. m_M , Δm_{theory} , Δm , and w are the initial mass content of Fe₃O₄, theoretical weight gain, actual weight gain, and oxidation degree.

3.3 Characterization methods

The polished micro section was observed via an optical light microscope (Nikon MM 40 measuring microscope system, Japan). The surface morphology of the samples was characterized by a scanning electron microscopy (Quanta 200Mk2, FEI, America). The element distribution was analyzed by energy dispersive spectroscopy (EDS, Oxford Instrument, England). The X-ray diffraction (XRD) patterns presented in publication 1 [56] were achieved by an D2phaser X-ray diffractometer (Bruker AXS GmbH, Germany) with a Co X-ray source. The scanning range was set between 20° and 80° at a speed of 2°/min. The pore structure in publication 5 [91] was assessed using N₂ gas adsorption method by a surface area analyzer (TriStar 3000, Micromeritics, America). All the samples were degassed at 200 °C for 2 h.

4 Results and discussions

4.1 Reduction of magnetite iron ore fines in a hydrogen-induced fluidized bed

The influence of pre-oxidation and MgO addition on the fluidization and reduction behaviors of magnetite iron ore fines are discussed. The multistep kinetic analysis of the reduction is discussed in the current chapter. More detailed results are given in Publication 1 [56], which is under the Creative Commons CC BY license and permits unrestricted use, distribution, and reproduction in any medium, provided the original work is properly cited.

4.1.1 Effect of pre-oxidation

Figure 35 (a) shows the reduction results of the raw sample and the deeply oxidized sample at reducing temperature of 600 °C. The RD for the raw sample initiates at approximately 11%, as specified by equation ((17) where magnetite is considered to present a reduction degree of 11%. In the case of the raw sample, even though de-fluidization occurs at the RD of 35%, a complete reduction can be reached within 110 min. Almost 50% of the raw sample is not in fluidized state at the end of the reduction. As shown in Figure 35 (b), no de-fluidization occurs during the reduction of the deeply oxidized sample. The reduction rate dramatically decreases when RD is higher than 80%. Figure 36 shows the polished section images of the raw sample and the deeply oxidized sample after reduction. The particles in the raw sample are completely reduced. However, in the deeply oxidized sample, small wüstite cores covered by iron shells

can be observed inside the particles. The iron shells inhibit the direct contact of the reducing gas with the reaction interface, which explains the low reduction rate at the final stage.

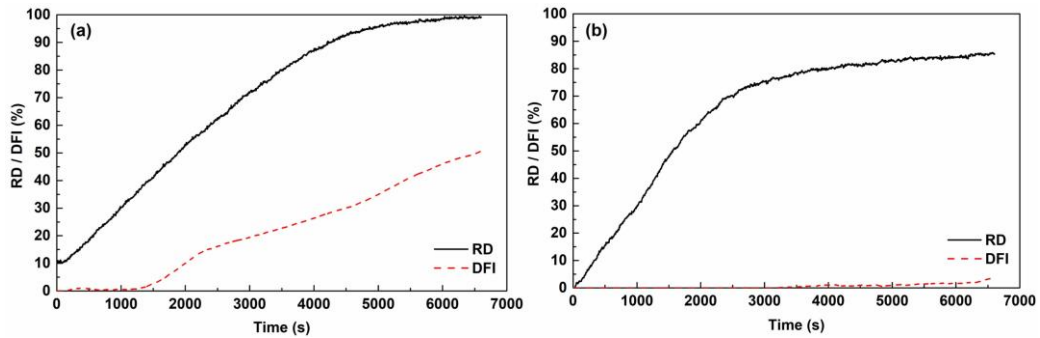


Figure 35: Reduction degree and de-fluidization index of raw sample and deeply oxidized sample at reducing temperature of 600 °C: (a) RD / DFI of raw sample; (b) RD / DFI of deeply oxidized sample.

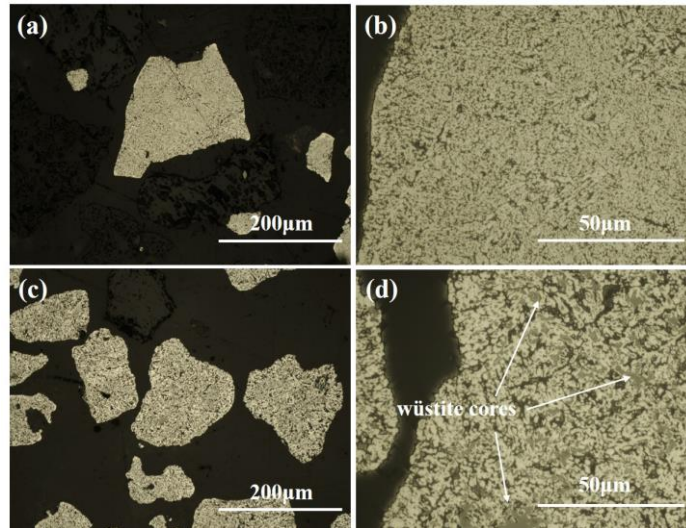


Figure 36: Polished section images of the raw sample and deeply oxidized sample after reduction tests at 600 °C under optical light microscope: (a), (b) raw sample; (c), (d) deeply oxidized sample.

The pre-oxidation treatment of the raw sample could improve the fluidization behavior at reducing temperature of 600 °C. However, at higher temperatures, fluidization issue is still a problem. The influence of reducing temperature on the fluidization time (t_f) is significant, as shown in Figure 37(a). With increasing temperature, the t_f decreases, for both raw and deeply oxidized sample. In Figure 37(b) the correlation between reduction temperature and RD at the initiation of de-fluidization is depicted. The RD values exhibit a decreasing pattern as the temperature increases, primarily due to the limited fluidization duration. Combined with Figure 37(a), it becomes evident that when the reduction temperature higher than 650 °C, the RDs for deeply oxidized samples, despite the shorter t_f of the deeply oxidized sample, the RDs are greater than those of raw sample. Especially at 800 °C, the deeply oxidized sample has similar

t_f but shows nearly 10 % higher RD, which indicates that the deeply oxidized sample has a better reduction behavior in the initial stage. Previous researchers [103] have showed that the reducibility of magnetite-based iron ore was enhanced by a prior-oxidation treatment; the results of this work are in agreement with their findings. It's worth highlighting that when the temperature exceeds 700 °C, the RD at the onset of de-fluidization for the raw sample remains consistent at 20%. This value could potentially be the critical RD that triggers de-fluidization [44],[104]. In practical scenarios, the formation of metallic iron can be formed before the reduction to FeO is fully accomplished, implying that the initial formation of metallic iron on particle surfaces may take place even when the RD is below 33%.

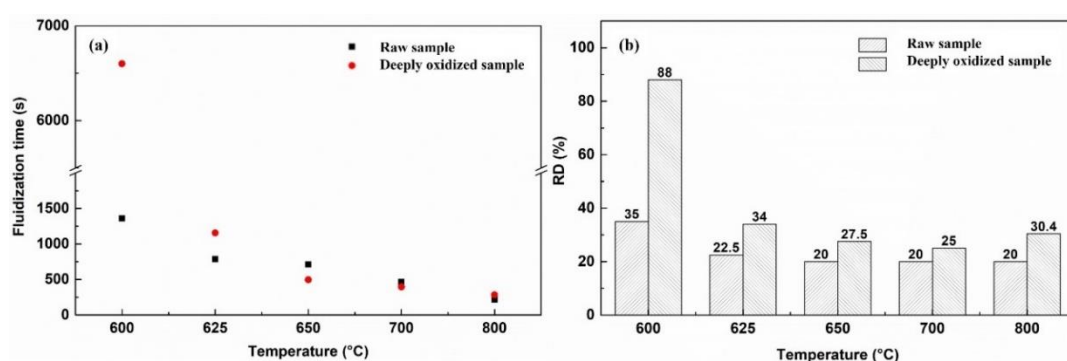


Figure 37: Fluidization and reduction behaviors of raw sample and deeply oxidized sample: (a) fluidization time; (b) reduction degree when de-fluidization starts.

The deeply oxidized sample exhibited sustained complete fluidization at 600 °C throughout the reduction experiment. Nevertheless, an increase in temperature also lead to the occurrence of de-fluidization. As shown in Table 8, when reducing temperature is higher than 650°C, the deeply oxidized sample can not be fluidized any more. Therefore, MgO coating method is tested combined with the pre-oxidation treatment.

Table 8: Fluidization state of the raw sample and the deeply oxidized sample

Reduction temperature	Fluidization State	
	Raw sample	Deeply oxidized sample
600 °C	Aggregating de-fluidized	Completely fluidized
625 °C	Completely de-fluidized	Partly de-fluidized
650 °C	Completely de-fluidized	Partly de-fluidized
700 °C	Completely de-fluidized	Completely de-fluidized
800 °C	Completely de-fluidized	Completely de-fluidized

4.1.2 Effect of MgO addition

The impact of MgO addition on the fluidization state and reducibility of the deeply oxidized sample is investigated. The MgO powder is mixed with the oxidized sample before the reduction tests. As indicated in Table 9 the addition of 0.25 wt.-% MgO leads to partial de-fluidization, with approximately 15% of the material exhibiting a non-fluidized state according to DFI value. However, de-fluidization can be prevented when the MgO addition exceeds 0.25 wt.-%. To illustrate the influence of MgO on the reduction behavior, the relationship between RD and MgO content is depicted in Figure 38. With increasing MgO content, the reduction degree curves, shown in Figure 38(a), shift slightly toward lower reduction times. It is important to emphasize that de-fluidization initiates after reduction times of 380 s and 500 s for the cases without MgO addition and with 0.25 wt.-% MgO addition, respectively. But only the reduction tests without de-fluidization, are discussed and compared. Figure 38(b) illustrates the reduction rate for various MgO addition. The reduction rate can be divided into three stages (I, II, and III). Stage I is regarded as the fast reduction from Fe_2O_3 to Fe_3O_4 . As given in Figure 38(d), it is observed that samples with a higher MgO content exhibit a slightly elevated reduction rate during Stage I. When coupled with Figure 38(c), it becomes apparent that the presence of MgO primarily exerts a beneficial influence in Stage I. However, as the reduction progresses further, the reduction rate lines become entangled in Stages II and III, revealing no distinct pattern. These findings align with previous studies by Muhammad [105] and Srinivas [106], which concluded that the addition of MgO can enhance the reduction Fe_2O_3 . It is easier for Mg^{2+} to migrate to vacancy than Fe^{2+} in wüstite (Fe_xO). Therefore, magnesiowüstite ($\text{Fe}_x\text{Mg}_{1-x}\text{O}$) is formed, which inhibits the reduction of wüstite. A similar phenomenon has also been observed in the reduction of pure hematite doped with MgO using CO [57]. In the study conducted by El-Geassy [57], the impact of MgO on the stepwise reduction of pure hematite compacts was examined. The findings indicates that in the hematite-magnetite reduction step, an initial enhancement effect is evident due to heightened porosity and the increased active sites resulting from the introduction of foreign cations into the Fe_2O_3 lattice. At later stages, the formation of phase $\text{MgO}\cdot\text{Fe}_2\text{O}_3$ with low reducibility retarded the reduction of Fe_2O_3 . In the magnetite-wüstite and wüstite-iron reduction steps, the decreases in reduction rate are attributed to the formation of magnesiowüstite. In the present study, the final reduction degrees are listed in Table 9. Although the deeply oxidized sample with 0.25 wt.-% MgO-addition becomes partially de-fluidized, the final RD is as high as 91.37 %. In general, the addition of MgO tends to have a promotional effect on the reduction rate.

Table 9: Influence of MgO addition on the fluidization behavior and the final RD

MgO content (wt.-%)	Fluidization state	Final reduction degree (%)
0	Completely fluidized	25.00
0.25	Partly de-fluidized	91.37
0.5	Completely fluidized	93.75
1.0	Completely fluidized	96.05
1.5	Completely fluidized	96.35

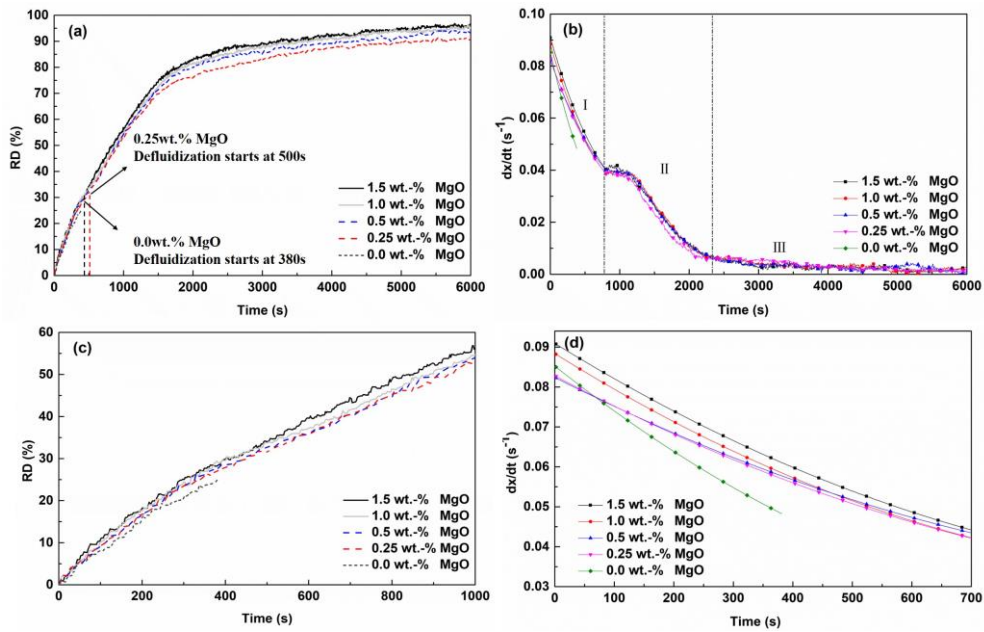


Figure 38: Influence of MgO on reduction behavior: (a), (c) reduction degree curves; (b), (d) reduction rate.

4.1.3 Multistep kinetic analysis

the fitting results for deeply oxidized sample with varying amounts of MgO is presented in Figure 39, where R1, R2 and R3 denote chemical reaction, nucleation and diffusion respectively. It should be noticed that in case of 0.25 wt.-% MgO addition, around 10% of the material was not fluidized. The results exhibit excellent match with the experimental data as indicated by the low root-mean-square deviation (RMSD) values listed in Table 10. Notably, the reaction process R1 primarily governs the initial portion of the overall reduction degree (RD), thereby exerting minimal influence on the subsequent reduction stages. In terms of long-time reaction processes, the total RD is primarily influenced by R2 and R3. The values of w_1 exhibit a slight increase with higher amounts of MgO addition, reflecting the enhancement

effect of the reaction in the initial stage. The values of w_2 and w_3 show no obvious trends but keep quite stable. In general, the quantity of MgO has a minor impact on the reaction mechanisms. The parallel reaction processes can be illustrated as follows. The initial reaction is dominated by a rapid chemical reaction. During the middle phase, nucleation and diffusion govern the reaction, with nucleation playing a dominant role. However, in the later stage of the reaction, nucleation becomes less significant, and diffusion becomes the limiting step for the reaction.

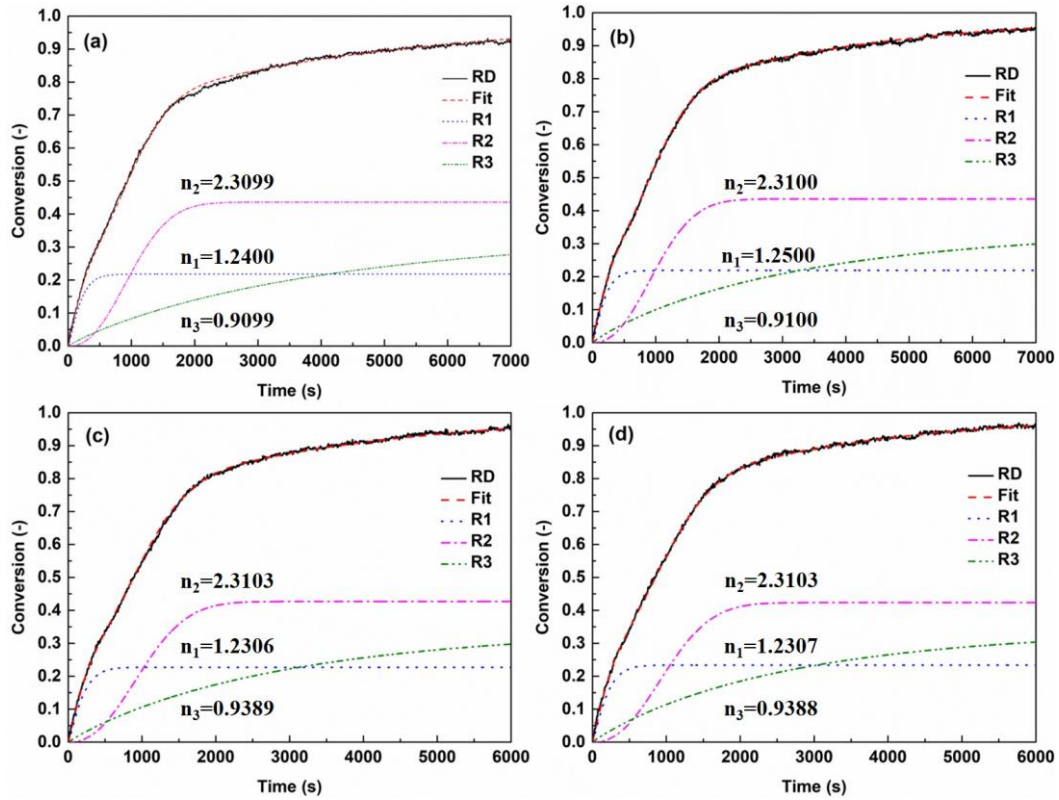


Figure 39: Fitting results for deeply oxidized sample with different amount of MgO: (a) 0.25 wt.-%; (b) 0.5 wt.-%; (c) 1.0 wt.-%; (d) 1.5 wt.-%.

Table 10: Kinetic analysis for Sample B with different amount of MgO

		MgO addition			
		0.25 wt.-%	0.5 wt.-%	1.0 wt.-%	1.5 wt.-%
Weight factors	w_1	0.2180	0.2190	0.2273	0.2340
	w_2	0.4361	0.4356	0.4268	0.4235
	w_3	0.3459	0.3454	0.3459	0.3425
Nucleation rate constants (s^{-1})	a_1	0.0013	0.0013	0.0014	0.0014

	a_2	8.40×10^{-8}	8.40×10^{-8}	8.40×10^{-8}	8.40×10^{-8}
	a_3	5.12×10^{-4}	6.37×10^{-4}	5.60×10^{-4}	6.18×10^{-4}
Kinetic exponents	n_1	1.2400	1.2500	1.2306	1.2307
	n_2	2.3099	2.3100	2.3103	2.3103
	n_3	0.9099	0.9100	0.9389	0.9388
Root-mean-square deviation	RMSD	0.0072	0.0050	0.0050	0.0046

4.2 Parameter optimization for the hydrogen-induced fluidized bed reduction of magnetite iron ore fines

It was confirmed, in the previous chapter, that the pre-oxidation treatment has the potential to enhance the fluidization behavior of magnetite iron ore fines. However, when the reducing temperature is as high as 700 °C, at least 0.5 wt.-% MgO powder should be added to prevent the de-fluidization. When reduction degree reaches around 80%, the reduction rate is very low, and the diffusion becomes the reaction limiting step. In the current chapter, to improve the reduction behavior in later stage, the pre-oxidation temperature of the sample is lowered from 1000 °C to 900 °C and 800°C. The oxidation content of the sample is changed from deeply oxidized to partly oxidized. The optimum operating parameters are confirmed by an orthogonal experiment. More detailed results are given in Publication 2 [61] and Publication 3 [62], which are under the Creative Commons CC BY license and permit unrestricted use, distribution, and reproduction in any medium, provided the original work is properly cited.

4.2.1 Reduction under various conditions

The effect of pre-oxidation temperature on the fluidization and reduction behavior is studied using DOX₁₂₅₋₂₅₀₋₁₀₀₀ and DOX₁₂₅₋₂₅₀₋₈₀₀. DOX and POX represent deeply oxidized sample and partly oxidized sample, respectively. The “125-250” represents the particle size range 125-250 μm. As shown in Figure 40(a), the RD curve of the DOX₁₂₅₋₂₅₀₋₈₀₀ is similar to that of DOX₁₂₅₋₂₅₀₋₁₀₀₀ in the early reduction stage. However, when RD reaches 80 %, DOX₁₂₅₋₂₅₀₋₈₀₀ shows a higher reduction rate than that of DOX₁₂₅₋₂₅₀₋₁₀₀₀. It should be noted that the DFI of DOX₁₂₅₋₂₅₀₋₈₀₀ is much higher than that of DOX₁₂₅₋₂₅₀₋₁₀₀₀. A better fluidization behavior is observed in a higher oxidation temperature pre-treatment. From the point of fluidization behavior, a high-temperature oxidation treatment is suggested. The reduction efficiency is a

crucial factor in the production of DRI. Figure 40(b) gives the characteristic reduction time to achieve a specific RD. It takes 8.45 min to reach RD of 33 % and another 20.26 min to reach RD of 80 % for DOX₁₂₅₋₂₅₀₋₁₀₀₀. DOX₁₂₅₋₂₅₀₋₈₀₀ requires the similar time to reach RD of 33 % (7.93 min) and 80 % (18.06 min). But compared with DOX₁₂₅₋₂₅₀₋₁₀₀₀, it takes nearly only half time for DOX₁₂₅₋₂₅₀₋₈₀₀ to reach RD of 95 %. Lower pre-oxidation temperatures tend to enhance the reduction rate during the later stage of the reduction process.

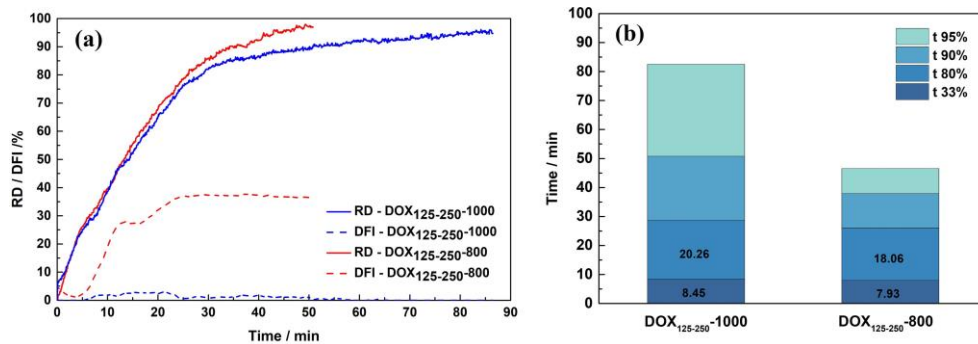


Figure 40: Effect of pre-oxidation temperature on the fluidization and reduction behaviors: (a) reduction degree and DFI; (b) reduction time to reach a specific RD.

The effect of pre-oxidation content on the fluidization and reduction behavior is studied using DOX₁₂₅₋₂₅₀₋₈₀₀ and POX₁₂₅₋₂₅₀₋₈₀₀. As shown in Figure 41(a), the RD curve of the DOX₁₂₅₋₂₅₀₋₈₀₀ is similar to that of POX₁₂₅₋₂₅₀₋₈₀₀ in the entire reduction stage. However, the fluidization behaviors exhibit slightly different. The POX₁₂₅₋₂₅₀₋₈₀₀ starts de-fluidization (DFI>5 %) when RD reaches around 65 %, while the DOX₁₂₅₋₂₅₀₋₈₀₀ starts de-fluidization earlier at around RD of 35 %. Both types of materials exhibit a partly de-fluidized state at the end of the process, with a DFI of 36%. In terms of the characteristic reduction time, as depicted in Figure 41(b), no significant difference is observed. The pre-oxidation degree appears to have no substantial impact on fluidization and reduction behaviors.

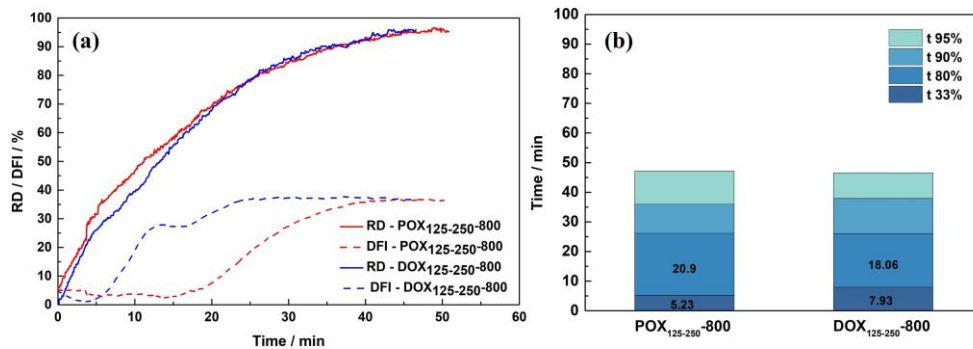


Figure 41: Effect of pre-oxidation degree on the fluidization and reduction behaviors: (a) reduction degree and DFI; (b) reduction time to reach a specific RD.

Figure 42 displays the surface morphology and polished-section images of the reduced samples. Specifically, the DOX₁₂₅₋₂₅₀₋₁₀₀₀, DOX₁₂₅₋₂₅₀₋₈₀₀ and POX₁₂₅₋₂₅₀₋₈₀₀ exhibit a lamellar shape, a conical-shape, and a cylindrical shape, respectively. Although in Figure 42(c), still few conical-shaped irons can be observed, most of the iron phase exhibits cylindrical shapes. Nicolle et al. [46] provided an explanation for the growth of iron nucleus on wüstite and established a correlation between the shape of the iron phase and the controlling mechanism. According to his findings, when the reaction was primarily limited by the inward diffusion of iron ions, the fresh metallic iron exhibited a layered structure on the particle surface. In cases where the reaction was predominantly controlled by chemical reactions, a cylindrical whisker structure might form. If the reaction involved a combination of diffusion and chemical reaction controls, a conical shape of iron phase was expected to develop.

Detailed kinetic analysis is discussed in Publication 2 [61]. In the initial reduction stage of the deeply oxidized sample, the rate-limiting step is attributed to diffusion control. A higher pre-oxidation temperature (1000 °C) impacts the final reduction stage, shifting the controlling mechanism to diffusion. On the other hand, for the partly oxidized sample treated at 800 °C, the entirety of the reduction process is governed by chemical reaction control. For DOX₁₂₅₋₂₅₀₋₁₀₀₀, the reaction is controlled by diffusion, chemical reaction and diffusion in the first (11%<RD<33%), second (33%<RD<80%) and third (80%<RD<95%) stage, respectively. The morphology shape observed in Figure 42(a) is characteristic of a diffusion-controlled reaction, which aligns with the kinetic analysis results for the third stage. As given in Figure 42(g), the polished-section image displays numerous wüstite islands, which is caused by the restriction of inward diffusion of iron ions. It can be concluded that the reduction of DOX₁₂₅₋₂₅₀₋₁₀₀₀ is mainly controlled by the diffusion of iron ions. As for DOX₁₂₅₋₂₅₀₋₈₀₀ and POX₁₂₅₋₂₅₀₋₈₀₀, the morphology shapes in Figure 42(b) and Figure 42(c) are typical shapes for a mixed-controlled reaction and a chemical-controlled reaction, respectively. According to the kinetic analysis, it can be inferred that in the third stage, diffusion is not the rate-limiting step for the reduction of DOX₁₂₅₋₂₅₀₋₈₀₀. In comparison with DOX₁₂₅₋₂₅₀₋₁₀₀₀, the occurrence of wüstite islands in DOX₁₂₅₋₂₅₀₋₈₀₀ is less pronounced, as shown in Figure 42(h). The kinetic analysis indicates that the entire reduction progress of POX₁₂₅₋₂₅₀₋₈₀₀ is solely controlled by chemical reaction. It was proved by the polished-section image, as shown in Figure 42(i), the wüstite islands in POX₁₂₅₋₂₅₀₋₈₀₀ almost disappeared.

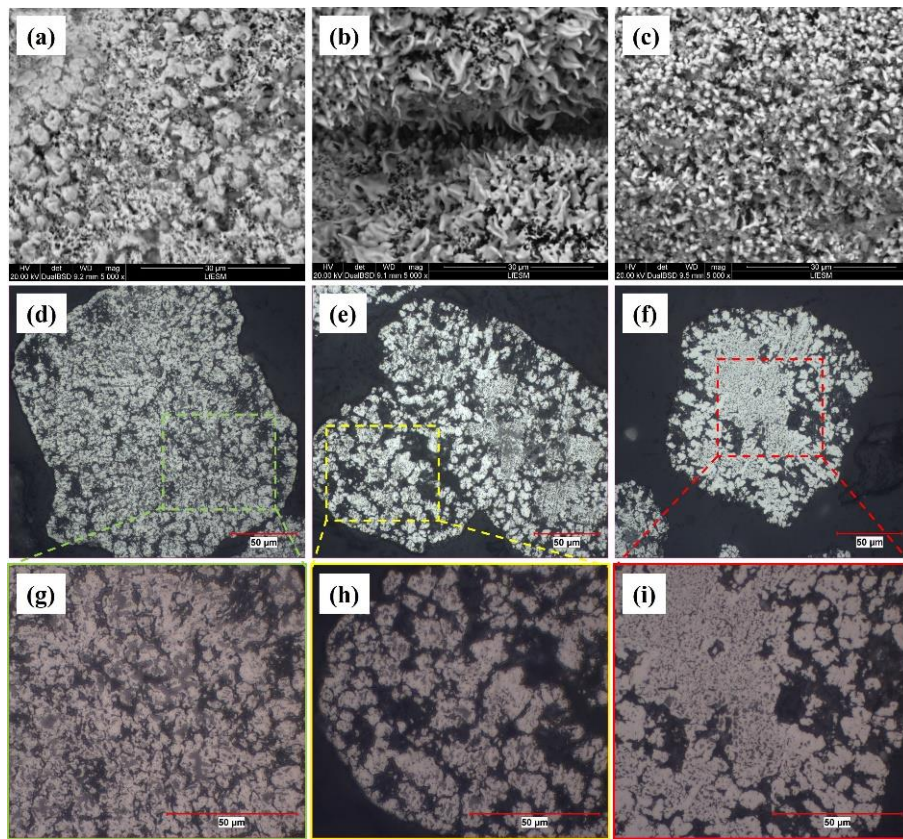


Figure 42: The reduced samples with the particle size of 125-250 μm : (a) surface morphology of $\text{DOX}_{125-250-1000}$; (b) surface morphology of $\text{DOX}_{125-250-800}$; (c) surface morphology of $\text{POX}_{125-250-800}$; (d),(g) polished-section images of $\text{DOX}_{125-250-1000}$; (e),(h) polished-section images of $\text{DOX}_{125-250-800}$; (f),(i) polished-section images of $\text{POX}_{125-250-800}$. Images of (a)-(c) were obtained by SEM; Images of (d)-(i) were obtained by optical microscope.

In general, structural analysis supports the findings of the kinetic analysis. Through both kinetic and structural analysis, it is evident that a pre-oxidation treatment at higher temperatures leads to a restriction of the diffusion of iron ions during the subsequent reduction process, particularly in the later stages. This effect is reflected in the flat surface morphology, which in turn contributes to enhanced fluidization behavior. A pre-oxidation treatment at lower temperatures facilitates the diffusion of iron ions. However, in such a case, the fluidization behavior is destroyed by the surface morphology with whiskers.

4.2.2 Orthogonal experiment analysis

The oxidation treatment applied to magnetite iron ore indeed exhibits an enhancement in fluidization behaviors. However, even with this treatment, additional MgO is necessary when conducting reduction at a temperature of 700 $^{\circ}\text{C}$. The outcomes from previous chapters show that the oxidation parameters of the magnetite have influences on its fluidization and reduction

behaviors. To confirm the dominant influencing factors and the optimal process condition, the orthogonal experimental method is conducted in this chapter. The fluidized reduction process is influenced by several key factors, including oxidation temperature (Factor A), oxidation content (Factor B), MgO addition amount (Factor C), and gas velocity (Factor D). The orthogonal experimental plan is designed using IBM SPSS Statistics 26 software, where three levels of each factor are taken. The reduction temperature and H₂ content are 700 °C and 15.9 NI/min, respectively, for all the experiments. The detailed experimental programs are given in Table 11 and Table 12.

Table 11: Orthogonal experimental factors and levels.

Factor	A			B			C			D		
	Oxidation temperature, °C			Oxidation content			MgO amount, wt. %			Gas velocity, m/s		
Level	A ₁	A ₂	A ₃	B ₁	B ₂	B ₃	C ₁	C ₂	C ₃	D ₁	D ₂	D ₃
	800	900	1000	Raw	Partly	Deeply	0.5	1.0	1.5	0.35	0.40	0.45

Table 12: Orthogonal experimental plan.

No.	A	B	C	D
1	A ₃	B ₂	C ₃	D ₁
2	A ₃	B ₃	C ₁	D ₂
3	A ₂	B ₁	C ₃	D ₂
4	A ₂	B ₃	C ₂	D ₁
5	A ₂	B ₂	C ₁	D ₃
6	A ₁	B ₃	C ₃	D ₃
7	A ₁	B ₁	C ₁	D ₁
8	A ₃	B ₁	C ₂	D ₃
9	A ₁	B ₂	C ₂	D ₂

The primary objective of a fluidized bed reduction process is to achieve a high reduction rate while maintaining a stable fluidization state. Therefore, the time to reach RD=90% ($t_{90\%}$) and the Ave.DFI are chosen as indicators for the optimization of reduction parameters. The result is shown in Table 13. In order to determine the dominant factors that influence fluidization and reduction behaviors and identify the optimal conditions, an orthogonal experiment analysis is conducted. The criterion used to determine whether reduction occurs in a completely fluidized state is the Ave.DFI smaller than 5%. The results are shown in Table 14 and Table 15. Among the experimental results, Experiment No.2 exhibits the lowest Ave.DFI and experiment No.6 gives the smallest $t_{90\%}$.

Table 13: The orthogonal experimental result

No.	$t_{90\%}$, min	Ave.DFI, %
1	50.80	2.32
2	70.92	1.73
3	56.64	2.89
4	47.73	16.81
5	49.86	16.95
6	38.62	4.23
7	56.92	18.52
8	66.24	4.56
9	46.95	2.80

Table 14: The orthogonal experimental analysis regarding $t_{90\%}$

	A	B	C	D
K ₁	142.49	179.80	177.70	155.45
K ₂	154.23	147.61	160.92	174.51
K ₃	187.96	157.27	146.06	154.72
k ₁	47.50	59.93	59.23	51.82
k ₂	51.41	49.20	53.64	58.17
k ₃	62.65	52.42	48.69	51.57
R	15.16	10.73	10.55	6.60
Primary and secondary factors			ABCD	
Optimization scheme			A ₁ B ₂ C ₃ D ₃	

Table 15: The orthogonal experimental analysis regarding Ave.DFI

	A	B	C	D
K ₁	25.55	25.97	37.20	37.65
K ₂	36.65	22.07	24.17	7.42
K ₃	8.61	22.77	9.44	25.74
k ₁	8.52	8.66	12.40	12.55
k ₂	12.22	7.36	8.06	2.47
k ₃	2.87	7.59	3.15	8.58
R	9.35	1.30	9.25	10.08
Primary and secondary factors			DACB	
Optimization scheme			D ₂ A ₃ C ₃ B ₂	

The K_i is obtained by summing the experiment result (see Table 13) corresponding to each level number i as shown in Table 12; The value of k_i is calculated by dividing K_i by the number n of occurrences of each level, where $n=3$; R is determined as the difference between the

maximum value of k_i and the minimum value of k_i . The experimental factor with the highest R -value indicates the most significant influencing factor. The experimental level associated with the smallest k_i value represents the optimal choice for the corresponding experimental factor. Hence, concerning reduction efficiency, specifically $t_{90\%}$, the primary and secondary influencing factors are oxidation temperature, oxidation content, MgO addition amount, and gas velocity. The optimal condition is determined as $A_1B_2C_3D_3$: the magnetite iron ore is partly oxidized at 800 °C, mixed with 1.5 wt.% of MgO, and reduced in the fluidized bed at a gas velocity of 0.45 m/s. In terms of fluidization behaviors, specifically Ave.DFI, the primary and secondary influencing factors are gas velocity, oxidation temperature, MgO addition amount, and oxidation content. The optimal condition is determined as $D_2A_3C_3B_2$: the magnetite iron ore is partly oxidized at 1000 °C, mixed with 1.5 wt.% of MgO, and reduced in the fluidized bed at a gas velocity of 0.4 m/s. From the orthogonal experimental result as shown in Table 13, the fluidization behavior shows no problem under experimental conditions. Experiment No.6 shows the highest reduction rate. Only experiments No. 4, 5, and 7 are partly de-fluidized. Subsequent discussions mainly focus on the reduction rate.

If the condition $A_1B_2C_3D_3$ shows the lowest $t_{90\%}$ with an acceptable Ave.DFI (<5.0%), it can be confirmed as the optimum condition. Thereafter, experiment No. 10 is carried out using the condition $A_1B_2C_3D_3$. The $t_{90\%}$ and Ave.DFI of No. 10 are 42.1 min and 2.4%, respectively. Figure 43 shows the reduction and de-fluidization curves. Experiment No. 10 shows a good reduction rate, albeit slightly lower than that of experiment No.6. Notably, the fluidization behaviors observed in both No. 10 and No. 6 are comparable. Thus, it can be deduced that the experiment. No.6 is the optimal condition instead of No.10. The detailed RD curves and structure analysis are given in Publication 3 [62].

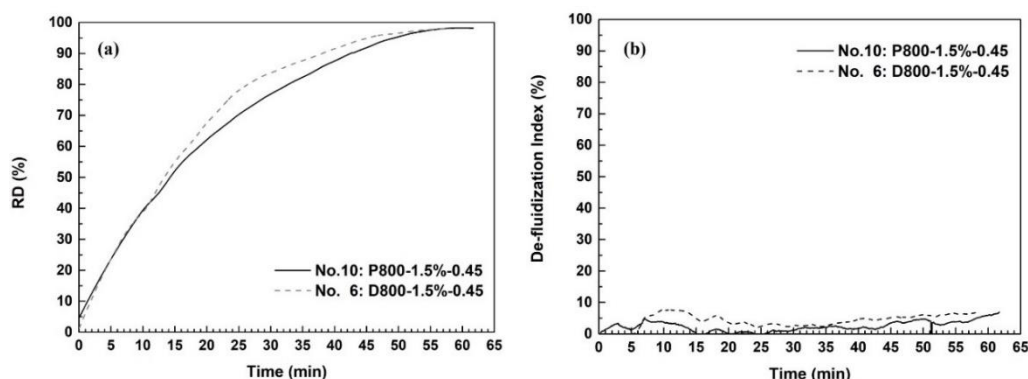


Figure 43: The fluidized reduction results of experiments No.6 and No.10: (a) reduction curve; (b) de-fluidization curve. P800-1.5%-0.45 represents that the magnetite iron ore is partly oxidized at 800 °C, mixed with 1.5 wt.% of MgO and reduced in the fluidized bed at a gas velocity of 0.45 m/s; D800-1.5%-0.45 represents that the magnetite iron ore is deeply oxidized at 800 °C, mixed with 1.5 wt.% of MgO and being reduced in the fluidized bed at a gas velocity of 0.45 m/s.

4.3 The oxidation behavior of the magnetite iron ore fines

The pre-oxidation of magnetite iron ore fines influences the subsequent reduction behaviors. For subsequent reduction, the sintering effect cannot be ignored during the oxidation treatment of magnetite-based iron ore fines. This effect often leads to a considerable reduction in the specific surface area [107],[108]. The sintering effect usually has a detrimental impact on the reduction of iron ore particles. In the current chapter, the oxidation behavior, pore structure, surface morphology and internal structure of the magnetite ore fines after pre-oxidation treatment are studied. The properties of the three commercial magnetite ore fines used for oxidation experiment are listed in Table 6 and Table 7. More detailed results are given in publication 5 [91], which is under the Creative Commons CC BY license and permit unrestricted use, distribution, and reproduction in any medium, provided the original work is properly cited.

4.3.1 The oxidation capacity index

Figure 44 shows the oxidation TG-DTG curves of different samples. From Figure 44(a), it is obvious that Sample B is the easiest one to be oxidized among the three samples. According to the result, as given in Figure 44(b-d), the oxidation reaction can be categorized into a minimum of three distinct stages. Peak 1 is consistently observed at approximately 330 °C in all the samples. In this temperature range, the oxidation primarily takes place at the particle surface, and the chemical reaction is the rate-limiting step [109]. The diffusion of Fe^{2+} and Fe^{3+} ions is also limited due to the low oxidation temperature. Therefore, the height of peak 1 is relatively low. The oxidation product is supposed to be $\gamma\text{-Fe}_2\text{O}_3$ [110]–[112]. At the temperature around peak 2 (550 °C), the $\gamma\text{-Fe}_2\text{O}_3$ becomes unstable and transforms to $\alpha\text{-Fe}_2\text{O}_3$ [65]. From the kinetic perspective, oxidation reaction of magnetite in particle scale is limited by solid-state diffusion. The diffusion rate constant remains unaffected by changing oxygen partial pressure but does increase with elevated temperatures [65]. The increasing temperature accelerates the movement of Fe^{2+} and Fe^{3+} ions, thus enhancing the oxidation rate. However, as the oxidation reaction progresses, the formed $\alpha\text{-Fe}_2\text{O}_3$ shell obstructs the diffusion of the iron and oxygen ions, leading to a decline in the oxidation rate [113]. At higher temperatures, the following peaks (peak 3 or peak 4) of different samples show diversities, which can be attributed to the side-reactions between impurities and iron oxides. The isomorphous substitution occurs widely within the structure of magnetite-based ores, resulting in impurity element existing in the magnetite lattice [114].

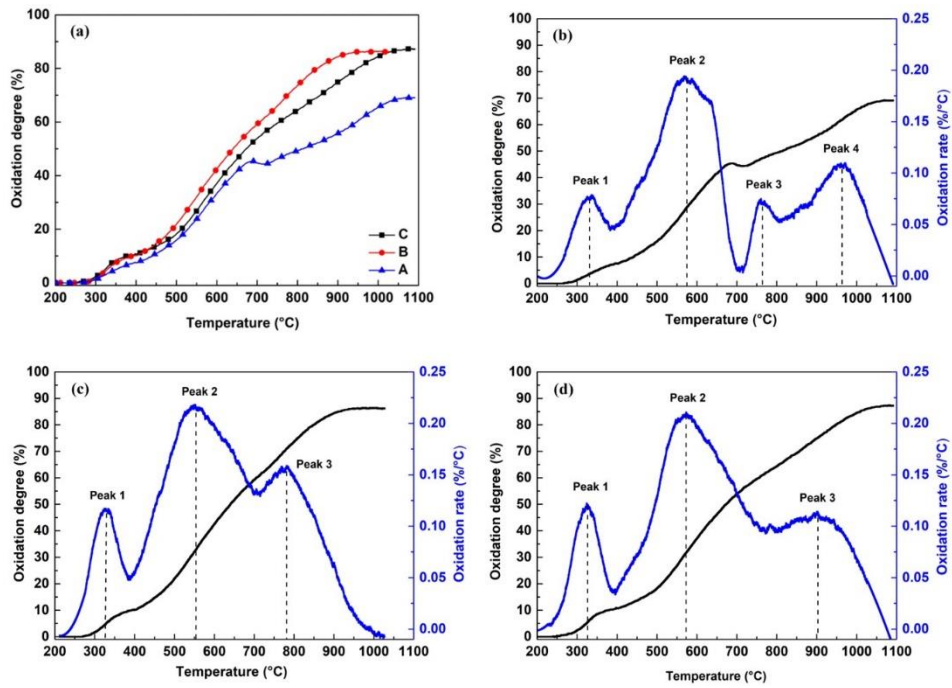


Figure 44: Oxidation TG-DTG curves of the samples: (a) TG curve of samples; (b) TG-DTG curve of Sample A; (c) TG-DTG curve of Sample B; (d) TG-DTG curve of Sample C.

The characteristic parameters of the oxidation are listed in Table 16. T_i is the temperature when the oxidation starts. The temperature when Ore B starts to be oxidized is much lower than that of Ore A and Ore C. T_{p-1} , T_{p-2} , T_{p-3} , and T_{p-4} are the temperatures of the peaks in the DTG curves. The highest oxidation rates are observed in the temperature range of 548 °C and 573 °C. Additionally, the second highest oxidation rates occur in the temperature range of 764 °C and 902 °C. The OCI represents the oxidation capacity index of magnetite-based iron ore. A higher OCI value for a magnetite-based ore represents that it is easier to be oxidized. Ore B shows the highest OCI, followed by Ore C and Ore A.

Table 16: The characteristic parameters of the oxidation.

Parameters	Ore A	Ore B	Ore C
T_i (°C)	265	214	239
T_{p-1} (°C)	337	325	326
T_{p-2} (°C)	570	548	573
T_{p-3} (°C)	764	778	902
T_{p-4} (°C)	962	/	/

T_e , (°C)	1083	1000	1091
$(dw/dt)_{\max-1}$, (%/min)	0.5663	0.8719	0.9050
$(dw/dt)_{\max-2}$, (%/min)	1.4375	1.6143	1.5784
$(dw/dt)_{\max-3}$, (%/min)	0.5318	1.1468	0.8558
$(dw/dt)_{\max-4}$, (%/min)	0.7971	/	/
$(dw/dt)_{\text{mean}}$, (%/min)	0.4778	0.6470	0.5998
$\text{OCI} \times 10^{-8}$, ($\%^2 \cdot \text{min}^{-2} \cdot ^\circ\text{C}^{-3}$)	0.9031	2.2807	1.5192

4.3.2 Structural evolution

The surface morphologies under different duration times are shown in Figure 45–Figure 47. As shown in Figure 45(b), Figure 46(b) and Figure 47(b), after only 2 min, the dense surface structure becomes rough and presents a nano-sized grid-like structure. This phenomenon has been also observed in the oxidation of vanadium-titanium magnetite ores [95],[102],[115]. The grid-like structures are supposed to be hematite phase and caused by the out-diffusion of Fe^{2+} . After 5 min, as shown in Figure 45(c), Figure 46(c) and Figure 47(c), the grid-like structures in the Ore B are much bigger than those in the other two samples. The larger grid-like structures observed in Sample A compared to Sample C could be attributed to the differences in impurity content. As indicated in Table 6, Ore B contains fewer impurity elements, while Sample C has the most impurities. These impurity elements may potentially replace iron ions in the lattice structure, thus affecting the diffusion behavior of cations. This influence on cation diffusion could lead to distinct growth patterns in the grid-like structures. With the oxidation time, these grid-like structures grow larger and eventually connect together.

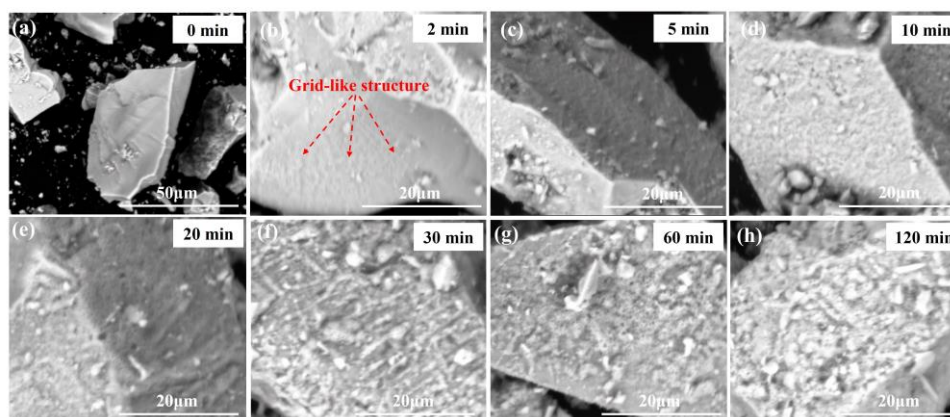


Figure 45: SEM images of the oxidized products of Sample A obtained under different duration times: (a) 0 min, (b) 2 min, (c) 5 min, (d) 10 min, (e) 20 min, (f) 30 min, (g) 60 min, (h) 120 min.

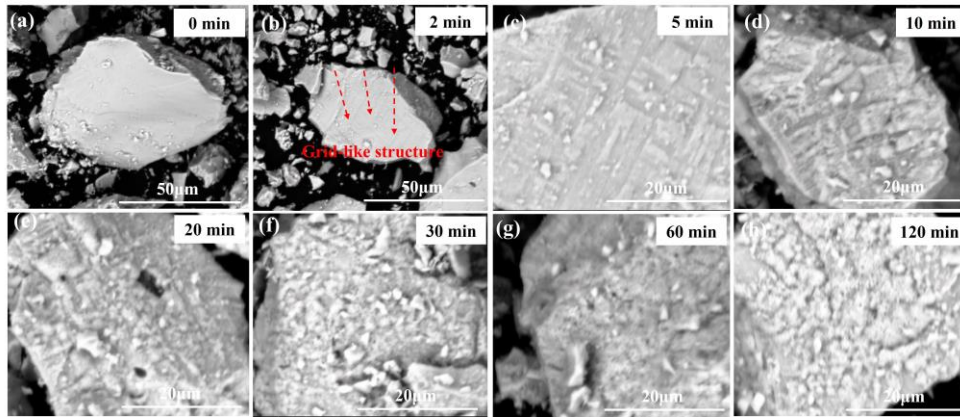


Figure 46: SEM images of the oxidized products of Sample B obtained under different duration times: (a) 0 min, (b) 2 min, (c) 5 min, (d) 10 min, (e) 20 min, (f) 30 min, (g) 60 min, (h) 120 min.

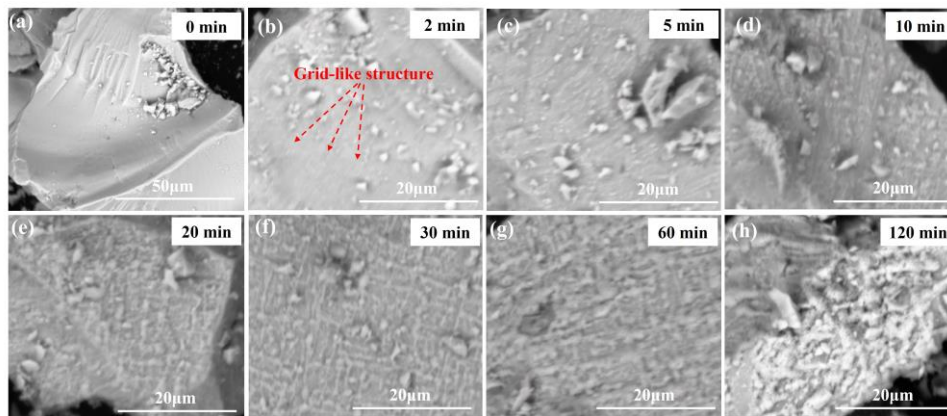


Figure 47: SEM images of the oxidized products of Sample C obtained under different duration times: (a) 0 min, (b) 2 min, (c) 5 min, (d) 10 min, (e) 20 min, (f) 30 min, (g) 60 min, (h) 120 min.

Figure 48 shows the samples under different oxidation time. The raw magnetite samples exhibit dense and compact structures. The oxidation progression in all three samples follows a consistent pattern: surface oxidation followed by internal oxidation. As shown in Figure 48 (b), (f) and (j), the oxidation firstly takes place at the surface of the magnetite particle. As the oxidation proceeds, as shown in Figure 48 (c), (g) and (k), the hematite shells are generated on the particle surface. In the final oxidation stage, as seen in Figure 48 (d), (h) and (l), the growth of hematite shell is not uniform. Instead, the needle-like hematite structures are generated from the surface hematite shell and extends inward within the particle. It's worth noting that there are no noticeable pores or cracks observed at the interfaces between the

hematite and magnetite phases. This suggests that the structural integrity remains largely intact, and the oxidized samples still exhibit compact structures.

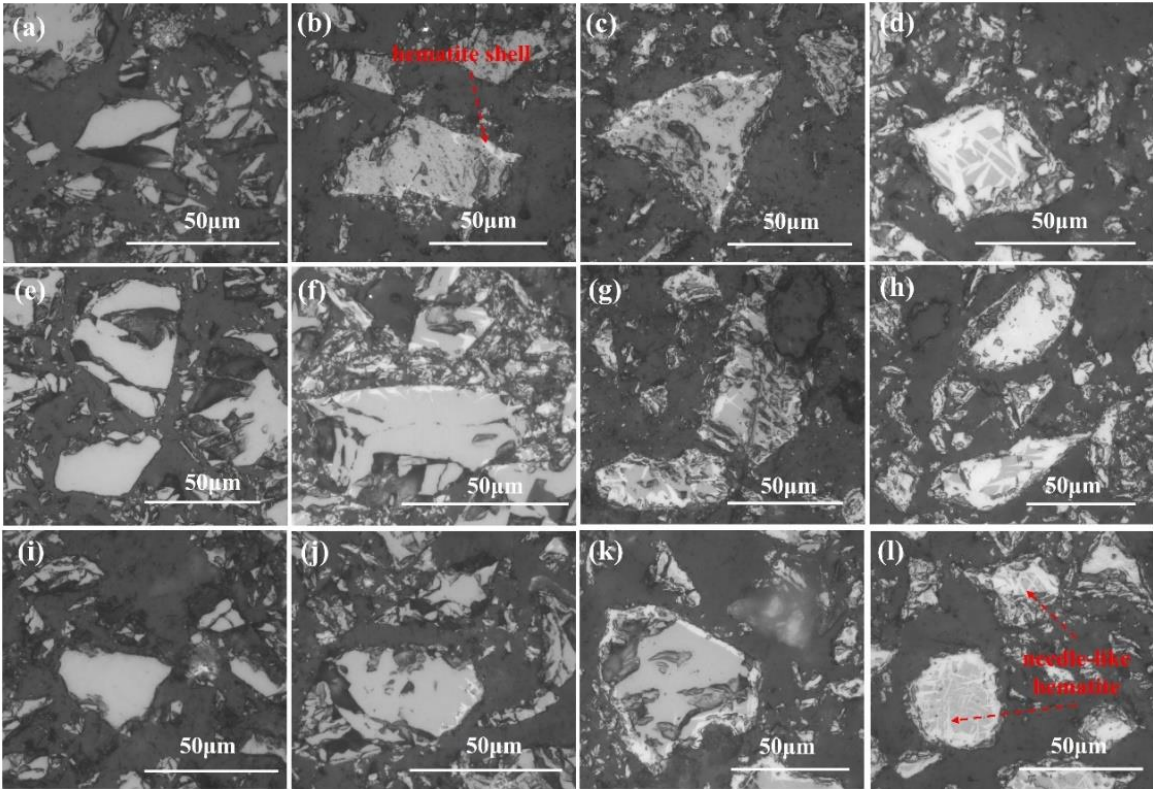


Figure 48: Polished section images of the oxidized samples obtained under different duration times: (a)-(d) Ore A under 0, 2, 5 and 60 min; (e)-(h) Ore B under 0, 5, 30 and 120 min; (i)-(l) Ore C under 0, 2, 30 and 120 min.

4.3.3 Pore structure parameters based on N₂ adsorption

Table 17 lists the results of the pore structure parameters of the raw and oxidized magnetite samples. The specific areas of the raw Ore A, Ore B and Ore C are 1.63, 0.94 and 0.83 m²/g, respectively. After 5 min of oxidation, the specific surface areas decrease significantly to 0.52, 0.38 and 0.29 m²/g. As the oxidation progresses, the specific surface areas of the samples consistently decrease. This trend is also reflected in the total pore volumes of all the samples. Meanwhile, the average pore sizes of the samples increase steadily with the oxidation. This phenomenon can be attributed to the closure of smaller pores, which is a consequence of the sintering effect. The pore size distributions of the samples after different oxidation time are shown in Figure 49. For the raw samples, the dominant pore size is between around 2 and 5 nm. However, in the oxidized samples, the pore size less than 3 nm is considerably decreased.

Table 17: The pore structure parameters of the samples within different oxidation time

Duration time (min)	Ore A			Ore B			Ore C		
	Average pore size (nm)	Total pore volume ($\times 10^{-4}$ cm ³ /g)	Specific surface area (m ² /g)	Average pore size (nm)	Total pore volume ($\times 10^{-4}$ cm ³ /g)	Specific surface area (m ² /g)	Average pore size (nm)	Total pore volume ($\times 10^{-4}$ cm ³ /g)	Specific surface area (m ² /g)
0	4.93	16.03	1.63	5.30	9.23	0.94	4.60	7.12	0.83
5	5.94	6.53	0.52	5.60	4.34	0.38	6.80	3.28	0.29
10	5.79	7.50	0.54	5.60	3.16	0.27	6.10	2.62	0.23
20	5.87	7.80	0.55	5.87	3.12	0.27	9.88	1.78	0.18
60	6.13	2.46	0.24	5.70	3.16	0.30	10.61	1.34	0.16

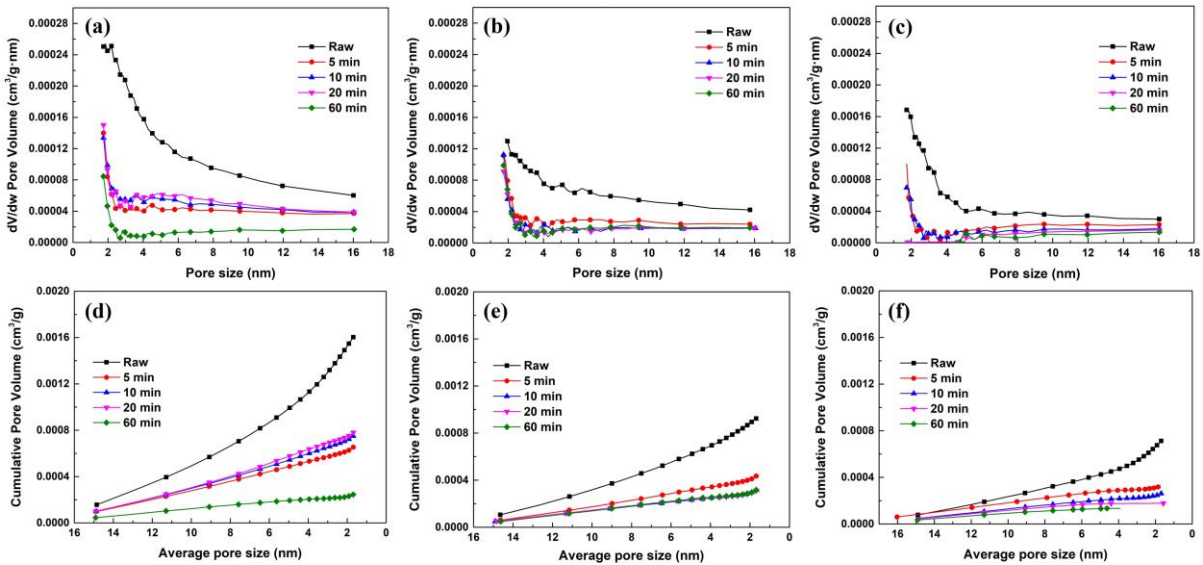


Figure 49: Pore size distribution of the samples: (a), (d) Ore A; (b), (e) Ore B; (c), (f) Ore C.

4.3.4 Oxidation mechanism

The magnetite crystal unit has 32 oxygen anions and 24 iron cations (16 Fe³⁺ and 8 Fe²⁺). The oxygen anions are cubic close-packed in the magnetite unit. With this arrangement, there are a total of 96 interstitial spaces between the oxygen anions. Among these interstitial spaces, 64 are tetrahedral interstices, while the remaining 32 are octahedral interstices. Notably, only 8 of the tetrahedral interstices are occupied by Fe³⁺ cations, while 16 out of 32 octahedral interstices are occupied by 8 Fe³⁺ cations and 8 Fe²⁺ cations [116]. This arrangement of vacant interstices enables the iron cations to move more freely within the crystal lattice compared to

the oxygen anions [117]. Moreover, the size of an O^{2-} anion (1.26 Å) is much larger than that of Fe^{2+} cation (0.75 Å) and Fe^{3+} cation (0.69 Å).

In the process of magnetite oxidation, when an oxygen atom diffuses into magnetite lattice, 2 electrons are trapped. The local charges in the crystal must be neutral, therefore, 2 positively charged holes $2 h^+$ are formed at the location of the previous electrons [118]. the schematic of the oxidation mechanism is shown in Figure 50. During the process, when the Fe^{2+} cation captures the charged hole h^+ , the valence increases, transforming the iron to trivalent state. However, as oxidation progresses, the occurrence of h^+ has a higher probability to collide with the Fe^{3+} cation. In such case, they equate to an impurity cation exhibiting a greater valence ($>3^+$) and compel the lattice to turn more compact [118]. Therefore, the diffusion of iron cations experiences a substantial decline, resulting in a significantly slower oxidation rate of magnetite at a later stage.

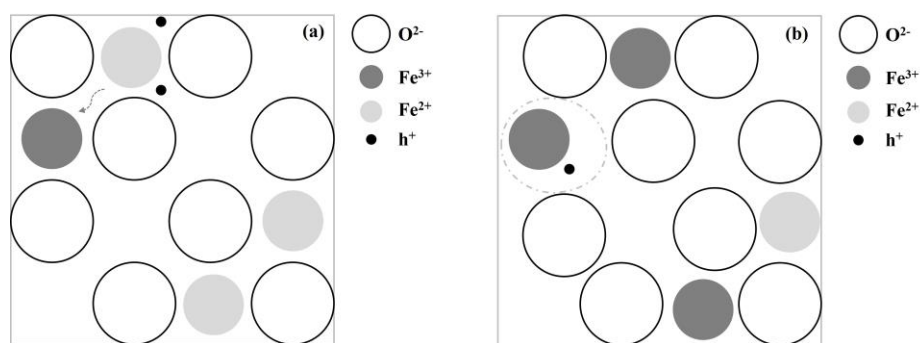


Figure 50: The schematic of the oxidation mechanism of magnetite: (a) the Fe^{2+} cation turns into the Fe^{3+} cation; (b) later oxidation period.

At the point of a single magnetite particle, the oxidation initials at the surface and then proceeds to its inner particle. Figure 51 shows the oxidation process of a single magnetite particle. Upon the absorption of electrons by oxygen atoms from the magnetite phase, the process of oxidation takes place. Initially, a hematite film emerges at the interface. Due to the limited concentration of iron cations, Fe cations exhibit a preference for diffusing towards the particle's surface. This concentration gradient serves as the driving force for the growth of hematite. On the other hand, the hematite phase has a preferred orientation along the (104) or (110) crystal face, resulting in the generation of the grid-like structure at the surface. As oxidation proceeds, hematite becomes the prevailing phase on the surface. Subsequently, the Fe^{3+} cations begin to diffuse into the particle center and form needle-like hematite structures. The needle-like hematite structures continue to grow and merge together until the oxidation ends.

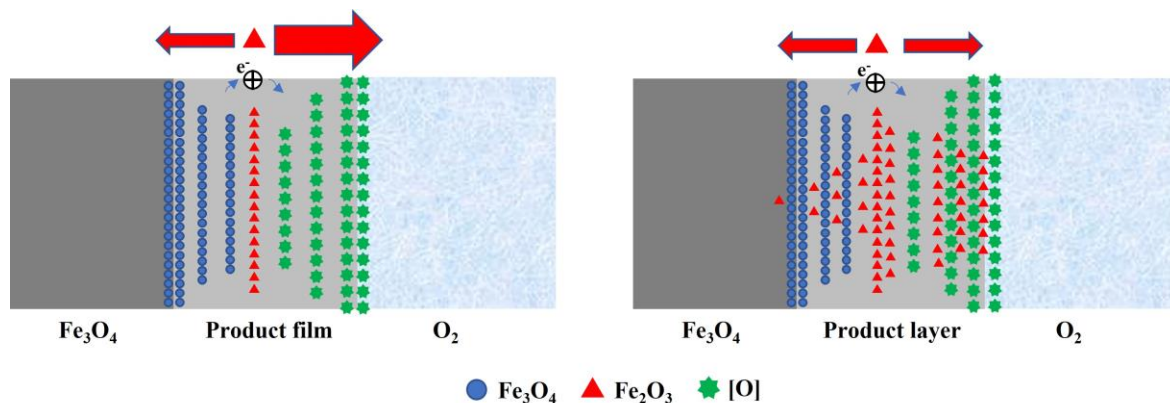


Figure 51: The oxidation process of a single magnetite particle.

4.4 Phase transition of magnetite via in situ high-temperature X-ray diffraction

The goal of the present chapter is to examine the thermal transformation of magnetite ore fines on a crystal scale via high-temperature X-ray diffraction (HT-XRD). The Ore B and Ore C, as listed in Table 6, are used for such investigation. More detailed results are given in publication 6 [119], which is under the Creative Commons CC BY license and permit unrestricted use, distribution, and reproduction in any medium, provided the original work is properly cited.

4.4.1 Oxidation degree

The patterns obtained from high-temperature X-ray diffraction (HT-XRD) are presented in Figure 52. All the peaks shift to a lower diffraction angle as the temperature rises, which is caused by thermal expansion [120]–[122]. The (104) peak of Fe_2O_3 is firstly observed at 400 °C, as presented in Figure 52(a) and (c). With elevated temperatures, the intensity of the (104) peak intensifies, indicating a greater proportion of Fe_2O_3 phase. The (311) peak of Fe_3O_4 disappears at 1000 °C, indicating a deep oxidation of Fe_3O_4 . The width of (104) peak becomes narrower with increasing temperature, which implies the enlargement of Fe_2O_3 crystallite.

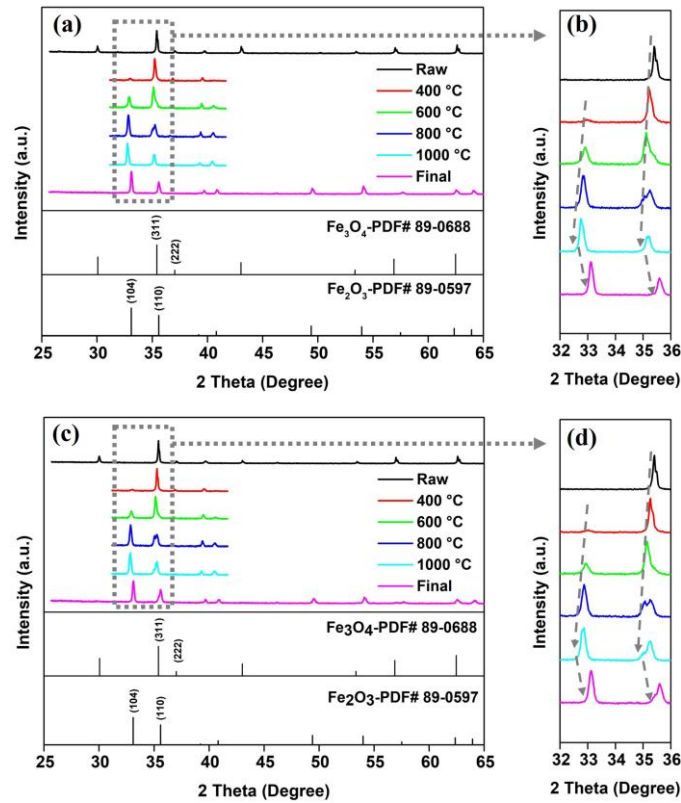


Figure 52: In situ HT-XRD patterns at different temperatures: (a), (b) Ore B; (c), (d) Ore C.

The oxidation degree (w) can be obtained by equation (38). The oxidation degrees of both ores at different temperatures are shown in Figure 53. Ore B is easier to be oxidized than Ore C, as indicated by its faster kinetics. The oxidation degree is lower than 10% at 400 °C in both cases. When the temperature reaches 600 °C, the oxidation degree becomes larger. However, above 800 °C, the oxidation rate slows down. The sigmoid-shaped oxidation degree curve suggests the rate-limiting step is the solid-diffusion control which can be described by parabolic law.

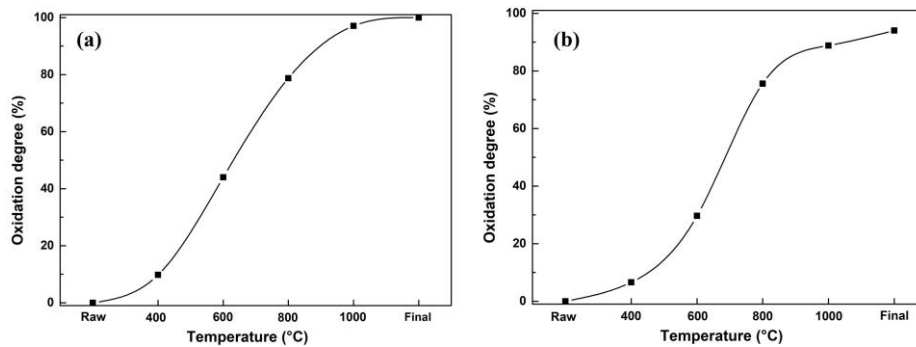


Figure 53: The oxidation degrees of Ore B and C at different temperatures: (a) Ore B; (b) Ore C.

4.4.2 Evolution of lattice constants

Table 18 summarizes the lattice constants of Fe₃O₄ in the ores at different temperatures. The obtained results align well with findings in existing literature. The alteration in lattice constant with increasing temperature is supposed to be caused by thermal expansion and lattice adjustments during oxidation [123]. As shown in Table 18, the lattice constant measured in this study is slightly larger than that reported in the literature at a specific temperature. Such a difference could be attributed to a much higher oxygen partial pressure in the current study, as the magnetite is oxidized under an air atmosphere. This condition could result in a larger lattice constant of magnetite due to partial oxidation [124] (i.e., a higher oxygen occupancy in the lattice). The temperature dependence of the lattice constant can be represented by polynomials up to the fifth order [125]. The correlation between lattice constant and temperature is successfully fitted with the second-order polynomials (Figure 54), within a temperature range of 25 °C to 800 °C. The temperature-dependent lattice constant of Fe₃O₄ can be described as: $a = 2.53 \times 10^{-8} \times T^2 + 8.64 \times 10^{-5} \times T + 8.4132$. At the higher temperature (e.g., 1000 °C), the (222) peak of Fe₃O₄ disappears, which reduces the accuracy in the assessment of the lattice constant. Thus, the lattice constant at 1000 °C is not considered.

Table 18: The lattice constant and volume of the Fe₃O₄ cell measured by high-temperature X-ray diffraction during the oxidation of Fe₃O₄ in air.

Temp.	Ore B		Ore C		Ref. [126]	Ref. [124]
	a=b=c (Å)	volume (Å ³)	a=b=c (Å)	volume (Å ³)	a=b=c (Å)	a=b=c (Å)
25 °C	8.4156±0.0021	596.0207	8.4165±0.0007	596.2214	8.3778	/
400 °C	8.4476±0.0035	602.8437	8.4473±0.0010	602.7819	8.4203	8.3888
600 °C	8.4796±0.0010	609.7186	8.4797±0.0005	609.7486	8.4547	8.4424
800 °C	8.4953±0.0042	613.1268	8.4974±0.0005	613.5637	8.4761	8.4698
*1000 °C	/	/	/	/	8.4969	8.4987

* The intensity of Fe₃O₄ peaks at 1000 °C is quite low and not suitable for the calculation of lattice constant.

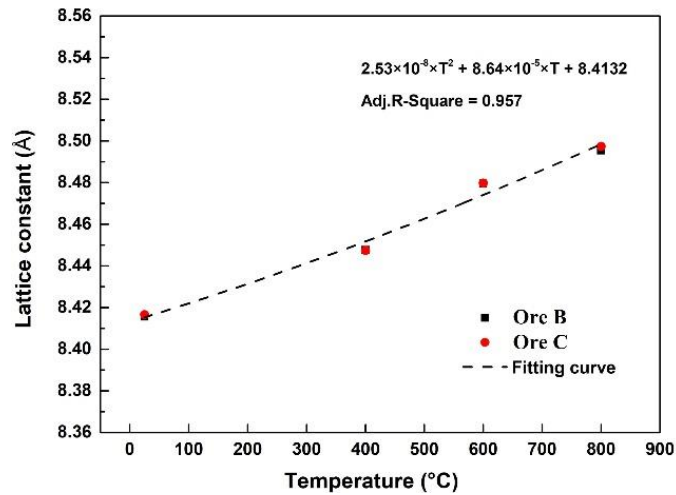


Figure 54: The lattice constant of Fe₃O₄ as a function of temperature measured by high-temperature X-ray diffraction during oxidation of Fe₃O₄ in air.

Table 19 lists the lattice constants of Fe₂O₃ at different temperatures. According to equations (27)-(29), a minimum two Fe₂O₃ peaks are needed for the calculation of lattice constants for a trigonal crystal structure. Hence, only one set of a and c can be obtained at each temperature in the current study. The lattice parameters of Fe₂O₃ obtained in this investigation are slightly larger than those in literature, where a was 5.01-5.04 Å and c was 13.68-13.73 Å in the temperature range of 300 °C to 800 °C [127]. The relative increase in a and c are shown in Figure 55, which agreed well with that in the literature. The correlation between lattice constants and temperature can be also fitted with second-order polynomials (Figure 56). The temperature-dependent lattice constant of Fe₂O₃ can be described as: $a = -2.81 \times 10^{-8} \times T^2 + 8.76 \times 10^{-5} \times T + 5.0368$; $c = 3.01 \times 10^{-8} \times T^2 + 1.09 \times 10^{-4} \times T + 13.7621$.

Table 19: The lattice constant and volume of the Fe₂O₃ cell

Temp.	Ore B			Ore C		
	a=b (Å)	c (Å)	volume (Å ³)	a=b (Å)	c (Å)	volume (Å ³)
25 °C	5.0391	13.7648	302.6958	5.0391	13.7648	302.6958
*400 °C	/	/	/	/	/	/
600 °C	5.0798	13.8282	309.0220	5.0769	13.8496	309.1470
800 °C	5.0884	13.8628	310.8451	5.0921	13.8717	311.4972
1000 °C	5.0972	13.9066	312.9067	5.0943	13.896	312.3125

* The intensity of Fe₂O₃ peaks at 400 °C is quite low and not suitable for the calculation of lattice constant.

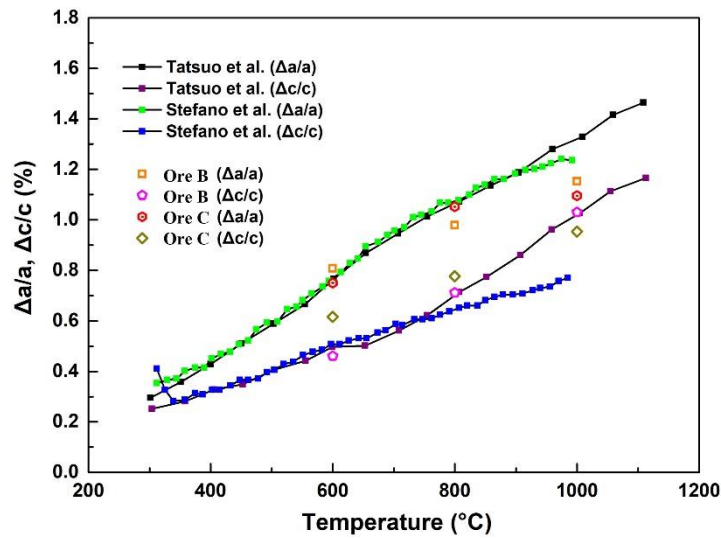


Figure 55: The relative increase in lattice parameters a and c of Fe_2O_3 at different temperatures [121],[128].

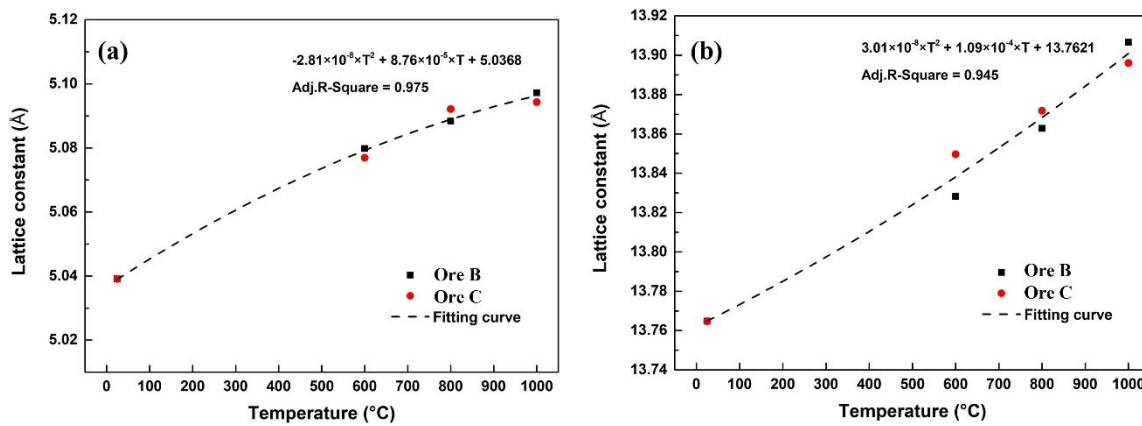


Figure 56: The lattice constants of Fe_2O_3 as a function of temperature: (a) lattice constant a; (b) lattice constant c.

4.4.3 Evolution of crystallite size of Fe_2O_3

In Figure 57, the Fe_2O_3 crystallite sizes long the c-axis and the a/b axis of Ore B and Ore C is presented. As temperature increases, a greater portion of Fe_3O_4 is oxidized into Fe_2O_3 , consequently inducing a growth of the Fe_2O_3 crystallite in both ores, as shown in Figure 57. Furthermore, the growth rate of Fe_2O_3 is more pronounced along a/b axis ($D_{a/b}$ in Figure 57) than c-axis (D_c in Figure 57) in the crystal unit. Moreover, the crystallite size along the a/b axis exhibits a larger size than that along the c-axis. Such findings suggest a growth habit of Fe_2O_3 during oxidation. It is worth noting that $D_{a/b}$ and D_c are calculated based on the (110) and (104) peaks, respectively. In our previous study [91], it was found that the surface energy of the (110)

crystal surface was larger than that of the (104) crystal surface. The growth rates of the crystal faces are proportional to their surface energies, indicating a larger crystallite size along the a/b axis, which concurs well with the current study. The growth habit of Fe₂O₃ was also observed in TEM micrographs of Fe₂O₃ during the decomposition of goethite, where the Fe₂O₃ phase showed acicular morphology [129]. In general, it is believed that the Fe₂O₃ phase presents acicular microcrystals due to its crystallographic-dependent properties. Besides, the crystallite sizes of Ore B are slightly larger than that of Ore C at specific temperatures. The current experimental data cannot explain this phenomenon. One possible factor contributing to this difference could be the higher contents of Al₂O₃ and MgO in Ore C, which inhibit the diffusion of Fe cations [117],[118]. On the other hand, the crystallite sizes, calculated based on the peak (311), of the parent Fe₃O₄ phase of the Ore B and Ore C are 1027.7 Å and 812.6 Å, respectively. The larger crystallite size of Fe₂O₃ might be inherited from the larger parent Fe₃O₄ phase.

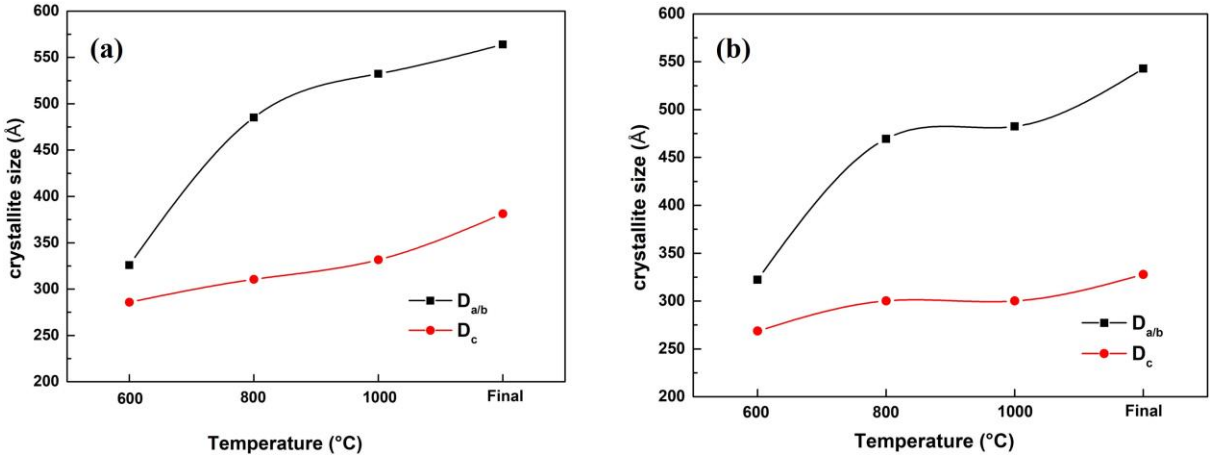


Figure 57: The crystallite sizes of Ore B and Ore C along the a/b axis and the c axis of a unit cell at different temperatures: (a) Ore B; (b) Ore C.

5 Main conclusion

For a stable process of the fluidized bed reactor, some pre-treatments of the magnetite ore fines are tested. The research work in this thesis is classified into four work packages. The first two work packages discuss the fluidization and reduction behaviors of the magnetite ore fines with pre-treatments, i.e., pre-oxidation and MgO addition. The last two work packages investigate the oxidation of magnetite phase during the pre-oxidation treatment of magnetite ore fines. All the research works presented here are available online in peer reviewed research journals. The main conclusions are given as follows [56],[61],[62],[65],[91],[119]:

1. The untreated magnetite-based iron ore fails to achieve complete fluidization during the reduction experiments. The fresh surface metallic iron on the particle forms an iron shell and covers the unreacted dense wüstite core. At a reducing temperature of 600 °C, de-fluidization could be avoided by a deep pre-oxidation treatment. After oxidation, the phase structure after reduction becomes porous. However, at a reducing temperature of 700 °C, an addition of at least 0.5 wt.-% MgO is required to maintain complete fluidization. MgO could promote the initial reaction because of an increase in active sites owing to the Mg²⁺ cations into Fe₂O₃ lattice. At later reduction stages, the formation of magnesiowüstite slows down the reduction rate. For deeply oxidized samples, the amount of MgO addition has little influence on the occurring rate-limiting mechanisms. The chemical reaction dominates the initial reaction. The diffusion becomes the reaction limiting step in the final stage.
2. At a reducing temperature of 700 °C, the samples with higher temperature pre-oxidation treatment show better fluidization behaviors due to the flat surface morphology. From the point of fluidization behavior, a high-temperature oxidation treatment is suggested. Regarding the reduction efficiency, a lower pre-oxidation temperature is more beneficial for the reduction rate, especially in the later reduction stage. The diffusion of the iron ions is improved. The pre-oxidation content of the magnetite iron ore fines shows no noticeable difference in fluidization and reduction behaviors. The primary and secondary influencing factors are pre-oxidation temperature, oxidation content, MgO addition amount, and gas velocity. The optimal condition, in current experimental series, is that the magnetite iron ore is deeply oxidized at 800 °C, mixed with 1.5 wt.-% of MgO, and reduced in the fluidized bed at a gas velocity of 0.45 m/s.

-
3. The oxidation reaction of magnetite iron ore fines can be divided into at least three stages. The first two oxidation rate peaks are observed at around 330 °C and 550 °C, respectively, indicating the formation of $\gamma\text{-Fe}_2\text{O}_3$ and $\alpha\text{-Fe}_2\text{O}_3$. The highest oxidation rate of these three samples is in the temperature range between 548 °C and 573 °C. The proposed oxidation capacity index (OCI) could successfully describe the oxidation behaviors of magnetite ore fines. The magnetite-based iron ore with a higher OCI value represents that it is easier to be oxidized. During the oxidation, the surface of the magnetite samples becomes rough and presents nano-sized grid-like structure due to the outgrowth of the hematite. With the oxidation time, the grid-like structures grow bigger and connect with each other. At the same time, the hematite phase also grows inward the particle, forming the needle-like structures. The specific areas of the oxidized samples are much smaller than the raw sample. The newly formed hematite phase shows a certain growth habit and preferentially orients themselves along the (104) or (110) crystal surfaces.
 4. The crystal information, such as lattice constant and crystallite size, can be successfully characterized by the HT-XRD. The intensity of the (104) peak of Fe_2O_3 increases with the increasing temperature, indicating an increase in the fraction of Fe_2O_3 . The width of the (104) peak become narrower with the increasing temperature, suggesting a growing crystallite size of Fe_2O_3 during oxidation. The lattice constants of Fe_3O_4 and Fe_2O_3 both increase with the temperature and follow second-order polynomials. The correlation of lattice constant and temperature can be expressed as follows: Fe_3O_4 : $a = 2.53 \times 10^{-8} \times T^2 + 8.64 \times 10^{-5} \times T + 8.4132$; Fe_2O_3 : $a = -2.81 \times 10^{-8} \times T^2 + 8.76 \times 10^{-5} \times T + 5.0368$; $c = 3.01 \times 10^{-8} \times T^2 + 1.09 \times 10^{-4} \times T + 13.7621$. The growth rates of Fe_2O_3 crystallite along the a/b axis is faster than that in the c-axis, thus showing acicular microcrystals.

6 List of references

- [1] European Commission, 2050 long-term strategy - Climate Action - European Commission, https://ec.europa.eu/clima/policies/strategies/2050_en, Access on: 26.01.2021.
- [2] Worldsteel, Steel Statistical Yearbook, <https://www.worldsteel.org/steel-by-topic/statistics/steel-statistical-yearbook.html>, Access on: 14.11.2021.
- [3] Berger, F.R., The future of steelmaking—How the European steel industry can achieve carbon neutrality, Roland Berger GMBH, 2020.
- [4] European Commission, Ultra-Low CO₂ steelmaking, <https://cordis.europa.eu/project/id/515960>, Access on: 14.11.2021.
- [5] Abdul Quader, M., Ahmed, S., Dawal, S.Z. and Nukman, Y., Present needs, recent progress and future trends of energy-efficient Ultra-Low Carbon Dioxide (CO₂) Steelmaking (ULCOS) program, *Renewable and Sustainable Energy Reviews* 55 (2016), pp. 537–549.
- [6] Bhaskar, A., Assadi, M. and Nikpey Somehsaraei, H., Decarbonization of the iron and steel industry with direct reduction of iron ore with green hydrogen, *Energies* 13 (2020), 3, pp. 758.
- [7] Chen, Y. and Zuo, H., Review of hydrogen-rich ironmaking technology in blast furnace, *Ironmaking & Steelmaking* 48 (2021), 6, pp. 749–768.
- [8] Liu, W., Zuo, H., Wang, J., Xue, Q., Ren, B. and Yang, F., The production and application of hydrogen in steel industry, *International Journal of Hydrogen Energy* 46 (2021), 17, pp. 10548–10569.

-
- [9] Patisson, F. and Mirgaux, O., Hydrogen Ironmaking: How It Works, *Metals* 10 (2020), 7, pp. 922.
- [10] Primetals, Enhanced Energy Efficient Steel Production –E³-SteP, Austria, 2019.
- [11] Schenk, J.L., Recent status of fluidized bed technologies for producing iron input materials for steelmaking, *Particuology* 9 (2011), 1, pp. 14–23.
- [12] Ma, Y., Souza Filho, I.R., Bai, Y., Schenk, J., Patisson, F., Beck, A., van Bokhoven, J.A., Willinger, M.G., Li, K., Xie, D., Ponge, D., Zaefferer, S., Gault, B., Mianroodi, J.R. and Raabe, D., Hierarchical nature of hydrogen-based direct reduction of iron oxides, *Scripta Materialia* 213 (2022), pp. 114571.
- [13] Daniel, S., Johann, W., Bernhard, H., Norbert, R., Thomas, W., Wolfgang, S. and Alexander, F., HYFOR - Hydrogen-based Fine-Ore Reduction, Mitsubishi Heavy Industries Technical Review Vol.59 No.2(2022), Mitsubishi Heavy Industries Technical Review 59 (2022), 2, pp. 1–5.
- [14] Guo, L., Gao, H., Yu, J., Zhang, Z. and Guo, Z., Influence of hydrogen concentration on Fe₂O₃ particle reduction in fluidized beds under constant drag force, *Int J Miner Metall Mater* 22 (2015), 1, pp. 12–20.
- [15] Processing of magnetite iron ores—comparing grinding options, Iron ore, Western Australia, Perth, 2009.
- [16] Department of the Premier and Cabinet, South Australia's Magnetite Strategy: Making our state's magnetite the world's choice for steelmaking, <https://sarigbasis.pir.sa.gov.au/WebtopEw/ws/samref/sarig1/image/DDD/BROCH028.pdf>, Accessed on: 06.08.2022.
- [17] Lee Blaney, Magnetite (Fe₃O₄): Properties, synthesis, and applications, 2007.
- [18] Zhu, D., Pan, J., Lu, L. and Holmes, R.J., Iron ore pelletization, *Iron Ore* (2015), pp. 435–473.
- [19] Han, H. and Lu, L., Recent advances in sintering with high proportions of magnetite concentrates, *Mineral Processing and Extractive Metallurgy Review* 39 (2018), 4, pp. 217–230.
- [20] Purohit, S., Brooks, G., Rhamdhani, M.A., Pownceby, M.I. and Webster, N.A.S., Alternative route for magnetite processing for lower carbon footprint iron-making through lime-magnetite pellets containing CaFe₃O₅, *Ironmaking & Steelmaking* 47 (2020), 6, pp. 674–685.

-
- [21] Purohit, S., Brooks, G., Rhamdhani, M.A., Pownceby, M.I. and Webster, N.A.S., Analyses of CWF (CaFe_3O_5) phase formation in lime-magnetite pellets, *Ironmaking & Steelmaking* 47 (2020), 8, pp. 852–864.
- [22] Alternative processing routes for magnetite ores, AISTech 2018 Proceeding, USA, Philadelphia (2018), 9.
- [23] Zhu, D., Mendes, V., Chun, T., Pan, J., Li, Q., Li, J. and Qiu, G., Direct reduction behaviors of composite binder magnetite pellets in coal-based grate-rotary kiln process, *ISIJ Int.* 51 (2011), 2, pp. 214–219.
- [24] Jiang, X., Wang, L. and Shen, F.M., Shaft furnace direct reduction technology - Midrex and Energiron, *Advanced Materials Research* 805-806 (2013), pp. 654–659.
- [25] Huitu, K., Helle, M., Helle, H., Kekkonen, M. and Saxén, H., Optimization of Midrex direct reduced iron use in ore-based steelmaking, *steel research int.* 86 (2015), 5, pp. 456–465.
- [26] Bellona Foundation, Hydrogen in steel production: what is happening in Europe – part two, <https://bellona.org/news/industrial-pollution/2021-05-hydrogen-in-steel-production-what-is-happening-in-europe-part-two>, Accessed on: 14.11.2021.
- [27] Vogl, V., Åhman, M. and Nilsson, L.J., Assessment of hydrogen direct reduction for fossil-free steelmaking, *Journal of Cleaner Production* 203 (2018), pp. 736–745.
- [28] Daniel Spreitzer, Development of characterization methods for the evaluation of kinetic behavior and the fluidization of iron ore fines during hydrogen-induced fluidized bed reduction, 2020.
- [29] Spreitzer, D. and Schenk, J., Reduction of iron oxides with hydrogen—A Review, *steel research international* 90 (2019), 10, pp. 1900108.
- [30] Johannes Schenk, Direct steelmaking with hydrogen plasma smelting reduction: Process concept and metallurgical basics, Lecture 2018.
- [31] World Steel Association, Total production of crude steel, <https://worldsteel.org/steel-topics/statistics/world-steel-in-figures-2022/>, Accessed on: 19.11.2022.
- [32] Li, Z. and Hanaoka, T., Plant-level mitigation strategies could enable carbon neutrality by 2060 and reduce non- CO_2 emissions in China's iron and steel sector, *One Earth* 5 (2022), 8, pp. 932–943.
- [33] International Energy Agency (IEA), *Iron and Steel Technology Roadmap*, OECD, 2020.

-
- [34] Material Economics, Industrial transformation 2050 - pathways to net-zero emissions from EU heavy industry, <https://media.sitra.fi/2019/05/30150529/industrial-transformation-2050.pdf>, Accessed on: 31.01.2021.
- [35] Midrex Technologies, Inc., Midrex STATS Book 2021.
- [36] Engineering, C., Relaunching a process that uses 100% H₂ for the direct reduction of iron ore, Chemical Engineering, 1 June 2022, <https://www.chemengonline.com/direct-reduction-of-iron-ore/>, Accessed on: 03.04.2023.
- [37] Metso Outotec, Circored fine ore direct reduction – a proven process to decarbonize steelmaking - Metso Outotec, <https://www.mogroup.com/insights/blog/mining-and-metals/circored-fine-ore-direct-reduction-a-proven-process-to-decarbonize-steelmaking/>, Accessed on: 03.04.2023.
- [38] Metso Outotec, Circored™ hydrogen-based reduction - Metso Outotec, <https://www.mogroup.com/portfolio/circored-hydrogen-based-reduction/>, Accessed on: 03.04.2023.
- [39] Allon, B., Peter, M., Tom, H., The Port Hedland FINMET (R) Project - Fluid bed production of high quality virgin iron for the 21st Century, AusIMM International Conference on Alternative Routes of Iron and Steelmaking, Perth (1997).
- [40] Rudra, T., POSCO's HyREX: cutting-edge green steel technology to watch out for, Green Steel World 2022, 7 October 2022, <https://greensteelworld.com/poscos-hyrex-cutting-edge-green-steel-technology-to-watch-out-for>, Abgerufen am: 03.04.2023.
- [41] Great conversion to low-carbon eco-friendly steelmaking process: HyREX, <https://newsroom.posco.com/en/special-project-for-great-conversion-to-low-carbon-eco-friendly-steelmaking-process-%e2%91%a0-hyrex/>, Accessed on: 03.01.2023.
- [42] Wong, P.L.M., Kim, M.J., Kim, H.S. and Choi, C.H., Sticking behaviour in direct reduction of iron ore, *Ironmaking & Steelmaking* 26 (1999), 1, pp. 53–57.
- [43] Gong, X., Zhang, B., Wang, Z. and Guo, Z., Insight of Iron whisker sticking mechanism from iron atom diffusion and calculation of solid bridge radius, *Metall and Materi Trans B* 45 (2014), 6, pp. 2050–2056.
- [44] Zhong, Y., Wang, Z., Guo, Z. and Tang, Q., Agglomeration/defluidization in a fluidized bed reduction of Fe₂O₃ particles by CO: Influences of iron precipitation on particle cohesiveness, *Powder Technology* 256 (2014), pp. 13–19.
- [45] Guo, L., Zhong, S., Bao, Q., Gao, J. and Guo, Z., Nucleation and growth of iron whiskers during gaseous reduction of hematite iron ore fines, *Metals* 9 (2019), 7, pp. 750.

-
- [46] Nicolle, R. and Rist, A., The mechanism of whisker growth in the reduction of wüstite, *Metall and Materi Trans B* 10 (1979), 3, pp. 429–438.
- [47] Iguchi, Y., Uyeda, Y., Goto, K. and Hayashi, S., In situ observation of nucleation and growth of iron whiskers from supersaturated wüstite, *Oxid Met* 42 (1994), 1, pp. 103–108.
- [48] Du, Z., Zhu, Q., Fan, C., Pan, F., Li, H. and Xie, Z., Influence of reduction condition on the morphology of newly formed metallic iron during the fluidized bed reduction of fine iron ores and its corresponding agglomeration behavior, *steel research int.* 87 (2016), 6, pp. 789–797.
- [49] Lu, F., Wen, L., Li, J., Wei, J., Xu, J. and Zhang, S., Numerical simulation of iron whisker growth with changing oxygen content in iron oxide using phase-field method, *Computational Materials Science* 125 (2016), pp. 263–270.
- [50] Lu, F., Wen, L., Zhong, H., Xu, J., Zhang, S., Duan, H. and Yang, Z., Microscopic behavior and metallic iron morphology from reduction of iron oxide by CO/H₂ in a fluidized bed, *J Appl Cryst* 51 (2018), 6, pp. 1641–1651.
- [51] Mikami, T., Kamiya, H. and Horio, M., The mechanism of defluidization of iron particles in a fluidized bed, *Powder Technology* 89 (1996), 3, pp. 231–238.
- [52] Kuwagi, K., Mikami, T. and Horio, M., Numerical simulation of metallic solid bridging particles in a fluidized bed at high temperature, *Powder Technology* 109 (2000), 1-3, pp. 27–40.
- [53] Shao, J., Guo, Z. and Tang, H., Effect of coating MgO on sticking behavior during reduction of iron ore concentrate fines in fluidized bed, *steel research int.* 84 (2013), 2, pp. 111–118.
- [54] Lu, F., Zhong, H., Liu, B., Xu, J., Zhang, S. and Wen, L., Particle agglomeration behavior in fluidized bed during direct reduction of iron oxide by CO/H₂ mixtures, *J. Iron Steel Res. Int.* 30 (2023), 4, pp. 626–634.
- [55] Guo, L., Bao, Q., Gao, J., Zhu, Q. and Guo, Z., A Review on prevention of sticking during fluidized bed reduction of fine iron ore, *ISIJ Int.* 60 (2020), 1, pp. 1–17.
- [56] Zheng, H., Spreitzer, D., Wolfinger, T., Schenk, J. and Xu, R., Effect of prior oxidation on the reduction behavior of magnetite-based iron ore during hydrogen-induced fluidized bed reduction, *Metall and Materi Trans B* 52 (2021), 4, pp. 1955–1971.
- [57] El-Geassy, A.A., Influence of doping with CaO and/or MgO on stepwise reduction of pure hematite compacts, *Ironmaking & Steelmaking* 26 (1999), 1, pp. 41–52.

-
- [58] Du, Z., Zhu, Q., Yang, Y., Fan, C., Pan, F., Sun, H. and Xie, Z., The Role of MgO powder in preventing defluidization during fluidized bed reduction of fine iron ores with different iron valences, *steel research int.* 87 (2016), 12, pp. 1742–1749.
- [59] Guo, L., Tang, J., Tang, H. and Guo, Z., Influence of different MgO coating methods on preventing sticking during reduction of Fe₂O₃ particles in a fluidized bed, *Materials Today: Proceedings 2* (2015), S332-S341.
- [60] Guo, L., Zhong, Y., Gao, J., Yang, Z. and Guo, Z., Influence of coating MgO with coprecipitation method on sticking during fluidized bed reduction of Fe₂O₃ particles, *Powder Technology 284* (2015), pp. 210–217.
- [61] Zheng, H., Daghighaleh, O., Wolfinger, T., Taferner, B., Schenk, J. and Xu, R., Fluidization behavior and reduction kinetics of pre-oxidized magnetite-based iron ore in a hydrogen-induced fluidized bed, *Int J Miner Metall Mater* 29 (2022), 10, pp. 1873–1881.
- [62] Zheng, H., Schenk, J., Daghighaleh, O. and Taferner, B., Parameter optimization for hydrogen-induced fluidized bed reduction of magnetite iron ore fines, *Metals* 13 (2023), 2, pp. 339.
- [63] Zhong, Y., Wang, Z., Guo, Z. and Tang, Q., Prevention of agglomeration/defluidization in fluidized bed reduction of Fe₂O₃ by CO: The role of magnesium and calcium oxide, *Powder Technology 241* (2013), pp. 142–148.
- [64] Du, Z., Zhu, Q., Fan, C., Pan, F. and Xie, Z., Enhanced effect and mechanism of Fe₂O₃ on CaO for defluidization inhibition during fluidized bed reduction of iron ore fines, *Powder Technology 313* (2017), pp. 82–87.
- [65] Zheng, H., Schenk, J., Spreitzer, D., Wolfinger, T. and Daghighaleh, O., Review on the oxidation behaviors and kinetics of magnetite in particle scale, *steel research international* 92 (2021), 8, pp. 2000687.
- [66] Colombo, U., G. Fagherazzi, F. Gazzarrini, G. Lanzavecchia, G. Sironi, Mechanisms in the first stage of oxidation of magnetites, *Nature* (1964), 202, pp. 175.
- [67] Colombo, U., F. Gazzarrini, G. Lanzavecchia, G. Sironi, Magnetite oxidation a proposed mechanism, *Science* 147 (1965), pp. 1033.
- [68] Chen T., Xu, H., Xie, Q., Chen, J., Ji, J. and LU, H., Characteristics and genesis of maghemite in Chinese loess and paleosols: Mechanism for magnetic susceptibility enhancement in paleosols, *Earth and Planetary Science Letters* 240 (2005), 3-4, pp. 790–802.

-
- [69] Vyazovkin, S., Burnham, A.K., Criado, J.M., Pérez-Maqueda, L.A., Popescu, C. and Sbirrazzuoli, N., ICTAC Kinetics Committee recommendations for performing kinetic computations on thermal analysis data, *Thermochimica Acta* 520 (2011), 1-2, pp. 1–19.
- [70] Brown, M.E., Maciejewski, M., Vyazovkin, S., Nomen, R., Sempere, J., Burnham, A., Opfermann, J., Strey, R., Anderson, H.L., Kemmler, A., Keuleers, R., Janssens, J., Desseyn, H.O., Li, C.-R., Tang, T.B., Roduit, B., Malek, J. and Mitsuhashi, T., Computational aspects of kinetic analysis, *Thermochimica Acta* 355 (2000), 1-2, pp. 125–143.
- [71] Monsen, B., Iron ore concentrate - oxidation and reduction, 1992, https://www.researchgate.net/publication/311457287_Iron_Ore_Concentrate_-_Oxidation_and_Reduction, Accessed on: 19.11.2022.
- [72] Johnson W.A. and R.F. Mehl, Reaction kinetics in processes of nucleation and growth, *Trans. Am. Inst. Min. Metall. Eng.* 135 (1939), pp. 416–442.
- [73] Avrami, M., Kinetics of phase change. I General theory, *The Journal of Chemical Physics* 7 (1939), 12, pp. 1103–1112.
- [74] Avrami, M., Kinetics of phase change. II Transformation - time relations for random distribution of nuclei, *The Journal of Chemical Physics* 8 (1940), 2, pp. 212–224.
- [75] Avrami, M., Granulation, Phase change, and microstructure kinetics of phase change. III, *The Journal of Chemical Physics* 9 (1941), 2, pp. 177–184.
- [76] H.J. Cho, P.P., The effects of concentrate source and particle size on oxidation behavior of magnetite, *AIStech Conference Proceedings, Indianapolis, USA* (2011), 8.
- [77] Pistorius, P.C. and Tang, M., Prediction of non-isothermal oxidation of magnetite pellets, 144th Annual Meeting and Exhibition, March 15-19, 2015, Florida, USA.
- [78] Hyeon Jeong Cho, Christiaan Pistorius, The rate determining step of the oxidation of natural magnetite concentrates, *AIStech 2012, Atlanta, USA* (2012), 9.
- [79] Cho, H.J., Tang, M. and Pistorius, P.C., Magnetite particle size distribution and pellet oxidation, *Metall and Materi Trans B* 45 (2014), 4, pp. 1213–1220.
- [80] Himmel, L., Mehl, R.F. and Birchenall, C.E., Self-diffusion of iron in iron oxides and the Wagner theory of oxidation, *JOM* 5 (1953), 6, pp. 827–843.
- [81] Sandeep Kumar, T.K., Viswanathan, N.N., Ahmed, H., Dahlin, A., Andersson, C. and Bjorkman, B., Investigation of magnetite oxidation kinetics at the particle scale, *Metall and Materi Trans B* 50 (2019), 1, pp. 150–161.

-
- [82] Hancock, J.D. and Sharp, J.H., Method of comparing solid-state kinetic data and its application to the decomposition of kaolinite, brucite, and BaCO₃, *Journal of the American Ceramic Society* 55 (1972), 2, pp. 74–77.
- [83] Pérez-Maqueda, L.A., Criado, J.M. and Málek, J., Combined kinetic analysis for crystallization kinetics of non-crystalline solids, *Journal of Non-Crystalline Solids* 320 (2003), 1-3, pp. 84–91.
- [84] Monazam, E.R., Breault, R.W. and Siriwardane, R., Kinetics of magnetite (Fe₃O₄) oxidation to hematite (Fe₂O₃) in air for chemical looping combustion, *Ind. Eng. Chem. Res.* 53 (2014), 34, pp. 13320–13328.
- [85] Sandeep Kumar, T.K., Viswanathan, N.N., Ahmed, H., Dahlin, A., Andersson, C. and Bjorkman, B., Developing the Oxidation Kinetic Model for Magnetite Pellet, *Metall and Materi Trans B* 50 (2019), 1, pp. 162–172.
- [86] A.M. Ginstling and B. Brounshteinl., Concerning the diffusion kinetics of reactions in spherical particles, *J. Appl. Chem. USSR* 23 (1950), 1327-1338.
- [87] Khawam, A. and Flanagan, D.R., Solid-state kinetic models: basics and mathematical fundamentals, *The journal of physical chemistry. B* 110 (2006), 35, pp. 17315–17328.
- [88] ThurnHoefer, A., Shachinger, M., Winter, F., Mali, H. and Schenk, J., Iron Ore Reduction in a Laboratory-scale Fluidized Bed Reactor-Effect of Pre-reduction on Final Reduction Degree, *ISIJ Int.* 45 (2005), 2, pp. 151–158.
- [89] Pichler, A., Mali, H., Plaul, F., Schenk, J., Skorianz, M. and Weiss, B., Reduction Behavior and Structural Evolution of Iron Ores in Fluidized Bed Technologies-Part 2: Characterization and Evaluation of Worldwide Traded Fine Iron Ore Brands, *steel research int.* 87 (2016), 5, pp. 642–652.
- [90] JO Edström, The mechanism of reduction of iron oxides, *J. Iron and steel institute* November (1953), pp. 289.
- [91] Zheng, H., Schenk, J., Xu, R., Daghighaleh, O., Spreitzer, D., Wolfinger, T., Yang, D. and Kapelyushin, Y., Surface Morphology and Structural Evolution of Magnetite-Based Iron Ore Fines During the Oxidation, *Metall and Materi Trans B* 53 (2022), 3, pp. 1644–1660.
- [92] Xiumin, J., Chuguang, Z., Jianrong, Q., Jubin, L. and Dechang, L., Combustion Characteristics of Super Fine Pulverized Coal Particles, *Energy Fuels* 15 (2001), 5, pp. 1100–1102.

-
- [93] Wang, Z.-Y., Zhang, J.-L., Xing, X.-D., Liu, Z.-J., Zhang, Y.-P., Liu, X.-L. and Liu, Y.-R., Phase Transitions and Atomic-Scale Migration During the Preoxidation of a Titania/Ferrous Oxide Solution, *JOM* 68 (2016), 2, pp. 656–667.
- [94] Sun, H., Adetoro, A.A., Pan, F., Wang, Z. and Zhu, Q., Effects of High-Temperature Preoxidation on the Titanomagnetite Ore Structure and Reduction Behaviors in Fluidized Bed, *Metall and Materi Trans B* 48 (2017), 3, pp. 1898–1907.
- [95] Fu, X., Wang, Y. and Wei, F., Phase Transitions and Reaction Mechanism of Ilmenite Oxidation, *Metall and Mat Trans A* 41 (2010), 5, pp. 1338–1348.
- [96] Tilley, R.J.D., *Crystals and crystal structures*, Reprinted with corrections, Wiley, Chichester, 2006.
- [97] Eneroth, E. and Bender Koch, C., Crystallite size of haematite from thermal oxidation of pyrite and marcasite—effects of grain size and iron disulphide polymorph, *Minerals Engineering* 16 (2003), 11, pp. 1257–1267.
- [98] Chung, F.H., Quantitative interpretation of X-ray diffraction patterns of mixtures. I. Matrix-flushing method for quantitative multicomponent analysis, *J Appl Crystallogr* 7 (1974), 6, pp. 519–525.
- [99] Chung, F.H., Quantitative interpretation of X-ray diffraction patterns of mixtures. II. Adiabatic principle of X-ray diffraction analysis of mixtures, *J Appl Cryst* 7 (1974), 6, pp. 526–531.
- [100] Kapelyushin, Y., Sasaki, Y., Zhang, J., Jeong, S. and Ostrovski, O., In-Situ Study of Gaseous Reduction of Magnetite Doped with Alumina Using High-Temperature XRD Analysis, *Metall and Materi Trans B* 46 (2015), 6, pp. 2564–2572.
- [101] Zhu, D., Yang, C., Pan, J. and Li, X., Comparison of the Oxidation Behaviors of High FeO Chromite and Magnetite Concentrates Relevant to the Induration of Ferrous Pellets, *Metall and Materi Trans B* 47 (2016), 5, pp. 2919–2930.
- [102] Pan, F., Zhu, Q., Du, Z. and Sun, H., Oxidation Kinetics, Structural Changes and Element Migration during Oxidation Process of Vanadium-titanium Magnetite Ore, *J. Iron Steel Res. Int.* 23 (2016), 11, pp. 1160–1167.
- [103] Adetoro, A.A., Sun, H., He, S., Zhu, Q. and Li, H., Effects of Low-temperature Pre-oxidation on the Titanomagnetite Ore Structure and Reduction Behaviors in a Fluidized Bed, *Metall and Materi Trans B* 49 (2018), 2, pp. 846–857.

-
- [104] Hayashi, S., Sawai, S. and Iguchi, Y., Influence of Coating Oxide and Sulfur Pressure on Sticking during Fluidized Bed Reduction of Iron Ores, *ISIJ International* 33 (1993), 10, pp. 1078–1087.
- [105] Barustan, M.I.A. and Jung, S.-M., Morphology of Iron and Agglomeration Behaviour During Reduction of Iron Oxide Fines, *Met. Mater. Int.* 25 (2019), 4, pp. 1083–1097.
- [106] Dwarapudi, S., Ghosh, T.K., Tathavadkar, V., Denys, M.B., Bhattacharjee, D. and Venugopal, R., Effect of MgO in the form of magnesite on the quality and microstructure of hematite pellets, *International Journal of Mineral Processing* 112-113 (2012), pp. 55–62.
- [107] Park, E. and Ostrovski, O., Effects of Preoxidation of Titania-Ferrous Ore on the Ore Structure and Reduction Behavior, *ISIJ Int.* 44 (2004), 1, pp. 74–81.
- [108] Park, E. and Ostrovski, O., Reduction of Titania-Ferrous Ore by Hydrogen, *ISIJ International* 44 (2004), 6, pp. 999–1005.
- [109] Sardari, A., Alamdari, E.K., Noaparast, M. and Shafaei, S.Z., Kinetics of magnetite oxidation under non-isothermal conditions, *Int J Miner Metall Mater* 24 (2017), 5, pp. 486–492.
- [110] Schmidt, E. R. and Vermaas, F.H., Differential thermal analysis and cell dimensions of some natural magnetites, *American Mineralogist: Journal of Earth and Planetary Materials* 40 (1955), pp. 422–431.
- [111] Henry. Lepp, 1957 stages in the oxidation of magnetite, *American Mineralogist* 42 (1957), pp. 679–681.
- [112] Basta, E.Z., Some Mineralogical Relationships in the System $\text{Fe}_2\text{O}_3\text{-Fe}_3\text{O}_4$ and the Composition of Titanomaghemite 54 (1959), pp. 698–729.
- [113] Wang, B.H., Non-isothermal Kinetics of Oxidation of Magnetite Pellets, National Ironmaking Production Technology Conference and Ironmaking Annual Conference, Beijing, China, 2009.
- [114] Dupuis, C. and Beaudoin, G., Discriminant diagrams for iron oxide trace element fingerprinting of mineral deposit types, *Miner Deposita* 46 (2011), 4, pp. 319–335.
- [115] Zhang, J., Zhu, Q., Xie, Z., Lei, C. and Li, H., Morphological Changes of Panzhihua Ilmenite During Oxidation Treatment, *Metall and Materi Trans B* 44 (2013), 4, pp. 897–905.
- [116] Kapelyushin, Y., Sasaki, Y., Zhang, J., Jeong, S. and Ostrovski, O., Formation of a Network Structure in the Gaseous Reduction of Magnetite Doped with Alumina, *Metall and Materi Trans B* 48 (2017), 2, pp. 889–899.

-
- [117] Roshchin, A. V. and Vasily Roshchin, Diffusion of anions and cations in oxide crystal lattices during the reduction and oxidation of metals, *Russian Metallurgy* (2003), 1.
- [118] Roshchin, A. V. and Vasily Roshchin, Electrical Conduction and Lattice Disorder in oxides upon the Reduction and Oxidation of Metals, *Russian Metallurgy* (2003), 3-9.
- [119] Zheng, H., Daghighaleh, O., Ma, Y., Taferner, B., Schenk, J. and Kapelyushin, Y., Phase Transition of Magnetite Ore Fines During Oxidation Probed by In Situ High-Temperature X-Ray Diffraction, *Metall and Materi Trans B* (2023), pp. 1–10.
- [120] Bhargava, S.K., Garg, A. and Subasinghe, N.D., In situ high-temperature phase transformation studies on pyrite, *Fuel* 88 (2009), 6, pp. 988–993.
- [121] Gialanella, S., Girardi, F., Ischia, G., Lonardelli, I., Mattarelli, M. and Montagna, M., On the goethite to hematite phase transformation, *J Therm Anal Calorim* 102 (2010), 3, pp. 867–873.
- [122] Kurpaska, L., Structural properties of zirconia – in-situ high temperature XRD characterization, *Journal of Molecular Structure* 1163 (2018), pp. 287–293.
- [123] Gokhale, K. V. G. K., Studies on the Oxidation of Magnetite, *Economic Geology* 56 (1961) 5, pp. 963–971.
- [124] Levy, D., Artioli, G. and Dapiaggi, M., The effect of oxidation and reduction on thermal expansion of magnetite from 298 to 1173K at different vacuum conditions, *Journal of Solid State Chemistry* 177 (2004), 4-5, pp. 1713–1716.
- [125] Langreiter, T. and Kahlenberg, V., TEV—A Program for the Determination of the Thermal Expansion Tensor from Diffraction Data, *Crystals* 5 (2015), 1, pp. 143–153.
- [126] Holcomb, G.R., A review of the thermal expansion of magnetite, *Materials at High Temperatures* 36 (2019), 3, pp. 232–239.
- [127] Paolo Venturelli, In situ study of the goethite-hematite phase transformation by real time synchrotron powder diffraction, *American Mineralogist* (1999), 5-6, pp. 895–904.
- [128] Saito, T., The Anomalous Thermal Expansion of Hematite at a High Temperature, *Bulletin of the Chemical Society of Japan* 38 (1965), 11, pp. 2008–2009.
- [129] Pérez-Maqueda, L.A., Criado, J.M., Real, C., Šubrt, J. and Boháček, J., The use of constant rate thermal analysis (CRTA) for controlling the texture of hematite obtained from the thermal decomposition of goethite, *J. Mater. Chem.* 9 (1999), 8, pp. 1839–1846.

Part II:

Publications within this PhD thesis:

- [1]. Zheng, H., Spreitzer, D., Wolfinger, T., Schenk, J. and Xu, R., Effect of Prior Oxidation on the Reduction Behavior of Magnetite-Based Iron Ore During Hydrogen-Induced Fluidized Bed Reduction, *Metall and Materi Trans B* 52 (2021), 4, pp. 1955–1971. <https://link.springer.com/article/10.1007/s11663-021-02215-5>
- [2]. Zheng, H., Daghighaleh, O., Wolfinger, T., Taferner, B., Schenk, J. and Xu, R., Fluidization behavior and reduction kinetics of pre-oxidized magnetite-based iron ore in a hydrogen-induced fluidized bed, *Int J Miner Metall Mater* 29 (2022), 10, pp. 1873–1881. <https://link.springer.com/article/10.1007/s12613-022-2511-7>
- [3]. Zheng, H., Schenk, J., Daghighaleh, O. and Taferner, B., Parameter Optimization for Hydrogen-Induced Fluidized Bed Reduction of Magnetite Iron Ore Fines, *Metals* 13 (2023), 2, pp. 339. <https://www.mdpi.com/2075-4701/13/2/339>
- [4]. Zheng, H., Schenk, J., Spreitzer, D., Wolfinger, T. and Daghighaleh, O., Review on the Oxidation Behaviors and Kinetics of Magnetite in Particle Scale, *steel research international* (2021), pp. 2000687. <https://doi.org/10.1002/srin.202000687>
- [5]. Zheng, H., Schenk, J., Xu, R., Daghighaleh, O., Spreitzer, D., Wolfinger, T., Yang, D. and Kapelyushin, Y., Surface Morphology and Structural Evolution of Magnetite-Based Iron Ore Fines During the Oxidation, *Metall and Materi Trans B* 53 (2022), 3, pp. 1644–1660. <https://link.springer.com/article/10.1007/s11663-022-02475-9>
- [6]. Zheng, H., Daghighaleh, O., Ma, Y., Taferner, B., Schenk, J. and Kapelyushin, Y., Phase Transition of Magnetite Ore Fines During Oxidation Probed by In Situ High-Temperature X-Ray Diffraction, *Metall and Materi Trans B* (2023), pp. 1–10. <https://link.springer.com/article/10.1007/s11663-023-02754-z>

Author's contribution table

	Conception	Experiments	Data analysis	Manuscript writing
Publication 1	70 %	70 %	70 %	95 %
Publication 2	95 %	100 %	95 %	95 %
Publication 3	95 %	100 %	95 %	95 %
Publication 4	95 %	/	95 %	95 %
Publication 5	95 %	95 %	95 %	95 %
Publication 6	95 %	70 %	95 %	95 %

Publications not included in this PhD thesis:

- [1]. Pfeiffer, A., Ernst, D., **Zheng, H.**, Wimmer, G. and Schenk, J., The Behavior of Direct Reduced Iron in the Electric Arc Furnace Hotspot, *metals*, 13 (2023), 5, pp. 978.
- [2]. Chen, X., Wang, W., Yang, D., **Zheng, H.**, Wang, L. and Chen, S., Influence Mechanism of Zn on the Iron Ore-Sintering Mineralization Process, *Metall and Materi Trans B* 54 (2023), 2, pp. 550–561.
- [3]. Xu, R., Zhang, Y., Huang, X., Cao, M., Yu, J., Zhang, J., **Zheng, H.** and Schenk, J., Preparation of Micro-Electrolytic Iron-Carbon Filler for Sewage by Recycling Metallurgical Dust, *Metals* 13 (2023), 4, pp. 673.
- [4]. Chen, X., Wang, W., Yang, D., **Zheng, H.** and Wang, B., Mineralization Characteristics of Iron Ore Sinter and the Effects of Cooling Rate on Mineral Phase Structure, *ISIJ Int.* 63 (2023), 2, pp. 261–270.
- [5]. Daghighaleh, O., Schenk, J., **Zheng, H.**, Taferner, B., Forstner, A. and Rosenfellner, G., Long - Term Reoxidation of Hot Briquetted Iron in Various Prepared Climatic Conditions, *steel research international* 94 (2023), 1, pp. 2200535.
- [6]. Wolfinger, T., Spreitzer, D., **Zheng, H.** and Schenk, J., Influence of a Prior Oxidation on the Reduction Behavior of Magnetite Iron Ore Ultra-Fines Using Hydrogen, *Metall and Materi Trans B* 53 (2022), 1, pp. 14–28.
- [7]. Xu, R., Deng, S., **Zheng, H.**, Huang, X., Daghighaleh, O., Schenk, J., Zhang, J. and Zhu, J., Gasification Behaviors of Ferrocake With and Without Water Vapor, *steel research international* 93 (2022), 11, pp. 2200575.
- [8]. **Zheng, H.**, Xu, R., Zhang, J., Daghighaleh, O., Schenk, J., Li, C. and Wang, W., A Comprehensive Review of Characterization Methods for Metallurgical Coke Structures, *materials*, 15 (2021), 1, pp. 174.
- [9]. Xu, R., Deng, S., Wang, W., **Zheng, H.**, Chen, S., Huang, X. and Wang, F., Effect of Binders on the Crushing Strength of Ferro-Coke, *Materials* 14 (2021), 4, pp. 850.
- [10]. Xu, R., Huang, X., Wang, W., Deng, S., **Zheng, H.**, Song, M. and Wang, F., Investigation on the Microstructure, Thermal Strength and Gasification Mechanism of Modified Ferro-Coke with Coal Tar Pitch, *Metall and Materi Trans B* 51 (2020), 4, pp. 1526–1539.
- [11]. Xu, R., Deng, S., **Zheng, H.**, Wang, W., Song, M., Xu, W. and Wang, F., Influence of initial iron ore particle size on CO₂ gasification behavior and strength of ferro-coke, *J. Iron Steel Res. Int.* 27 (2020), 8, pp. 875–886.

Effect of Prior Oxidation on the Reduction Behavior of Magnetite-Based Iron Ore During Hydrogen-Induced Fluidized Bed Reduction



HENG ZHENG, DANIEL SPREITZER, THOMAS WOLFINGER, JOHANNES SCHENK, and RUNSHENG XU

Magnetite-based iron ore usually shows a high sticking tendency and a poor reducibility in the fluidized bed because of its dense structure. To enhance the fluidization and reduction behaviors of magnetite-based iron ore during hydrogen-induced fluidized bed reduction, the effect of a prior oxidation treatment is investigated. The results show that the untreated magnetite-based iron ore cannot be fluidized successfully in the tested temperature range between 600 °C and 800 °C. At 600 °C reduction temperature, the de-fluidization can be avoided by a prior oxidation treatment. At higher reduction temperatures, the fluidization behavior can be further improved by an addition of 0.5 wt pct MgO. Magnesiowüstite ($\text{Fe}_x\text{Mg}_{1-x}\text{O}$) is formed, which decreases the contact chance of the sticky surface between particles. Regarding to the reduction rate, a prior partial oxidation is more beneficial compared to deep oxidation. The kinetic analysis shows that MgO could promote the initial reaction. The reaction rate limiting step is no longer diffusion but chemical reaction for prior partly oxidized samples. A prior partial oxidation combined with an addition of MgO is considered to be a promising pretreatment method for a successful processing of magnetite-based iron ore.

<https://doi.org/10.1007/s11663-021-02215-5>
© The Author(s) 2021

I. INTRODUCTION

TODAY, the two dominating process routes for steelmaking are the blast furnace–basic oxygen furnace (BF–BOF) route and the scrap-based electric arc furnace (EAF) route.^[1] In order to achieve the goal of climate neutrality (net-zero greenhouse gas emissions) by 2050, breakthrough technologies are crucial for further decreasing the overall CO₂ emissions from steel production.^[2,3] One option is the use of H₂ as a reducing agent to produce direct reduced iron (DRI), followed by a melting stage, typically an electric arc furnace for crude steel production (DRI–EAF). Currently, methane is commonly used to produce a syngas of H₂ and CO as a reducing gas. In this case, if decarbonized electricity is

used, the greenhouse gas intensity of the DRI–EAF route can be decreased to around 0.7 t CO₂/t steel.^[4–6] The amount of scrap return is supposed to increase within the next few years. As a result, the production of EAF steel will also grow, which requires a considerable amount of DRI product to produce high quality steel grades.^[7,8]

The fluidized bed technology has been widely used since the 1950s for the production of DRI; it has been well developed in the past decades. H₂ and iron ore fines can be used as a reducing gas and solid burden in the fluidized bed ironmaking process, respectively.^[9] Aside from hematite-based iron ores, the occurrence of magnetite-based iron ore is also very common in nature. The use of magnetite-based iron ore during hydrogen-induced fluidized bed reduction is therefore of great interest. As reported, it is impossible for magnetite-based iron ore fines guaranteeing a stable fluidization during the total reduction procedure.^[10] Reduction by H₂ is an endothermic reaction; therefore, pre-heating of iron ore is one opportunity for ensuring a sufficient energy supply. Generally, the preheating process occurs in oxidizing atmosphere. As a result, the magnetite iron ore becomes oxidized. The oxidation of magnetite is an exothermic reaction which generates considerable heat, which is beneficial for reducing the primary energy input for pre-heating.

HENG ZHENG and DANIEL SPREITZER are with the Montanuniversität Leoben, Franz-Josef-Straße 18, 8700 Leoben, Austria. Contact e-mails: heng.zheng@stud.unileoben.ac.at; daniel.spreitzer@unileoben.ac.at THOMAS WOLFINGER is with the K1-MET GmbH, Stahlstraße 14, 4020 Linz, Austria. JOHANNES SCHENK is with the Montanuniversität Leoben and also with the K1-MET GmbH. RUNSHENG XU is with the State Key Laboratory of Refractories and Metallurgy, Wuhan University of Science and Technology, Wuhan 430081, China.

Manuscript submitted December 9, 2020; accepted April 23, 2021.
Article published online June 1, 2021.

Many researchers investigated the effect of pre-oxidation on the reduction behavior of titanomagnetite in a fixed bed. Eungyeul *et al.*^[11,12] conducted the reduction test using both H₂ and CO. It was found that although the initial surface area of pre-oxidized titanomagnetite was much lower than that of raw material, the reducibility was greatly enhanced due to the structural transformation from rhombohedral (titanohematite) to spinel cubic (titanomagnetite) during the reduction, which led to about 25 pct volume expansion resulting in open structures. Wang *et al.*^[13] did the reduction kinetic analysis of titanomagnetite iron ore and found that the chemical reaction controlled the early stage of the reaction, while the mechanism of later stage was considered to be diffusion controlled. After pre-oxidation treatment, the reduction was entirely controlled by the chemical reaction. The diffusion was no more the rate-limiting step due to the formation of micro-cracks which served as channels for the reducing gas.

The most common problem for the fluidized bed reduction was the de-fluidization phenomenon caused by sticking of the reduced metallic iron, which would decrease the reduction efficiency and make a process control of the system impossible.^[14] The reduction temperature,^[15] fluidizing gas^[16] and particle size distributions^[17] showed significant impacts on the fluidization behavior. In CO-induced fluidized bed, the bonding effect of iron whisker was the common cause for de-fluidization.^[18,19] The addition of H₂ in CO could control the surface morphology of particles from fibrous/whisker shape to dense structure and improved the fluidization behavior significantly.^[20] In H₂-induced fluidized bed, although there was no iron whisker on the surface, the newly generated iron resulted in the agglomeration of particles.^[21] In order to prevent de-fluidization, many researchers focused on the coating treatment of iron ore. Zhong *et al.*^[22] found the MgO was more effective to prevent de-fluidization, comparing with CaO. Under the condition of CO-H₂ reducing gas mixture, MgO could insulate the contact of metallic iron between particles effectively, which decrease the particle stickiness. The same time, because of the deposition of CO, part of the iron in the particle surface was converted to Fe₃C, which also helped to decrease the sticky tendency.^[23] Guo *et al.*^[24,25] discussed five different coating methods on Fe₂O₃ particles (briquetting-sintering method, high temperature injection method, powder method, slurry-sintering method and coprecipitation method) in the H₂-induced fluidized bed. It is found that, if MgO addition is above 1.5 wt pct, all the methods could help to keep a stable fluidization. The reason can be explained by the formation of MgFe₂O₄ on the particle surface, which shows a high melting point. An effective coating method was important for avoiding de-fluidization problem. In the coprecipitation method, the Fe₂O₃ particles are coated with MgO in the liquid solution of Mg(NO₃)₃·6H₂O and Na₂CO₃ to get more effective and uniformly adsorption of MgO particles.^[25] From coprecipitation method, only 0.411 wt pct of coating MgO content was required to avoid the sticking problem. The inhibiting effect of MgO could be summarized as physical and chemical barrier. The

main mechanism prevention of coating MgO at a reduction temperature below 800 °C was physical isolation. When the reduction temperature was above 900 °C, the magnesia compounds (Fe₂MgO₄ or FeMgO₂) would appear on the surface which served as a chemical barrier.^[26,27]

The above studies have explored the effects of pre-oxidation on the reduction and addition of MgO on fluidization behaviors. But the influences of prior oxidation treatment on magnetite-based iron ores are rarely discussed in H₂-induced fluidization conditions. Currently, no general concept is available for a successful treatment of magnetite-based iron ore during hydrogen-induced fluidized bed reduction. The purpose of this study is to use magnetite-based iron ore directly as a raw material and to investigate methods preventing the de-fluidization. The present work aims at (1) a comparison of the fluidization behaviors between raw magnetite-based iron ore and oxidized one; (2) an examination of the reducibility of the raw and oxidized magnetite-based iron ore during the fluidized bed reduction; (3) an investigation of the effect of prior oxidation on improving the fluidization and reduction behaviors; (4) an analysis of the effect of MgO addition on the fluidization and reduction behaviors of the pre-oxidized magnetite-based iron ore; (5) a multistep kinetic analysis of the reduction mechanism of the magnetite-based iron ore. This work could provide precursory theoretical guidance for the pretreatment of magnetite-based iron ore for a successful H₂-induced fluidized bed reduction.

II. EXPERIMENTAL

A. Materials

In this work, a commercial magnetite-based iron ore was used. The raw magnetite-based iron ore is defined as Sample A. The samples after deep and partial oxidation treatments were named Sample B and Sample C, respectively. The surface morphology of samples before reduction tests were shown in Figure 1. The raw magnetite-based iron ore fines had clear edges and corners, presenting irregular shapes. After oxidation, the sharp-edged corners disappear and the surface became less smooth, which provides more adsorption sites for the MgO powder. The particle size distribution of the samples consisted of 50 wt pct 125-250 μm and 50 wt pct 250-500 μm. The chemical compositions of the Sample A, Sample B and Sample C were characterized by the inductively coupled plasma-mass spectrometry (ICP-MS) method and listed in Table 1. MgO powder with high purity was used in this work (> 99.5 wt pct, – 44 μm).

B. Experimental apparatus and procedure

The experimental apparatus used was a laboratory-scale fluidized bed reactor, which is schematically shown in Figure 2. The inner diameter of the reactor was 68 mm. The upper part of the reactor was designed

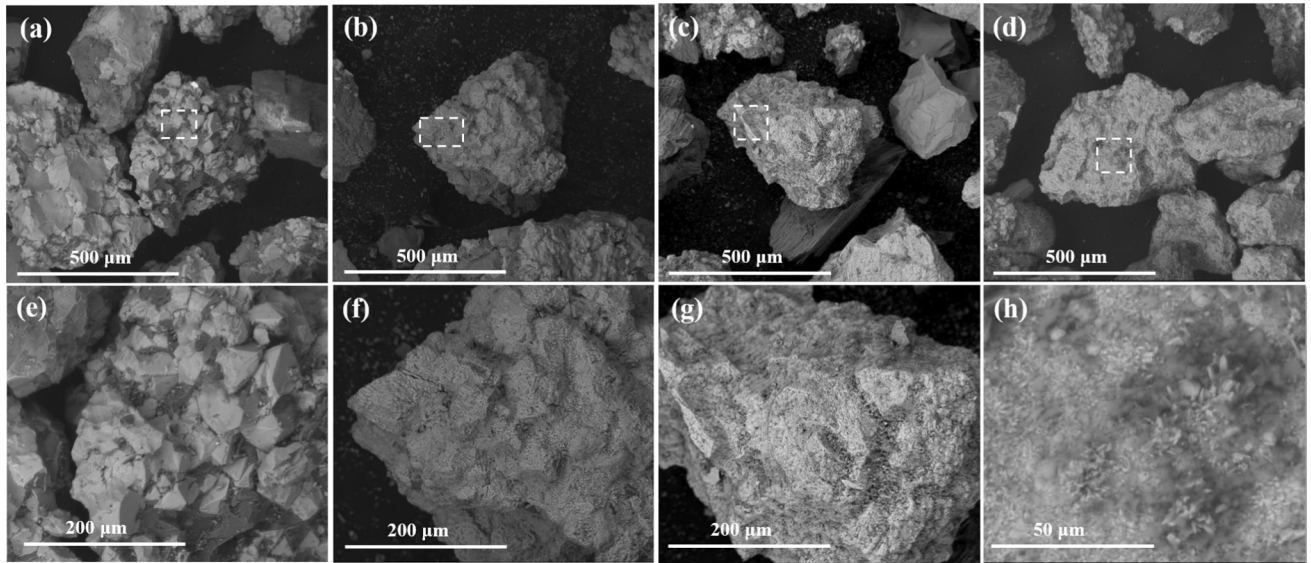
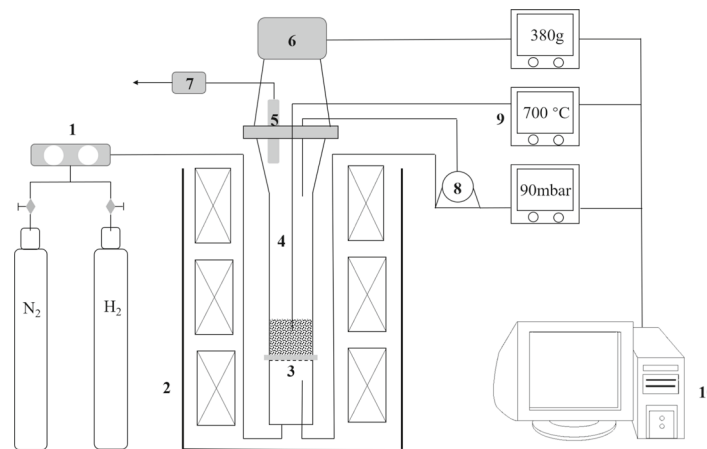


Fig. 1—Surface morphology of materials before reduction under SEM: (a), (e) Sample A; (b), (f) Sample B; (c), (g) Sample C; (d), (h) Sample B with additional 0.50 wt pct MgO.

Table I. Chemical Compositions of the Samples (Wt Pct)

	Fe _{tot}	FeO	SiO ₂	Al ₂ O ₃	CaO	MgO	MnO	P
Sample A (Raw Magnetite)	59.50	19.66	7.05	1.13	3.03	2.00	0.17	0.70
Sample B (Deep Oxidized)	57.80	0.50	6.84	1.11	2.97	1.96	0.17	0.68
Sample C (Partially Oxidized)	58.64	12.89	6.90	1.12	3.01	1.99	0.17	0.69



1. Gas mixture unit; 2. Three-stage electrical furnace; 3. Distributor; 4. Fluidized bed reactor; 5. Dust filter; 6. Scale; 7. Pressure regulator; 8. Differential pressure monitor; 9. Temperature control; 10. Computer system unit

Fig. 2—Schematic layout of laboratory fluidized bed reactor.

in a conical shape to reduce the superficial gas velocity and, therefore, to reduce the sample losses in the form of entrainment during fluidization. H₂ and N₂ were mixed in the gas mixing unit and preheated while passing through the supply pipe inside the furnace. The temperature of the reducing gas mixture and specimen temperature in the fluidized bed reactor were measured by

thermocouples (Type N) below the grid and inside the sample. These temperature measurements were used to control the power for the three-stage electrical resistance heating of the furnace. The three-stage heating system could work independently, which helped to maintain the reduction temperature. The sample temperature was measured by the thermocouple that inside the bed

Table II. Experimental Process Conditions

Iron Ore	MgO Additive	Reducing Gas H ₂	Gas Velocity	Temperature	Pressure
400 g	0–1.5 wt pct	15.9 L/min (SATP)	0.4 m/s	600–800 °C	1 atm.

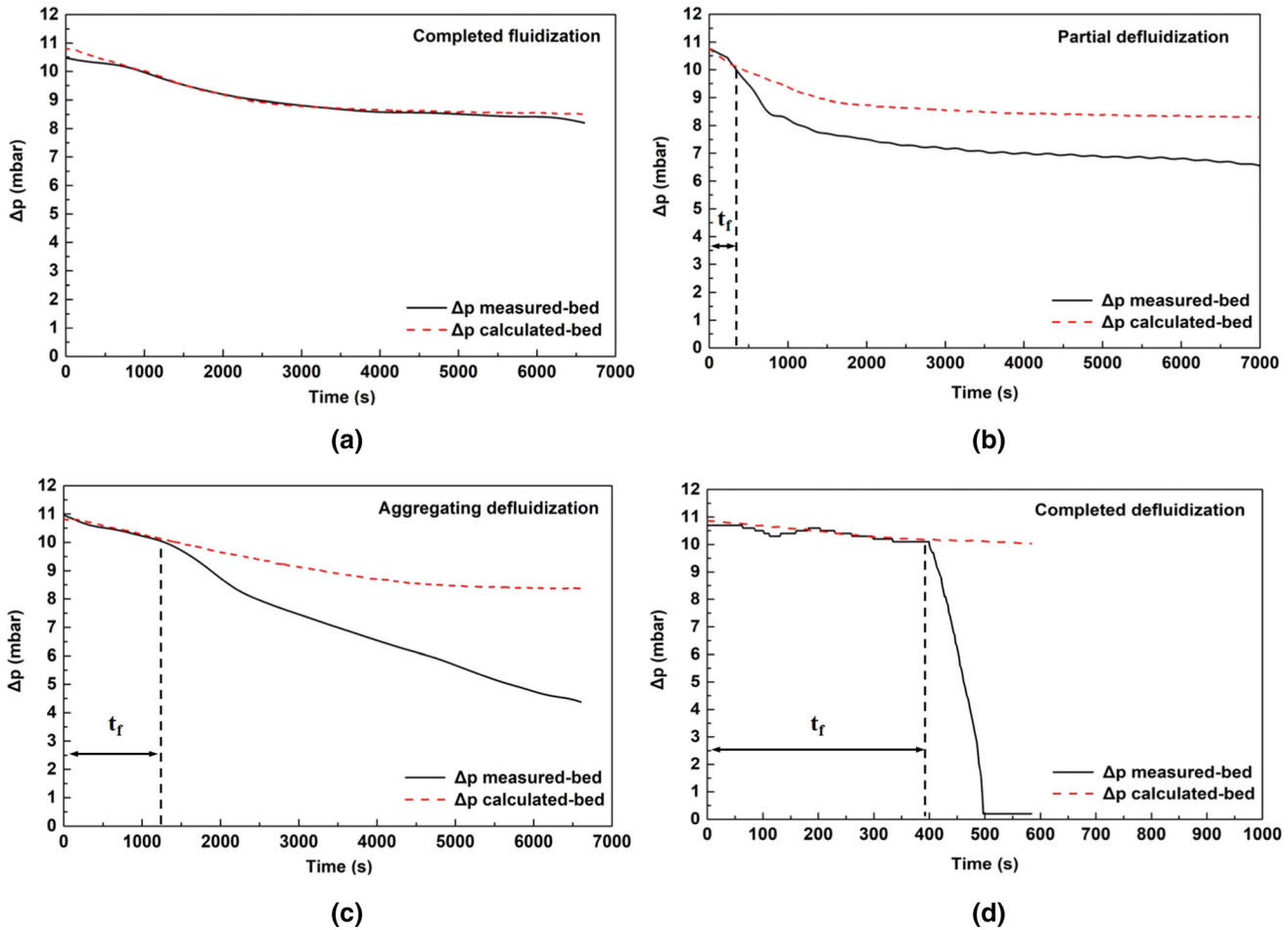


Fig. 3—Four states of fluidization behavior: (a) completed fluidization; (b) partial de-fluidization; (c) aggregating de-fluidization; (d) completed de-fluidization.

material. The fluidization behavior was characterized by the differential pressure measurement between the gas distributor and the material. The real-time pressure drop and weight change of the material were measured and these measurements were stored automatically by the system.

All reduction tests followed the same procedure. The material was charged through a small aperture at the top of the reactor at 500 °C during the preheating stage and purged with N₂. When the material reached the target temperature, followed by a 10-minutes temperature equilibrium period, the atmosphere was changed to the reducing atmosphere. If de-fluidization occurred, or when the reaction time reached 110 minutes, the reducing gas was again replaced by N₂ and sample cooling under N₂ atmosphere began. The superficial gas velocity was kept constant at 0.4 m/s at all different

temperatures. This was achieved by a constant H₂ flow rate, balanced by different nitrogen flow rates. The H₂ was maintained as 15.9 L/minutes at standard ambient temperature and pressure (SATP).

The deep oxidation of magnetite iron ore was performed in a muffle furnace at 1000 °C under air atmosphere for 20 hours to ensure a deep oxidation. The partial oxidation took place at 800 °C for 4 hours. The MgO particles were mixed directly with the material before charging it into reactor. The MgO-content was represented by the weight percentage of MgO corresponding to the charged iron ore material. The experimental conditions are listed in Table II.

The weight loss measured during the reduction can be converted into the reduction degree (RD) by chemical analysis of the iron ore. The RD can be calculated based on Eqs. [1] through [3].^[28,29]

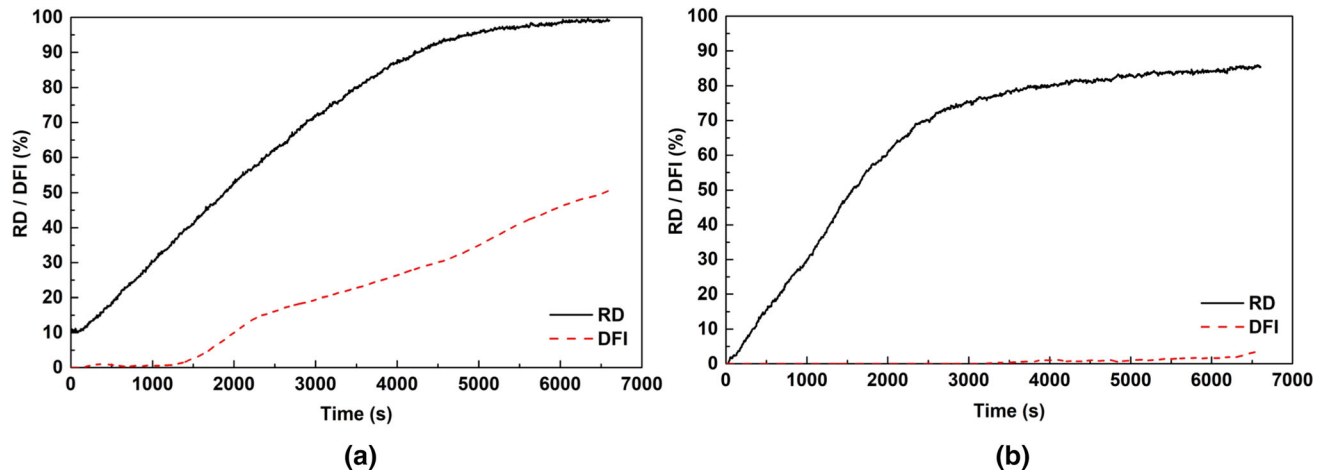


Fig. 4—Reduction degree and de-fluidization index of Sample A and Sample B at 600 °C: (a) RD/DFI of Sample A; (b) RD / DFI of Sample B.

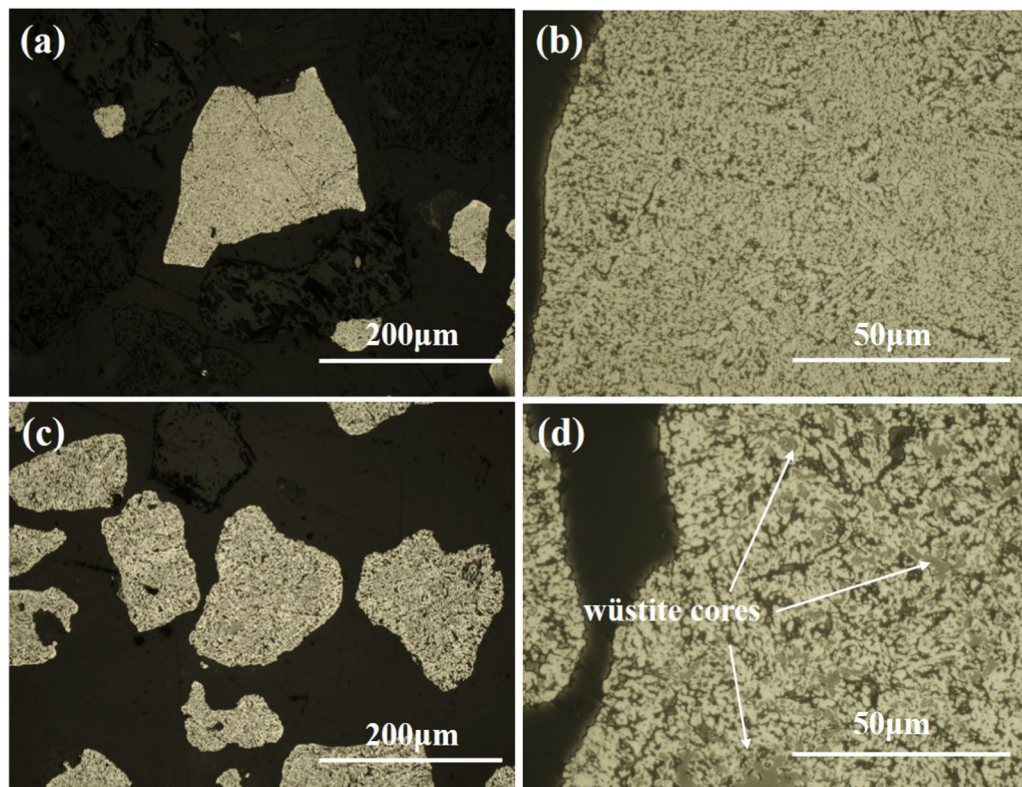


Fig. 5—Polished section images of the Sample A and Sample B after reduction tests at 600 °C under optical light microscope: (a), (b) Sample A; (c), (d) Sample B.

$$RD = 1 - \frac{O_{\text{bounded to Fe at } t=ti}}{O_{\text{bounded to Fe at } t=t0}} \times 100 \text{ pct}, \quad [1]$$

$$O_{\text{bounded to Fe at } t=ti} = \frac{O_{\text{bounded to Fe}_2\text{O}_3} + O_{\text{bounded to FeO}} - \Delta m}{M_{\text{O}}} \text{ (in mol)}, \quad [2]$$

$$O_{\text{bounded to Fe at } t=t0} = 1.5 \cdot \frac{m_0 \cdot \text{Fe}_{\text{tot}}}{M_{\text{Fe}}} \text{ (in mol)}, \quad [3]$$

where $O_{\text{bounded to Fe at } t=t0}$ and $O_{\text{bounded to Fe at } t=ti}$ represent the amounts of O that are bounded to Fe at the start and during the reduction; Δm and m_0 are the

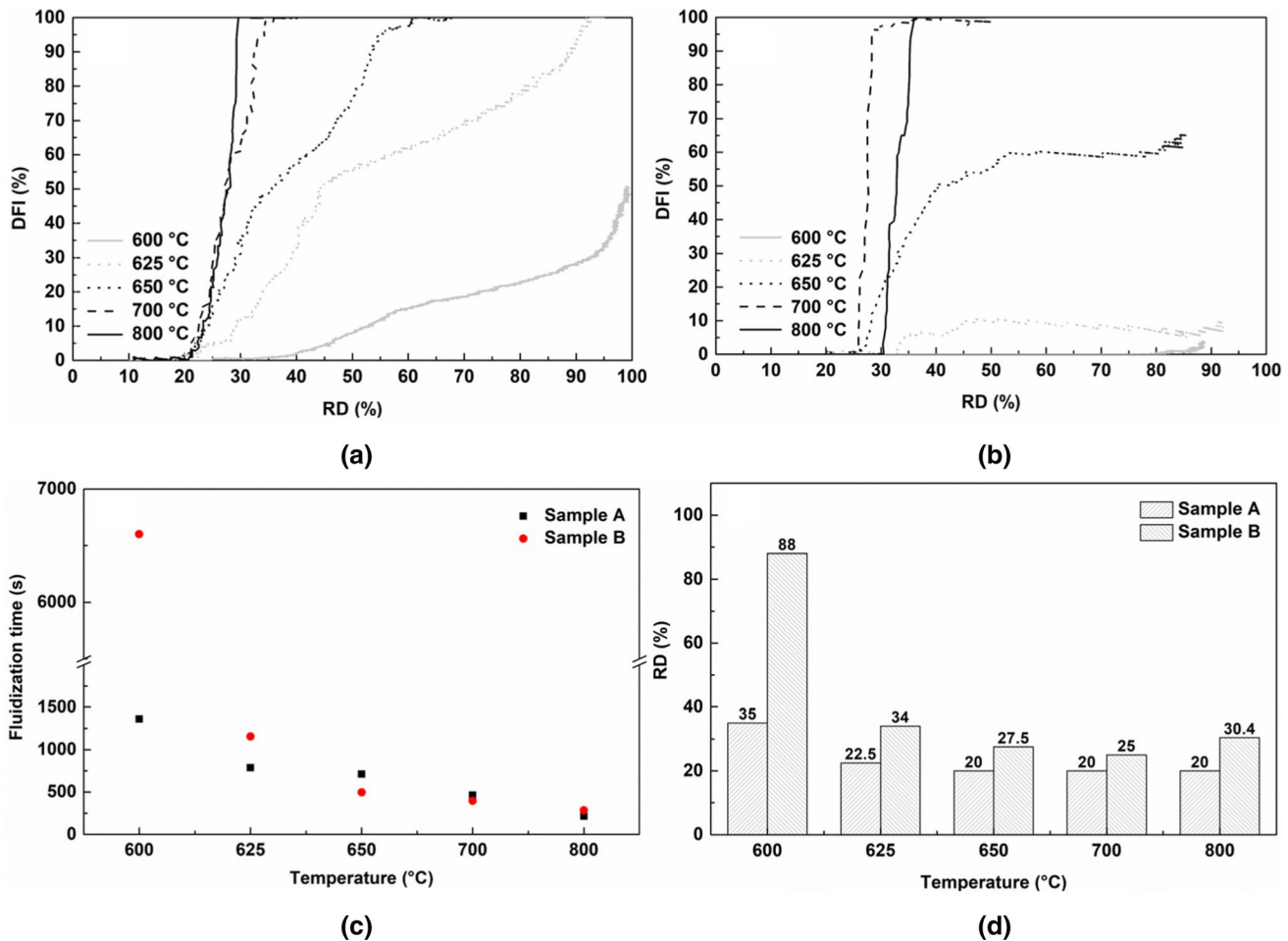


Fig. 6—Fluidization and reduction behaviors of Sample A and Sample B: (a) DFI of Sample A against RD; (b) DFI of Sample B against RD; (c) fluidization time; (d) reduction degree when de-fluidization starts.

weight loss due to the loss of O and the mass of input material; M_O and M_{Fe} are the constant molar masses for O and Fe.

C. Determination of the Fluidization Behavior

The fluidization behavior was characterized by the pressure drop measurement across the material during the test, which is explained in detail in previous publications.^[8] In the actual investigations, four typical curves of pressure drop were observed, which represent four types of fluidization states—namely, completed fluidization, partial de-fluidization, aggregating de-fluidization, and completed de-fluidization. Figure 3 shows examples for the four pressure drop curves. The fluidization states can be summarized as follows:

- (1) Completed fluidization (CF): The two lines are equal during the whole reduction, as shown in Figure 3(a).
- (2) Partial de-fluidization (PD): The differential pressure decreases at the beginning and then remains stable afterwards, as shown in Figure 3(b).
- (3) Aggregating de-fluidization (AD): The two lines are equal at the beginning. Then, the differential pressure decreases during the whole reduction, as shown in Figure 3(c).

Table III. Influence of Temperature on the Fluidization State

Reduction Temperature °C	Fluidization State	
	Sample A	Sample B
600 °C	AD	CF
625 °C	CD	PD
650 °C	CD	PD
700 °C	CD	CD
800 °C	CD	CD

- (4) Completed de-fluidization (CD): The two lines are equal at the beginning. After a certain time, a sudden differential pressure drop occurs and turns to low values of pressure drop within quite a short time, representing a fixed bed, as shown in Figure 3(d).

The fluidization time (t_f) can be determined as the duration when the dotted grey line ($\Delta p_{\text{calculated-bed}}$) and the black line ($\Delta p_{\text{measured-bed}}$) are distinguished from each other. The buoyancy force in this case was not considered. The $\Delta p_{\text{calculated-bed}}$ is assumed only because of the mass of the sample portion inside the fluidized

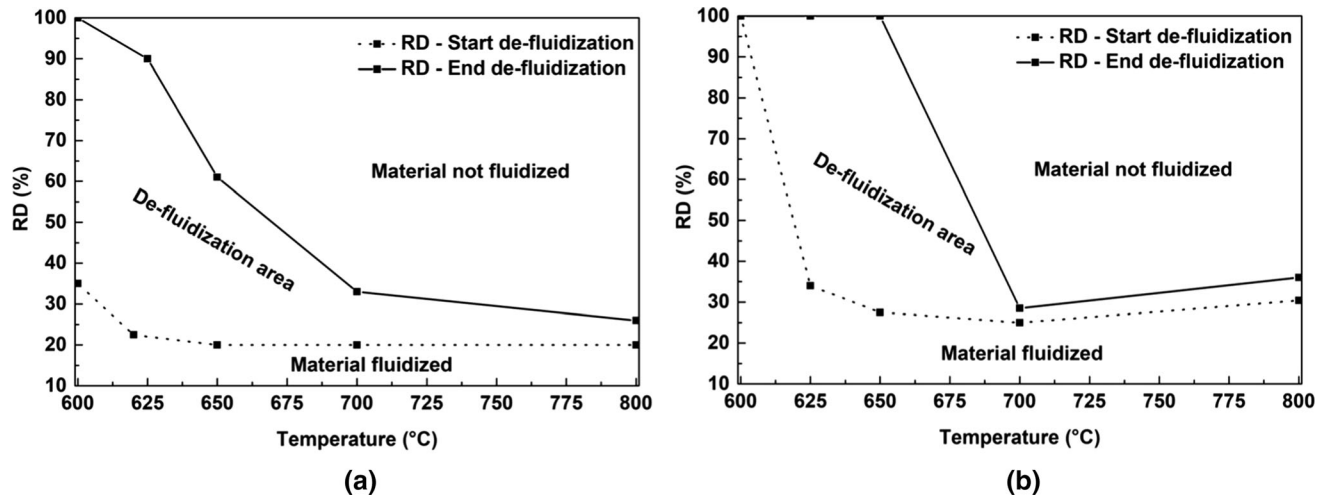


Fig. 7—Influence of temperature on the fluidization area: (a) Sample A, (b) Sample B.

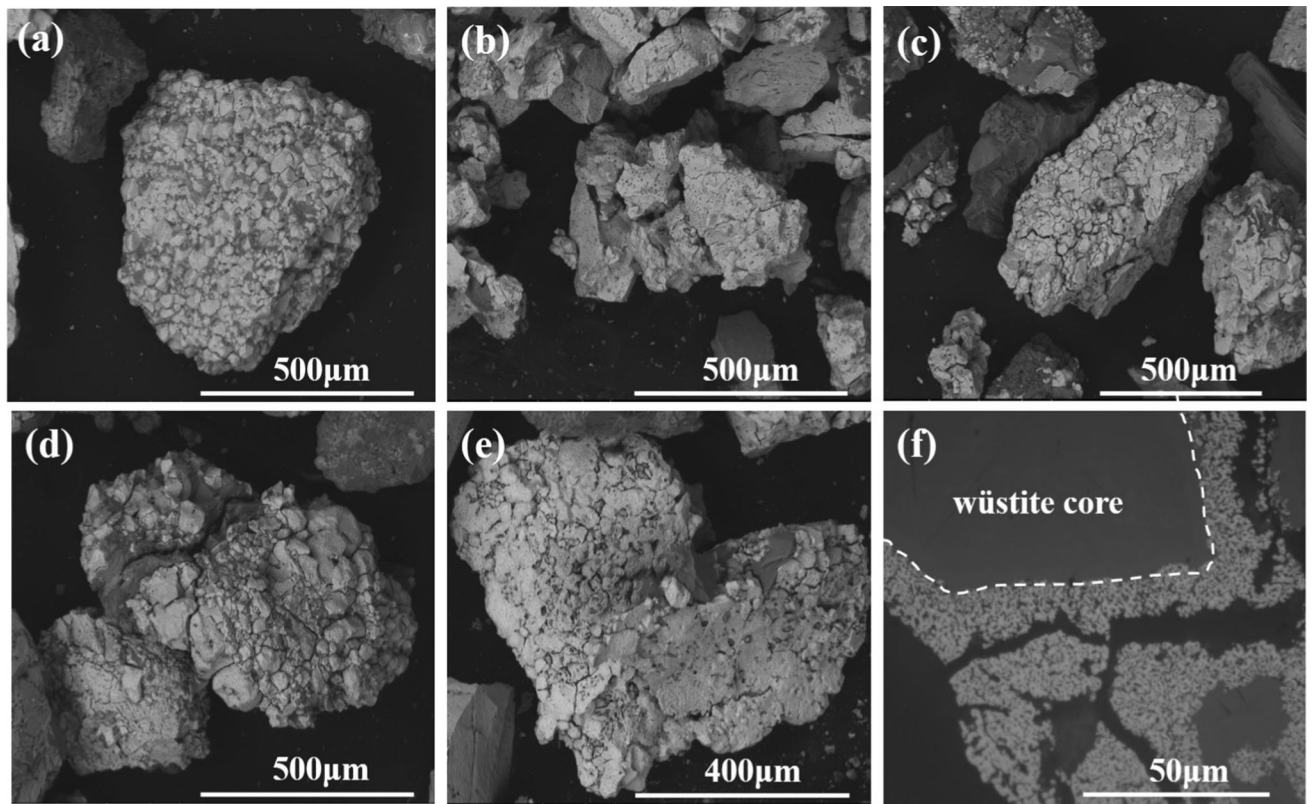


Fig. 8—Surface morphology of (partly) reduced Sample A, (a through e) are under SEM, (f) is under optical light microscope: (a) 600 °C; (b) 625 °C; (c) 650 °C; (d) 700 °C; (e) 800 °C; (f) polished section from raw magnetite iron ore reduced in 650 °C; (f) is reproduced with permission,^[30] copyright 2020 by Montanuniversität Leoben.

bed. To assess the fluidization during the experiment, a de-fluidization index (DFI), which describes the percentage of material, which is not fluidized, is defined as shown in Eq. [4].

$$DFI = \frac{\Delta p_{\text{calculated-bed}} - \Delta p_{\text{measured-bed}}}{\Delta p_{\text{calculated-bed}} - \Delta p_{\text{fixed-bed}}}, \quad [4]$$

$$\Delta p_{\text{calculated-bed}} = \frac{m_t \cdot g}{\text{Reactor area}}, \quad [5]$$

where $\Delta p_{\text{calculated-bed}}$ represents the theoretical differential pressure drop over material, which is calculated from the initial material mass and the weight loss sustained during the reduction if it is in a completed

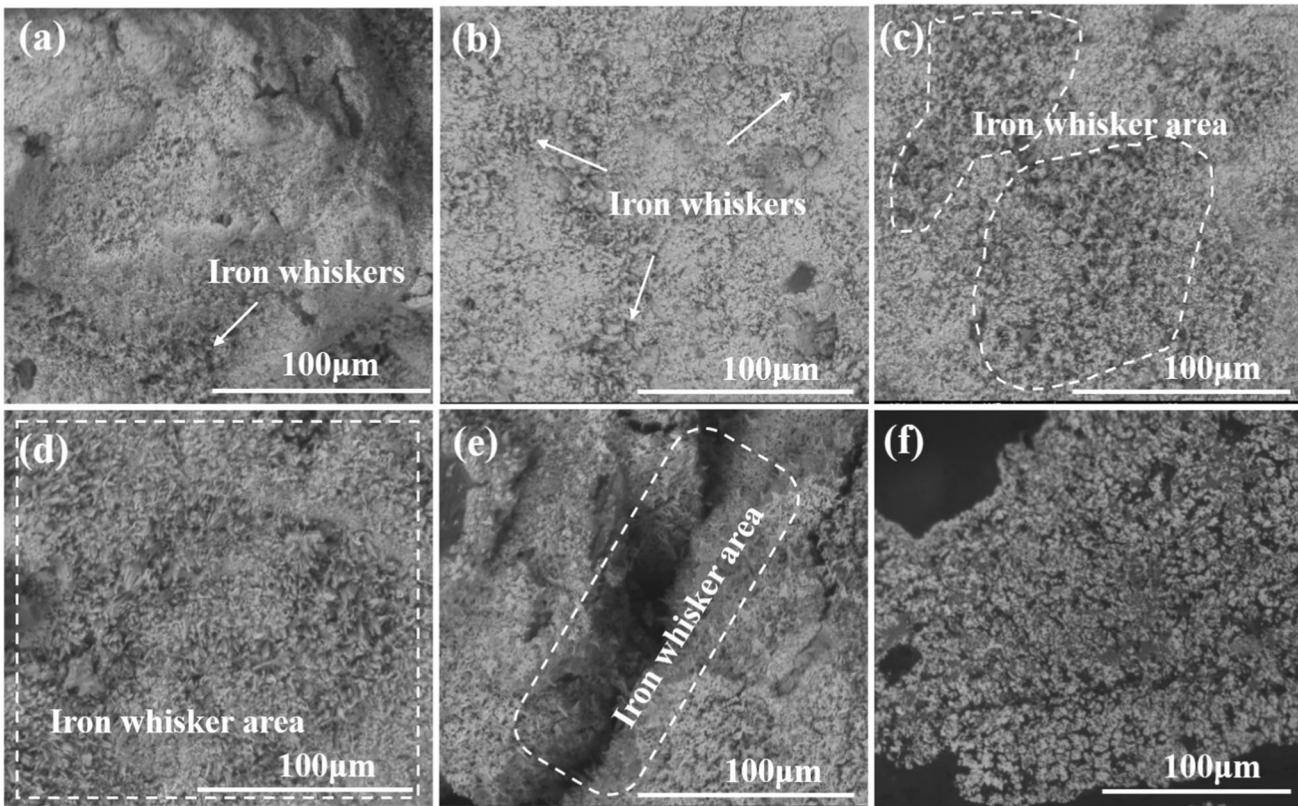


Fig. 9—Surface morphology of (partly) the reduced Sample B, (a through e) are under SEM, (f) is under optical light microscope: (f) polished section for Sample B reduced in 650 °C. (f) is reproduced with permission,^[30] copyright 2020 by Montanuniversität Leoben.

Table IV. Influence of MgO Addition on the Fluidization Behavior and the Final RD

MgO Content (Wt Pct)	Fluidization State	Final Reduction Degree (Pct)
0	CD	25.00
0.25	PD	91.37
0.5	CF	93.75
1.0	CF	96.05
1.5	CF	96.35

fluidized state; m_t is the mass of the material during the reduction; $\Delta p_{\text{measured-bed}}$ represents the measured differential pressure drop for the material; the value of $\Delta p_{\text{fixed-bed}}$ is defined as when $\Delta p_{\text{measured-bed}}$ is smaller than 2 mbar referring to completed de-fluidization.

D. Sample Characterization

The polished micro section and the surface morphology of the samples were observed using an optical light microscope (Nikon MM 40 measuring microscope system, Japan) and a scanning electron microscopy (Quanta 200Mk2, FEI, America). The element distribution was analyzed by energy dispersive spectroscopy (EDS, Oxford Instrument, England). The XRD patterns were achieved by an D2phaser X-ray diffractometer (Bruker AXS GmbH, Germany) using Co as the X-ray source. The scanned angular range varied from 20 to 80 deg with a scanning speed of 2°/min.

III. RESULTS AND DISCUSSION

A. Effect of Prior Deep Oxidation on the Fluidization and Reduction Behaviors of the Magnetite-Based Iron Ore

Figure 4(a) shows the reduction results of Sample A and Sample B at 600 °C including the RD and DFI. The RD for Sample A always starts at 11 pct, because according to Eq. [1] magnetite is defined to have already a reduction degree of 11 pct. For Sample A, although de-fluidization starts at the reduction degree of 35 pct, indicated by the DFI, a complete reduction can be achieved within 110 minutes. Almost 50 pct of the Sample A is not in fluidized state at the end of the reduction. As shown in Figure 4(b), no de-fluidization occurs during the reduction of Sample B at 600 °C. The reduction rate dramatically decreases when RD is higher than 80 pct. Figure 5 shows the polished section images of Sample A and Sample B after reduction. The particles

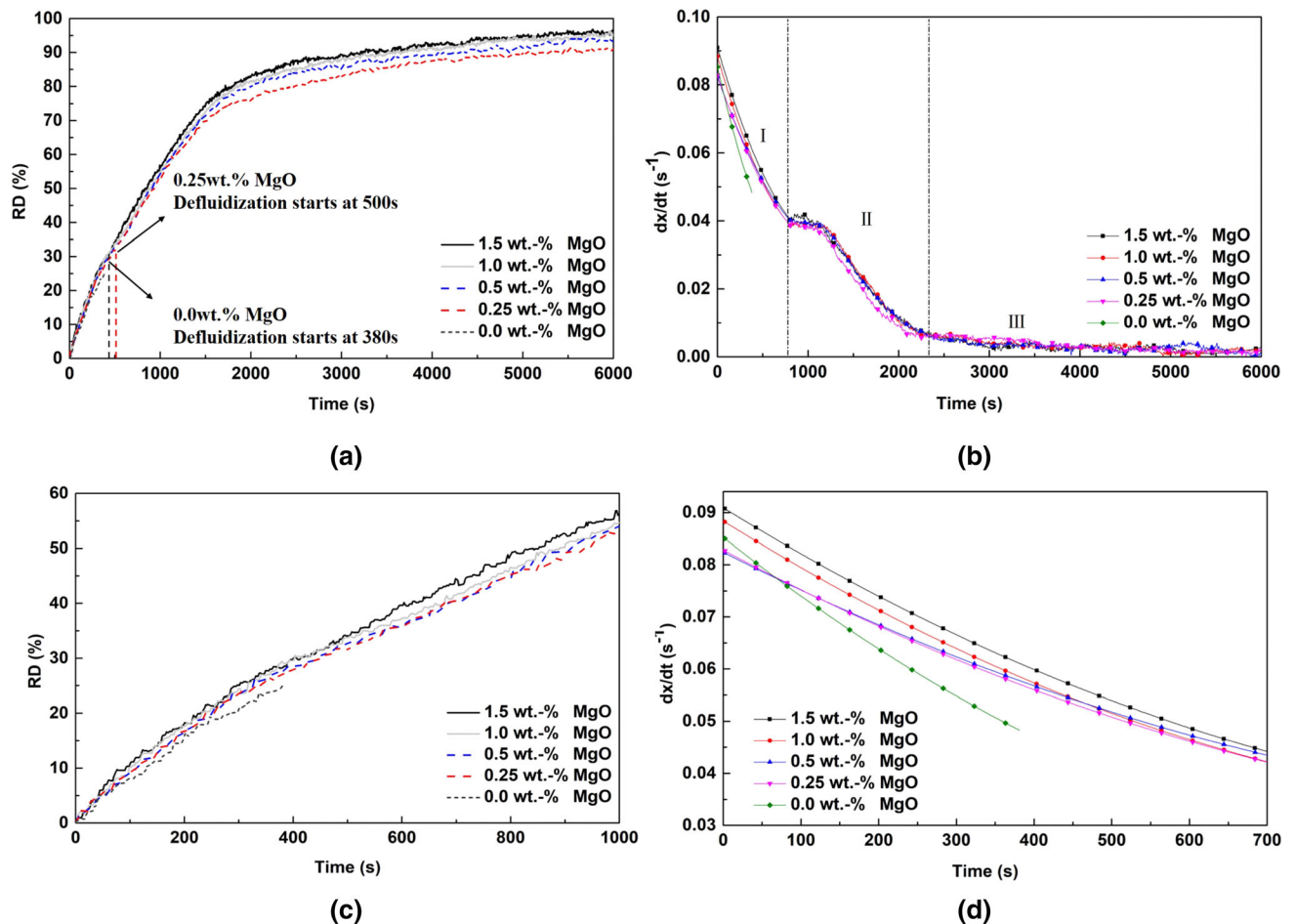


Fig. 10—Influence of MgO on reduction behavior: (a), (c) reduction degree curves; (b), (d) reduction rate.

in Sample A are completely reduced. However, in Sample B, small wüstite cores covered by iron shells can be observed inside the particles. The iron shells inhibit the direct contact of the reducing gas with the reaction interface, which explains the low reduction rate at the final stage.

The relationships between DFI, t_f , RD, and temperature are summarized in Figure 6. As given in Figure 6(a), for the Sample A, only at 600 °C reduction temperature a complete reduction can be achieved without de-fluidization problem. While for Sample B, as shown in Figure 6(b), the complete de-fluidization only occurred at temperatures higher than 700 °C. The influence of temperature on t_f is significant, as shown in Figure 6(c). With increasing temperature, the t_f decrease, for both raw and oxidized magnetite-based iron ore. Figure 6(d) shows the relationship between reduction temperature and RD when de-fluidization starts. The RDs present a decreasing trend, along with the temperature, due to the short fluidization time. Combined with Figure 6(c), it can be seen that when the reduction temperature is above 650 °C, even if the t_f of Sample B is smaller, the RDs are higher than those of Sample A. Especially at 800 °C, the oxidized magnetite-based iron ore has similar t_f but shows nearly 10 pct higher RD, which indicates that the Sample B has

a better reduction behavior in the initial stage. Previous researchers^[31,32] have confirmed that the reducibility of magnetite-based iron ore could be improved by pre-oxidation treatment; the results of this work are in agreement with their findings. It can be noted that if the temperature is higher than 700 °C, the RD of the raw magnetite-based iron ore remains stable at 20 pct, which could be the critical RD for starting the de-fluidization.^[33,34] In actual case, metallic iron can be formed before the reduction to FeO completed, indicating that even RD is smaller than 33 pct the formation of first metallic could occur at the surface of the particles.

The fluidization states at different temperatures are shown in Table III. It can be seen that de-fluidization of Sample A occurs at all tested temperatures. The Sample B could maintain completed fluidization at 600 °C during the whole reduction test. However, with increasing temperature de-fluidization also takes place in the Sample B.

Based on the relations between temperature and RD, when de-fluidization starts and completes, a fluidization regime diagram can be defined, as shown in Figure 7. The area of completed de-fluidization expands with the increasing temperature. The starting points of de-fluidization of Sample B are higher than that of Sample A. In general, the effect of the prior oxidation treatment is

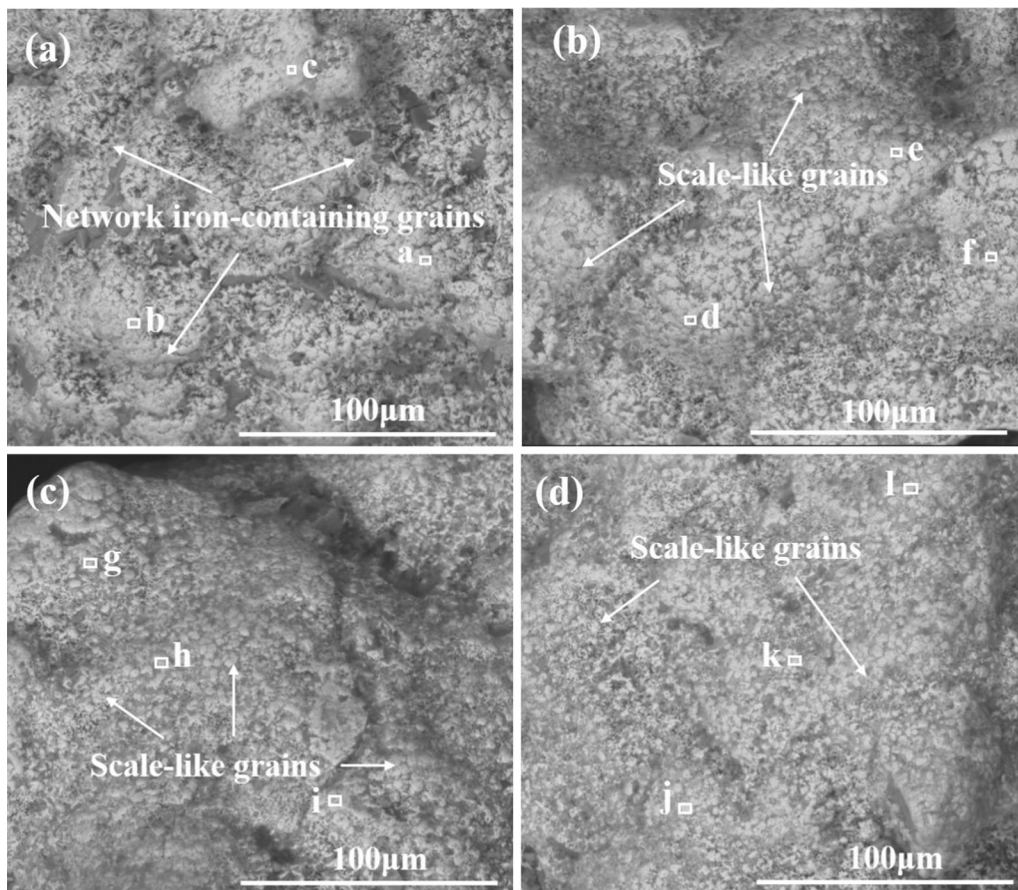


Fig. 11—Surface morphology of reduced Sample B with different amount of MgO under SEM: (a) 0.25 wt pct; (b) 0.50 wt pct; (c) 1.00 wt pct; (d) 1.50 wt pct.

beneficial for the fluidization behavior. It should be noted that, in Figure 7, de-fluidization starts or ends at RD equals 100 pct, which means that no de-fluidization or completed de-fluidization occur. At 600 °C, the Sample B shows a completed fluidization state. Therefore, the start de-fluidization point of Sample B at 600 °C is set as 100 pct. At higher reduction temperature, it is not sufficient to ensure a stable fluidization by only prior oxidation treatment. MgO is a typical and effective additive that can be used preventing the de-fluidization phenomenon.^[23–26] Therefore, the effect of MgO on the fluidization behavior is discussed afterwards.

Figure 8 shows the surface morphology of Sample A after reduction at different temperatures. It can be seen that more and larger cracks appear on the particle surfaces with increasing reduction temperature. Although a crack formation occurs, the particles after reduction still have a dense structure. As shown in Figure 8(f), when reduction temperature is higher than 650 °C, typical iron shells around the particles are formed and fewer pores exist in the remaining wüstite core. The de-fluidization of the Sample A happens due to the sticky precipitated iron shell. When the newly formed iron aggregates to certain content on the particle surface and iron shells are formed, the de-fluidization starts.^[21,35]

As shown in Figure 9, no cracks occur in Sample B after reduction. The pre-oxidation treatment promotes the formation of a porous structure during reduction, as shown in Figure 9(f). The porous structure does not only improve the reducibility, but also avoids the exclusive formation of metallic iron on the particle surface, thus decreasing the de-fluidization tendency. The iron is uniformly distributed in the whole particle area and the remaining wüstite can be also found throughout the whole particle. The formation of iron whiskers on the surface of the particles can be observed in Figures 9(a) through (e). The whisker usually occurred during the reduction from wüstite to iron.^[36] With increasing temperature, the iron whiskers become bigger and the whisker area expands. No precipitated iron shell, covering the particles, can be found in the particles of Sample B. Hence, the iron whiskers play an important role influencing the fluidization behavior during reduction. The whiskers can act as hooks between the particles, as it can be observed in Figure 9(e). The friction between the particles can be increased by the whiskers during fluidization, which requires a higher exertion force of the fluidization gas on the particles in order to break the newly formed connections. If the friction between the particles becomes too big, fluidization might be not possible anymore at given process conditions. The friction

Table V. EDS Analysis With Different MgO Contents

	0.25 Wt Pct Point a, b, c	0.50 Wt Pct Point d, e, f	1.00 Wt Pct Point g, h, i	1.50 Wt Pct Point j, k, l
Fe, At. Pct	69.19 ± 3.02	63.40 ± 3.33	59.81 ± 3.55	53.38 ± 3.83
Mg, At. Pct	11.39 ± 1.05	14.66 ± 1.23	16.61 ± 0.91	22.41 ± 2.42
O, At. Pct	19.41 ± 3.99	21.93 ± 3.24	23.57 ± 2.84	24.19 ± 5.55

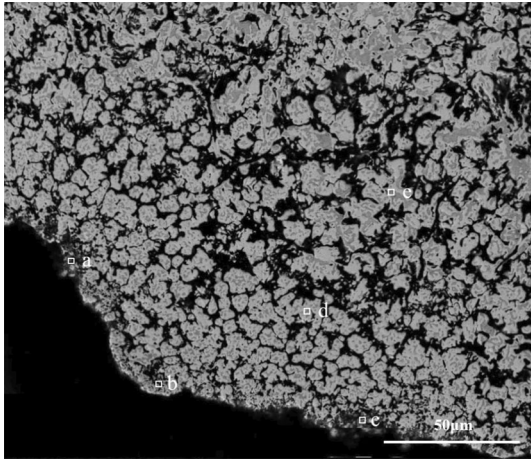


Fig. 12—Polished cross-section of Sample B with 1.5 wt pct MgO after reduction under SEM.

Table VI. EDS Analysis of Sample B With 1.5 Wt Pct MgO After Reduction

	Point a	Point b	Point c	Point d	Point e
Fe, At. Pct	58.49	65.52	40.08	65.33	58.45
Mg, At. Pct	7.13	7.11	25.28	0	0
O, At. Pct	34.38	27.37	34.66	34.67	41.55

becomes higher in case of a large quantity of such iron whiskers. That is why higher reduction degrees are required for Sample B to become de-fluidized.

B. Effect of MgO-Addition on the Fluidization and Reduction Behaviors of Deep Oxidized Magnetite Iron Ore

The effect of MgO-addition on the fluidization state and reducibility of Sample B was examined. The MgO powder was mixed with the oxidized magnetite-based iron ore before the reduction tests, which were conducted at 700 °C. It can be seen in Table IV that if an MgO amount of 0.25 wt pct is added, a partial de-fluidization occurs, with around 15 pct of the material not fluidized according to the DFI. De-fluidization can be avoided when the addition amount of MgO is higher than 0.25 wt pct. To demonstrate the influence of MgO on the reduction behavior, the relation between RD and MgO-content is shown in Figure 10. With an increasing

amount of MgO, the reduction degree curves in Figure 10(a), moving slightly toward lower reduction times. It should be noted that with no and with 0.25 wt pct MgO-addition, de-fluidization starts after a reduction time of 380 s and 500 s, respectively. But only for the reduction tests without de-fluidization, the reduction degree and reduction rate are discussed and compared. Figure 10(b) shows the reduction rate for different values of MgO addition. The reduction rate can be divided into three stages (I, II, and III). Stage I is regarded as the fast reduction from Fe₂O₃ to Fe₃O₄. From Figure 10(d), it can be seen that samples with a higher amount of MgO exhibit a slightly higher reduction rate in Stage I. Combined with Figure 10(c), it seems that the MgO mainly has a promotion effect in Stage I. However, at further reduction, the reduction rate lines intertwine in Stages II and III and show no obvious pattern. The results are consistent with the previous researches from Muhammad^[37] and Srinivas^[38] that the addition of MgO could improve the reduction of Fe₂O₃. However, through molecular dynamics simulation, it is easier for Mg²⁺ to migrate to vacancy than Fe²⁺ in wüstite (Fe_xO).^[39] Therefore, magnesiowüstite (Fe_xMg_{1-x}O) is formed, which inhibits the reduction of wüstite. The similar phenomenon is also found in the reduction of pure hematite doped with MgO using CO.^[40] El-Geassy^[40] studied the influence of MgO on the stepwise reduction of pure hematite compacts. He found that in the hematite-magnetite reduction step the promotion effect occurred in the early stage because of an increase in porosity and an increase in active sites owing to the foreign cations into Fe₂O₃ lattice. At later stages, the formation of phase MgO-Fe₂O₃ with low reducibility retarded the reduction of Fe₂O₃. In the magnetite-wüstite and wüstite-iron reduction steps, the decreases in reduction rate was attributed to the formation of magnesiowüstite. In the present study, the final reduction degrees after 6000 seconds reduction time are listed in Table IV. Although Sample B with 0.25 wt pct MgO-addition became partially de-fluidized, the final RD was as high as 91.37 pct. Generally, the addition of MgO shows a promotion effect on the reduction rate.

After reduction at 700 °C, as shown in Figure 11, the surface of particles of the samples doped with different amounts of MgO have quite a smooth structure. The formation of iron whiskers cannot be observed, explaining the stable fluidization during the whole reduction procedure. Three EDS spots were conducted on every particle to obtain the composition of the surface region of the particles. The average result of element contents,

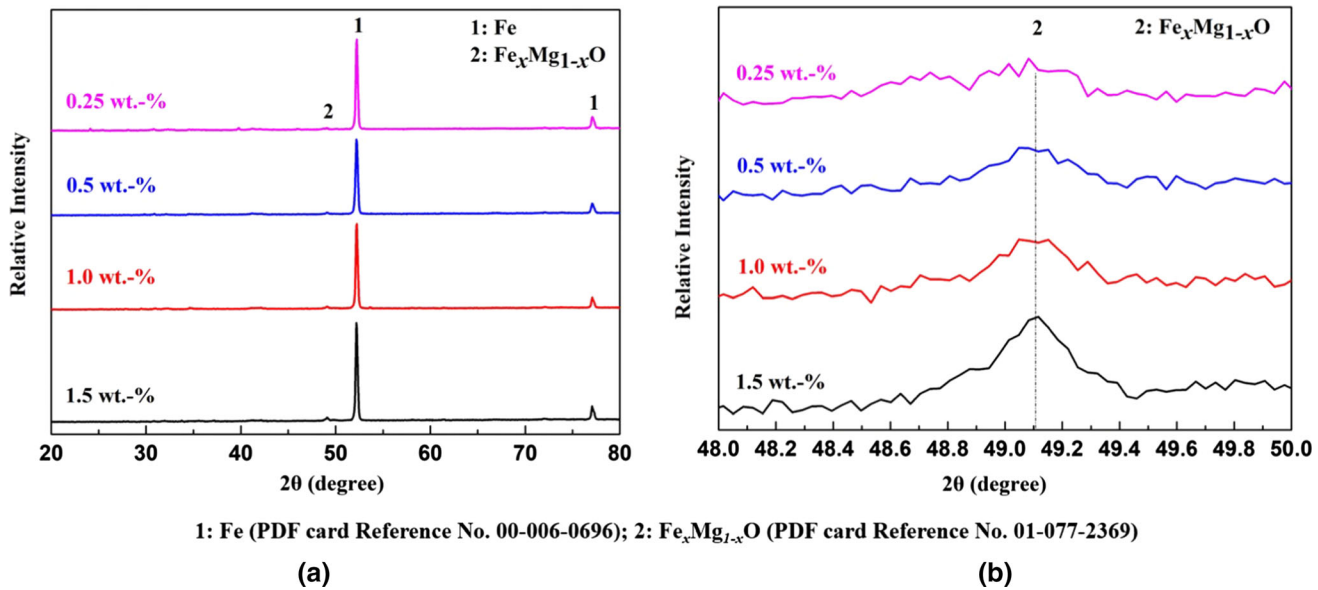


Fig. 13—XRD patterns of reduced Sample B with different amount of MgO: (a) scanning angle (2θ) ranges from 20 to 80 deg; (b) enlarged scanning angle (2θ) between 48 and 50 deg.

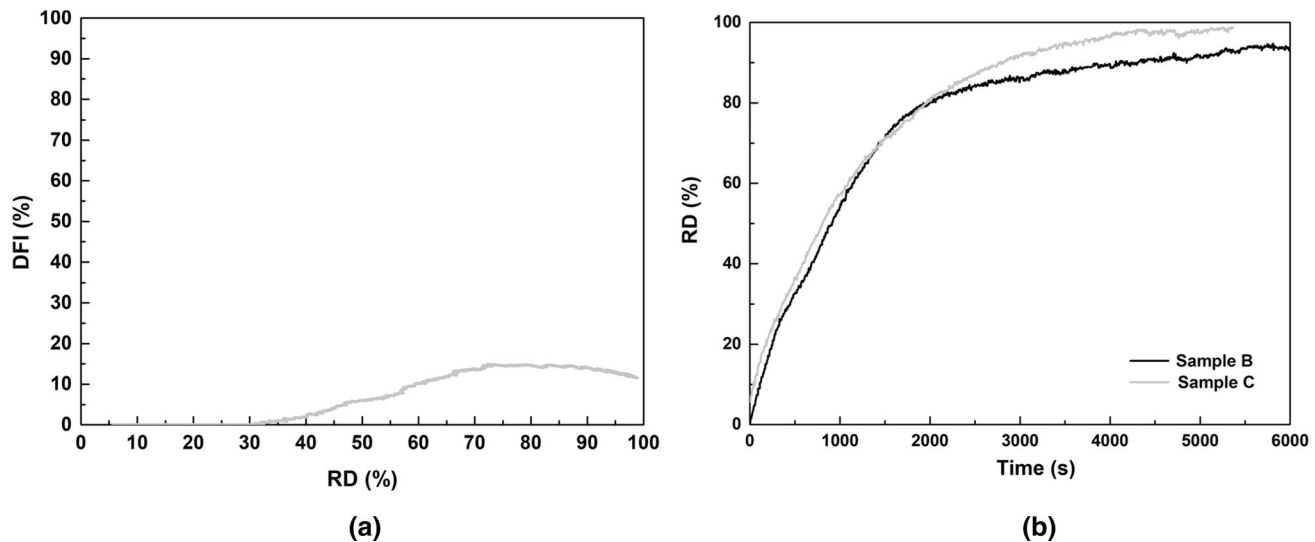


Fig. 14—Fluidization and reduction behaviors of Sample B and Sample C With 0.5 wt pct MgO addition: (a) DFI of Sample C; (b) reduction degree.

given in at. pct, are listed in Table V. The EDS analysis shows that the particle surface contains Fe, Mg, and O, indicating that the compound on the surface is composed of oxides and metallic iron. It is found that with the additional amount of MgO, the Mg element on the particle surface increases. In a similar way, the oxygen content increases. The particle surface is covered by scale-like iron-containing grains. If 0.25 wt pct MgO was added, the grains showed a better connection with each other, forming a network structure. With the increased content of MgO, the grains became smaller. Therefore, these scale-like grains are regarded as a critical structure. The total area of the grains can be treated as an effective sticking area during fluidization. MgO prevents the growth of such grain structures by

hindering lattice expansion during the oxide reduction and slowed down the diffusion rate of iron ions,^[41] which results in decreasing the contact chance of the sticky surface.

Figure 12 shows a polished cross section of Sample B with 1.5 wt pct MgO after reduction. The element contents of the particle from the edge to the inside is shown in Table VI. The Mg element was distributed around a seam at the particle surface, which indicates that effect of MgO is mainly exerted on the surface of the particles. No Mg element is observed inside the particle. The high content of the element O inside the particle was caused by the preparation of the samples. The re-oxidation of iron may occur during mounting and polishing procedures.

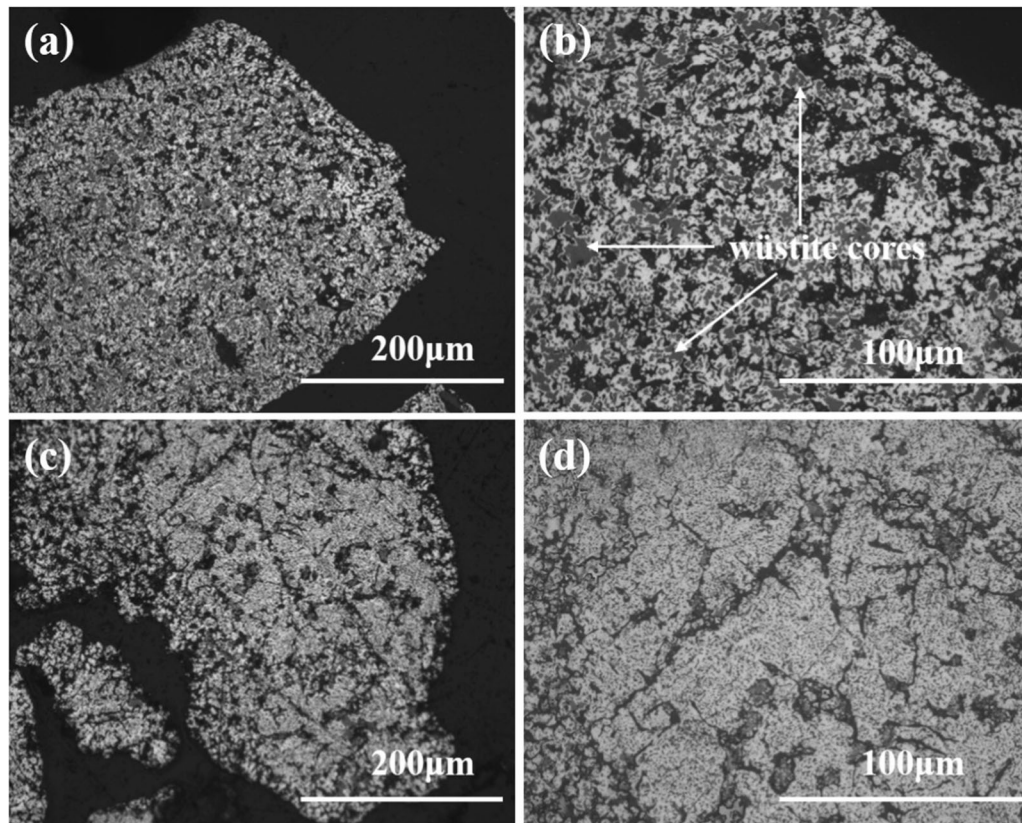


Fig. 15—Polished section images of the Sample B and Sample C after reduction tests at 700 °C with 0.5 wt pct MgO addition under optical light microscope: (a), (b) Sample B; (c), (d) Sample C.

Figure 13 shows the XRD results of the reduced Sample B with different amounts of MgO-addition. It can be seen from Figure 13(a), the main phases of the reduced samples are metallic iron. As shown in Figure 13(b), due to the low amount, the peak intensities of magnesiowüstite ($\text{Fe}_x\text{Mg}_{1-x}\text{O}$) phase are quite small compared with that of iron but increases with the addition amounts of MgO. MgO can be completely dissolved into FeO and form a continuous solid solution.^[42,43] The iron whiskers generally grow on the wüstite during the reduction.^[36,44] The formation of magnesiowüstite phase inhibits the further reduction of wüstite at the particle surface, thus prevents the formation of iron whiskers and scale-like iron-containing grains.

C. Effect of Prior Partial Oxidation on the Fluidization and Reduction Behavior of Magnetite Iron Ore

Considering the low reaction rate in the final stage of reduction, as discussed in Section III-A, the improvement by replacing deep oxidation to partial oxidation treatment is discussed. Figure 14 shows the DFI and RD curves of the reduction tests at 700 °C with 0.5 wt pct MgO addition for Sample B and Sample C. As shown in Figure 14(a), with prior partial oxidation treatment and 0.5 wt pct MgO addition, only about 10 pct material becomes de-fluidized. Figure 14(b) compares the reduction process of the Sample B (completed fluidized) and the Sample C (~ 10 pct de-fluidization).

The reduction behavior Sample C is similar to that of Sample B until RD equals ~ 80 pct and shows a higher reduction rate during the final stage of reduction. As a result, it takes less time for Sample C to get nearly complete reduced.

Figure 15 shows the polished section images of the Sample B and Sample C after reduction tests at 700 °C with 0.5 wt pct MgO addition. For Sample B, small wüstite cores, which are covered by iron shells, can be observed inside the particles. The shells avoid the reducing gas diffuse into the particles resulting in a low reduction rate at the final stage. While the particles of Sample C were nearly completely reduced and no obvious wüstite cores can be found, which explained why Sample C shows higher reduction rate at final stage. Kinetic analyses should explain the reason for the differences.

D. Multistep Kinetic Analysis

The fluidization behavior of the raw magnetite-based iron ore is improved significantly by the prior oxidation treatment and the addition of MgO. As discussed above, it seems that MgO promotes the initial reaction and prior partial oxidation treatment shows more beneficial reduction rates compared to a prior deep oxidation treatment. In order to investigate the mechanism behind, a multistep kinetic analysis is carried out based on the model, developed by Johnson–Mehl–Avrami.^[45–48]

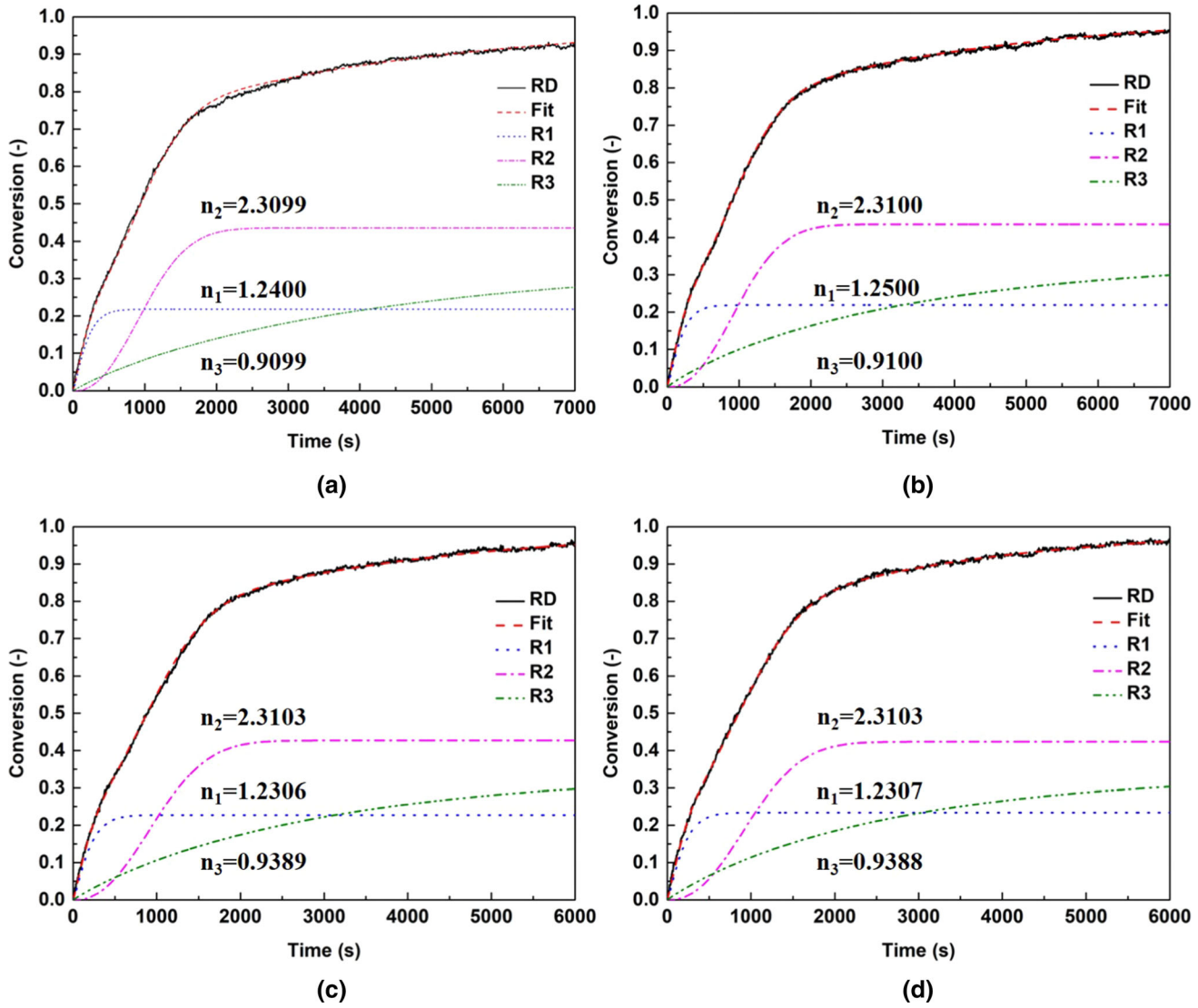


Fig. 16—Fitting results for Sample B with different amount of MgO: (a) 0.25 wt pct; (b) 0.5 wt pct; (c) 1.0 wt pct; (d) 1.5 wt pct.

Table VII. Kinetic Analysis for Sample B With Different Amount of MgO

		MgO Addition			
		0.25 Wt Pct	0.5 Wt Pct	1.0 Wt Pct	1.5 Wt Pct
Weight Factors	w_1	0.2180	0.2190	0.2273	0.2340
	w_2	0.4361	0.4356	0.4268	0.4235
	w_3	0.3459	0.3454	0.3459	0.3425
Nucleation Rate Constants (s^{-1})	a_1	0.0013	0.0013	0.0014	0.0014
	a_2	8.40×10^{-8}	8.40×10^{-8}	8.40×10^{-8}	8.40×10^{-8}
	a_3	5.12×10^{-4}	6.37×10^{-4}	5.60×10^{-4}	6.18×10^{-4}
Kinetic Exponents	n_1	1.2400	1.2500	1.2306	1.2307
	n_2	2.3099	2.3100	2.3103	2.3103
	n_3	0.9099	0.9100	0.9389	0.9388
Root Mean Square Deviation	RMSD	0.0072	0.0050	0.0050	0.0046

The parallel reaction process can be defined as shown in Eq. [6]. The root mean square deviation (RMSD) is used to assess the fitting procedure—the smaller RMSD, the better the fitting result.^[8,10]

$$x_t = w_1(1 - e^{-a_1 t^{n_1}}) + w_2(1 - e^{-a_2 t^{n_2}}) + w_3(1 - e^{-a_3 t^{n_3}}), \quad [6]$$

where $w_{1,2,3}$ are the weight factors representing the relative importance of the resulting rate limiting mechanism; $a_{1,2,3}$ are the nucleation rate constants; $n_{1,2,3}$ are the kinetic exponents which can be linked to the occurring rate-limiting mechanism. If $n < 1$, the rate-limiting step is considered to be diffusion controlled; If n is close to 1, the reaction mechanism belongs to the reaction kinetics; If $n > 1.5$ the reaction is controlled by the nucleation process. Based on the definition of reduction degree (RD), the Fe_2O_3 , Fe_3O_4 , FeO and Fe exhibit the RDs of 0, 11.1 pct, 33.3 pct and 100 pct, respectively. A similar kinetics analysis procedure was used by Chen *et al.*[49] and Monazam *et al.*[50] for the reduction of Fe_2O_3 to Fe by CO and CH_4 , respectively, where w was fixed to a certain RD or n was fixed to a certain rate limiting mechanism. In the present study, both w and n were not fixed to a specific value to be able to analyze if more than one rate limiting step acts together in parallel.^[8,10]

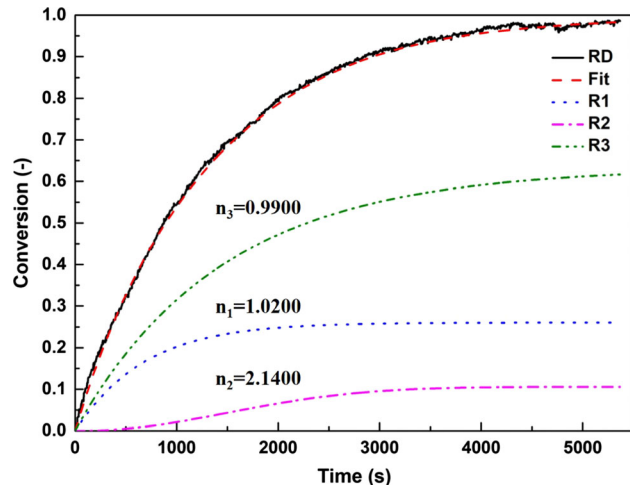


Fig. 17—Fitting results for Sample C with 0.5 wt pct MgO addition.

Table VIII. Kinetic Analysis for Sample C with 0.5 Wt Pct MgO-Addition

Partly Oxidized Magnetite Iron Ore with 0.5 wt pct MgO Addition						RMSD
w_1	0.2608	a_1	1.31×10^{-3}	n_1	1.0200	0.0081
w_2	0.1060	a_2	8.41×10^{-8}	n_2	2.1400	
w_3	0.6332	a_3	7.38×10^{-4}	n_3	0.9900	

1. Deep Oxidized Magnetite-Based Iron Ore with Different Amounts of MgO-Addition

Figure 16 shows the fitting results for Sample B with different amounts of MgO-addition, where R1, R2 and R3 represent chemical reaction, nucleation and diffusion respectively. It should be noticed that in case of 0.25 wt pct MgO addition, around 10 pct of the material was not fluidized. The results fit very well to the experimental data as shown by the low RMSD values in Table VII. It can be seen that the reaction process R1 dominates the initial portion of the total RD. Hence, R1 will have little influence on the later reduction stage. In terms of long-time reaction processes, the total RD is dominated by R2 and R3. The values of w_1 slightly increase with the amount of MgO-addition, representing the promotion effect of the reaction in the initial stage. The values of w_2 and w_3 show a small decline trends but keep quite stable. In general, the amount of MgO has little influence on the reaction mechanisms. The parallel reaction processes can be described as follows. More than one rate limiting step acts together in parallel in each reduction stage. The fast-chemical reaction dominates the initial reduction stage, where the Fe_2O_3 is reduced into Fe_3O_4 . While nucleation and diffusion rule the middle reduction stage, but nucleation is in a dominant position. The reduction from Fe_3O_4 to FeO is mainly controlled by nucleation. After an incubation time for the nucleation of metallic iron, in the later reaction, nucleation is not important anymore. The diffusion becomes the reaction limiting step, which is in good agreement with Figures 15(a) and (b), where small remaining wüstite cores are cover by dense iron shells.

2. Partly oxidized magnetite-based iron ore with 0.5 wt pct MgO addition

Figure 17 shows the fitting result of partly Sample C with 0.5 wt pct MgO-addition. The reaction mechanism experienced a significant change comparing with that of Sample B (Figure 16(b)). It can be seen that the reaction process R3 and R1 dominate the total RD, especially in the initial stage. Since n_3 and n_1 are close to 1, the reaction process R3 and R1 are both considered to be chemical reaction. Hence, diffusion is not the limiting step anymore, which is in good agreement with the Figures 15(c) and (d), where nearly no small unreacted wüstite cores can be found. The reaction is mainly controlled by the chemical reaction, also at the later stage. In the middle reduction stage, nucleation still plays the limiting role but not as big as that in Sample B. Table VIII shows the kinetic analysis result. Compared with Sample B, the value of w_1 and w_3 are much higher, representing that the prior partial oxidation promotes both the diffusion and the chemical reaction.

IV. CONCLUSIONS

The purpose of this research work is to use magnetite-based iron ore directly for hydrogen-induced fluidized bed reduction and examine methods preventing de-fluidization. The effect of a prior oxidation treatment is discussed and the MgO is examined to prevent de-fluidization. The following conclusions are obtained:

- (1) The raw magnetite-based iron ore without pretreatment could not be successful fluidized during the reduction experiments. The newly formed metallic iron agglomerated on the surface of the magnetite particle and an iron shell is formed surrounding a dense wüstite core. At 600 °C, de-fluidization could be avoided by a prior deep oxidation treatment. After oxidation, the phase structure during reduction became porous. This porous structure allows the reducing gas to penetrate into the particle resulting in a higher reduction rate until certain degrees of reduction and decreasing the aggregation of metallic iron on the surface.
- (2) At a higher reduction temperature, the inhibition effect of prior deep oxidation was reduced. An addition of at least 0.5 wt pct MgO was required to maintain complete fluidization. After reduction, the particle surface of the sample doped with MgO shows a quite smooth structure instead of whiskers. The formation of magnesiowüstite ($\text{Fe}_x\text{Mg}_{1-x}\text{O}$) phase inhibits the further reduction of wüstite at the particle surface, thus prevents the formation of iron whiskers and the growth of scale-like iron-containing grains on the particle surface.
- (3) Although the fluidization state was improved by deep prior oxidation treatment, the reduction rate dramatically decreased in the final reduction period because of the unreacted wüstite cores inside the particles. This problem could be improved *via* replacing prior deep oxidation by a partial oxidation treatment. These two kinds of samples have similar reduction behaviors until RDs approximate 80 pct, the partly oxidized sample showed higher reduction rates during the final stage of reduction. As a result, it takes less time to get a nearly complete reduction. The optimum pretreatment for magnetite-based iron ore during hydrogen-induced fluidized bed reduction is considered to be a prior partial oxidation combined with an addition of MgO. The prior oxidation temperature may also influence the reduction behaviors, which will be investigated in the future work.
- (4) MgO could promote the initial reaction because of an increase in active sites owing to the Mg^{2+} cations into Fe_2O_3 lattice. At later reduction stages, the formation of magnesiowüstite slows down the reduction rate. Generally, in the present experimental conditions, the addition of MgO shows a

promotion effect on the reduction rate. For deep oxidized sample, the amount of MgO addition has little influence on the occurring rate-limiting mechanisms. The chemical reaction dominates the initial reaction. The diffusion becomes the reaction limiting step in the final stage. The occurring rate-limiting mechanisms of the partly oxidized sample are totally different compared to the deep oxidized sample. The chemical reaction dominates the reduction process. The reaction rate limiting step is no longer diffusion but chemical reaction.

ACKNOWLEDGMENTS

The authors gratefully acknowledge the funding support of K1-MET GmbH, metallurgical competence center. The research program of the K1-MET competence center is supported by COMET (Competence Center for Excellent Technologies), the Austrian program for competence centers. COMET is funded by the Federal Ministry for Climate Action, Environment, Energy, Mobility, Innovation and Technology, the Federal Ministry for Digital and Economic Affairs, the provinces of Upper Austria, Tyrol and Styria and the Styrian Business Promotion Agency (SFG). In addition, the research work is partially financed by Montanuniversität Leoben. Zheng Heng greatly acknowledges the financial support from the program of China Scholarship Council (No.201908420284).

FUNDING

Open access funding provided by Montanuniversität Leoben.

OPEN ACCESS

This article is licensed under a Creative Commons Attribution 4.0 International License, which permits use, sharing, adaptation, distribution and reproduction in any medium or format, as long as you give appropriate credit to the original author(s) and the source, provide a link to the Creative Commons licence, and indicate if changes were made. The images or other third party material in this article are included in the article's Creative Commons licence, unless indicated otherwise in a credit line to the material. If material is not included in the article's Creative Commons licence and your intended use is not permitted by statutory regulation or exceeds the permitted use, you will need to obtain permission directly from the copyright holder. To view a copy of this licence, visit <http://creativecommons.org/licenses/by/4.0/>.

REFERENCES

1. K. He and L. Wang: *Renew. Sustain. Energy Rev.*, 2017, vol. 70, pp. 1022–39.
2. World Steel Association: Climate change mitigation, <https://www.worldsteel.org/publications/fact-sheets.html>. Accessed 22 October 2020.
3. European Commission: 2050 long-term strategy, https://ec.europa.eu/clima/policies/strategies/2050_en. Accessed 30 October 2020.
4. Material Economics: Industrial transformation 2050 - pathways to net-zero emissions from EU heavy industry, 2019, pp. 68–75 <https://media.sitra.fi/2019/05/30150529/industrial-transformation-2050.pdf>. Accessed 30 October 2020.
5. Columbia Climate Center: Mitigating iron and steel emissions, <https://www.yumpu.com/en/document/read/8268353/mitigating-iron-and-steel-emissions>, Accessed 30 October 2020.
6. J. Rissman, C. Bataille, E. Masanet, N. Aden, W.R. Morrow, III, N. Zhou, N. Elliott, R. Dell, N. Heeren, and B. Huckestein: *Appl. Energy*, 2020, vol. 266, art. no. 114848.
7. B. Stelter, R. Haslehner, and N. Osio: Steel as a Model for a Sustainable Metal Industry in 2050, <https://www.bcg.com/publications/2015/metals-mining-sustainability-steel-as-a-model-for-a-sustainable-metal-industry-in-2050>. Accessed 30 October 2020.
8. D. Spreitzer and J. Schenk: *Metall. Mater. Trans. B*, 2019, vol. 50B, pp. 2471–94.
9. J. Schenk: *Particuology*, 2011, vol. 9, pp. 14–23.
10. D. Spreitzer and J. Schenk: *Particuology*, 2020, vol. 52, pp. 36–46.
11. E. Park and O. Ostrovski: *ISIJ Int.*, 2004, vol. 44, pp. 74–81.
12. E. Park and O. Ostrovski: *ISIJ Int.*, 2004, vol. 44, pp. 999–1005.
13. Z.Y. Wang, J.L. Zhang, K.X. Jiao, Z.J. Liu, and M. Barati: *J. Alloy. Compd.*, 2017, vol. 729, pp. 874–83.
14. B. Zhang, X.Z. Gong, Z. Wang, and Z.C. Guo: *ISIJ Int.*, 2011, vol. 51, pp. 1403–09.
15. H.J. Shao, Z.C. Guo, and H.Q. Tang: *ISIJ Int.*, 2011, vol. 51, pp. 1290–95.
16. Y.W. Zhong, Z. Wang, Z. Guo, and Q. Tang: *Powder Technol.*, 2012, vol. 230, pp. 225–31.
17. Y.W. Zhong, J.T. Gao, Z. Wang, and Z.C. Guo: *ISIJ Int.*, 2017, vol. 57, pp. 649–55.
18. X.Z. Gong, B. Zhang, Z. Wang, and Z.C. Guo: *Metall. Mater. Trans. B*, 2019, vol. 50B, pp. 2471–94.
19. F. Lu, L.Y. Wen, X. Han, W.H. Jiang, H.M. Duan, J. Xu, and S.F. Zhang: *J. Iron. Steel Res. Int.*, 2019, vol. 26, pp. 829–37.
20. Z. Du, Q.S. Zhu, C.L. Fan, F. Pan, H.Z. Li, and Z.H. Xie: *Steel Res. Int.*, 2016, vol. 87, pp. 789–97.
21. L. Guo, H. Gao, J.T. Yu, Z.L. Zhang, Z.C. Guo: *Int. J. Miner. Metall. Mater.*, 2015, vol. 22, pp. 12–20.
22. Y.W. Zhong, Z. Wang, Z.C. Guo, and Q. Tang: *Powder Technol.*, 2013, vol. 241, pp. 142–48.
23. H.J. Shao, Z.C. Guo, and H. Tang: *Steel Res. Int.*, 2013, vol. 84, pp. 111–18.
24. L. Guo, J. Tang, H. Tang, Z.C. Guo: *Mater. Today: Proc.*, vol. 2, pp. S332–S341.
25. L. Guo, Y.W. Zhong, J.T. Gao, Z.R. Yang, and Z.C. Guo: *Powder Technol.*, 2015, vol. 284, pp. 210–17.
26. Z. Du, Q.S. Zhu, Y.F. Yang, C.L. Fan, F. Pan, H.Y. Sun, and Z.H. Xie: *Steel Res. Int.*, 2016, vol. 87, pp. 1742–49.
27. L. Guo, Q.P. Bao, J.T. Gao, Q.S. Zhu, and Z.C. Guo: *ISIJ Int.*, 2020, vol. 60, pp. 1–17.
28. A. Pichler, H. Mali, F. Plaul, J. Schenk, M. Skorianz, and B. Weiss: *Steel Res. Int.*, 2016, vol. 87, pp. 642–52.
29. M. Skorianz, H. Mali, A. Pichler, F. Plaul, J. Schenk, and B. Weiss: *Steel Res. Int.*, 2016, vol. 87, pp. 633–41.
30. D. Spreitzer: Development of characterization methods for the evaluation of kinetic behavior and the fluidization of iron ore fines during hydrogen-induced fluidized bed reduction, Montanuniversitaet Leoben, PhD thesis, unpublished research, 2020.
31. A.A. Adetoro, H.Y. Sun, S.Y. He, Q.S. Zhu, and H.Z. Li: *Metall. Mater. Trans. B*, 2018, vol. 49B, pp. 846–57.
32. K.S. Zhu, Y.L. Fu: *J. Anhui Univ. Technol. (Natural Science)*, 1992, pp. 21–25.
33. S. Hayashi, S. Sawai, and Y. Iguchi: *ISIJ Int.*, 1993, vol. 33, pp. 1078–87.
34. Z.Y. Zhong, Z. Wang, Z. Guo, and Q. Tang: *Powder Technol.*, 2014, vol. 256, pp. 13–19.
35. YW Zhong, XZ Gong, Z Wang, and ZC Guo: *J. Univ. Sci. Technol. Beijing*, 2011, vol. 33, pp. 406–12.
36. R. Nicolle and A. Rist: *Metall. Mater. Trans. B*, 1979, vol. 10B, pp. 429–38.
37. M.I.A. Barustan and S.M. Jung: *Met. Mater. Int.*, 2019, vol. 25, pp. 1083–97.
38. S. Dwarapudi, T.K. Ghosh, V. Tathavadkar, and M.B. Denys: *Int. J. Miner. Process.*, 2012, vols. 112–113, pp. 55–62.
39. J.L. Li: Study on the surface morphology and the growth of iron crystal in the fluidized reduction process, Chongqing University, Master thesis, 2017.
40. A.A.El-Geassy: *Ironmaking Steelmaking*, 1999, vol. 26, pp. 41–52.
41. K.S.A. Halim, M. Bahgat, H.A. El-Kelesh, and M.I. Nasr: *Ironmak. Steelmak.*, 2009, vol. 36, pp. 631–40.
42. I. Strandkvist, A. Sandstrom, and F. Engstrom: *Steel Res. Int.*, 2017, vol. 88, p. 1600322.
43. K. Narita, M. Maekawa, I. Shigaki, and Y. Seki: *Tetsu to Hagane*, 1977, vol. 10, pp. 1623–32.
44. L. Guo, Q.P. Bao, J.T. Gao, Q.S. Zhu, and Z.C. Guo: *ISIJ Int.*, 2020, vol. 60, pp. 1–17.
45. W.A. Johnson and R.F. Mehl: *Trans. Am. Inst. Min. Metall. Eng.*, 1940, vol. 135, pp. 416–42.
46. M.P. Avrami: *J. Chem. Phys.*, 1939, vol. 7, pp. 1103–12.
47. M.P. Avrami: *J. Chem. Phys.*, 1940, vol. 8, pp. 212–24.
48. M.P. Avrami: *J. Chem. Phys.*, 1941, vol. 9, pp. 177–84.

Publisher's Note Springer Nature remains neutral with regard to jurisdictional claims in published maps and institutional affiliations.

Fluidization behavior and reduction kinetics of pre-oxidized magnetite-based iron ore in a hydrogen-induced fluidized bed

Heng Zheng^{1),✉}, Oday Daghagheleh¹⁾, Thomas Wolfinger²⁾, Bernd Taferner¹⁾, Johannes Schenk^{1,2)}, and Runsheng Xu³⁾

1) Chair of Ferrous Metallurgy, Montanuniversitaet Leoben, Franz-Josef-Straße 18, 8700, Leoben, Austria

2) K1-MET GmbH, Stahlstraße 14, 4020 Linz, Austria

3) The State Key Laboratory of Advanced Metallurgy, University of Science and Technology Beijing, Beijing 100083, China

(Received: 28 January 2022; revised: 25 April 2022; accepted: 28 April 2022)

Abstract: The influence of different pre-oxidation temperatures and pre-oxidation degrees on the reduction and fluidization behaviors of magnetite-based iron ore was investigated in a hydrogen-induced fluidized bed. The raw magnetite-based iron ore was pre-oxidized at 800 and 1000°C for a certain time to reach a partly oxidation and deeply oxidation state. The structure and morphology of the reduced particles were analyzed via optical microscope and scanning electron microscopy (SEM). The reaction kinetic mechanism was determined based on the double-logarithm analysis. The results indicate that the materials with higher oxidation temperature and wider particle size range show better fluidization behaviors. The lower oxidation temperature is more beneficial for the reduction rate, especially in the later reduction stage. The pre-oxidation degree shows no obvious influence on the fluidization and reduction behaviors. Based on the kinetic analysis, the reduction progress can be divided into three stages. The reduction mechanism was discussed combining the surface morphology and phase structure.

Keywords: magnetite-based iron ore; prior oxidation; fluidization behavior; kinetic analysis; hydrogen reduction

1. Introduction

The European Union (EU) aims to reach the goal of climate neutrality (net-zero greenhouse gas emissions) by 2050 [1]. It is noticed that, nowadays, about 60% of the crude steel from Europe is produced through the blast furnace-basic oxygen furnace (BF-BOF) route [2]. The BF-BOF route has a high production efficiency but produces more CO₂ per ton of crude steel than other alternative steelmaking routes. Currently, steelmaking industry is still one of the major CO₂ emission sectors in Europe, which emits 4% of the EU's total CO₂ emissions [3]. The breakthrough technologies are required to further cut down CO₂ emissions [1,4–5]. Already, different alternative steelmaking processes have been investigated under the European Ultra Low CO₂ Steelmaking (ULCOS) program [4–5]. One of the interesting topics is using hydrogen as a reducing agent instead of CO [6–11]. Hence no CO₂ will be generated during the reduction of iron oxides. There are some promising related projects in the EU [12], such as HYBRIT in Sweden [13], SALCOS in Germany [14], and SuSteel and HYFOR[®] in Austria [15].

Direct reduction of iron ore fines receives increasing attention in ore-based ironmaking. The fluidized bed technology provides a possibility to produce direct reduced iron (DRI) with H₂ and iron ore fines [16]. A pre-heating system

for the iron ore is required when using hydrogen as the reducing agent due to the endothermic reaction. It is also difficult to process all types of iron oxides in the form of iron ore fines. In the case of magnetite-based iron ore, the pre-heating can be done via a gas with a remaining amount of oxygen to utilize the exothermic oxidation reaction from Fe₃O₄ to Fe₂O₃. Based on our previous work [17–20], in an H₂-induced fluidized bed reactor, the magnetite-based iron ore showed the lowest reducibility and the worst fluidization behaviors due to the formation of a dense iron shell on the particle surface. Though, the same amount of the generated energy due to the oxidation is needed for the reduction afterwards, the pre-oxidation treatment improves the reduction efficiency and fluidization behaviors significantly. Some other researchers studied the influence of the pre-oxidation treatment using thermogravimetric analyzers. Based on the research from Wolfinger *et al.* [21], Park and Ostrovski [22], and Wang *et al.* [23], the reducibility was also greatly enhanced due to the structural transformation from dense to porous phase, and the diffusion was not the rate-limiting step due to the formation of micro-cracks.

However, the above studies mainly focused on the reduction and fluidization behavior under various reducing conditions. Little attention has been given to the pre-oxidation treatment process. Furthermore, the influences of different

✉ Corresponding author: Heng Zheng E-mail: heng.zheng@stud.unileoben.ac.at

© The Author(s) 2022

pre-oxidation temperatures and pre-oxidation degree on the reducibility of magnetite-based iron ores are rarely discussed. The scope of this work is to study the effect of different pre-oxidation treatments, i.e., different pre-oxidation temperatures and pre-oxidation degrees, on the fluidization behaviors, morphology, and thus reduction kinetics using hydrogen as reducing agent. The structure and morphology of the reduced particles were analyzed via optical microscope and scanning electron microscopy (SEM). The reaction kinetic mechanism was determined based on the double-logarithm analysis. This work will provide preliminary guidance for the performance optimization in a possible novel industrial-scale direct reduction process.

2. Experimental

2.1. Preparation of the oxidized material

In this work, a low-grade magnetite-based iron ore was used as the raw material. The chemical composition was characterized by the inductively coupled plasma-mass spectrometry (ICP-MS) method and is listed in Table 1. The MgO powder (>99.5wt% MgO, size below 44 μm) with high purity was used as anti-sticking agent during the experiments. The raw material was divided into three particle size ranges: 125–250 μm , 250–500 μm , and full size. The full size was achieved by mixing 50wt% of 125–250 μm and 50wt% of 250–500 μm . It should be noted that the particle size was defined by conventional dry sieving. For a pre-oxidation treatment, 1000 g of the raw material was charged into a 250 mm \times 350 mm steel vessel and put into a conventional heat treatment furnace at 800 and 1000°C for a defined oxid-

Table 1. Chemical composition of the sample wt%

Sample	Fe _{tot}	FeO	SiO ₂	Al ₂ O ₃	CaO	MgO	MnO	P
Raw magnetite	59.50	19.66	7.05	1.13	3.03	2.00	0.17	0.70

Note: Fe_{tot}—Total iron content.

ation time to reach a so-called deeply oxidation and partly oxidation. The bed height of the material layer was around 2.5 mm, ensuring a uniform contact between gas and solid. Based on the previous study [20], the raw magnetite-based iron ore could not maintain completed fluidized at 700°C reducing conditions. A deeply oxidation treatment and an addition of 0.5wt% MgO powder improved the fluidization significantly. Therefore, 7 different pre-oxidized materials were prepared for further reduction tests in this study, as shown in Table 2. It should be noted that for the material with bigger particle size, it took 8 h to reach a partly oxidation at 800°C. The additional amount of MgO powder was chosen as 0.5wt% for all the pre-oxidized materials. The oxidation degree (w) was determined by the weight gain as given in Eq. (1) [24–25]. It was impossible to obtain the oxidized material with a fixed oxidation degree, even under the same oxidation conditions. The oxidation degrees of the deeply oxidized material (DOX) and partly oxidized material (POX) were in the ranges of 50%–65% and 94%–97%, respectively.

$$w = \frac{\Delta m}{\Delta m_{\text{theory}}} \times 100\% \quad (1)$$

where Δm and Δm_{theory} are the measured weight gain and the theoretical weight gain for complete oxidation, respectively. Δm_{theory} is calculated based on the FeO content from the chemical analysis of the magnetite-based iron ore.

Table 2. The pre-oxidation treatments and oxidation degrees of the pre-oxidized materials

No.	Oxidized material	Size range / μm	Pre-oxidation temperature / °C	Oxidation time / h	Oxidation degree / %
1	DOX _{125–250} -1000	125–250	1000	8	97.67
2	DOX _{250–500} -1000	250–500	1000	8	96.61
3	DOX _{125–500} -1000	125–500	1000	8	94.61
4	POX _{125–250} -800	125–250	800	4	54.93
5	POX _{250–500} -800	250–500	800	8	59.51
6	POX _{125–500} -800	125–500	800	8	58.91
7	DOX _{125–250} -800	125–250	800	8	96.14

2.2. Experimental procedure

The experimental apparatus, a fluidized bed reactor with a bed diameter of 68 mm [19] and the reduction test procedure [20], have been already described in detail in previous publications. The basic concept of the experimental apparatus was to maintain a constant temperature and measure the weight loss and pressure drops during the reduction process. The reduction degree (RD) was defined through Eqs. (2)–(4) [18–21].

$$\text{RD} = \left(1 - \frac{O_{\text{bonded to Fe at } t=t_i}}{O_{\text{bonded to Fe at } t=t_0}}\right) \times 100\% \quad (2)$$

$$O_{\text{bonded to Fe at } t=t_i} = \frac{O_{\text{bonded to Fe}_2\text{O}_3} + O_{\text{bonded to FeO}} - \Delta m}{M_{\text{O}}}, \text{ in mol} \quad (3)$$

$$O_{\text{bonded to Fe at } t=t_0} = 1.5 \times \frac{m_0 \times \text{Fe}_{\text{tot}}}{M_{\text{Fe}}}, \text{ in mol} \quad (4)$$

where $O_{\text{bonded to Fe at } t=t_0}$ and $O_{\text{bonded to Fe at } t=t_i}$ are the amount of O bonded to Fe at the start and during the reduction; Δm and m_0 are the weight loss due to the loss of O and the mass of input material; M_{O} and M_{Fe} are the constant molar masses for O and Fe; $O_{\text{bonded to Fe}_2\text{O}_3}$ and $O_{\text{bonded to FeO}}$ are the amount of O bonded to Fe₂O₃ and the amount of O bonded to FeO; t is the reduction time; t_0 and t_i are the times of reaction where it starts and is during the reduction.

The superficial gas velocity was kept constant at 0.4 m/s at 700°C reduction temperature. This was achieved by a constant H₂ flow rate of 15.9 L·min⁻¹ and balanced by nitrogen with a flow rate of 8.5 L·min⁻¹. When the RD reached 95% or the reaction time reached 85 min, the reducing gas was replaced by N₂ and the sample was cooled under N₂ atmosphere to ambient conditions. The obtained reduced samples were sealed in a plastic sample bag for further analysis.

2.3. Determination of the de-fluidized index

Some researchers defined the sticking ratio based on the weight ratio of the agglomerates and the total bed material after reduction [26–28]. However, in this work, no agglomerates were observed. To quantitatively describe the fluidization behavior, a de-fluidized index (DFI) was defined, as shown in Eq. (5), based on the measured ($\Delta p_{\text{measured-bed}}$) and theoretical ($\Delta p_{\text{calculated-bed}}$) differential pressure drops over the material [20]. The measured pressure drop caused by the grid and the material portion (dot gray line) is shown in Fig. 1(a). The black line represents the theoretical differential pressure drop over the material, which can be calculated based on Eq.

(6) [18,20]. The red dashed line represents the differential pressure for only the material in the fluidized bed without the pressure drop of the grid. This line should equal the black line when the material is entirely fluidized. However, when the material was completely fluidized, there were still minor deviations between $\Delta p_{\text{measured-bed}}$ and $\Delta p_{\text{calculated-bed}}$. This can be explained by the entrained material and some inaccuracies while measuring the differential pressure across the grid during the reduction [18]. Fig. 1(b) shows the DFI and RD against the reduction time. When DFI is smaller than 5%, it can be considered as a completely fluidization state.

$$\text{DFI} = \frac{\Delta p_{\text{calculated-bed}} - \Delta p_{\text{measured-bed}}}{\Delta p_{\text{calculated-bed}} - \Delta p_{\text{Fixed-bed}}} \quad (5)$$

$$\Delta p_{\text{calculated-bed}} = \frac{m_t \cdot g}{\text{Reactor area}} \quad (6)$$

where $\Delta p_{\text{Fixed-bed}}$ is the differential pressure drop when the material is in a fixed bed state; $\Delta p_{\text{Fixed-bed}}$ is 2 mbar (200 Pa) in this work; m_t is the mass of the material in the fluidized bed during the reduction; g is acceleration of gravity, where the value is 9.8 N/kg.

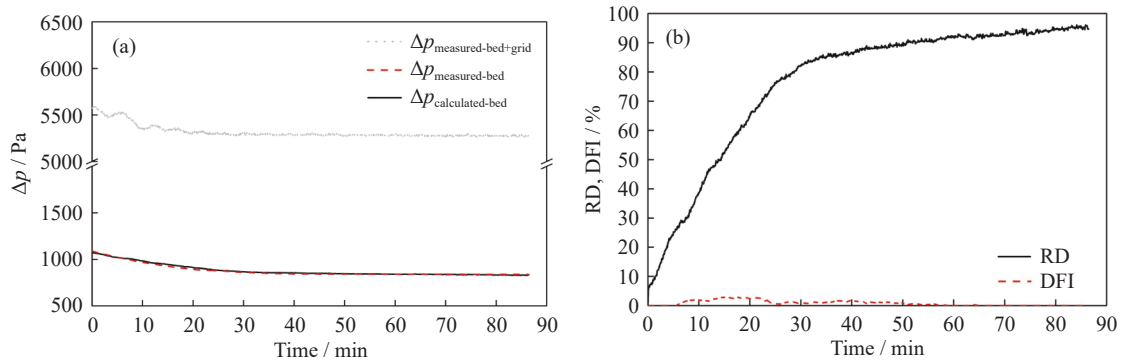


Fig. 1. Fluidized reduction results for DOX₁₂₅₋₂₅₀₋₁₀₀₀: (a) pressure drop against time; (b) RD and DFI against time.

2.4. Sample characterization

The morphology and internal structure of the samples were observed by scanning electron microscopy (Quanta 200Mk2, FEI, America) and optical light microscope (Nikon MM 40 measuring microscope system, Japan). The pore structures of the oxidized materials were evaluated by N₂ gas adsorption method using TriStar 3000 surface area analyzer (Micromeritics, America). The specific surface area was determined by Brunauer–Emmett–Teller (B.E.T.) method after degassing of the samples at 200°C for 2 h. The cumulative pore volume and average pore diameter were analyzed using Barrett–Joyner–Halenda (B.J.H.) method.

3. Results and discussion

3.1. BET-BJH analysis of pore structure

In this study, B.E.T. and B.J.H. methods were used to investigate the pore structures after the oxidation of the magnetite-based iron ore fines. Each test was repeated three times. The results of the pore structure parameters are listed in Table 3. The material oxidized at 1000°C is not shown due to the very low specific surface area (<0.01 m²/g), which was beyond the valid range of the testing facility. The material with a smaller particle size presented slightly higher specific surface area and total pore volume. The specific surface area and the total pore volume of the raw magnetite were 0.092–

Table 3. Pore structure parameters of the raw magnetite and oxidized samples

Sample	Particle size / μm	Specific surface area / (m ² ·g ⁻¹)	Average pore size / nm	Total pore volume / (10 ⁻⁴ cm ³ ·g ⁻¹)
Raw magnetite	125–250	0.092 ± 0.001	10.887 ± 0.091	0.880 ± 0.014
	250–500	0.093 ± 0.003	10.467 ± 0.521	0.850 ± 0.085
POX-800	125–250	0.173 ± 0.002	5.160 ± 0.037	2.710 ± 0.057
	250–500	0.141 ± 0.006	5.120 ± 0.012	2.400 ± 0.078
DOX-800	125–250	0.025 ± 0.013	5.019 ± 0.261	0.350 ± 0.071

0.093 m²/g and 0.850×10^{-4} – 0.880×10^{-4} cm³/g, respectively. The values of the specific surface area of POX_{125–250}–800 and POX_{250–500}–800 increased to 0.173 and 0.141 m²/g. The values of the total pore volume increased to 2.710×10^{-4} and 2.400×10^{-4} cm³/g, which were approximately three times larger than those of the raw magnetite. The specific surface area and total pore volume of DOX_{125–250}–800, however, decreased to 0.025 m²/g and 0.350×10^{-4} cm³/g. When the oxidation temperature increased to 1000°C, the specific surface area sharply reduced to less than 0.01 m²/g. Theoretically, the crystal transformation from magnetite phase to hematite phase involves a volume expansion, but sintering effect would weaken the expansion trend and even contract the volume [29]. The average pore size of the raw magnetite was around 10 nm. After oxidation, the average pore size of all the materials decreased to around 5 nm. The average pore size gave a hint that microcracks occurred after the oxidation. The cracks generated many more pores with sizes around 5 nm.

Fig. 2 shows the surface morphology of the samples before and after oxidation. The raw magnetite showed a smooth surface with clear edges and corners. As shown in Fig. 2(f), the surface of the POX_{125–250}–800 sample was porous and covered by tiny whiskers. These whisker structures still showed clear edges, while, due to the sintering effect, as

shown in Fig. 2(g), the DOX_{125–250}–800 sample presented a smoother and denser surface. The sintering effect was more obvious for the oxidation temperature of 1000°C, as shown in Fig. 2(h).

3.2. Effect of pre-oxidation temperature

The effect of pre-oxidation temperature on the fluidization and reduction behavior was studied using DOX_{125–250}–1000 and DOX_{125–250}–800. As shown in Fig. 3(a), the RD curve of the DOX_{125–250}–800 was similar to that of DOX_{125–250}–1000 in the early reduction stage. However, when RD reached 80%, DOX_{125–250}–800 showed a higher reduction rate than DOX_{125–250}–1000. It should be noted that the DFI of DOX_{125–250}–800 was much higher than that of DOX_{125–250}–1000. A higher oxidation temperature showed a better fluidization behavior. From the point of fluidization behavior, a high-temperature oxidation treatment is suggested. The reduction efficiency is also an essential issue in DRI production. Fig. 3(b) shows the characteristic reduction time to reach a specific RD. It took 8.45 min to reach RD of 33% and another 20.26 min to reach RD of 80% for DOX_{125–250}–1000. DOX_{125–250}–800 required the similar time to reach RD of 33% (7.93 min) and 80% (18.06 min). But compared with DOX_{125–250}–1000, it took nearly only half time for DOX_{125–250}–800 to reach RD of 95%. The lower pre-oxidation temperat-

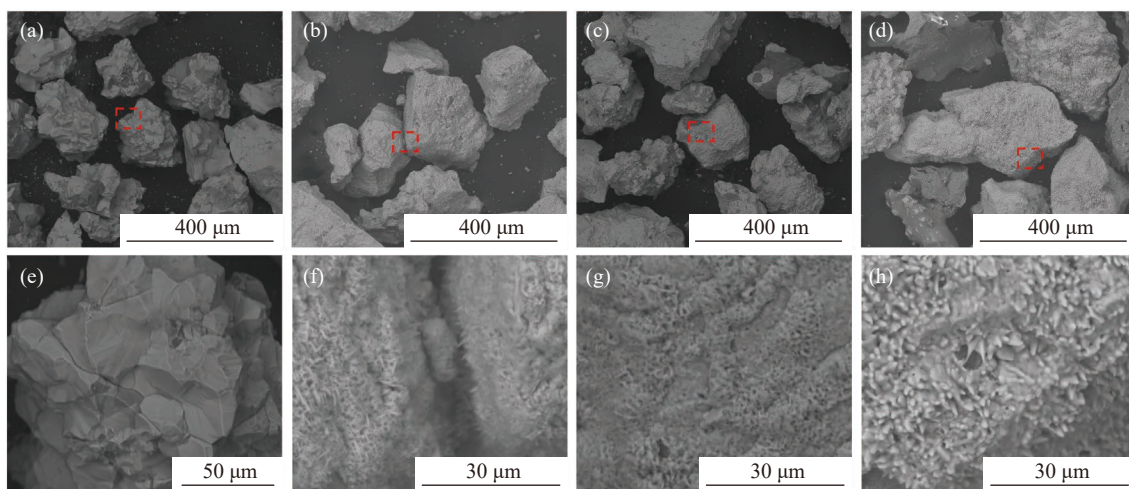


Fig. 2. Samples with a particle size distribution of 125–250 μm: (a, e) raw magnetite; (b, f) POX_{125–250}–800; (c, g) DOX_{125–250}–800; (d, h) DOX_{125–250}–1000.

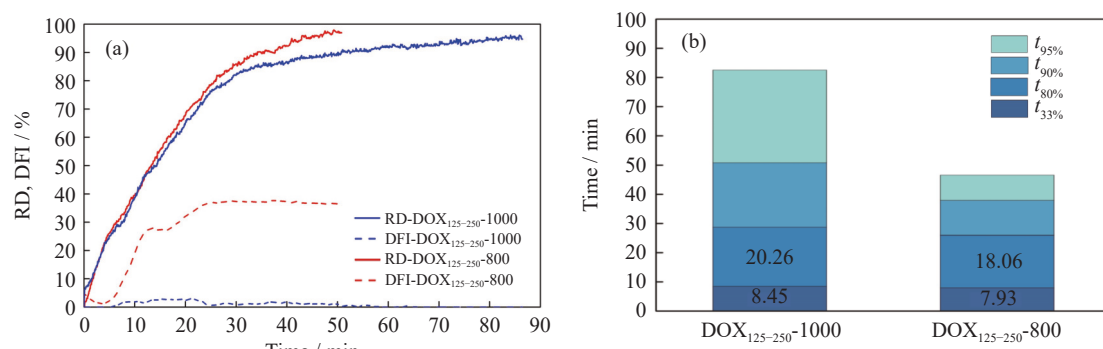


Fig. 3. Effect of pre-oxidation temperature on the fluidization and reduction behaviors: (a) RD and DFI; (b) reduction time to reach a specific RD. $t_{33\%}$, $t_{80\%}$, $t_{90\%}$, and $t_{95\%}$ represent the required time for RD reaching 33%, 80%, 90%, and 95%, respectively.

ure is more beneficial for the reduction rate in the later reduction stage, which is explained from kinetic point of view in Section 3.5.

3.3. Effect of pre-oxidation degree

The effect of pre-oxidation degree on the fluidization and reduction behavior was studied using $\text{DOX}_{125-250-800}$ and $\text{POX}_{125-250-800}$. As shown in Fig. 4(a), the RD curve of the $\text{DOX}_{125-250-800}$ was similar to that of $\text{POX}_{125-250-800}$ in the entire reduction stage. However, the fluidization behaviors exhibited slightly different. The $\text{POX}_{125-250-800}$ started de-fluidization (DFI > 5%) when RD reached around 65%, while the $\text{DOX}_{125-250-800}$ started de-fluidization earlier at around RD of 35%. The two types of materials both showed a partly de-fluidized state in the end with a DFI of 36%. As for the characteristic reduction time, as shown in Fig. 4(b), there was no significant difference. Thus, the pre-oxidation degree shows no obvious difference in fluidization and reduction behaviors.

3.4. Effect of particle size

The effect of the particle size was investigated using the $\text{POX}_{125-250-800}$, $\text{POX}_{125-500-800}$, $\text{POX}_{250-500-800}$, $\text{DOX}_{125-250-1000}$, $\text{DOX}_{125-500-1000}$, $\text{DOX}_{250-500-1000}$. As shown in Fig. 5(a), $\text{POX}_{125-250-800}$ presented the highest reduction rate, which can be explained by the higher specific area and the better fluidization behavior of the material. The RDs of $\text{POX}_{125-500-800}$ and $\text{POX}_{250-500-800}$ exhibited similar trends before reaching 85%. It should be noted that the weight sig-

nal system is slightly influenced by the fluidization state of the materials in the fluidized bed. After reduction tests, the remaining materials were weighted again and compared to the final mass from the weight signal. The differences were within 1 g, which confirmed the mass balance and the accuracy of the data. Fig. 5(b) shows the DFI against RD of the partially oxidized material. $\text{POX}_{250-500-800}$ started partly de-fluidized at the beginning of the reduction process, indicating that the superficial gas velocity is not high enough for this particle size range. $\text{POX}_{125-250-800}$ and $\text{POX}_{125-500-800}$ started the de-fluidization when RD reached around 30% and 60%, respectively. In terms of the fluidization behavior, in this case, a wider particle size (125–500 μm) is more beneficial. The characteristic reduction times are listed in Table 4. For higher reduction efficiency, a small particle size (125–250 μm) is recommended.

Fig. 6 shows the effect of the particle size using $\text{DOX}_{125-250-1000}$, $\text{DOX}_{125-500-1000}$, and $\text{DOX}_{250-500-1000}$. As shown in Fig. 6(a), the $\text{DOX}_{125-250-1000}$ presented the highest reduction rate. The $\text{DOX}_{125-500-1000}$ exhibited a slightly higher reduction rate than $\text{DOX}_{250-500-1000}$, while the $\text{DOX}_{125-500-1000}$ and $\text{DOX}_{125-250-1000}$ showed much better fluidization behavior, as shown in Fig. 6(b), than $\text{DOX}_{250-500-1000}$. According to Table 4, it took 50.77 min for $\text{DOX}_{125-250-1000}$ to reach the RD of 90%, which was much less than those for the other two particle size range materials. $\text{DOX}_{250-500-1000}$ and $\text{DOX}_{125-500-1000}$ cannot reach the RD of 95% within the defined reduction time.

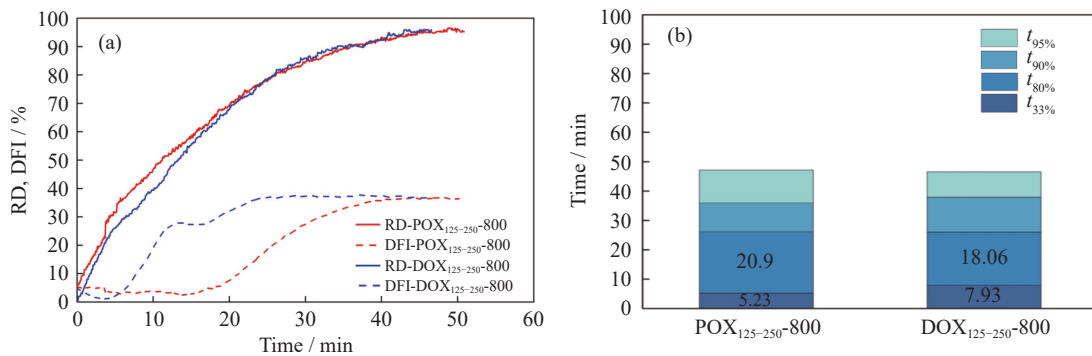


Fig. 4. Effect of pre-oxidation degree on the fluidization and reduction behaviors: (a) RD and DFI; (b) reduction time to reach a specific RD.

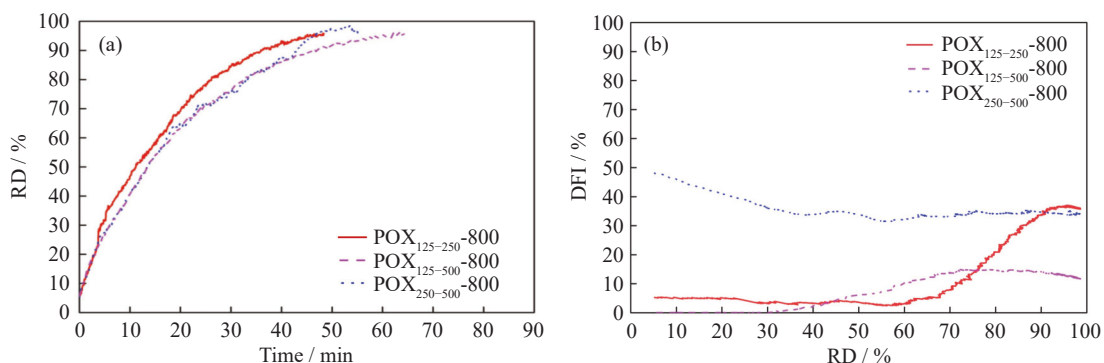


Fig. 5. Effect of particle size on the fluidization and reduction behaviors after pre-oxidized at 800°C: (a) RD; (b) DFI against RD.

Table 4. The characteristic reduction times

Oxidized material	$t_{33\%}$ / min	$t_{80\%}$ / min	$t_{90\%}$ / min	$t_{95\%}$ / min
POX ₁₂₅₋₂₅₀ -800	5.23	26.13	35.96	47.16
POX ₂₅₀₋₅₀₀ -800	7.11	33.32	43.04	47.33
POX ₁₂₅₋₅₀₀ -800	7.20	32.54	46.95	60.01
DOX ₁₂₅₋₂₅₀ -1000	8.45	28.71	50.77	82.54
DOX ₂₅₀₋₅₀₀ -1000	8.94	37.07	74.48	—
DOX ₁₂₅₋₅₀₀ -1000	8.70	33.27	71.86	—

3.5. Analysis of the kinetic reaction mechanisms

3.5.1. Double-logarithm analysis method

The Avrami-Erofeev model is described as given in Eq. (7). Eq. (8) is obtained by taking double logarithm of both sides of Eq. (7). According to Hancock and Sharp [30], the value of n provides the information of the involved reaction mechanisms. Generally, if $n < 1$, the mechanism is considered as diffusion-controlled; if n is close to 1, the reaction is controlled by chemical reaction; if $n > 1.5$, the reaction is described by nucleation process [18,31–32].

$$1 - x = e^{-kt^n} \quad (7)$$

$$\ln[-\ln(1 - x)] = n \ln t + \ln k \quad (8)$$

where x is the conversion (RD), n is the kinetic exponent, t is the reduction time (s), and k is rate constant. As shown in Fig. 7, the entire reduction process is divided into three stages: the

first stage ($0.11 < x < 0.33$), the second stage ($0.33 < x < 0.80$), and the third stage ($0.80 < x < 0.95$). An unavoidable fluctuation may occur when at the beginning of the reduction due to changing the atmosphere from inert to the reducing gas, which ends in a fluctuation of the system pressure. This kind of influence cannot be ignored due to the fast reduction in this stage. Therefore, the data from $x < 0.10$ was not taken into consideration. The n values are presented in Table 5.

For the first stage, the values of n were 0.76, 0.87, and 1.21 for DOX₁₂₅₋₂₅₀-1000, DOX₁₂₅₋₂₅₀-800, and POX₁₂₅₋₂₅₀-800, respectively. For the second stage, all the n values were close to 1, representing the chemical reaction control. For the third stage, the values of n were 0.49, 1.07, and 1.15 for DOX₁₂₅₋₂₅₀-1000, DOX₁₂₅₋₂₅₀-800, and POX₁₂₅₋₂₅₀-800, respectively. Therefore, the rate-limiting step was considered diffusion control in the early reduction stage for the deeply oxidized material. Higher pre-oxidation temperature (1000°C) influenced the final reduction stage, making the reaction controlled by diffusion, consistent with our previous result [20]. For partly oxidized material treated at 800°C, the whole reduction process was controlled by chemical reaction.

The double logarithm method considered the whole reaction process as three successive stages, each of which followed a single reaction model. The reduction of the iron oxide was regarded as several multiple reactions, where several reaction mechanisms may contribute to the same reaction

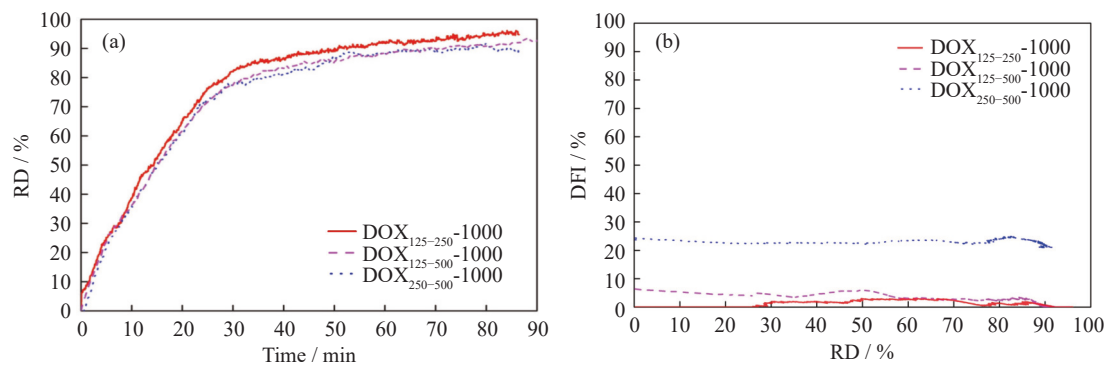


Fig. 6. Effect of particle size on the fluidization and reduction behaviors after pre-oxidation at 1000°C: (a) RD; (b) DFI against RD.

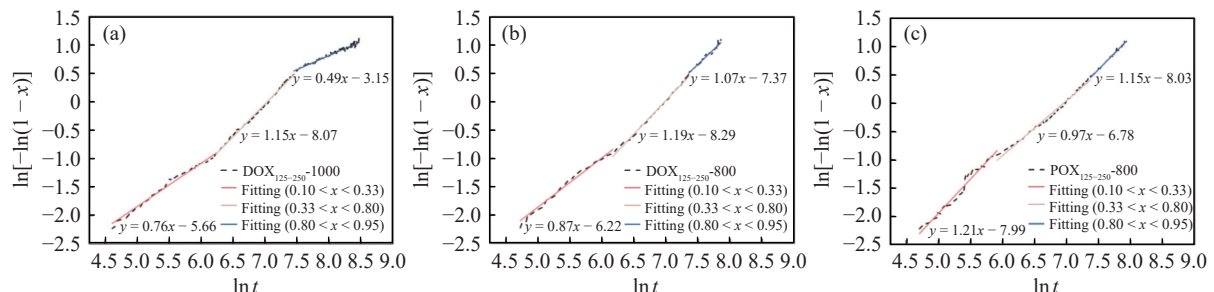


Fig. 7. $\ln[-\ln(1 - x)]$ vs. $\ln t$ for different materials: (a) DOX₁₂₅₋₂₅₀-1000; (b) DOX₁₂₅₋₂₅₀-800; (c) POX₁₂₅₋₂₅₀-800.

Table 5. The n values of the materials at different reduction stages

Reduction stage	DOX ₁₂₅₋₂₅₀ -1000	DOX ₁₂₅₋₂₅₀ -800	POX ₁₂₅₋₂₅₀ -800
First stage ($0.11 < x < 0.33$)	0.76	0.87	1.21
Second stage ($0.33 < x < 0.80$)	1.15	1.19	0.97
Third stage ($0.80 < x < 0.95$)	0.49	1.07	1.15

stage at the same time [18–19,31–36]. However, there is not a criterion for how to select a suitable method for the multiple reactions. Although the double-logarithm method cannot give information about the multiple reactions, this method shows the dominant reaction mechanism in each stage and is easier to be understood. To further confirm the kinetic reaction mechanism, the surface morphology and polished-section images of the samples should be examined.

3.5.2. Structural analysis

The surface morphology and the polished-section images of the reduced samples are shown in Fig. 8. The surfaces of the DOX_{125–250}-1000, DOX_{125–250}-800, and POX_{125–250}-800 presented a lamellar shape, a conical-shape, and a cylindrical shape, respectively. In Fig. 8(c), few conical-shaped irons can be observed, most of the iron phase exhibited cylindrical shapes. Nicolle and Rist [37] explained the growth of iron nucleus on wüstite and found a relationship between the shape of iron phase and the mechanism controlling step: when the reaction is restricted by the inward diffusion of iron ions, the newly formed iron phase shows a layer structure on the particle surface; when the reaction follows a chemical re-

action control, a cylindrical whisker may occur; if the reaction is under a mixed control by diffusion and chemical reaction, a conical shape of iron phase is supposed to be formed.

As discussed in Section 3.5.1, for DOX_{125–250}-1000, the reaction is controlled by diffusion, chemical reaction, and diffusion in the first, second, and third stage, respectively. The morphology shape in Fig. 8(a) is a typical shape for a diffusion-controlled reaction, which agrees the kinetic analysis for the third stage. As shown in Fig. 8(g), the polished-section image presents many wüstite islands due to the restriction of inward diffusion of iron ions. It can be concluded that the reduction of DOX_{125–250}-1000 is mainly controlled by the diffusion of iron ions. As for DOX_{125–250}-800 and POX_{125–250}-800, the morphology shapes in Fig. 8(b) and (c) are typical shapes for a mixed-controlled reaction and a chemical-controlled reaction, respectively. Based on the kinetic analysis, in the third stage, the diffusion is not the rate-limiting step for the reduction of DOX_{125–250}-800. Compared with DOX_{125–250}-1000, the wüstite islands in DOX_{125–250}-800 are less, as shown in Fig. 8(h). The whole reduction progress of POX_{125–250}-800 is only controlled by chemical reaction according to the kinetic ana-

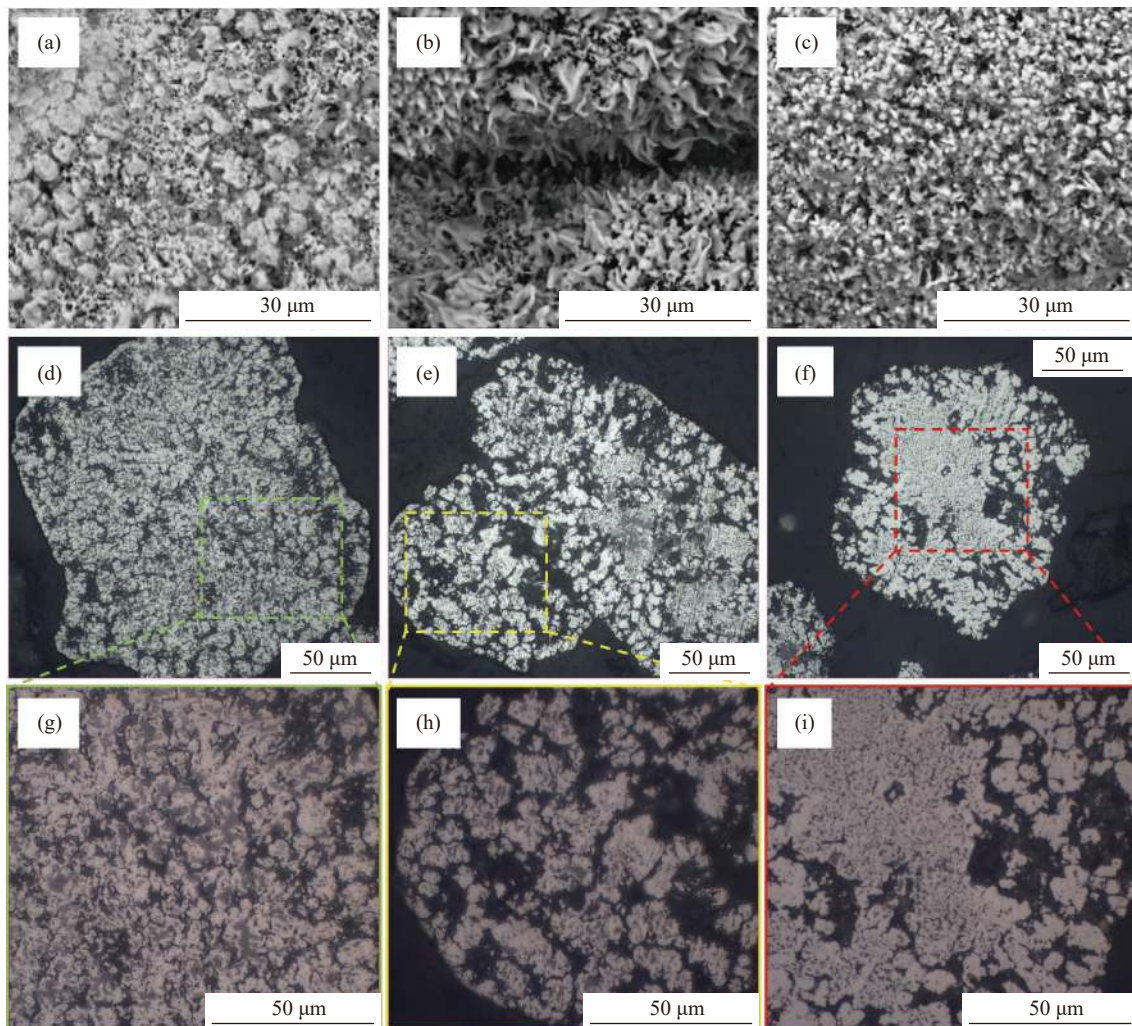


Fig. 8. The reduced samples with the particle sizes of 125–250 μm : surface morphology of (a) DOX_{125–250}-1000, (b) DOX_{125–250}-800, and (c) POX_{125–250}-800; polished-section images of (d, g) DOX_{125–250}-1000, (e, h) DOX_{125–250}-800, and (f, i) POX_{125–250}-800. (a)–(c) were obtained by SEM; (d)–(i) were obtained by optical microscope.

lysis. Therefore, the diffusion of the iron ions is not a rate-limiting step. It is proved by the polished-section image, as shown in Fig. 8(i), the wüstite islands in POX_{125–250}-800 almost disappear.

Generally, the structure analysis supports the kinetic analysis. From the kinetic and structure analysis, it is found that a higher temperature pre-oxidation treatment results in a restriction of iron ion diffusion during the following reduction progress in the later stage. The surface morphology was flat and no whiskers were observed, which is beneficial to the fluidization behavior. A lower temperature pre-oxidation treatment helps to improve the diffusion of the iron ions. However, the surface morphology with whiskers destroys the fluidization behavior. In future work, more reduction conditions and pre-oxidation treatment parameters will be conducted to obtain a stable complete fluidization state.

4. Conclusions

The purpose of this work is to study the influence of the pre-oxidation temperature and pre-oxidation degree on the reduction and fluidization behaviors of the magnetite-based iron ore. Based on the current results, the following conclusions can be drawn:

(1) A partly oxidation of the magnetite-based iron ore with particle size of 125–500 µm at 800°C increased the specific surface area and total pore volume. Compared with the raw magnetite-based iron ore, the specific surface area and total pore volume for a deeply oxidation treatment at 800 and 1000°C decreased significantly.

(2) Under present experimental conditions, the materials with higher temperature pre-oxidation treatment showed better fluidization behaviors due to the flat surface morphology. The materials with lower temperature pre-oxidation treatment presented morphology with whiskers. From the point of fluidization behavior, a high-temperature oxidation treatment is suggested.

(3) Regarding on the reduction efficiency, a lower pre-oxidation temperature is more beneficial for the reduction rate, especially in the later reduction stage. The diffusion of the iron ions is improved. The pre-oxidation degree shows no noticeable difference in fluidization and reduction behaviors.

Acknowledgements

The authors gratefully acknowledge the funding support of K1-MET GmbH, metallurgical competence center. The research program of the K1-MET competence center is supported by COMET (Competence Center for Excellent Technologies), the Austrian program for competence centers. COMET is funded by the Federal Ministry for Climate Action, Environment, Energy, Mobility, Innovation and Technology, the Federal Ministry for Digital and Economic Affairs, the provinces of Upper Austria, Tyrol and Styria, and the Styrian Business Promotion Agency (SFG). In addition, the research work is partially financed by Montanuniversität

Leoben. Heng Zheng greatly acknowledges the financial support from the program of China Scholarship Council (No. 201908420284).

Conflict of Interest

All authors declare no financial/commercial conflicts of interest.

Open Access funding provided by Montanuniversität Leoben.

Open Access This article is licensed under a Creative Commons Attribution 4.0 International License, which permits use, sharing, adaptation, distribution and reproduction in any medium or format, as long as you give appropriate credit to the original author(s) and the source, provide a link to the Creative Commons licence, and indicate if changes were made. The images or other third party material in this article are included in the article's Creative Commons licence, unless indicated otherwise in a credit line to the material. If material is not included in the article's Creative Commons licence and your intended use is not permitted by statutory regulation or exceeds the permitted use, you will need to obtain permission directly from the copyright holder. To view a copy of this licence, visit <http://creativecommons.org/licenses/by/4.0/>.

References

- [1] European Commission, *Climate Action - 2050 Long-term Strategy* [2021-11-13]. https://ec.europa.eu/clima/policies/strategies/2050_en
- [2] Worldsteel, *Steel Statistical Yearbooks* [2021-11-14]. <https://www.worldsteel.org/steel-by-topic/statistics/steel-statistical-yearbook.html>
- [3] Roland Berger, *The Future of Steelmaking—How the European Steel Industry can Achieve Carbon Neutrality*, Roland Berger GMBH, Munich, 2020.
- [4] European Commission, *Ultra-Low CO₂ Steelmaking* [2021-11-14]. <https://cordis.europa.eu/project/id/515960>
- [5] M.A. Quader, S. Ahmed, S.Z. Dawal, and Y. Nukman, Present needs, recent progress and future trends of energy-efficient Ultra-Low Carbon Dioxide (CO₂) Steelmaking (ULCOS) program, *Renewable Sustainable Energy Rev.*, 55(2016), p. 537.
- [6] A. Bhaskar, M. Assadi, and H.N. Somehsaraei, Decarbonization of the iron and steel industry with direct reduction of iron ore with green hydrogen, *Energies*, 13(2020), No. 3, art. No. 758.
- [7] Y.B. Chen and H.B. Zuo, Review of hydrogen-rich ironmaking technology in blast furnace, *Ironmaking Steelmaking*, 48(2021), No. 6, p. 749.
- [8] W.G. Liu, H.B. Zuo, J.S. Wang, Q.G. Xue, B.L. Ren, and F. Yang, The production and application of hydrogen in steel industry, *Int. J. Hydrogen Energy*, 46(2021), No. 17, p. 10548.
- [9] F. Patisson and O. Mirgaux, Hydrogen ironmaking: How it works, *Metals*, 10(2020), No. 7, art. No. 922.
- [10] Primetals, *Enhanced Energy Efficient Steel Production – E³-SteP*, Primetals Technologies, 2019 [2021-11-14]. https://nachhaltigwirtschaften.at/resources/nw_pdf/events/20191009_highlights/spreitzer-rein-eisl_e3-step.pdf
- [11] J. Tang, M.S. Chu, F. Li, C. Feng, Z.G. Liu, and Y.S. Zhou, Development and progress on hydrogen metallurgy, *Int. J. Miner. Metall. Mater.*, 27(2020), No. 6, p. 713.
- [12] Bellona Europa, *Hydrogen in Steel Production: What is Happening in Europe – Part Two*, Bellona, 2021 [2021-11-14]. <https://www.bellona.org/publications/hydrogen-in-steel-production-what-is-happening-in-europe-part-two>

- tps://bellona.org/news/industrial-pollution/2021-05-hydrogen-in-steel-production-what-is-happening-in-europe-part-two
- [13] Hybrit, *Fossil-free Steel – A Joint Opportunity!* [2021-11-14]. <https://www.hybritdevelopment.se/en/>
- [14] SALCOS®, *Our Program SALCOS* [2021-11-14]. <https://salcos.salzgitter-ag.com/en/>
- [15] Voestalpine, *H2FUTURE* [2021-11-14]. <https://www.voestalpine.com/greentecsteel/en/breakthrough-technologies/>
- [16] J.L. Schenk, Recent status of fluidized bed technologies for producing iron input materials for steelmaking, *Particuology*, 9(2011), No. 1, p. 14.
- [17] S. Daniel, *Development of Characterization Methods for the Evaluation of Kinetic Behavior and the Fluidization of Iron Ore Fines during Hydrogen-induced Fluidized Bed Reduction* [Dissertation], Montanuniversitaet Leoben, Leoben, 2000.
- [18] D. Spreitzer and J. Schenk, Iron ore reduction by hydrogen using a laboratory scale fluidized bed reactor: Kinetic investigation—Experimental setup and method for determination, *Metall. Mater. Trans. B*, 50(2019), No. 5, p. 2471.
- [19] D. Spreitzer and J. Schenk, Fluidization behavior and reducibility of iron ore fines during hydrogen-induced fluidized bed reduction, *Particuology*, 52(2020), p. 36.
- [20] H. Zheng, D. Spreitzer, T. Wolfinger, J. Schenk, and R.S. Xu, Effect of prior oxidation on the reduction behavior of magnetite-based iron ore during hydrogen-induced fluidized bed reduction, *Metall. Mater. Trans. B*, 52(2021), No. 4, p. 1955.
- [21] T. Wolfinger, D. Spreitzer, H. Zheng, and J. Schenk, Influence of a prior oxidation on the reduction behavior of magnetite iron ore ultra-fines using hydrogen, *Metall. Mater. Trans. B*, 53(2022), No. 1, p. 14.
- [22] E. Park and O. Ostrovski, Reduction of titania-ferrous ore by hydrogen, *ISIJ Int.*, 44(2004), No. 6, p. 999.
- [23] Z.Y. Wang, J.L. Zhang, K.X. Jiao, Z.J. Liu, and M. Barati, Effect of pre-oxidation on the kinetics of reduction of ironsand, *J. Alloys Compd.*, 729(2017), p. 874.
- [24] D.Q. Zhu, C.C. Yang, J. Pan, and X.B. Li, Comparison of the oxidation behaviors of high FeO chromite and magnetite concentrates relevant to the induration of ferrous pellets, *Metall. Mater. Trans. B*, 47(2016), No. 5, p. 2919.
- [25] F. Pan, Q.S. Zhu, Z. Du, and H.Y. Sun, Oxidation kinetics, structural changes and element migration during oxidation process of vanadium-titanium magnetite ore, *J. Iron Steel Res. Int.*, 23(2016), No. 11, p. 1160.
- [26] Q.Y. Xu, Z.Z. Liu, Z.P. Li, J.J. Wang, and L. Zhou, The effect of carbon dissection of waste plastics on inhibiting the adhesion of fine iron ore particles during hydrogen reduction, *Metals*, 8(2018), No. 7, art. No. 523.
- [27] Q.Y. Xu, Z.P. Li, Z.Z. Liu, J.J. Wang, and H.C. Wang, The effect of pressurized decarbonization of CO on inhibiting the adhesion of fine iron ore particles, *Metals*, 8(2018), No. 7, art. No. 525.
- [28] M.I.A. Barustan and S.M. Jung, Morphology of iron and agglomeration behaviour during reduction of iron oxide fines, *Met. Mater. Int.*, 25(2019), No. 4, p. 1083.
- [29] H. Zheng, J. Schenk, D. Spreitzer, T. Wolfinger, and O. Dagha-gheleh, Review on the oxidation behaviors and kinetics of magnetite in particle scale, *Steel Res. Int.*, 92(2021), No. 8, art. No. 2000687.
- [30] J.D. Hancock and J.H. Sharp, Method of comparing solid-state kinetic data and its application to the decomposition of kaolinite, brucite, and BaCO₃, *J. Am. Ceram. Soc.*, 55(1972), No. 2, p. 74.
- [31] E.R. Monazam, R.W. Breault, and R. Siriwardane, Reduction of hematite (Fe₂O₃) to wüstite (FeO) by carbon monoxide (CO) for chemical looping combustion, *Chem. Eng. J.*, 242(2014), p. 204.
- [32] E.R. Monazam, R.W. Breault, R. Siriwardane, G. Richards, and S. Carpenter, Kinetics of the reduction of hematite (Fe₂O₃) by methane (CH₄) during chemical looping combustion: A global mechanism, *Chem. Eng. J.*, 232(2013), p. 478.
- [33] H.S. Chen, Z. Zheng, Z.W. Chen, and X.T. Bi, Reduction of hematite (Fe₂O₃) to metallic iron (Fe) by CO in a micro fluidized bed reaction analyzer: A multistep kinetics study, *Powder Technol.*, 316(2017), p. 410.
- [34] H.S. Chen, Z. Zheng, Z.W. Chen, W.Z. Yu, and J.R. Yue, Multistep reduction kinetics of fine iron ore with carbon monoxide in a micro fluidized bed reaction analyzer, *Metall. Mater. Trans. B*, 48(2017), No. 2, p. 841.
- [35] K. He, Z. Zheng, Z.W. Chen, H.S. Chen, and W.P. Hao, Kinetics of hydrogen reduction of Brazilian hematite in a micro-fluidized bed, *Int. J. Hydrogen Energy*, 46(2021), No. 5, p. 4592.
- [36] K. He, Z. Zheng, and Z.W. Chen, Multistep reduction kinetics of Fe₃O₄ to Fe with CO in a micro fluidized bed reaction analyzer, *Powder Technol.*, 360(2020), p. 1227.
- [37] R. Nicolle and A. Rist, The mechanism of whisker growth in the reduction of wüstite, *Metall. Trans. B*, 10(1979), No. 3, p. 429.

Article

Parameter Optimization for Hydrogen-Induced Fluidized Bed Reduction of Magnetite Iron Ore Fines

Heng Zheng ^{1,*} , Johannes Schenk ^{1,2,*} , Oday Daghighaleh ¹ and Bernd Taferner ¹¹ Department of Metallurgy, Montanuniversitaet Leoben, Franz-Josef-Straße 18, 8700 Leoben, Austria² K1-MET GmbH, Stahlstraße 14, 4020 Linz, Austria

* Correspondence: heng.zheng@stud.unileoben.ac.at (H.Z.); johannes.schenk@unileoben.ac.at (J.S.)

Abstract: Hydrogen-based direct reduced iron (HyDRI) produced by fluidized bed has great potential for achieving the target of net-zero carbon in steelmaking. However, when magnetite ores were used as feedstock, several process parameters showed influences on its fluidization and reduction behaviors. To confirm the dominant influencing factors and its optimum process condition, the orthogonal experimental method was conducted in the present study. The result shows that the primary and secondary influencing factors are oxidation temperature, oxidation content, MgO addition amount, and gas velocity. The optimum condition is that the magnetite iron ore is deeply oxidized at 800 °C, mixed with 1.5 wt.% of MgO powder, and reduced in the fluidized bed at a gas velocity of 0.45 m/s.

Keywords: hydrogen-based direct reduced iron; fluidized bed; influencing factors; optimum condition



Citation: Zheng, H.; Schenk, J.; Daghighaleh, O.; Taferner, B. Parameter Optimization for Hydrogen-Induced Fluidized Bed Reduction of Magnetite Iron Ore Fines. *Metals* **2023**, *13*, 339. <https://doi.org/10.3390/met13020339>

Academic Editor: Chenguang Bai

Received: 30 December 2022

Revised: 28 January 2023

Accepted: 6 February 2023

Published: 8 February 2023



Copyright: © 2023 by the authors. Licensee MDPI, Basel, Switzerland. This article is an open access article distributed under the terms and conditions of the Creative Commons Attribution (CC BY) license (<https://creativecommons.org/licenses/by/4.0/>).

1. Introduction

Steel is the world's most important engineering and construction material [1]. The total production of crude steel in 2020 was 1.95 billion tons, and the top three steel-producing countries were China, India, and Japan, respectively [2]. With the development of developing countries, the steel demand will further increase [3,4]. It is estimated that the global steel demand will grow by more than 60% by 2050 [5]. Iron and steel production is a CO₂ emissions-intensive sector, which was responsible for 2.6 Gt CO₂ emission (about 7% of global anthropogenic CO₂ emissions) in 2019 [6]. The two dominant steelmaking processes are the blast furnace–basic oxygen furnace (BF–BOF) route and the scrap-based electric arc furnace (EAF) route [7,8]. In terms of CO₂ emission, the BF–BOF route emits 1.6–2.2 tons CO₂ per ton of crude steel, which is more than twice the amount CO₂ emission than that of the EAF route (0.6 tons CO₂ per ton of crude steel) [9–11]. To achieve the goal of CO₂ neutrality within the process, the shift from BF–BOF to EAF is a trend for future steelmaking [8]. Due to the limited access to high-quality scrap, it can be partly replaced by direct reduced iron (DRI). The ongoing development of the hydrogen-based direct reduced iron (HyDRI)—EAF route has a high potential for reducing CO₂ emission. When EAF is operated with pure HyDRI, CO₂ emission can be reduced to 25–53 kg per ton of crude steel [12,13]. Therefore, how to produce HyDRI properly and efficiently becomes an interesting topic.

Many commercial processes use shaft furnaces or fluidized bed reactors as iron ore reduction units [14,15]. Fluidized beds usually show better reduction efficiency because of faster mass and heat transfer. An ongoing hydrogen-based-fine-ore reduction process, namely HYFOR, developed by Primetals Technologies, is one of the successful examples [16]. However, if the de-fluidization phenomenon occurs, i.e., the iron ore fines cannot be fluidized by the gas flow, the reduction efficiency would drop dramatically, and process control of the system would become impossible. In a hydrogen-induced fluidized bed, the newly formed metallic iron on the particle surface is sticky and has a high probability

of forming iron aggregates [17]. To prevent de-fluidization, the particle surface can be modified by coating treatment [18]. One practical method is to mix MgO with the iron ore fines before charging into the fluidized bed reactor. The MgO acts as a physical barrier to reduce the frequency of contact between particles [19]. When the reduction temperature is higher than 900 °C, MgO reacts with Fe₂O₃/FeO and forms Fe₂MgO₄/FeO·MgO on the particle surface, which serves as a chemical barrier [20].

Hydrogen reduction of iron oxide is an endothermic reaction that requires external heat input into the system such as preheating the iron ore. When magnetite iron ore is used, it becomes oxidized in a preheat process. Based on our previous study, the raw magnetite iron ore could not be completely fluidized at the temperature range of 600–800 °C. The generated fresh metallic iron accumulated on the surface of the magnetite particle and an iron shell was formed. While an oxidation treatment of magnetite iron ore improved the fluidization behaviors. The pre-oxidation treatment promoted the formation of a porous structure. The porous structure improved the reducibility and also avoids the formation of iron shell on the particle surface, thus decreasing the de-fluidization tendency. However, additional MgO was still needed when the reduction temperature was higher than 650 °C [21]. It was also found that the oxidation temperature and oxidation content (deeply oxidized or partly oxidized) of magnetite influenced the fluidization and reduction behaviors [22]. Higher oxidation temperature shows a better fluidization improvement effect but leads to a lower reduction rate in the later reduction stage. According to kinetic analysis, the diffusion of the iron ions was the rate-limiting step. A lower pre-oxidation temperature could improve the diffusion of the iron ions.

The current study determines the proper operating parameters through an orthogonal experimental method. Furthermore, the dominant factors that influence the fluidization and reduction behaviors of the magnetite iron ore are confirmed. Based on the results, practical guidance can be provided for pilot or industrial trials.

2. Experimental

2.1. Materials

A low raw-grade magnetite iron ore was used as raw material, and the chemical composition is shown in Table 1. The high-purity MgO powder (>99.5 wt.% MgO, size below 44 µm) was used as an anti-sticking additive. The particle size of the raw magnetite ore is in the range of 125–500 µm, which is achieved by mixing 50 wt.% of 125–250 µm and 50 wt.% of 250–500 µm. For the oxidation treatment, 1000 g of the raw magnetite ore was charged into a steel vessel and put into a conventional heat treatment furnace at 800, 900, and 1000 °C for a specific time. To endure a uniform oxidation of magnetite particles within the material layer, the material was stirred manually during the oxidation. Two types of oxidized material, namely partly oxidized material and deeply oxidized material were obtained at each oxidation temperature. It should be noted that oxidation degrees of the deeply oxidized material and partly oxidized material range from 94% to 97% and 50% to 65%, respectively. The oxidation degree was confirmed by the actual weight gain and theoretical weight gain. The theoretical weight gain can be calculated according to FeO content from the chemical analysis of the raw magnetite iron ore. The detailed calculation has been described in detail elsewhere [23].

Table 1. Chemical composition of the raw magnetite iron ore, wt.%.

¹ Fe _{tot}	FeO	SiO ₂	Al ₂ O ₃	CaO	MgO	MnO	P
59.50	19.66	7.05	1.13	3.03	2.00	0.17	0.7

¹ Fe_{tot}—Total iron content.

2.2. Apparatus and Methods

The main apparatus in this study, as shown in Figure 1, was a fluidized bed reactor with a 68 mm inner diameter [21,24]. The principle of the experimental apparatus was

to measure the weight change and differential pressure drop continuously during the reduction process. The factors affecting the fluidized bed reduction were selected as oxidation temperature (Factor A), oxidation content (Factor B), MgO addition amount (Factor C), and gas velocity (Factor D). The orthogonal experimental plan was designed using IBM SPSS software (Statistics 26, IBM, Armonk, NY, USA), where three levels of each factor were taken. The reduction temperature and H₂ content were 700 °C and 15.9 Nl/min, respectively, for all the experiments. The gas velocity was controlled by changing N₂ content. A sample of 400 g of the material was taken for each experiment. When the reduction degree reached 95% or the reaction time reached 90 min, the reducing gas was changed to N₂ for cooling. The detailed experimental programs are given in Tables 2 and 3.

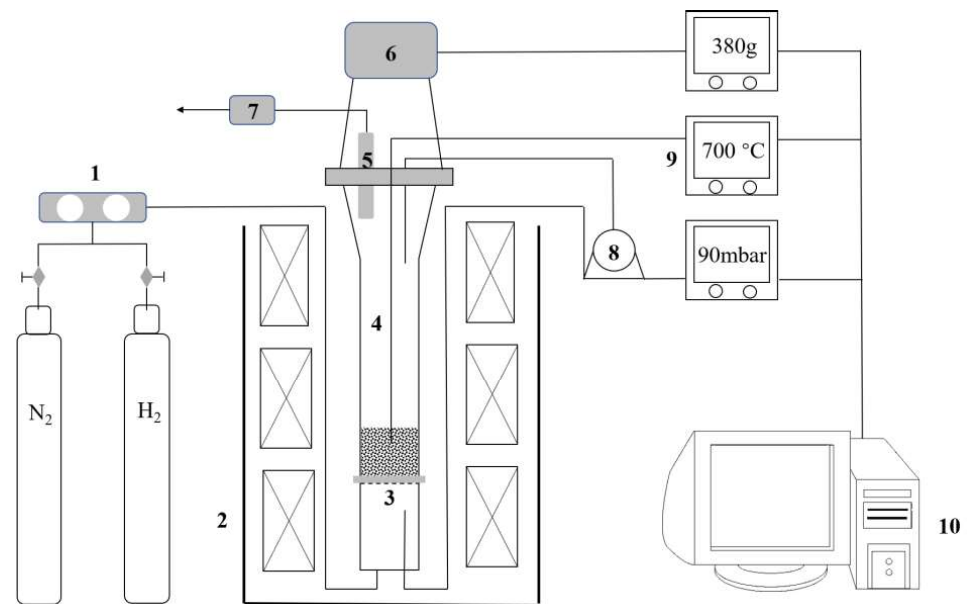


Figure 1. Schematic layout of laboratory fluidized bed reactor [21]: (1) gas system; (2) three-stage electrical furnace; (3) gas distributor; (4) fluidized bed reactor; (5) dust filter; (6) scale; (7) pressure regulator; (8) differential pressure monitor; (9) temperature control; and (10) computer system unit.

Table 2. Orthogonal experimental factors and levels.

Factor	A			B			C			D		
	Oxidation Temperature, °C			Oxidation Content			MgO Amount, wt.%			Gas Velocity, m/s		
Level	A ₁	A ₂	A ₃	B ₁	B ₂	B ₃	C ₁	C ₂	C ₃	D ₁	D ₂	D ₃
	800	900	1000	Raw	Partly	Deeply	0.5	1.0	1.5	0.35	0.40	0.45

Table 3. Orthogonal experimental plan.

No.	A	B	C	D
1	A ₃	B ₂	C ₃	D ₁
2	A ₃	B ₃	C ₁	D ₂
3	A ₂	B ₁	C ₃	D ₂
4	A ₂	B ₃	C ₂	D ₁
5	A ₂	B ₂	C ₁	D ₃
6	A ₁	B ₃	C ₃	D ₃
7	A ₁	B ₁	C ₁	D ₁
8	A ₃	B ₁	C ₂	D ₃
9	A ₁	B ₂	C ₂	D ₂

2.3. Definition of Reduction Degree (RD) and Average De-Fluidization Index (Ave.DFI)

The RD was defined as the ratio of removed oxygen to the total oxygen bonded to iron, where the removed oxygen was measured by the weight loss. The RD can be calculated based on Equations (1)–(3) [21,25,26].

$$RD = \left(1 - \frac{O_{\text{bounded to Fe at } t=ti}}{O_{\text{bounded to Fe at } t=t0}} \right) \times 100\% \quad (1)$$

$$O_{\text{bounded to Fe at } t=ti} = \frac{O_{\text{bounded to Fe}_2\text{O}_3} + O_{\text{bounded to FeO}} - \Delta m}{M_O} \quad (2)$$

$$O_{\text{bounded to Fe at } t=t0} = 1.5 \times \frac{m_0 \times Fe_{tot}}{M_{Fe}} \quad (3)$$

where $O_{\text{bounded to Fe at } t=t0}$ and $O_{\text{bounded to Fe at } t=ti}$ represent the amounts of oxygen that are bounded to iron at the start and during the reduction, Δm and m_0 are the weight loss due to the loss of oxygen and the mass of input material, and M_O and M_{Fe} are the constant molar masses for oxygen and iron.

A de-fluidization index (DFI) was introduced previously, as expressed by Equations (4) and (5) [22]. The DFI was a real-time value, which represented the portion of material that was not fluidized. For an easier comparison among the experiments in this study, an Ave.DFI was defined as shown in Equation (6). The differential pressure data were collected every two seconds. Dividing the total DFI by the amount of data gives Ave.DFI.

$$DFI = \frac{\Delta p_{\text{calculated-bed}} - \Delta p_{\text{measured-bed}}}{\Delta p_{\text{calculated-bed}} - \Delta p_{\text{Fixed-bed}}} \quad (4)$$

$$\Delta p_{\text{calculated-bed}} = \frac{m_t \times g}{\text{Reactor area}} \quad (5)$$

$$\text{Ave.DFI} = \frac{\sum DFI}{N_{DFI}} \quad (6)$$

where $\Delta p_{\text{Fixed-bed}}$ is the differential pressure drop when the material is in a fixed bed state. $\Delta p_{\text{Fixed-bed}}$ is 2 mbar in this work; m_t is the mass of the remaining material in the fluidized bed during the reduction. N_{DFI} is the amount of DFI data.

3. Results and Discussions

3.1. Orthogonal Experiment Analysis

The goal of a fluidized bed reduction is to obtain a high reduction rate at a stable fluidization state. Therefore, the time to reach $RD = 90\%$ ($t_{90\%}$) and the Ave.DFI were chosen as indicators for the optimization of reduction parameters. The result is shown in Table 4. Considering the fluctuation of the collected differential pressure data, it can be considered as a completely fluidized bed when the Ave.DFI is smaller than 5% [22]. Experiment No.2 shows the lowest Ave.DFI, and experiment No.6 shows the smallest $t_{90\%}$. The orthogonal experiment analysis is conducted to confirm the dominant factors that influence the fluidization and reduction behaviors and to figure out the optimum condition. The results are shown in Tables 5 and 6. This analysis method is also conducted by Zhang et al. [27] and Xu et al. [28] to determine the optimum fluidized conditions during the reduction of hematite using a CO and CO-H₂ mixture.

The K_i is the sum of the experiment result (see Table 4) for the corresponding level number I as given in Table 3; k_i equals K_i divided by n , where n is the number occurrences of each level and $n = 3$; $R = \max\{k_i\} - \min\{k_i\}$. The experimental factor with the highest R-value represents the most dominant influencing factor. The experimental level with the smallest k_i value indicates the optimum choice in the corresponding experimental factor. Therefore, regarding reduction efficiency, i.e., $t_{90\%}$, the primary and secondary influencing factors are oxidation temperature, oxidation content, MgO addition amount, and gas velocity. The optimum condition should be A₁B₂C₃D₃: the magnetite iron ore

is partly oxidized at 800 °C, mixed with 1.5 wt.% of MgO, and reduced in the fluidized bed at a gas velocity of 0.45 m/s. Regarding the fluidization behaviors, i.e., *Ave.DFI*, the primary and secondary influencing factors are gas velocity, oxidation temperature, MgO addition amount, and oxidation content. The optimum condition should be D₂A₃C₃B₂: the magnetite iron ore is partly oxidized at 1000 °C, mixed with 1.5 wt.% of MgO, and reduced in the fluidized bed at a gas velocity of 0.4 m/s. From the orthogonal experimental result given in Table 4, fluidization is not a significant concern under experimental conditions. Experiment No.6 shows the fastest reduction rate. Only experiments No. 4, 5, and 7 are partly de-fluidized. The following discussions mainly concentrate on the reduction rate.

Table 4. The orthogonal experimental result.

No.	t _{90%} , min	<i>Ave.DFI</i> , %
1	50.80	2.32
2	70.92	1.73
3	56.64	2.89
4	47.73	16.81
5	49.86	16.95
6	38.62	4.23
7	56.92	18.52
8	66.24	4.56
9	46.95	2.80

Table 5. The orthogonal experimental analysis regarding t_{90%}.

Factor	A	B	C	D
K ₁	142.49	179.80	177.70	155.45
K ₂	154.23	147.61	160.92	174.51
K ₃	187.96	157.27	146.06	154.72
k ₁	47.50	59.93	59.23	51.82
k ₂	51.41	49.20	53.64	58.17
k ₃	62.65	52.42	48.69	51.57
R	15.16	10.73	10.55	6.60
Primary and secondary factors Optimization scheme			ABCD A ₁ B ₂ C ₃ D ₃	

Table 6. The orthogonal experimental analysis regarding *Ave.DFI*.

Factor	A	B	C	D
K ₁	25.55	25.97	37.20	37.65
K ₂	36.65	22.07	24.17	7.42
K ₃	8.61	22.77	9.44	25.74
k ₁	8.52	8.66	12.40	12.55
k ₂	12.22	7.36	8.06	2.47
k ₃	2.87	7.59	3.15	8.58
R	9.35	1.30	9.25	10.08
Primary and secondary factors Optimization scheme			DACB D ₂ A ₃ C ₃ B ₂	

If the condition A₁B₂C₃D₃ shows the lowest t_{90%} with an acceptable *Ave.DFI* (<5.0%), it can be confirmed as the optimum condition. Thereafter, experiment No.10 is carried out using the condition A₁B₂C₃D₃. The t_{90%} and *Ave.DFI* of No.10 are 42.1 min and 2.4%, respectively. The reduction and de-fluidization curves are shown in Figure 2. Experiment No.10 shows a good reduction rate, but still, less than that of experiment No.6. The fluidization behaviors of No.10 and No.6 are similar. Thus, it can be concluded that the experiment. No.6 is the optimum condition instead of No.10.

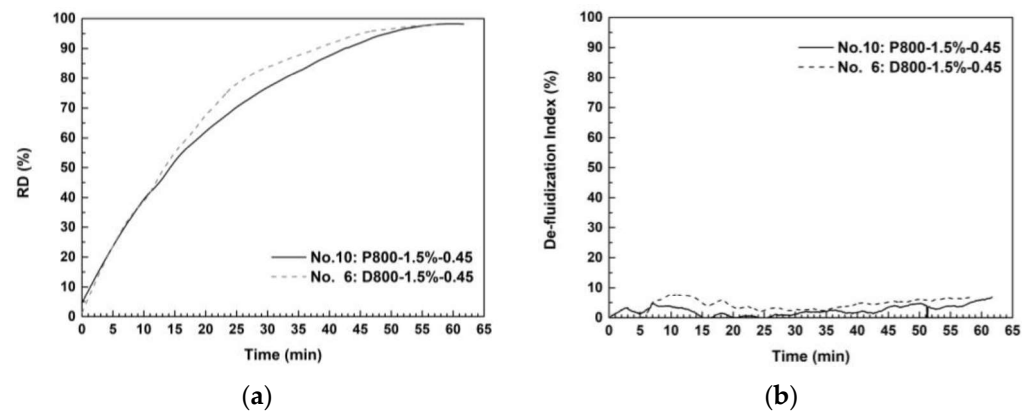


Figure 2. The fluidized reduction results of experiments No.6 and No.10: (a) reduction curve; (b) de-fluidization curve. P800-1.5%-0.45 represents that the magnetite iron ore was partly oxidized at 800 °C, mixed with 1.5 wt.% of MgO and reduced in the fluidized bed at a gas velocity of 0.45 m/s; D800-1.5%-0.45 represents that the magnetite iron ore was deeply oxidized at 800 °C, mixed with 1.5 wt.% of MgO and being reduced in the fluidized bed at a gas velocity of 0.45 m/s.

3.2. The Reduction Curve Analysis

To further understand the orthogonal experimental result, a detailed reduction curve analysis is required. As discussed in Section 3.1, the oxidation temperature and oxidation content are the first two dominant influencing factors. Hence, Figure 3 shows the comparison reduction curve between the samples with different oxidation treatments, where the MgO amount and gas velocity are varied. In Figure 3a, it is shown that the deeply oxidized materials with a higher oxidation temperature give a lower reduction rate. The gaps between the reduction curves are bigger, especially when the reduction degree reaches 80%. As for the raw magnetite sample, the reduction curve presents a different shape, where the reduction rate is not restricted significantly in the later reduction stage. The partly oxidized materials show the same trend that a higher oxidation temperature gives a lower reduction rate (see Figure 3b), whereas the later reduction stages are improved compared with the deeply oxidized materials. This phenomenon is more obvious in the sample oxidized at 1000 °C, as shown in Figure 3c. The samples oxidized at 800 °C are an exception, as it is shown in Figure 2a that the deeply oxidized sample still shows a higher reduction rate than the partly oxidized sample even after reaching the target reduction degree i.e., >90%. For the raw magnetite sample, comparing tests No.8 and No.7, (see Figure 4), it is interesting to note that the test with a higher MgO addition amount and a higher velocity shows a lower reduction rate. It gives a hint that when using magnetite iron ore as raw material, a critical velocity must be determined. It is not that the higher the gas velocity, the faster the reduction rate.

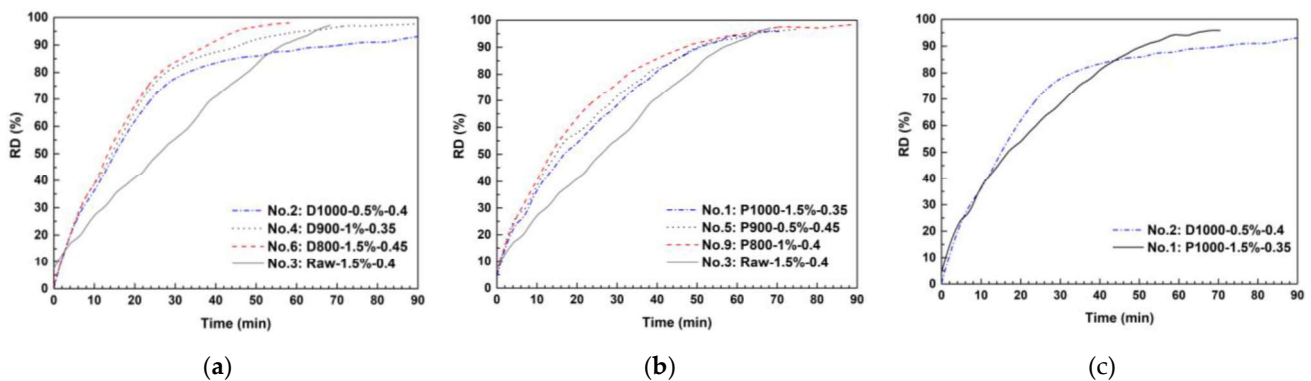


Figure 3. The reduction curves of the samples with different oxidation treatments: (a) deeply oxidized at different temperatures; (b) partly oxidized at different temperatures; (c) oxidized at 1000 °C.

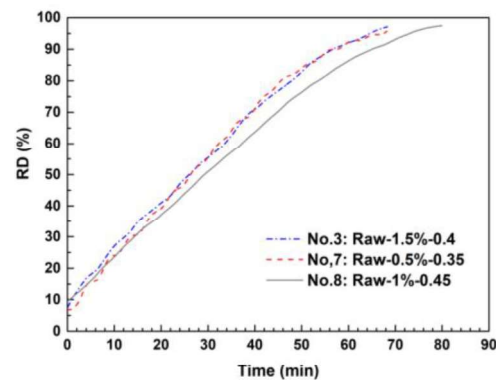


Figure 4. The reduction curves of raw magnetite samples.

3.3. Structural Analysis

To figure out the reason for the reduction behaviors, the morphology of the reduced samples was analyzed via an optical microscope. The reduced particles of the raw magnetite sample are shown in Figure 5. According to Hayes et al. [29,30], the iron morphology obtained by reducing magnetite is mainly controlled by the reduction mechanism. Wolfinger et al. [31] share a similar opinion and found that, for magnetite iron ore ultra-fines, when the reduction is conducted at low temperatures ($<675\text{ }^{\circ}\text{C}$) and controlled by the chemical reaction in the initial reduction stage, a porous iron layer can be formed. However, at higher temperatures ($>750\text{ }^{\circ}\text{C}$), a dense iron layer is formed due to the fast generation of iron and built up in the wüstite. In the present study, the surfaces of the reduced magnetite particles are covered by porous iron layers. From Figure 5a,d, a dense wüstite core is observed, and the porous iron layer is thinner than the other two reduced magnetite samples. It indicates that the reduction of the raw magnetite sample is controlled by the chemical reaction in the initial stage. As the reaction continues, the newly formed iron nuclei accumulate and build a dense iron core within the particles. Iron nuclei accumulate more rapidly at higher gas velocities and form a thinner, porous iron shell, leading to difficulties in gas diffusion within the particles. As shown in Figure 5b,c,e,f, the porous iron shells are much bigger than those in Figure 5a,d. The gas diffuses more easily into the particles, resulting in a higher reduction rate.

As shown in Figure 6a,b,d,e, for the oxidized samples oxidized at $800\text{ }^{\circ}\text{C}$, the obtained iron morphology is different from that of raw magnetite samples. Instead of porous iron layers, many coarse iron grains are observed on the surface of the particles. From Figure 6c,f, it is seen that, in the sample with oxidation treatment at $1000\text{ }^{\circ}\text{C}$, the inner part of the reduced particle is porous as well. However, many wüstite islands are observed, indicating a poor reduction behavior. The iron morphology is consistent with our previous study [22]. The oxidation treatment parameters, including oxidation temperature and oxidation content, lead to changes in the reduction kinetic mechanism. The changes in kinetic mechanism are due to the coarse porous wüstite obtained during the reduction of oxidized magnetite [31]. The target of the present study is to confirm the optimum condition for reduction of magnetite ore. The polished section images of reduced samples support the conclusion drawn from the reduction curves, as discussed in Section 3.2.

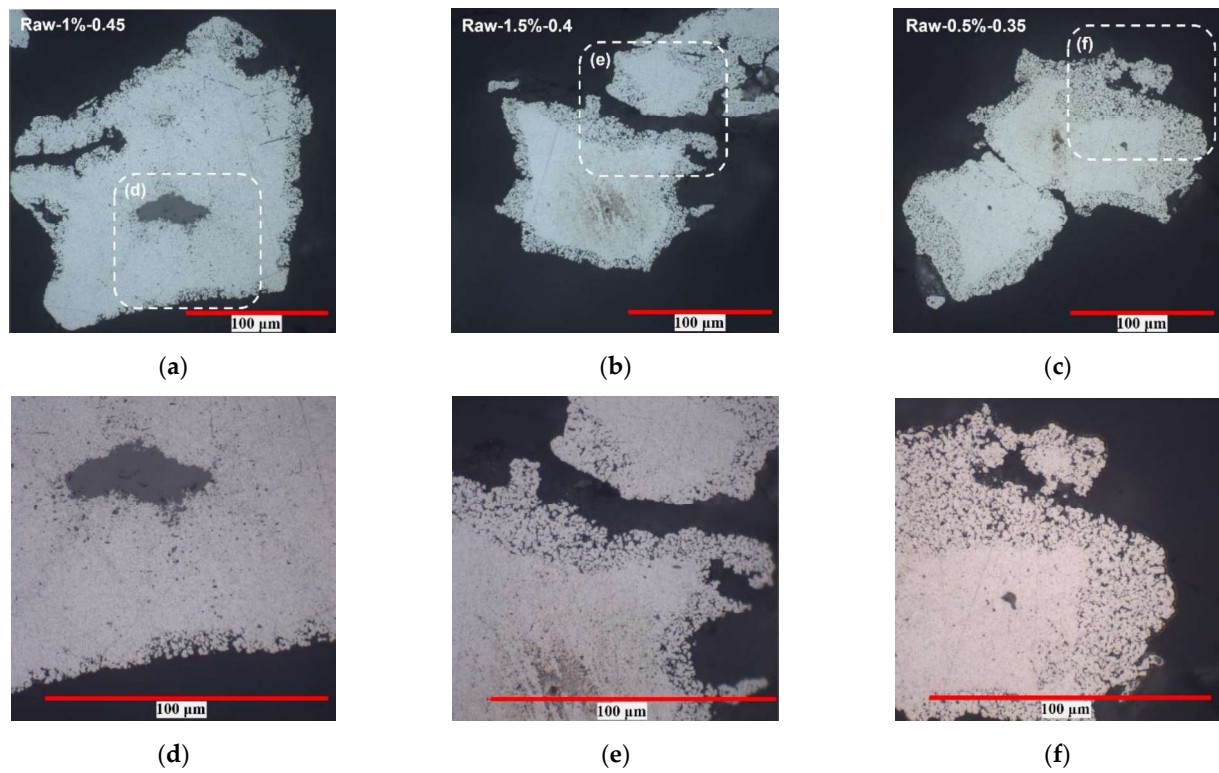


Figure 5. The polished section images of reduced iron ores: (a,d) Experiment No.8; (b,e) Experiment No.3; (c,f) Experiment No.7.

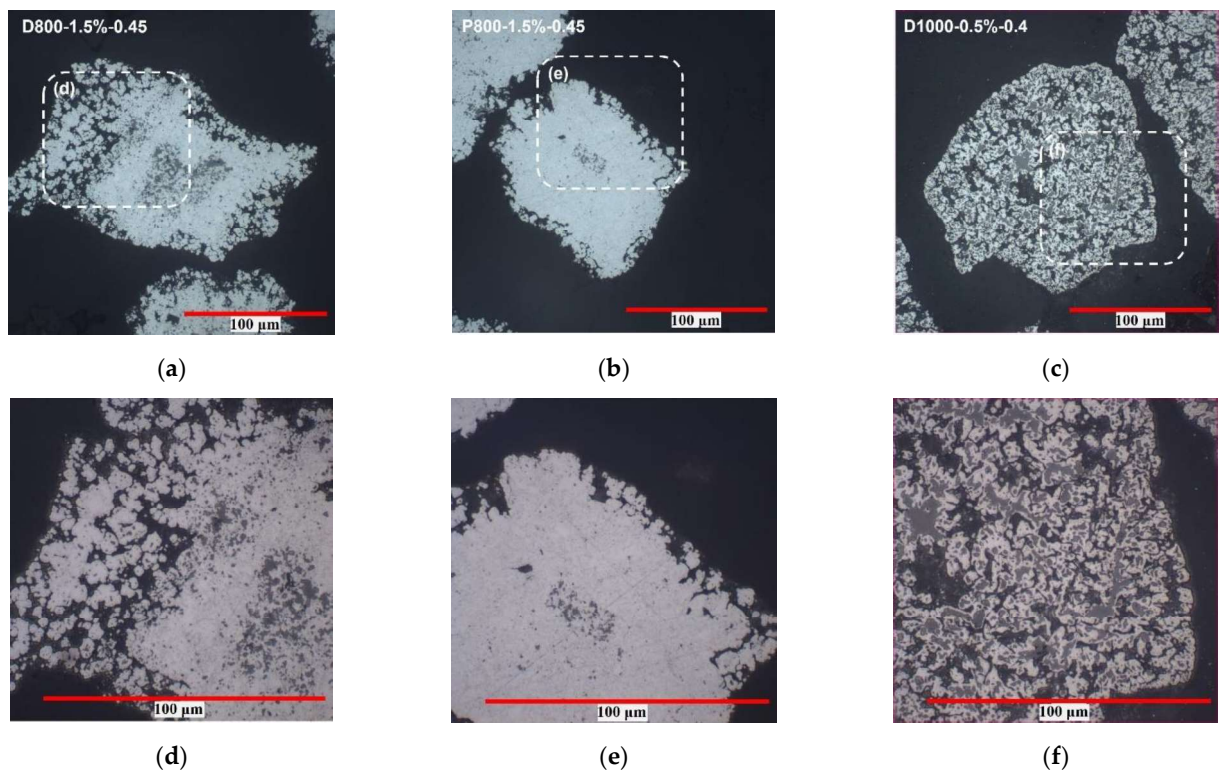


Figure 6. The polished section images of reduced iron ores: (a,d) Experiment No.6; (b,e) Experiment No.10; (c,f) Experiment No.2.

4. Conclusions

In conclusion, the optimum condition for hydrogen-induced fluidized bed reduction of magnetite iron ore fines is successfully determined by an orthogonal experimental method. Furthermore, the dominant factors that influence the reduction behaviors of the magnetite iron ore are confirmed. Under the experiment's conditions, the fluidization behavior is not a problem. Regarding reduction efficiency, the primary and secondary influencing factors are oxidation temperature, oxidation content, MgO addition amount, and gas velocity. The optimum condition is that the magnetite iron ore is deeply oxidized at 800 °C, mixed with 1.5 wt.% of MgO, and reduced in the fluidized bed at a gas velocity of 0.45 m/s.

Author Contributions: Conceptualization, H.Z.; methodology, H.Z. and B.T.; investigation, H.Z. and O.D.; writing—original draft preparation, H.Z.; writing—review and editing, J.S., O.D. and B.T.; supervision, J.S.; project administration, J.S.; funding acquisition, J.S. All authors have read and agreed to the published version of the manuscript.

Funding: This research was funded by K1-MET GmbH, metallurgical competence center (funding number FFG No. 869295). The research work was partially financed by Montanuniversitaet Leoben. Heng Zheng greatly acknowledges the financial support from the program of China Scholarship Council (No.201908420284).

Data Availability Statement: Not applicable.

Acknowledgments: All authors greatly acknowledge the funding support of K1-MET GmbH. The research program of the K1-MET competence center is supported by COMET (Competence Center for Excellent Technologies), the Austrian program for competence centers. COMET is funded by the Federal Ministry for Climate Action, Environment, Energy, Mobility, Innovation and Technology, the Federal Ministry for Digital and Economic Affairs, the provinces of Upper Austria, Tyrol and Styria, and the Styrian Business Promotion Agency (SFG).

Conflicts of Interest: The authors declare no conflict of interest.

Nomenclature

Symbol	Description	Unit
HyDRI	Hydrogen-based direct reduced iron	-
BF-BOF	Blast furnace–basic oxygen furnace	-
EAF	Electric arc furnace	-
RD	Reduction degree	%
DFI	De-fluidization index	%
Ave.DFI	Average de-fluidization index	%
$t_{90\%}$	The time to reach the reduction degree of 90%	min

References

- World Steel Association. About Steel. Available online: <https://worldsteel.org/about-steel/about-steel/> (accessed on 19 November 2022).
- World Steel Association. Total Production of Crude Steel. Available online: <https://worldsteel.org/steel-topics/statistics/world-steel-in-figures-2022/> (accessed on 19 November 2022).
- Bhaskar, A.; Assadi, M.; Nikpey Somehsaraei, H. Decarbonization of the Iron and Steel Industry with Direct Reduction of Iron Ore with Green Hydrogen. *Energies* **2020**, *13*, 758. [CrossRef]
- Kim, J.; Sovacool, B.K.; Bazilian, M.; Griffiths, S.; Lee, J.; Yang, M.; Lee, J. Decarbonizing the iron and steel industry: A systematic review of sociotechnical systems, technological innovations, and policy options. *Energy Res. Soc. Sci.* **2022**, *89*, 102565. [CrossRef]
- Rethink. Global Steel Demand to Grow 60% through 2050 Global Steel Demand to Grow 60% through 2050. Available online: <https://rethinkresearch.biz/articles/global-steel-demand-to-grow-60-through-2050/> (accessed on 19 November 2022).
- International Energy Agency. *Iron and Steel Technology Roadmap*; OECD: Paris, France, 2020; p. 37. [CrossRef]
- He, K.; Wang, L. A review of energy use and energy-efficient technologies for the iron and steel industry. *Renew. Sustain. Energy Rev.* **2017**, *70*, 1022–1039. [CrossRef]
- Li, Z.; Hanaoka, T. Plant-level mitigation strategies could enable carbon neutrality by 2060 and reduce non-CO₂ emissions in China's iron and steel sector. *One Earth* **2022**, *5*, 932–943. [CrossRef]
- Patisson, F.; Mirgaux, O. Hydrogen Ironmaking: How It Works. *Metals* **2020**, *10*, 922. [CrossRef]

10. Toktarova, A.; Karlsson, I.; Rootzén, J.; Göransson, L.; Odenberger, M.; Johnsson, F. Pathways for Low-Carbon Transition of the Steel Industry—A Swedish Case Study. *Energies* **2020**, *13*, 3840. [[CrossRef](#)]
11. Birat, J.-P. Society, Materials, and the Environment: The Case of Steel. *Metals* **2020**, *10*, 331. [[CrossRef](#)]
12. Bellona Foundation. Hydrogen in Steel Production: What Is Happening in Europe—Part Two. Available online: <https://bellona.org/news/industrial-pollution/2021-05-hydrogen-in-steel-production-what-is-happening-in-europe-part-two> (accessed on 14 November 2021).
13. Vogl, V.; Åhman, M.; Nilsson, L.J. Assessment of hydrogen direct reduction for fossil-free steelmaking. *J. Cleaner Prod.* **2018**, *203*, 736–745. [[CrossRef](#)]
14. Schenk, J.L. Recent status of fluidized bed technologies for producing iron input materials for steelmaking. *Particuology* **2011**, *9*, 14–23. [[CrossRef](#)]
15. Ma, Y.; Souza Filho, I.R.; Bai, Y.; Schenk, J.; Patisson, F.; Beck, A.; van Bokhoven, J.A.; Willinger, M.G.; Li, K.; Xie, D.; et al. Hierarchical nature of hydrogen-based direct reduction of iron oxides. *Scr. Mater.* **2022**, *213*, 114571. [[CrossRef](#)]
16. Daniel, S.; Johann, W.; Bernhard, H.; Norbert, R.; Thomas, W.; Wolfgang, S.; Alexander, F. HYFOR—Hydrogen-based Fine-Ore Reduction. *Mitsubishi Heavy Ind. Tech. Rev.* **2022**, *59*, 1–5. Available online: <https://www.mhi.co.jp/technology/review/pdf/e592/e592070.pdf> (accessed on 19 November 2022).
17. Guo, L.; Gao, H.; Yu, J.; Zhang, Z.; Guo, Z. Influence of hydrogen concentration on Fe₂O₃ particle reduction in fluidized beds under constant drag force. *Int. J. Miner. Metall. Mater.* **2015**, *22*, 12–20. [[CrossRef](#)]
18. Guo, L.; Bao, Q.; Gao, J.; Zhu, Q.; Guo, Z. A Review on Prevention of Sticking during Fluidized Bed Reduction of Fine Iron Ore. *ISIJ Int.* **2020**, *60*, 1–17. [[CrossRef](#)]
19. Shao, J.; Guo, Z.; Tang, H. Effect of Coating MgO on Sticking Behavior during Reduction of Iron Ore Concentrate Fines in Fluidized Bed. *Steel Res. Int.* **2013**, *84*, 111–118. [[CrossRef](#)]
20. Du, Z.; Zhu, Q.; Yang, Y.; Fan, C.; Pan, F.; Sun, H.; Xie, Z. The Role of MgO Powder in Preventing Defluidization during Fluidized Bed Reduction of Fine Iron Ores with Different Iron Valences. *Steel Res. Int.* **2016**, *87*, 1742–1749. [[CrossRef](#)]
21. Zheng, H.; Spreitzer, D.; Wolfinger, T.; Schenk, J.; Xu, R. Effect of Prior Oxidation on the Reduction Behavior of Magnetite-Based Iron Ore During Hydrogen-Induced Fluidized Bed Reduction. *Metall. Mater. Trans. B* **2021**, *52*, 1955–1971. [[CrossRef](#)]
22. Zheng, H.; Daghighaleh, O.; Wolfinger, T.; Taferner, B.; Schenk, J.; Xu, R. Fluidization behavior and reduction kinetics of pre-oxidized magnetite-based iron ore in a hydrogen-induced fluidized bed. *Int. J. Miner. Metall. Mater.* **2022**, *29*, 1873–1881. [[CrossRef](#)]
23. Zheng, H.; Schenk, J.; Xu, R.; Daghighaleh, O.; Spreitzer, D.; Wolfinger, T.; Yang, D.; Kapelyushin, Y. Surface Morphology and Structural Evolution of Magnetite-Based Iron Ore Fines During the Oxidation. *Metall. Mater. Trans. B* **2022**, *53*, 1644–1660. [[CrossRef](#)]
24. Spreitzer, D.; Schenk, J. Fluidization behavior and reducibility of iron ore fines during hydrogen-induced fluidized bed reduction. *Particuology* **2020**, *52*, 36–46. [[CrossRef](#)]
25. Skorianz, M.; Mali, H.; Pichler, A.; Plaul, F.; Schenk, J.; Weiss, B. Reduction Behavior and Structural Evolution of Iron Ores in Fluidized Bed Technologies. Part 1: Method for the Determination. *Steel Res. Int.* **2016**, *87*, 633–641. [[CrossRef](#)]
26. Pichler, A.; Mali, H.; Plaul, F.; Schenk, J.; Skorianz, M.; Weiss, B. Reduction Behavior and Structural Evolution of Iron Ores in Fluidized Bed Technologies-Part 2: Characterization and Evaluation of Worldwide Traded Fine Iron Ore Brands. *Steel Res. Int.* **2016**, *87*, 642–652. [[CrossRef](#)]
27. Zhang, B.; Wang, Z.; Gong, X.; Guo, Z. A comparative study of influence of fluidized conditions on sticking time during reduction of Fe₂O₃ particles with CO. *Powder Technol.* **2012**, *225*, 1–6. [[CrossRef](#)]
28. Xu, Q.; Wang, H.; Fu, Y.; Wang, J. Parameters Optimization, Sticking Mechanism and Kinetics Analysis of Fine Iron Ore in Fluidized-Reduction Process. *ISIJ Int.* **2016**, *56*, 1929–1937. [[CrossRef](#)]
29. Matthew, S.P.; Cho, T.R.; Hayes, P.C. Mechanisms of porous iron growth on wustite and magnetite during gaseous reduction. *Metall. Mater. Trans. B* **1990**, *21*, 733–741. [[CrossRef](#)]
30. Matthew, S.P.; Hayes, P.C. Microstructural changes occurring during the gaseous reduction of magnetite. *Metall. Mater. Trans. B* **1990**, *21*, 153–172. [[CrossRef](#)]
31. Wolfinger, T.; Spreitzer, D.; Zheng, H.; Schenk, J. Influence of a Prior Oxidation on the Reduction Behavior of Magnetite Iron Ore Ultra-Fines Using Hydrogen. *Metall. Mater. Trans. B* **2022**, *53*, 14–28. [[CrossRef](#)]

Disclaimer/Publisher’s Note: The statements, opinions and data contained in all publications are solely those of the individual author(s) and contributor(s) and not of MDPI and/or the editor(s). MDPI and/or the editor(s) disclaim responsibility for any injury to people or property resulting from any ideas, methods, instructions or products referred to in the content.

Review on the Oxidation Behaviors and Kinetics of Magnetite in Particle Scale

Heng Zheng,* Johannes Schenk, Daniel Spreitzer, Thomas Wolfinger, and Oday Daghagheleh

One possible route for ironmaking process is using a hydrogen-gas-based fluidized bed to produce direct reduced iron (DRI), which allows to use the natural magnetite directly in particle scale. The magnetite particles are oxidized during the preheating stage before being charged into the reduction unit. The exothermic effect, the crystal transformation, and the structural evolution during the oxidation of magnetite are introduced. The oxidation of magnetite is summarized in both thermodynamics and kinetics aspects. Furthermore, the influence of the oxidation of magnetite on its subsequent reduction behavior is examined.

directly within the blast furnace or in common direct reduction facilities. The current practice of ironmaking from magnetite concentrates usually involves a pelletization process before charging it into the ironmaking facility.^[10–13] Reduction of iron ore fines is an economically reasonable process. For a net-zero greenhouse gas emission, one possible route for future crude steel production is using a hydrogen-gas-based fluidized bed to produce hydrogen direct reduced iron (HDRI), followed by an electric arc furnace.^[14,15] The fluidized bed provides an

1. Introduction

In the past few decades, the ironmaking industry has consumed most of the high-grade hematite ore, which was used as the main iron carrier in the blast furnace process.^[1,2] As a result, good quality hematite ores are about to run out. The available ores are becoming much more expensive and the quality is decreasing. The global production of magnetite iron ore in 2015 is 583 million tons, which accounts for 28% of the total iron ore production.^[3] It is time to come up with an idea to use lower-cost iron ores with sufficient reserves for ironmaking.^[4,5]

The natural magnetite is widely present in various rock minerals.^[6,7] Because isomorphous substitution occurs in the structure of such magnetite iron ores, a beneficiation process is required to decrease the gangue and increase the total iron content.^[8,9] Usually, the magnetite iron ore is ground to a small particle size to release magnetite from its rock matrix, followed by magnetic separation.^[7] These kinds of magnetite iron ore fines cannot be used

opportunity to directly use the magnetite in particle scale.

Reduction by H₂ is an endothermic reaction. Before charging the iron ore into the reduction unit, a preheating system could help to ensure a sufficient energy supply. Generally, the preheating process occurs in oxidizing atmosphere. As a result, the magnetite particles become oxidized. The oxidation of magnetite is an exothermic reaction, generating considerable heat, which in turn helps to reduce the primary energy.^[16,17]


Rarely literature quantitatively evaluated the exothermic effect of the oxidation magnetite iron ore. The fundamental structural evolution and crystal transformation of magnetite during oxidation is essential and necessary information, which helps to understand the oxidation process and effect of oxidation on the subsequent reduction behavior. The aim of this article is to provide a brief review and overall appraisal of the published works that related to the oxidation of magnetite in particle scale. Furthermore, the influence of oxidation of magnetite on its subsequent reduction behavior is discussed.

2. Stages of the Oxidation Process

Natural magnetite, which is purified by magnetic separation, still contains small amounts of impurities. The oxidation of magnetite at least contains two stages. Colombo et al.^[18,19] investigated the first stage of oxidation of magnetite. The results confirm that in the first oxidation stage, an intermediate phase exists, which consists of a solid solution of γ -Fe₂O₃ in Fe₃O₄. The impurities could stabilize the γ -Fe₂O₃ phase. However, the final oxidation product depends largely on oxidation temperature. Chen et al.^[20] illustrated the main structural and chemical difference between γ -Fe₂O₃ and Fe₃O₄. The difference is the existence of vacancies in γ -Fe₂O₃, which reduces the symmetry of γ -Fe₂O₃ (primitive Bravais lattice) with respect to Fe₃O₄ (face-centered Bravais lattice). Fe²⁺ in Fe₃O₄ is completely replaced by Fe³⁺ (Fe²⁺ → Fe³⁺ + e⁻), so the positions that were occupied by 1/3Fe²⁺ in octahedron

H. Zheng, Prof. J. Schenk, Dr. D. Spreitzer, O. Daghagheleh
Chair of Ferrous Metallurgy
Montanuniversität Leoben
Franz-Josef-Straße 18, 8700 Leoben, Austria
E-mail: heng.zheng@stud.unileoben.ac.at

T. Wolfinger
Area 3, Low Carbon Energy Systems
K1-MET GmbH
Stahlstraße 14, 4020 Linz, Austria

 The ORCID identification number(s) for the author(s) of this article can be found under <https://doi.org/10.1002/srin.202000687>.

© 2021 The Authors. Steel Research International published by Wiley-VCH GmbH. This is an open access article under the terms of the Creative Commons Attribution-NonCommercial License, which permits use, distribution and reproduction in any medium, provided the original work is properly cited and is not used for commercial purposes.

DOI: 10.1002/srin.202000687

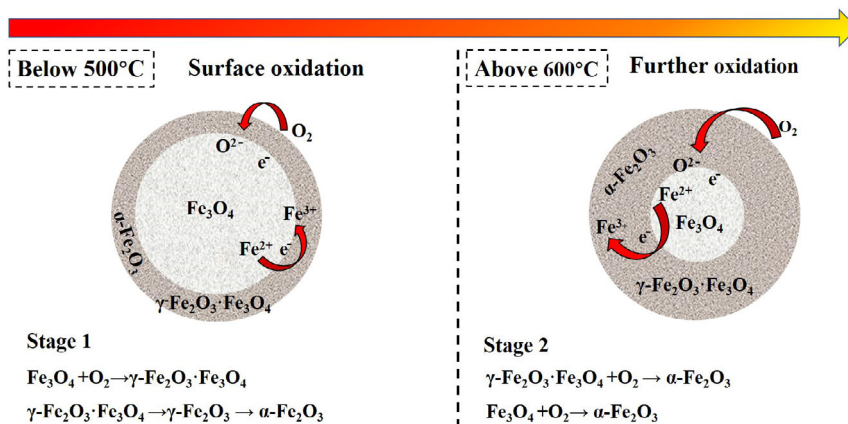


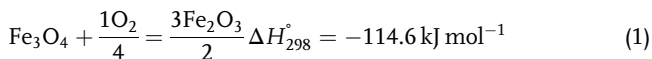
Figure 1. Stages of magnetite during nonisothermal oxidation.

become the vacancies. $\gamma\text{-Fe}_2\text{O}_3$ shows a ferromagnetic behavior, whereas $\alpha\text{-Fe}_2\text{O}_3$ shows an antiferromagnetic behavior.

The oxidation mechanism of magnetite is assumed as the following. The oxidation of Fe^{2+} to Fe^{3+} causes diffusion of iron ions from inside the crystals of Fe_3O_4 toward the surface. The solid solution of $\gamma\text{-Fe}_2\text{O}_3$ in Fe_3O_4 is formed at the beginning of the oxidation. As the oxidation proceeds, the formation of $\alpha\text{-Fe}_2\text{O}_3$ and the solid solution appears at the surface of the magnetite particle. Later, through a reaction catalyzed by the presence of $\alpha\text{-Fe}_2\text{O}_3$, the solid solution is transformed into $\alpha\text{-Fe}_2\text{O}_3$ and Fe_3O_4 . The secondary Fe_3O_4 will be oxidized directly to $\alpha\text{-Fe}_2\text{O}_3$ at high temperatures. Therefore, the oxidation stages of magnetite particles can be interpreted, as shown in **Figure 1**.

3. Oxidation Behaviors

The oxidation of magnetite, which is an exothermic reaction, can be simply expressed by Equation (1).^[16] The heat generated from the oxidation of 1 mol Fe_3O_4 is roughly equivalent to that of 0.29 mol carbon combusted into CO_2 .^[17] In addition to the exothermic effect, the oxidation behavior is also accompanied by crystal transformation and structural evolution.



3.1. Exothermic Effect

One possible technique for the description of the exothermic behavior is differential thermal analysis (DTA). The sample is heated side by side with a thermally inert material in a suitable sample holder, recording the occurring temperature difference ΔT between the two materials while heating.^[21] When the temperature reaches a certain characteristic value for the sample, physical changes or chemical reactions will occur, accompanied by heat absorption or heat release. By recording the temperature difference ΔT and time, the thermal effect can be identified.

DTA tests have been widely used to study the oxidation of magnetite.^[22,23] The latest quantitative study on the exothermic effect of the oxidation of natural magnetite was conducted by Yur'ev et al.^[24] The natural magnetite, which contained

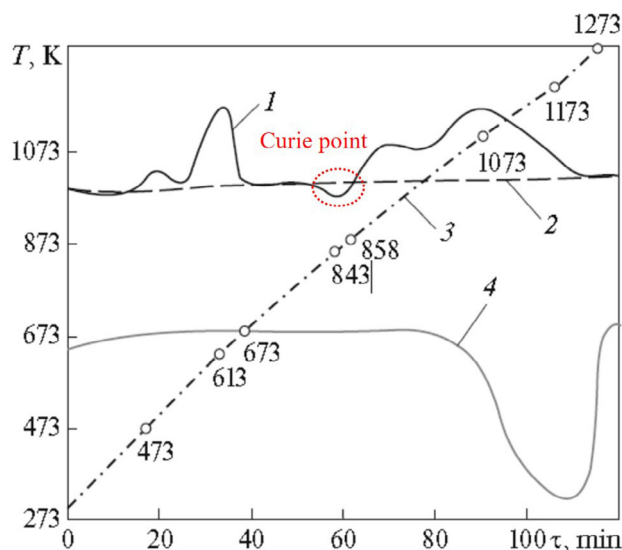


Figure 2. Temperature variation on sample heating: 1) differential heating curve of natural magnetite; 2) baseline with $\Delta T = 0$; 3) temperature variation of the material; and 4) differential heating curve for calcium carbonate. Adapted with permission.^[24] Copyright 2016, CC BY 4.0.

99.2 wt.% Fe_3O_4 , 0.12 wt.% SiO_2 , 0.12 wt.% TiO_2 , 0.30 wt.% Al_2O_3 , 0.12 wt.% MgO , and few other oxide gangues, was heated under air flow. As shown in **Figure 2**, the two peaks represent two reaction stages. The first exothermic effect is assumed as a surface oxidation of magnetite forming an $\alpha\text{-Fe}_2\text{O}_3$ layer. After the complete surface oxidation of the magnetite grains, the oxidation process slows down significantly due to the low diffusion coefficients of oxygen atoms and iron ions through the product layer. This corresponds to the horizontal line between the two peaks in **Figure 2**. After surface oxidation, the formation of microcracks and lattice defects is accelerated with increasing temperature. In addition, the diffusion coefficients increase with the temperature and therefore speed up the oxidation process, which corresponds to the second exothermic effect in **Figure 2**. Schmidt et al.^[23] pointed out that the peak shapes can be linked to the magnetite particle size. With increasing particle size, the height of the first peak decreases but leads to an increase in the second peak.

As discussed by Yur'ev et al.,^[24] the quantitative calculation of the thermal effect of magnetite oxidation can be conducted in reference to the analytical-grade calcium carbonate sample, as shown in Figure 2. The Curie point of magnetite is at around 573 °C (846.15 K). On reaching the Curie point, accounting for the sharp change in magnetic state and the internal magnetic energy of the material, heat is absorbed or liberated. Consequently, the Curie point appears on the differential heating curves as a slight reversible endothermal peak shown in the red circle part of Figure 2. Based on Equation (2), the heat liberated in the oxidation of 1 kg of magnetite is about 491 kJ kg⁻¹ (=113.9 kJ mol⁻¹), which is close to the ideal value of 114.6 kJ mol⁻¹ shown in Equation (1).

$$Q(\text{Fe}_3\text{O}_4) = Q(\text{CaCO}_3)S(\text{Fe}_3\text{O}_4)/S(\text{CaCO}_3) \quad (2)$$

where $Q(\text{CaCO}_3)$ is the heat required for the decomposition of 1 kg CaCO_3 ; $S(\text{Fe}_3\text{O}_4)$ is the total area of the figure for the differential heating curve associated with magnetite oxidation; and $S(\text{CaCO}_3)$ is the area of the figure for the differential heating curve associated with CaCO_3 decomposition.

Assuming under adiabatic conditions, if the composition of natural magnetite and the amount of oxidation heat are available, the increasing temperature due to the oxidation heat can be calculated by Equation (3)–(4).

$$\Delta T = Q/(m_{\text{mixture}}C_{\text{mixture}}) \quad (3)$$

$$C_{\text{mixture}} = (m_1/m_{\text{mixture}})C_1 + (m_2/m_{\text{mixture}})C_2 + \dots + (m_n/m_{\text{mixture}})C_n \quad (4)$$

where ΔT is the increasing temperature, Q is the amount of heat, m_{mixture} is the sample mass, C_{mixture} is the specific heat capacity of the sample, and $m_1, 2, \dots, n$ and $C_1, 2, \dots, n$ are the mass and specific heat capacity of each component in the sample.

The specific heat capacity of each component can be referred to from the National Institute of Standards and Technology (NIST).^[25] The specific heat capacity changes with temperatures. For an easier calculation, the specific heat capacities at 926.85 °C (1200 K) are chosen. Based on earlier case, the C_{mixture} is 866.63 J (kg °C)⁻¹. For 1 kg of natural magnetite, the increasing temperature ΔT is roughly 566 °C (839.15 K).

3.2. Crystal Transformation

The crystal parameters of magnetite can be characterized by X-ray diffraction (XRD) measurement. The crystal consists of regularly arranged unit cells. If a monochromatic X-ray beam enters the crystal, the X-ray is to be scattered by different atoms and interferes with each other. In general, it is difficult to distinguish maghemite ($\gamma\text{-Fe}_2\text{O}_3$) and magnetite (Fe_3O_4) using XRD analysis because of their similar crystal structure. The formation and identification of $\gamma\text{-Fe}_2\text{O}_3$ are not further discussed because they are beyond the research scope of this Review. There is no evidence to show the relations between the lattice constants and the oxidation behaviors. But it is interesting to know how the crystal transforms during oxidation.

Schmidt et al.^[23] found that the lattice constants of magnetite from different mines are likely to be slightly different. Table 1 shows the lattice constants measured from six different

Table 1. Lattice constants and chemical data.

Magnetite ore	Lattice constant a_0 [Å]	MgO [wt.%]	Al_2O_3 [wt.%]
A	8.394 (± 0.001)	1.48	0.38
B	8.389 (± 0.003)	1.73	0.45
C	8.398 (± 0.001)	0.67	0.09
D	8.386 (± 0.001)	1.05	0.07
E	8.387 (± 0.002)	2.55	0.75
F	8.392 (± 0.001)	0.095	0.46

magnetite ores. The theoretical lattice constant of Fe_3O_4 is 8.4045 Å. There seems to be a tendency for the size of the unit cell of Fe_3O_4 to decrease with a replacement of Fe^{2+} by Mg^{2+} . During oxidation, the lattice constant also changes. Gokhale^[26] oxidized magnetite at the heating rate of 10 °C min⁻¹ from ambient temperature to target temperature and then quenched them in cooling air. The oxidation degree was not mentioned. The lattice constants after oxidation were measured after cooling and are shown in Table 2. The lattice constant decreases with temperature up to 600 °C. He states that the diversity of the lattice constant is caused by the compromise between thermal expansion and lattice modification during oxidation.

The volume and crystallite size can also be calculated using the XRD method. Each unit cell of Fe_3O_4 and Fe_2O_3 contains eight Fe_3O_4 and six Fe_2O_3 molecules, respectively, as shown in Figure 3. The detailed information on the unit cell structure can be found in the ICSD database^[27] and other literatures.^[28,29] During oxidation, 8 $\text{Fe}_3\text{O}_4 \rightarrow 12 \text{Fe}_2\text{O}_3$, 8 Fe_3O_4 molecules would be oxidized into 12 Fe_2O_3 molecules (two units of structure). Without considering the effects of sintering between magnetite particles, the volume should be expanded due to the crystal transformation. Based on this

Table 2. Cell dimensions of magnetite at various stages of oxidation.

$a = b = c$ [Å]	Temperature
8.425	Magnetite at room temperature
8.402	Oxidized till 400 °C
8.395	Oxidized till 600 °C
8.457	Oxidized till 800 °C

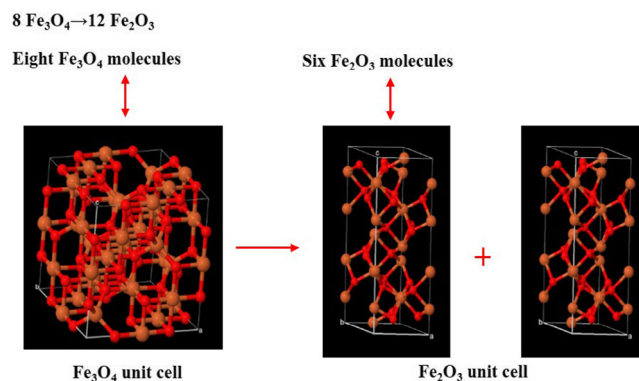


Figure 3. Transformation from magnetite unit to hematite units.

method, the expansion is defined to be 5.2%.^[30] It is also reported that the change of magnetite to hematite by natural metamorphism results in a volume increase of 2.5%.^[31] However, when temperature is higher than 330 °C, the volume shows contraction during oxidation due to the sintering effect.^[32] In our previous study, after oxidation of natural magnetite, the weight increases from 400 to 410 g. The apparent densities of the natural magnetite and the oxidized magnetite with oxidation degree higher than 90% are 4.96 and 5.02 g cm⁻³, respectively.^[33] Based on the weights and densities, the volume expansion is 1.27%.

The crystallite size of magnetite and hematite can be calculated using Scherrer's equation, as shown in Equation (5). **Figure 4** shows the crystallite size of Fe₂O₃ after oxidation of titanomagnetite ore. It is reported that the smaller the size of the crystallite, the more rapid the diffusion from one crystal to

another.^[30,34,35] The oxidation processes are regarded as the diffusion of oxygen and iron atoms in the lattice. The crystallite size could be a reason for the diversities of the oxidation rate for different magnetite iron ores and could result in different reduction rates in the subsequent reduction section.

$$D = \frac{K\lambda}{\beta \cos \theta} \quad (5)$$

where D is crystallites size (nm); K is equal to 0.94 (Scherrer constant); λ is equal to 0.15406 nm (the wavelength of X-ray source); β is full width at half maximum (radians), and θ is peak position (radians).

3.3. Structural Evolution

During the oxidation of magnetite, two different typical surface morphologies would be formed—whiskers and rough pleated structures, which are related to oxidation conditions. Song et al.^[36] found that during the oxidation of magnetite in air atmosphere, the hematite whiskers occur. During the oxidation of magnetite, the diameter of whiskers does not change much, as shown in **Figure 5**, indicating that the whiskers are likely to be generated in the early oxidation stages. It is explained that the whisker formation is caused by the volume increase when magnetite oxidizes to hematite. The driving force for the evolution of hematite whiskers is the compressive stress. Similar whisker structures are also found in the oxidation of fayalite and pure iron. Gaballah et al.^[37] observed the hematite whiskers in an oxidation experiment of fayalite. The particle surface is first covered by a granular layer, which then breaks before the whisker formation starts. Microprobe analysis showed that the whiskers are made of iron oxide growing on a silica substrate. Shao et al.^[38] conducted an in situ oxidation experiment of pure iron using an environmental scanning electron microscope, the growth path of the whiskers is explained, as shown in **Figure 6**. Above the Fe surface, there are

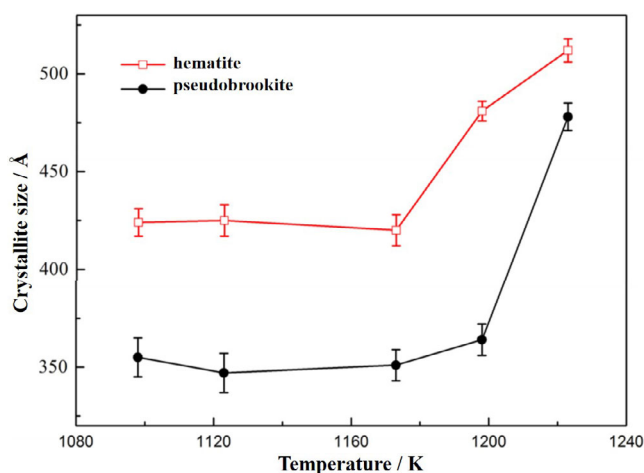


Figure 4. Average crystallite sizes of Fe₂O₃ and Fe₂TiO₅ at different temperatures. Adapted with permission.^[34] Copyright 2017, Springer Nature.

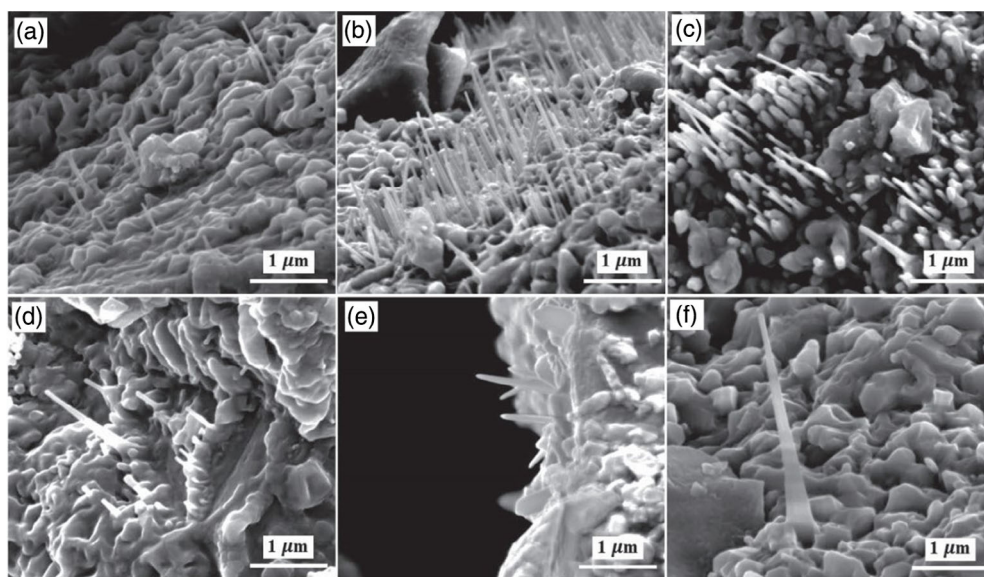


Figure 5. Formation of hematite whiskers during the oxidation: a–c) 800 °C for 10, 30, and 60 min; d–f) 900 °C for 10, 20, and 30 min. Adapted with permission.^[36] Copyright 2019, The Iron and Steel Institute of Japan.

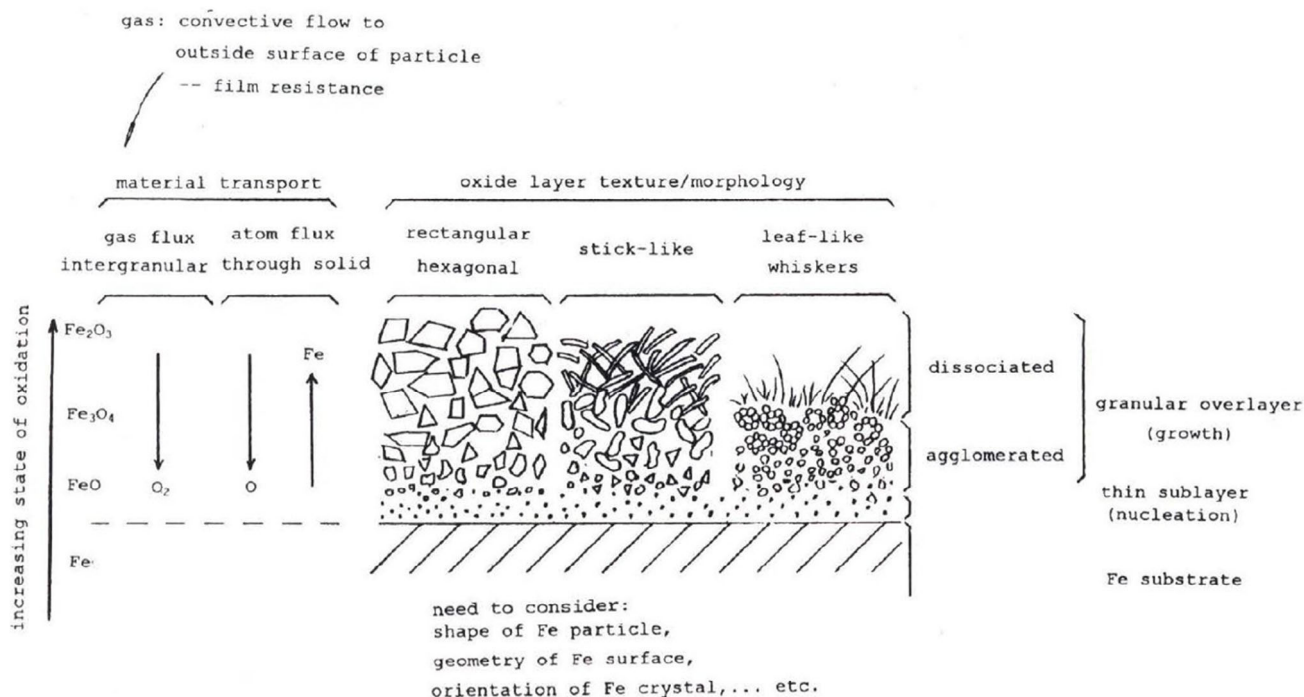
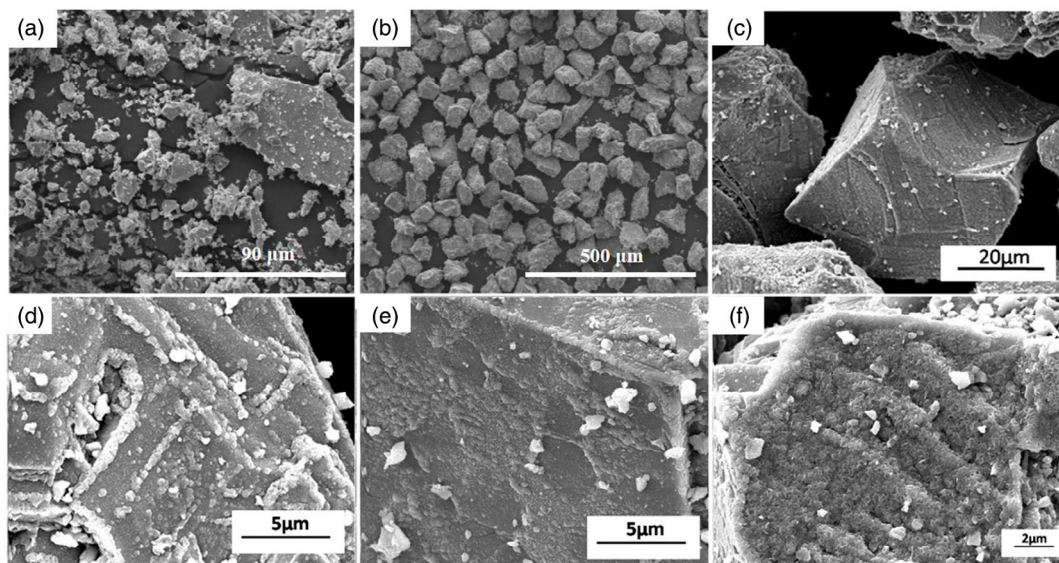


Figure 6. Plausible physical model for the oxidation of Fe based on environmental scanning electron microscope observations. Reproduced with permission.^[38] Copyright 1997, John Wiley and Sons.

three oxide layers. Close to the Fe surface is a thin layer composed of small nascent oxide nuclei. Above this first layer is a relatively compact intermediate layer, which consists of agglomerated grains. Next to the intermediate layer is another layer of younger grains. The morphology of the last oxide layer depends on the inherent nature of the iron base and the reaction conditions.

However, it should be pointed out that the formation of hematite whiskers does not always occur during the oxidation of magnetite. Cho et al.^[39] observed that the magnetite particle surface becomes rough after oxidation, which is explained by the outward growth of hematite. **Figure 7** shows the outgrowth of hematite, which is also the common surface morphology of



(a) Unoxidized magnetite concentrate;
(b) Wet screened material; material collected between 53 μ m to 63 μ m;
(c-f) After oxidation in air at 600 °C for 30 minutes.

Figure 7. scanning electron microscope image of magnetite concentrate after oxidation in air at 600 °C for 30 min. Adapted with permission.^[39] Copyright 2011, Association for Iron & Steel Technology (AIST).

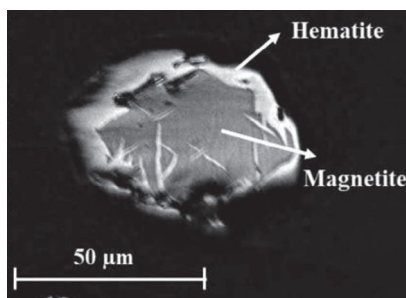


Figure 8. Inward growth of hematite. Adapted with permission.^[36] Copyright 2019, The Iron and Steel Institute of Japan.

oxidized magnetite particles. Hematite is generated along preferential planes, forming laths of hematite product on the surface. Wang et al.^[40] conducted the oxidation of iron-sand (Ti–magnetite ore). They found from BET tests that the hysteresis loop in the adsorption–desorption isotherms shows that the pores in the preoxidized iron-sand are connected in a network, whereas for the raw iron-sand, the pores are blocked and separated from each other.

The surface hematite layer of the particle does not grow uniformly. The hematite in the product layer could grow inward to the magnetite core and generates a needle-like structure, as shown in **Figure 8**. It is postulated that the hematite needles are formed by solid-state diffusion of ions into the magnetite matrix.^[41]

4. Thermodynamics of Magnetite Oxidation

Spreitzer et al.^[42] calculated the thermodynamically stable phases in the binary Fe–O system, as shown in **Figure 9**. Hematite phase is the oxide with the highest oxygen content, followed by magnetite. The ideal stoichiometries of hematite and magnetite are Fe_2O_3 and Fe_3O_4 , respectively. Theoretically, magnetite is in equilibrium with hematite at low temperature. There are two small magnetite-phase stable areas at high temperatures. A closer look into the equilibrium of Fe_3O_4 and Fe_2O_3 under different temperatures and O_2 partial pressures is shown in **Figure 10**. The diagram shows the stable area of a single Fe_3O_4 phase under different temperatures and O_2 partial pressures. From a thermodynamic point of view, magnetite can be completely oxidized to hematite even at normal ambient conditions. However, because of the complexity of the oxidation process and the restriction of kinetic conditions, a complete oxidation of magnetite is generally impossible. In the following sections, the oxidation kinetic analysis is examined.

5. Rate-Limiting Mechanisms

The International Confederation for Thermal Analysis and Calorimetry (ICTAC) recommended the kinetics-analyzing methods and guidance for reliable evaluation of kinetic parameters.^[43,44] It must be pointed out that the oxidation process is not only influenced by the oxidation conditions but also

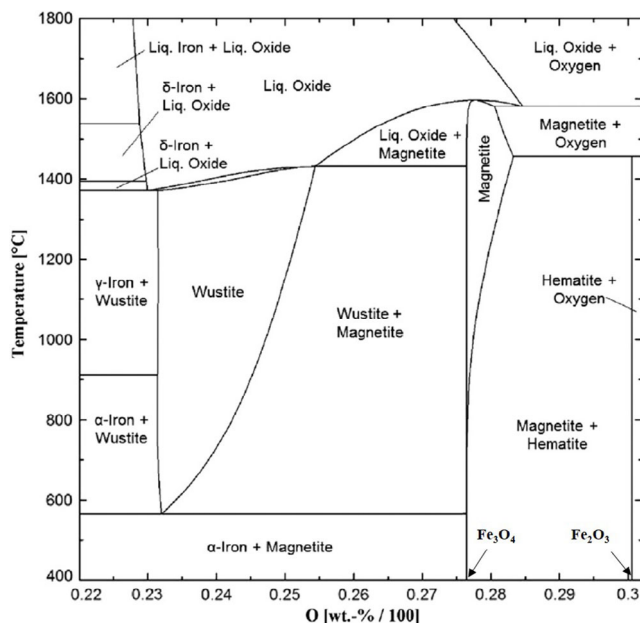


Figure 9. Binary Fe–O system. Reproduced with permission.^[42] Copyright 2020, CC BY-NC-ND 4.0.

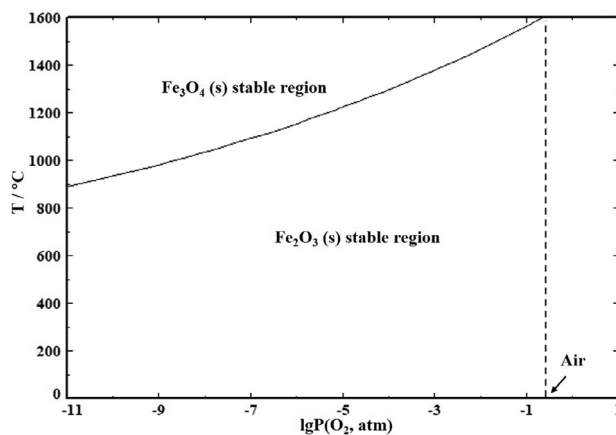


Figure 10. Stable region of Fe_3O_4 and Fe_2O_3 (calculated by Fact Sage 7.2, Database: FactPS, FToxid).

the facilities and even the sample containers. **Figure 11** shows three typical thermogravimetric analysis (TGA) apparatuses. The differences are the direction of gas flow and the sample containers. It is difficult to decide which kind of apparatus is the best option. When a crucible is used as the container, the gas flow can only penetrate the sample from top to bottom, because the gas flow cannot pass through the crucible. The interruption of the gas flow caused by the crucible and the thickness of the sample layer may influence the kinetic analysis. In the case of the basket, the gas flow is able to pass through the sample from the bottom to top with minor disturbances. In the oxidation TGA test of magnetite in particle scale, the most important thing is to prevent the experimental errors that are caused by mass transfer or mixing issues.

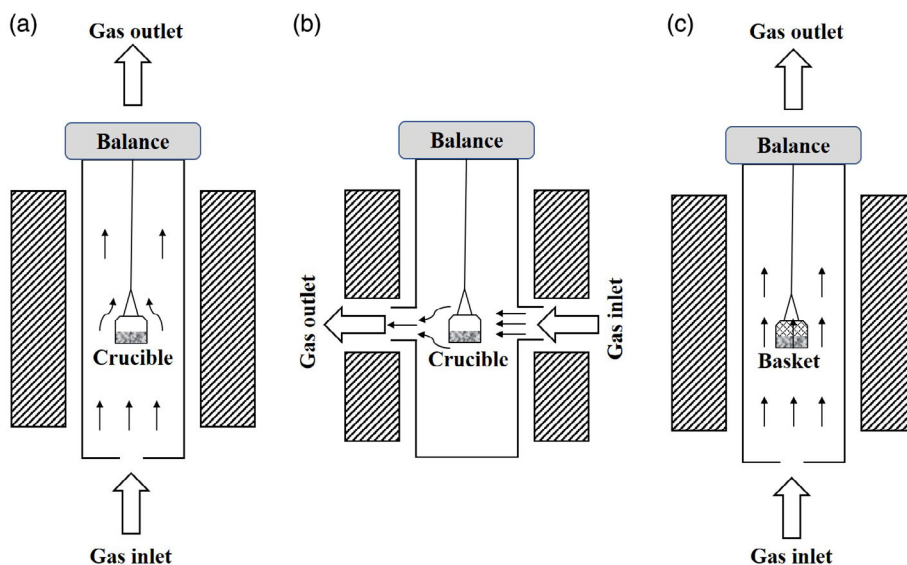


Figure 11. Schematic of oxidation facilities and sample containers.

From a thermodynamic point of view, the oxidation of magnetite to hematite is a spontaneous reaction. The chemical reaction is rarely the rate-limiting step. It is well established that, for oxidation of the pellet, the oxidation kinetics follows mixture rate-limiting steps: gaseous mass transfer of molecular oxygen through macroscopic pores into the pellet and solid-state diffusion within the oxidized particles.^[45] However, in particle scale, the gaseous mass transfer between particles is usually neglected. It is almost impossible for oxygen molecules to diffuse into the particle due to the dense structure of both magnetite and hematite layer. The rate-limiting step for oxidation of magnetite in particle scale is considered as solid-state diffusion. The solid-state diffusion can be described by parabolic law. In this case, the nature of solid-state diffusion is ion (Fe^{2+} , Fe^{3+} , or O^{2-}) diffusion through the hematite layer. When the chemical reaction at the interface occurs much faster than the diffusion, the interface should move uniformly inward to the center of the particle. However, the magnetite particles usually are not spherical. The magnetite shows being preferentially oxidized in a certain orientation, where the ion diffusion is faster than other orientations, resulting in the inward growth of hematite needles. The irregular shape of the particles and the inward-growth hematite may have an impact on kinetic analysis. Monsen^[46] believes that the O^{2-} has limited mobility in magnetite and hematite, which is only possible to diffuse along the hematite–magnetite boundaries to a small extent. In pellet oxidation, the effect of inward-growth hematite is usually ignored because it contributes to a limited oxidation degree. Therefore, the oxidation process of magnetite in pellet and particle scale is shown in **Figure 12**.

Monsen^[46] found that under a polarized light microscope, hematite that oxidized from the magnetite particle was found to be formed by several subgrain structures. The higher the oxidation temperature, the bigger each hematite subgrain. **Figure 13** shows the schematic of hematite subgrains in an oxidized magnetite particle. It is possible to describe the growth of subgrain structures by nucleation and growth mechanism. The model is

known as the JMA model that is developed by Johnson, Mehl, and Avrami.^[47–50] The nucleation and growth mechanism do not contradict with the parabolic law. The nature of these two mechanisms both involves ion diffusions. In the following sections, these two kinetic mechanisms are discussed.

5.1. Parabolic Law

Cho and Pistorius^[39,45,51,52] investigated the oxidation kinetics of magnetite concentrates using parabolic law. The parabolic law refers to solid-state diffusion. Taking particle size into consideration, then, oxidation process is shown in Equation (6). The particle size was obtained by wet screening.

$$t = \left[\frac{d^2}{24k_p} \right] \times [3 - 2\alpha - 3(1 - \alpha)^{\frac{2}{3}}] \quad (6)$$

where t is the oxidation time, d is the diameter of magnetite particle, k_p is the parabolic rate constant, and α is the oxidation degree. To quantitatively estimate the parabolic rate constant, magnetite concentrate particles with a narrow size range between 53 μm and 63 μm were oxidized at 500, 600, and 800 °C under 80 pct N_2 –20 pct O_2 gas mixture for 24 h. If the oxidation progress follows the parabolic law, a straight line would be obtained based on Equation (6). Monsen^[46] analyzed the oxidation of magnetite concentrate particles with size range between 74 and 100 μm in air flow at the temperature range of 400–800 °C using the same model. The oxidation process follows the parabolic law in these two works. The parabolic rate constant was estimated from the changes in hematite thickness. In another word, the measured parabolic rate constant indicates the macroscopic movement of the reaction front. Cho^[51] found that the parabolic rate constants in his work were similar to those calculated by Monsen^[46] and the oxidation rate is independent of oxygen contents (20 pct and higher). Pistorius^[45] found that only in extremely low partial pressure of oxygen can the parabolic rate

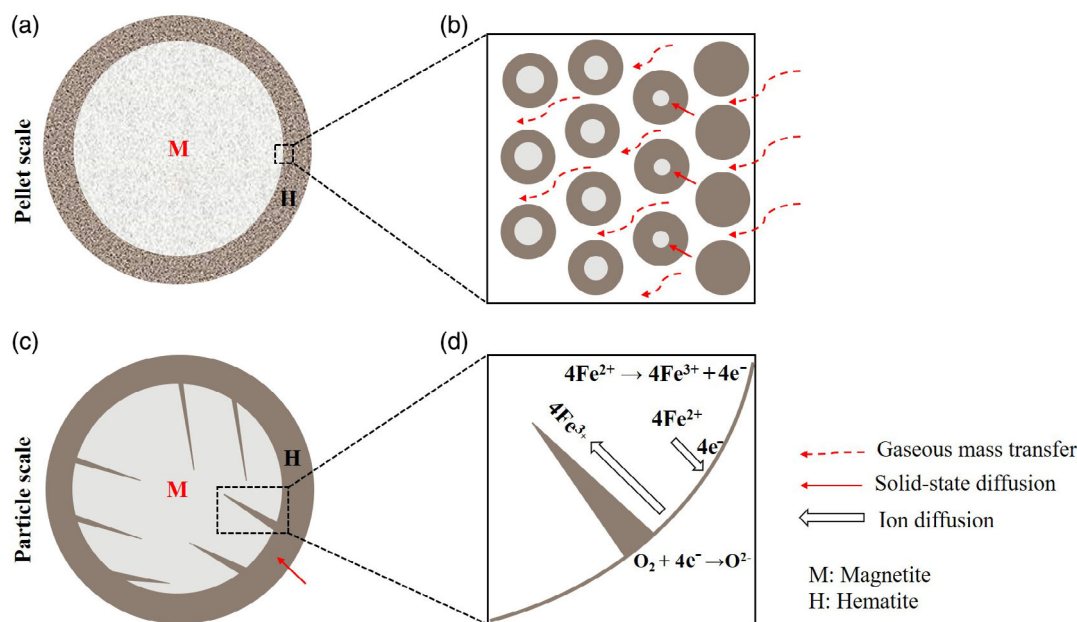


Figure 12. Schematic illustration of the oxidation kinetics: a,b) in pellet scale and c,d) in particle scale.

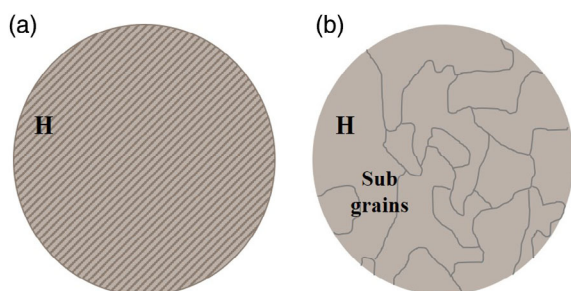


Figure 13. The schematic of hematite subgrains in an oxidized magnetite particle: a) under reflected light and b) under polarized light.

constant change with the oxygen content. The relationships between parabolic rate constants and partial pressure and temperature are shown in **Figure 14**. The parabolic rate constant is supposed to be stable in the same temperature. The average parabolic rate constant calculated by Cho and Pistorius is as follows.

$$k_p = 220 \exp\left(-\frac{65100}{RT}\right) \mu\text{m}^2 \text{min}^{-1} \quad (7)$$

Himmel et al.^[53] measured the self-diffusion coefficient (D) for iron in magnetite and hematite. For an easier comparison between k_p and D , they are transferred into the same unit with $\mu\text{m}^2/\text{min}$ and shown in **Table 3** and **4**. Table 3 indicates that the diffusion rate of iron in magnetite is several orders higher than that in hematite. The parabolic rate constants shown in Table 4 are similar to the self-diffusion coefficients for iron in magnetite. Therefore, the solid-state diffusion mechanism is plausible. The movement of the reaction front is probably the diffusion of iron in magnetite.

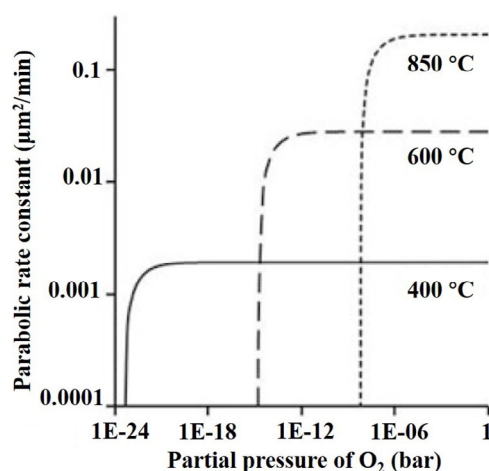


Figure 14. The calculated parabolic rate constants in different temperatures and partial pressures. Reproduced with permission.^[45] Copyright 2015, the Minerals, Metals & Materials Society (TMS).

Table 3. The self-diffusion coefficients for iron in magnetite and hematite.

Specimen	Temperature [°C]	D [$\mu\text{m}^2 \text{min}^{-1}$]
Magnetite	≈800	5.9×10^{-2}
	≈900	5.3×10^{-1}
Hematite	≈1000	6.0×10^{-5}
	≈1200	1.2×10^{-2}

Kumar et al.^[54] conducted an isothermal oxidation of magnetite concentrate particles by TGA in the temperature range of 500–800 °C. The concentrate is wet sieved into a narrow size

Table 4. The parabolic rate constants.

Temperature [°C]	k_p [$\mu\text{m}^2 \text{min}^{-1}$]	Average k_p [$\mu\text{m}^2 \text{min}^{-1}$]
400	2.5×10^{-3}	$220 \exp\left(-\frac{65100}{RT}\right)$
500	1.9×10^{-2}	
600	8.0×10^{-2}	
800	3.2×10^{-1}	

range from 38 to 53 μm with average particle diameter of 45.5 μm . The oxidizing gas flow rate was set as 200 ml min^{-1} to ensure the gas diffusion to be negligible. The result shows that the later stage of oxidation follows the solid-state diffusion mechanism. As discussed earlier, the parabolic rate constant should only depend on temperature. As shown in **Figure 15**, the slopes of the fitted lines indicate the values of the parabolic rate constants. The slopes in Figure 15a increase with temperature, whereas those in Figure 15b are almost constant. The resulting data support the mechanism of parabolic law.

5.2. Nucleation and Growth

The oxidation process can be also regarded as the nucleation and growth of hematite grains. The growth of hematite grain is realized by the solid-state diffusion of iron ions. The JMA model is a typical approach to describe such a reaction, which is defined in Equation (8) or (9). This model can be used for isothermal reactions, which follow multistep kinetics in parallel or in series. This model can be occupied even when the data do not fit any other commonly used models.^[55] It should be noted that this model can also be used for nonisothermal reactions, but in that case, different heating rates should be conducted for determination of the kinetic parameters.^[56] In some literatures, the JMA model is also known as the Avrami kinetic model (AKM).^[41,54]

$$\alpha = 1 - e^{-an^t} \quad (8)$$

or

$$\ln(-\ln(1 - \alpha)) = n \ln(t) + \ln(a) \quad (9)$$

where α is the oxidation degree, which is achieved after a reaction time t ; a represents the Avrami constant, which depends on the nucleation frequency or the linear rate of grain growth; and n is the kinetic exponent that provides insight into the type of nucleation and growth mechanism. Sharp and Hancock^[55] summarized the relationship between the value of n and the reaction mechanism. Generally, if n is smaller than 1, the reaction is controlled by solid-state diffusion; if n is close to 1, the reaction is likely to be controlled by first-order reaction; if n is close to 2, the reaction is controlled by nucleation.

Kumar et al.^[54] assumed that the oxidation process of magnetite occurred in series and analyzed the same data from Figure 15 by JMA model. Because only few data points can be obtained in the initial stage by the weighing system, further analysis from his work was only focused on the later stage of the oxidation process. **Figure 16** shows results analyzed by the JMA model. The measured value of n is expressed as follows.

$$n = 1.76 \times 10^{-4}T + 0.1255 \ln(p_{\text{O}_2}) - 2.03 \times 10^{-4}T \ln(p_{\text{O}_2}) \quad (10)$$

The values of n obtained in the experimental conditions are all smaller than 1 and show more sensitivity to temperature than partial pressure of oxygen, which is consistent with solid-state diffusion mechanism.

Monazam et al.^[41] used this model to examine the oxidation of magnetite particles, which are generated from reduced hematite. The difference is that he assumed a parallel process of two reactions occurring during oxidation. Pursuant to the JMA model, a parallel process of two reactions is defined by the Equations (11)–(12).

$$\alpha_t = w_1(1 - e^{-a_1 n_1^t}) + w_2(1 - e^{-a_2 n_2^t}) \quad (11)$$

$$w_1 + w_2 = 1 \quad (12)$$

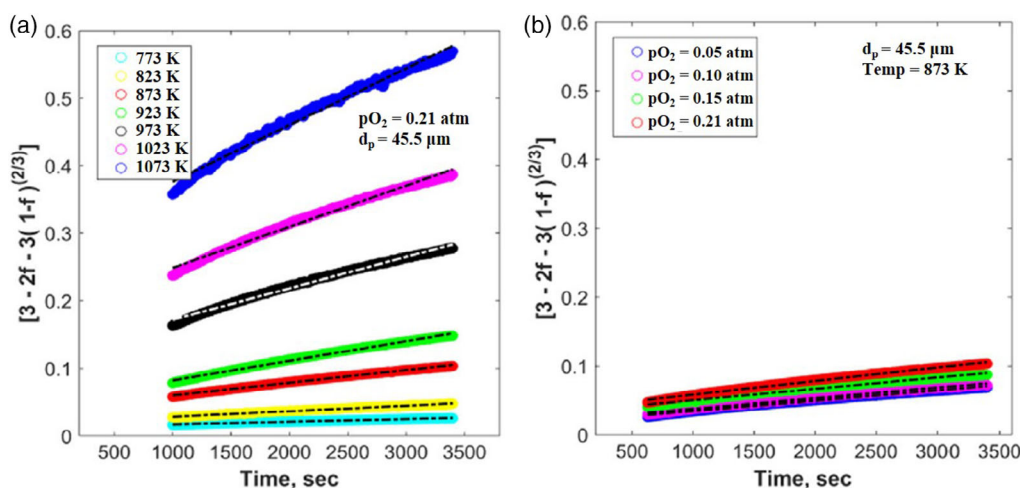


Figure 15. Isothermal oxidation evaluated by the solid-state diffusion: a) different oxidation temperatures and b) different partial pressures of oxygen. Adapted with permission.^[54] Copyright 2018, CC BY 4.0.

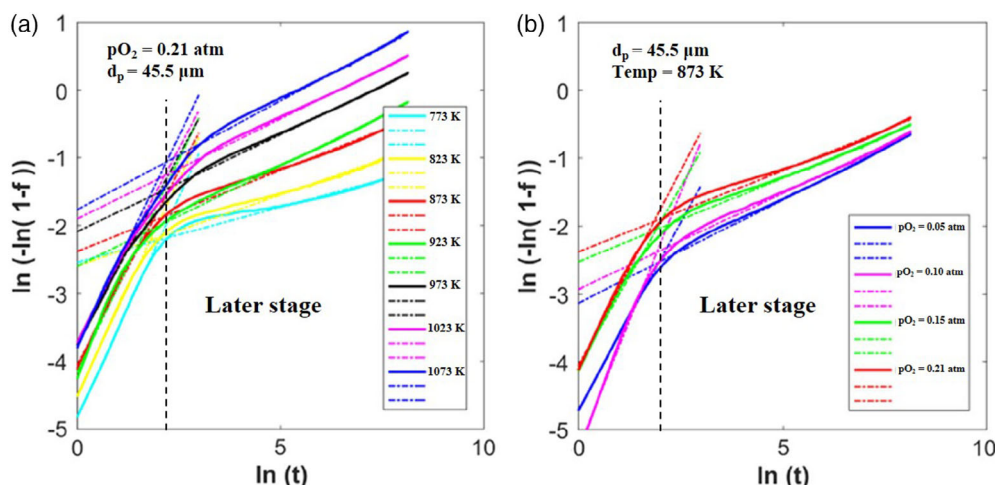


Figure 16. Isothermal oxidation evaluated by the nucleation and growth: a) different oxidation temperatures and b) different partial pressures of oxygen. Adapted with permission.^[54] Copyright 2018, CC BY 4.0.

The model hypothesizes that isothermal conversion of particles proceeds by nucleation and growth in parallel. Each process is manifested by the value of the weight factors w_1 and w_2 . The parallel processes P_1 and P_2 corresponding to nucleation and diffusion are shown in **Figure 17**. It should be noted that the particle size he used is between 100 and 300 μm , which is quite a wider size fraction compared with other works. The wide size range may cause the fitting result to be less reliable.

In the initial stage of oxidation, P_1 dominates the two processes, which indicates that P_1 is the rate-limiting step. Regarding the reaction time, P_2 dominated the whole oxidation. P_2 , which can be related to diffusion, has little influence on the initial part of the oxidation process. In other words, the nucleation of hematite dominates initially, whereas the solid-state diffusion dominates the later stage of oxidation. There is no evidence to confirm that the multistep kinetics of the oxidation reaction is in parallel or in series.

5.3. Discussion on the Kinetic Models

The two models based on the parabolic law and the nucleation and growth mechanisms can be occupied to describe the oxidation process of magnetite. The nature of these two mechanisms both involves ion diffusions. The solid-state diffusion is derived based on parabolic law, which can be simply described by Equation (13). The reaction rate is supposed to decrease with the thickness of the product layer. Equation (13) can be integrated in Equation (14), which is known as the parabolic law.

$$\frac{dl}{dt} = k \frac{1}{l} \quad (13)$$

$$l^2 = k_p t \quad (14)$$

where l is the thickness of the product layer and k_p is the parabolic rate constant. Ginstling and Brounshtein^[57] provided a solid-state diffusion model in the reaction taking place in

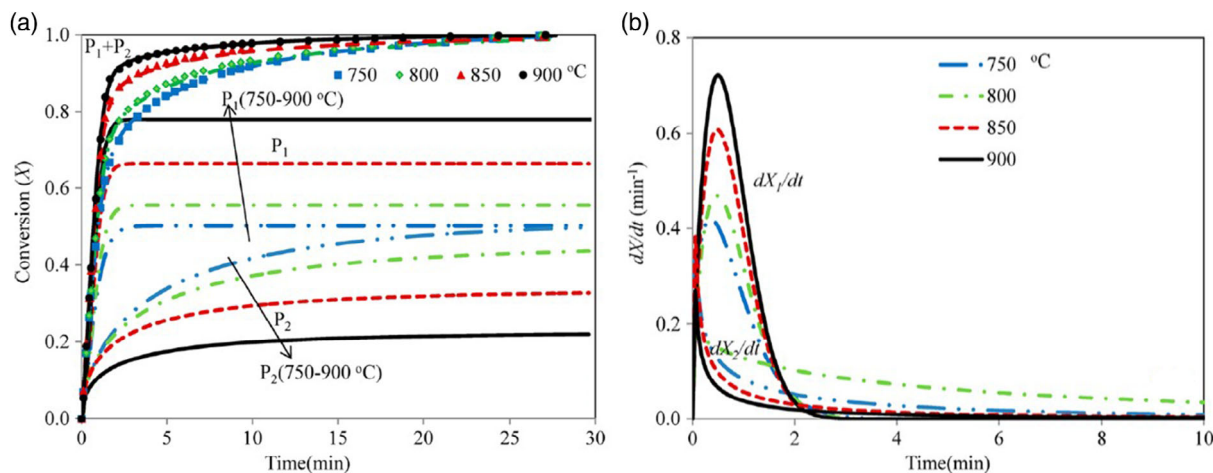


Figure 17. Conversion curve as a function of time. Curve P_1 is a single Avrami equation; curve P_2 is a single diffusion equation. Adapted with permission.^[41] Copyright 2014, American Chemical Society.

spherical particles based on parabolic law. This model is known as Ginstling–Brounshtein’s diffusion model or D4 model and gives the expression in Equation (6). Khawam et al.^[58] summarized other forms of the solid-state diffusion models derived from 1D (D1), 2D (D2), and 3D (D3) diffusion. Cho et al.^[51] found that the inward growth of hematite ahead of the reaction interface would have a small influence on the fitting result, but the solid-state diffusion by D4 model still describes the oxidation kinetics very well.

The advantage of JMA model is that it can be applied when the data do not fit commonly used models and it can describe the multistep kinetics in both the parallel and series way. According to the works from Kumar et al.^[54] and Monazam et al.,^[41] the later oxidation stage of magnetite follows solid-state diffusion no matter in parallel or series way. It is difficult to determine whether the multistep kinetics occurs in parallel or series. The current approach is to fit the data using both parallel and series methods and then choose the method with the better fitting result.

As discussed earlier, the kinetic analysis of the oxidation of magnetite in particle scale generally follows the solid-state diffusion. As for how to decide the kinetic models, the current method is to choose the model that fits the experimental data better.

6. The Influence of Oxidation of Magnetite on Its Subsequent Reduction

It is well established that hematite iron ores show better reducibility than that of magnetite iron ores.^[59,60] It is of great interest to know the difference of reduction behavior between oxidized magnetite and hematite in particle scale. Edström^[61] oxidized natural single crystals of magnetite (Fe_3O_4) and compared the reduction rate with that of hematite (Fe_2O_3) in CO atmosphere at 1000 °C. The results show that the reduction rate of the oxidized Fe_3O_4 is slightly lower than that of Fe_2O_3 . After 120 min reduction, both Fe_2O_3 and oxidized Fe_3O_4 reach more than 90% reduction degree, whereas that of Fe_3O_4 only reaches around 40%. Monsen^[46] has done a series of works to investigate the influence of oxidation temperatures of magnetite concentrates on its subsequent reduction in H_2 atmosphere at the temperature range between 700 and 800 °C. Magnetite was almost completely oxidized at the defined temperatures (850–1250 °C). He found that the hematite oxidized from magnetite at relatively low temperatures (850–1050 °C) shows better reducibility than that oxidized at high temperatures (1150–1250 °C) because hematite that is derived at a relatively low temperature contains more and smaller subgrain structures. The boundaries of these sub grains serve as preferential reduction sites, which promote the reduction process.

7. Conclusion

This Review summarizes the oxidation behaviors and kinetics during the oxidation of magnetite in particle scale. The oxidation kinetic mechanism is introduced and summarized. Furthermore, the influence of the oxidation of magnetite

on its subsequent reduction behavior is examined. Four oxidation characteristics of magnetite are summarized as follows.

1) The oxidation of magnetite proceeds through two oxidation stages. During the initial stage, the magnetite is oxidized into an intermediate phase, which is substable and further oxidized to α - Fe_2O_3 . 2) The oxidation process of magnetite is accompanied by the exothermic phenomenon, transformation of crystal, and evolution of morphology. The heat liberated in the oxidation of 1 kg of magnetite is about $113.9 \text{ kJ mol}^{-1}$. 3) Without considering the interaction between magnetite particles, the change of magnetite to hematite should result in a volume increase. However, when temperature is higher than 330 °C, the volume shows contraction during oxidation due to the sintering effect. 4) During the oxidation of magnetite, two different typical surface morphologies would be formed—whiskers and rough pleated structures, which are related to oxidation conditions. Whisker structures are likely to occur at a higher oxidation temperature. One possible cause for the hematite whisker structure is the compressive stress that is generated due to the volume increase when magnetite oxidizes to hematite. However, the favorable conditions for the formation of hematite whiskers or rough pleated structures are not fully examined. Further investigations have to be conducted.

The rate-limiting step for oxidation of magnetite in particle scale is generally solid-state diffusion. Solid-state diffusion can be well described by both parabolic law and the nucleation and growth mechanisms. The parabolic rate constant increases with temperature but is the same at different oxygen partial pressures. In another word, the oxidation process depends largely on the temperature rather than oxygen partial pressure.

The preoxidation of magnetite could greatly improve its reducibility. The hematite that is derived at a relatively low oxidation temperature contains more and smaller subgrain structures. In terms of the subsequent reduction rate, lower oxidation temperature is more beneficial than higher oxidation temperature.

Acknowledgements

This research was supported by K1-MET GmbH, Metallurgical Competence Center, project number 869295. The research program of the K1-MET competence center was supported by Competence Center for Excellent Technologies (COME), the Austrian program for competence centers. COMET is funded by the Federal Ministry for Climate Action, Environment, Energy, Mobility, Innovation and Technology, the Federal Ministry for Digital and Economic Affairs, the provinces of Upper Austria, Tyrol, and Styria, and the Styrian Business Promotion Agency (SFG). In addition, the research work was partially financed by Montanuniversitaet Leoben. Z.H. greatly acknowledges the financial support from the program of China Scholarship Council (no. 201908420284).

Conflict of Interest

The authors declare no conflict of interest.

Keywords

magnetite, oxidation behaviors, oxidation kinetics

Received: December 11, 2020

Revised: April 12, 2021

Published online: May 3, 2021

- [1] J. Pal, S. Ghorai, S. Agarwal, B. Nandi, T. Chakraborty, G. Das, S. Prakash, *Miner. Process. Extr. Metall. Rev.* **2015**, *36*, 83.
- [2] B. Das, B. Mishra, S. Prakash, S. Das, P. Reddy, S. Angadi, *Int. J. Miner., Metall. Mater.* **2010**, *17*, 675.
- [3] Department of the Premier and Cabinet, South Australia's Magnetite Strategy, **2017**, <https://sarigbasis.pir.sa.gov.au/WebtopEw/ws/samref/sarig1/image/DDD/BROCH028.pdf> (accessed: December 2020).
- [4] R. Upadhyay, A. Venkatesh, *Appl. Earth Sci.* **2006**, *115*, 187.
- [5] G. Singh, R. Choudhary, H. Vardhan, M. Aruna, A. Akolkar, *Proc. Earth Planetary Sci.* **2015**, *11*, 582.
- [6] L. Blaney, Magnetite (Fe₃O₄): Properties, synthesis, and applications, **2007**, https://scholar.google.com/scholar?hl=en&as_sdt=0%2C5&q=Magnetite+%28Fe3O4%29%3A+Properties%2C+synthesis%2C+and+applications.&btnG= (accessed: December 2020).
- [7] B. McNab, A. Jankovic, D. David, P. Payne, in *Proc. of Iron Ore Conf.*, Perth, Australia, July **2009**.
- [8] C. Dupuis, G. Beaudoin, *Miner. Depos.* **2011**, *46*, 319.
- [9] X. L. Liang, S. J. Yang, Y. H. Zhong, W. Tan, H. P. He, *Bull. Miner. Petro. Geoch.* **2019**, *38*.
- [10] S. Purohit, M. Rhamdhani, G. Brooks, in *AISTech Conf. Proc.*, Philadelphia, USA, **2018**.
- [11] S. Purohit, G. Brooks, M. A. Rhamdhani, M. I. Pownceby, N. A. S. Webster, *Ironmaking Steelmaking* **2020**, *47*, 674.
- [12] D. Q. Zhu, V. Mendes, T. J. Chun, J. Pan, Q. H. Li, J. Li, G. Z. Qiu, *ISIJ Int.* **2011**, *51*, 214.
- [13] H. L. Han, L. M. Lu, *Miner. Process. Extr. Metall. Rev.* **2018**, *39*, 217.
- [14] SALCOS@: SALCOS Official webpage, <https://salcos.salzgitter-ag.com/en/> (accessed: March 2021).
- [15] V. Vogl, M. Åhman, L. J. Nilsson, *J. Cleaner Prod.* **2018**, *203*, 736.
- [16] Q. F. Kang, J. L. Zhang, D. H. Liu, Z. J. Liu, J. Yan, in *Proc. of the 3rd Pan American Materials Congress*, Warrendale, USA **2017**, p. 643.
- [17] L. X. Yang, E. Matthews, *ISIJ Int.* **1997**, *37*, 854.
- [18] U. Colombo, G. Fagherazzi, F. Gazzarrini, G. Lanzavecchia, G. Sironi, *Nature* **1964**, *202*, 175.
- [19] U. Colombo, F. Gazzarrini, G. Lanzavecchia, G. Sironi, *Science* **1965**, *147*, 1033.
- [20] T. Chen, H. Xu, Q. Xie, J. Chen, J. Ji, H. Lu, *Earth Planet. Sci. Lett.* **2005**, *240*, 790.
- [21] R. Mackenzie, B. Mitchell, *Analyst* **1962**, *87*, 420.
- [22] M. A. Gheith, *Am. J. Sci.* **1952**, *250*, 677.
- [23] E. Schmidt, F. Vermaas, *Am. Mineral.* **1955**, *40*, 422.
- [24] B. Yur'ev, V. Goltsev, *Steel Transl.* **2016**, *46*, 718.
- [25] National Institute of Standards and Technology, <https://webbook.nist.gov/chemistry/form-ser/> (accessed: March 2021).
- [26] K. V. G. K. Gokhale, *Econ. Geol.* **1961**, *56*, 963.
- [27] Inorganic Crystal Structure Database (ICSD), <https://icsd.fiz-karlsruhe.de/> (accessed: December 2020).
- [28] Y. Shi, Y. Bai, L. B. Mo, Q. Y. Xiang, Y. L. Huang, J. L. Cao, *Acta Phys. Sin.* **2015**, *64*, 116301.
- [29] G. S. Parkinson, *Surf. Sci. Rep.* **2016**, *71*, 272
- [30] J. W. Gruner, *Econ. Geol.* **1926**, *21*, 375.
- [31] C. R. Van Hise, *A Treatise on Metamorphism*, US Government Printing Office, Washington, DC **1904**, p. 467.
- [32] S. P. E. Forsmo, S. E. Forsmo, P. O. Samskog, B. M. T. Björkman, *Powder Technol.* **2008**, *183*, 247.
- [33] J. Engel, Master Thesis, Montanuniversitaet Leoben, **2021**.
- [34] H. Sun, A. A. Adetoro, F. Pan, Z. Wang, Q. Zhu, *Metall. Mater. Trans. B* **2017**, *48*, 1898.
- [35] B. Gillot, A. Rousset, G. Dupre, *J. Solid State Chem.* **1978**, *25*, 263.
- [36] S. Q. Song, P. C. Pistorius, *ISIJ Int.* **2019**, *59*, 1765.
- [37] I. Gaballah, S. El Raghy, C. Gleitzer, *J. Mater. Sci.* **1978**, *13*, 1971.
- [38] M. Shao, H. Li, M. Kwauk, *Part. Part. Syst. Character.* **1997**, *14*, 35.
- [39] H. J. Cho, P. C. Pistorius, presented at *AISTech Conference Proceedings*, Indianapolis, USA, May **2011**.
- [40] Z. Y. Wang, J. L. Zhang, K. X. Jiao, Z. J. Liu, M. Barati, *J. Alloy. Compd.* **2017**, *729*, 874.
- [41] E. R. Monazam, R. W. Breault, R. Siriwardane, *Ind. Eng. Chem. Res.* **2014**, *53*, 13320.
- [42] D. Spreitzer, J. Schenk, *Steel Res. Int.* **2019**, *90*, 1900108.
- [43] S. Vyazovkin, A. K. Burnham, J. M. Criado, L. A. Pérez-Maqueda, N. Sbirrazzuoli, *Thermochim. Acta* **2011**, *520*, 1.
- [44] M. E. Brown, M. Maciejewski, S. Vyazovkin, R. Nomen, J. Sempere, A. Burnham, J. Opfermann, R. Strey, H. L. Anderson, A. Kemmler, *Thermochim. Acta* **2000**, *355*, 125.
- [45] P. C. Pistorius, M. Tang, presented at *144th TMS Annual Meeting & Exhibition*, Pittsburgh, USA, March **2015**.
- [46] B. E. Monsen, PhD Thesis, University of Trondheim, **1992**.
- [47] W. A. Johnson, R. F. Mehl, *Trans. Am. Inst. Min. Metall. Eng.* **1940**, *135*, 416.
- [48] M. P. Avrami, *J. Chem. Phys.* **1939**, *7*, 1103.
- [49] M. P. Avrami, *J. Chem. Phys.* **1940**, *8*, 212.
- [50] M. P. Avrami, *J. Chem. Phys.* **1941**, *9*, 177.
- [51] H. J. Cho, M. Tang, P. C. Pistorius, *Metall. Mater. Trans. B.* **2014**, *45*, 1213.
- [52] H. J. Cho, PhD thesis, Carnegie Mellon University, USA, **2012**.
- [53] L. Himmel, R. F. Mehl, C. E. Birchenall, *J. Met.* **1953**, *5*, 827.
- [54] T. K. S. Kumar, N. N. Viswanathan, H. Ahmed, A. Dahlin, C. Andersson, B. Bjorkman, *Metall. Mater. Trans. B* **2019**, *50*, 150.
- [55] J. D. Hancock, J. H. Sharp, *J. Am. Ceram. Soc.* **1972**, *52*, 74.
- [56] L. P. Maqueda, J. M. Criado, J. Malek, *J. Non-Cryst. Solids* **2003**, *320*, 84.
- [57] A. M. Ginstling, B. I. Brounshtein, *J. Appl. Chem. USSR* **1950**, *23*, 1327.
- [58] A. Khawam, D. R. Flanagan, *J. Phys. Chem. B.* **2006**, *110*, 17315.
- [59] A. Thurnhofer, M. Schachinger, F. Winter, H. Mali, J. Schenk, *ISIJ Int.* **2005**, *45*, 151.
- [60] A. Pichler, H. Mail, F. Plaul, J. Schenk, M. Skorianz, B. Weiss, *Steel Res. Int.* **2016**, *87*, 642.
- [61] J. O. Edström, *J. Iron Steel Inst.* **1953**, *175*, 289.



Heng Zheng finished his master's in Department of Metallurgical Engineering at Wuhan University of Science and Technology (WUST) in 2019, focusing on low-carbon ironmaking process. At the moment, he is doing his Ph.D. at the Chair of Ferrous Metallurgy, Montanuniversitaet Leoben. His research interests are in the fluidized bed reduction of iron ore fines using hydrogen.



Johannes Schenk has been a professor of Ferrous Metallurgy at the Montanuniversitaet Leoben since 2008 and Chief Scientific Officer (CSO) of the Austrian Metallurgical Competence Center K1–Met since 2015. He obtained his Ph.D. in Chemical Engineering at Graz University of Technology in 1989 and then worked for Siemens VAI in the research and development of new direct and smelting reduction technologies. One of his current research focuses is carbon-lean technologies for iron and steelmaking.



Thomas Wolfinger finished his master's in Metallurgy in 2018, focusing on iron and steel metallurgy at Montanuniversitaet Leoben. At the moment, he is working at the Austrian Metallurgical Competence Center K1–Met and is doing his Ph.D. at the Chair of Ferrous Metallurgy, Montanuniversitaet Leoben. His research activities are focused on the development of hydrogen-based direct reduction technology for ultrafine iron ores.



Surface Morphology and Structural Evolution of Magnetite-Based Iron Ore Fines During the Oxidation

HENG ZHENG, JOHANNES SCHENK, RUNSHENG XU, ODAY DAGHAGHELEH, DANIEL SPREITZER, THOMAS WOLFINGER, DAIWEI YANG, and YURY KAPELYUSHIN

The use of magnetite-based iron ore fines by means of fluidized bed technology has become a promising route to produce direct reduced iron. The significant influence of a prior oxidation treatment, which occurs in the preheating stage, on the subsequent fluidization and reduction behavior was observed in our previous study. As a result, it is important to investigate the oxidation of magnetite-based iron ore fines for an optimization of the proposed route. Three magnetite-based iron ore brands were analyzed. The oxidation characteristics are investigated based on thermogravimetric analysis. The surface morphology, structural evolution, and phase transformation were studied with a scanning electron microscope, an optical light microscope, and a high-temperature-X-ray diffraction (HT-XRD), respectively. The three samples showed different oxidation capacity indexes (OCIs) but similar TG-DTG curves. The oxidation rate peaks at around 330 °C and 550 °C indicated the formation of γ -Fe₂O₃ and α -Fe₂O₃. The hematite phase shows a particular growth habit. The oxidation first occurs at the surface, forming gridlike hematite structures, and then extends to the inside, resulting in hematite needles. The specific surface area and pore volume decrease significantly due to the sintering effect during oxidation.

<https://doi.org/10.1007/s11663-022-02475-9>

© The Author(s) 2022

I. INTRODUCTION

OVER the past few decades, the ironmaking industry has consumed a great deal of high-grade hematite-based iron ores, which were used as iron carriers in the blast furnace process. Natural magnetite is widely present in

various rock minerals.^[1] In 2015, the world production of magnetite-based iron ore was approximately 583 million tons, which accounts for 28 pct of the total iron ore production.^[2] Generally, the magnetite-based iron ore is ground to a small particle size to release magnetite minerals from its rock matrix, followed by a magnetic separation (or flotation) to increase the iron content.^[1,3] The current practice of ironmaking from magnetite-based iron ore involves a pelletization^[4] or sintering process^[5] to obtain an appropriate size range before charging in the ironmaking facilities, such as a blast furnace,^[6–8] grate-rotary kiln,^[9] and Midrex shaft furnace.^[10,11] Nowadays, reducing CO₂ emissions is one of the most critical issues. To reach the goal of climate neutrality (net-zero greenhouse gas emissions) by 2050, new ironmaking and steelmaking technologies and concepts are required for further decreasing the overall CO₂ emissions.^[12,13]

Compared with the traditional blast furnace-basic oxygen furnace (BF-BOF) integrated route, the natural gas-based direct reduction–electric arc furnace route provides a 40 to 60 pct reduction in CO₂ emissions, from 1.6 to 2.2 tons CO₂ emission to 0.6 to 1.15 tons CO₂ emission per ton of crude steel.^[14] One possible concept for future crude steel production is using the hydrogen-gas-based fluidized bed technology to produce

HENG ZHENG and ODAY DAGHAGHELEH are with the Chair of Ferrous Metallurgy, Montanuniversitaet Leoben, Franz-Josef-Straße 18, 8700 Leoben, Austria. Contact e-mail: heng.zheng@stud.unileoben.ac.at JOHANNES SCHENK is with the Chair of Ferrous Metallurgy, Montanuniversitaet Leoben and also with the K1-MET GmbH, Stahlstraße 14, 4020, Linz Austria. RUNSHENG XU is with the The State Key Laboratory of Advanced Metallurgy, University of Science and Technology Beijing, Beijing 100083, China. DANIEL SPREITZER is with the Primetals Technologies Austria GmbH, Turmstraße 44, 4020 Linz, Austria. THOMAS WOLFINGER is with the K1-MET GmbH. DAIWEI YANG is with the The State Key Laboratory of Refractories and Metallurgy, Wuhan University of Science and Technology, Wuhan 430081, China. YURY KAPELYUSHIN is with the South Ural State University (National Research University), Lenina Avenue 76, Chelyabinsk, Russian Federation, 454080.

Manuscript submitted October 17, 2021; accepted February 13, 2022.

Article published online March 23, 2022.

carbon-free direct reduced iron (DRI), followed by use of an electric arc furnace.^[15,16] Compared to current BF-BOF production, when the process is operated with 55 pct green hydrogen together with 45 pct natural gas, theoretically, 82 pct CO₂ emission can be avoided. When 100 pct green hydrogen is used, CO₂ emission can be reduced by more than 95 pct.^[17] Therefore, the production of DRI using magnetite-based iron ores in a hydrogen-induced fluidized bed becomes of great interest. In our previous study, direct use of magnetite-based iron ore for hydrogen-induced fluidized bed reduction was introduced.^[18,19] A series of laboratory-scale experiments were carried out to test the potential industrial application. The proposed route involves a prior oxidation treatment occurring in the preheating stage, which could improve both fluidization and reduction behavior. Compared with the deep oxidation treatment, partial oxidation of the magnetite-based iron ore was more beneficial during the final reduction stage.^[18,19] As a result, it is important to investigate the oxidation of magnetite-based iron ore for an optimization of the proposed route. However, most of the research about oxidation of magnetite-based iron ores was conducted in briquettes or pellets and mainly discussed the thermal volume change, porosity evolution, and oxidation kinetics.^[20–27] Limited literature is available for oxidation of magnetite-based iron ore in particle scale.

Colombo *et al.*^[28,29] and Basta^[30] used differential thermal analysis (DTA) and X-ray diffraction (XRD) measurements to test the oxidation of natural magnetite particles and found that the oxidation was a two-stage process: surface oxidation and further inside oxidation. In the first stage, the oxidation of Fe²⁺ to Fe³⁺ caused the diffusion of iron ions from inside the crystals of the Fe₃O₄ toward the surface. An intermediate-phase solid solution of γ -Fe₂O₃ in Fe₃O₄ was formed at the beginning of the oxidation. Then, the stable α -Fe₂O₃ (hematite) phase appeared at the surface of the magnetite particle. In the following stage, the intermediate phase transformed into α -Fe₂O₃ and completed the oxidation of the individual particle. Hyeon *et al.*^[31,32] investigated the oxidation of magnetite concentrates, which were assumed to follow a Rosin–Rammler size distribution. The oxidation behavior of the magnetite pellet was then predicted based on the oxidation kinetics of the magnetite concentrates. Apart from the oxidation kinetic analysis of magnetite particles,^[24,33–35] Song and Pistorius^[36] observed the hematite whiskers during the oxidation of magnetite concentrates. The whiskers formed in the early oxidation process and did not grow during the further oxidation. The formation of hematite whiskers was explained by a volume increase during the

structure change from magnetite to hematite, which may cause a considerable compressive stress. The formation of hematite helped to relieve the compressive stress and make the structure stable.

Zheng *et al.*^[37] summarized the oxidation behaviors and kinetics of magnetite in particle scale. Theoretically, after oxidation from magnetite to hematite, the volume will increase around 2.5^[38] to 5.2 pct.^[39] In fact, during the oxidation of magnetite-based iron ore fines, the sintering effect cannot be ignored. The specific surface area usually decreases greatly after oxidation.^[40,41] The sintering effect also shows a negative influence on the reduction of iron ore particles. The purpose of this study is to investigate the oxidation behavior of the magnetite-based iron ore fines and characterize the pores, morphology, and internal structure after oxidation. The *in-situ* high-temperature–X-ray diffraction (HT-XRD) was used to investigate the phase transformation during the oxidation process.

II. EXPERIMENTAL

A. Materials

Three commercial magnetite-based iron ore fines were used in this study. The main chemical analyses of samples A through C are listed in Table I. The particle size distributions and apparent particle densities of the samples were characterized by a CILAS 1064 particle size analyzer and Ultracycrometer 1000 density analyzer, respectively. The results are listed in Table II. The raw samples were dried at 110 °C for 6 hours before all the following tests.

B. Experimental Procedures

The oxidation behavior analysis was conducted by thermogravimetric analysis (TGA). The TGA tests were conducted using an STA 409 PG thermal analyzer. For a typical test, 50 mg of the sample was heated in an Al₂O₃ crucible (5 × 8 mm o.d.) to 1100 °C under air

Table II. Particle Size Distributions and Density of the Raw Magnetite Samples

Sample	D10 (μm)	D50 (μm)	D90 (μm)	Density (g/cm ³)
A	4.84	31.16	72.94	4.95
B	4.81	28.35	62.66	4.94
C	6.10	32.25	70.16	5.09

Table I. Chemical Analysis of the Raw Magnetite Samples (Weight Percent)

Sample	Fe _{tot}	FeO	SiO ₂	Al ₂ O ₃	MgO	CaO	TiO ₂	P	S
A	67.03	25.70	2.33	0.69	0.56	0.93	0.039	<0.001	0.13
B	68.78	27.71	5.60	0.18	0.17	0.17	—	0.017	0.05
C	65.65	27.66	3.33	1.16	1.62	1.62	0.22	0.017	0.1

flow (100 mL/min) at a heating rate of 7.5 °C/min. Each test was carried out twice and showed good reproducibility.

The isothermal oxidation was performed under a laboratory air atmosphere in a muffle furnace. To minimize the sintering effect, the oxidation temperature was set as 700 °C. One gram of the sample was placed in a 60 × 10 × 7 mm magnesia boat. Based on the bulk density of the sample, the thickness of the material layer in the boat was supposed to be around 0.35 mm. The oxidation process was assumed to proceed evenly within the material layer. Four boats of samples were oxidized for a specific controlled time in a typical isothermal oxidation test. After holding for a certain period, the boats were rapidly removed from the furnace and quenched in the open air.

The HT-XRD analyses were run on a Rigaku Ultima IV XRD diffractometer using Cu as the X-ray source, with a step size of 0.02 deg and scanning time per step of 0.15 seconds. To conduct high-temperature measurements, the samples were placed on a platinum heating strip in the HTK-16 high-temperature chamber (Anton Paar). To avoid the influences of sample area and position on the XRD patterns, each HT-XRD measurement followed the same procedure: 0.3 g of raw sample was put on the heating strip and heated in vacuum to 400 °C, 600 °C, 800 °C, and 1000 °C, respectively, at a heating rate of 100 °C/min. The positions and areas of all samples should be the same. Figure 1 shows the HT-XRD measurement profile. The raw and the final oxidized samples were measured at room temperature in the scanning angle range between 25 and 65 deg. At the target temperature, one XRD measurement was conducted before changing the vacuum to the air

atmosphere. After that, the XRD measurements were conducted every 10 minutes in the scanning angle range between 32 and 41 deg.

C. Analysis and Characterization

The weight gain measured during the TGA test can be converted into the oxidation degree (w). The w is defined as shown in Eq. [1]^[42,43]:

$$w = \frac{\Delta m}{\Delta m_{theory}} \cdot 100 \text{ pct}, \quad [1]$$

where Δm and Δm_{theory} are the measured weight gain and the theoretical weight gain during the oxidation, respectively. Δm_{theory} is calculated based on the FeO content from the chemical analysis of each magnetite-based iron ore. It should be noted that the loss on ignition of the samples was ignored.

The morphology and internal structure of the samples were observed using a scanning electron microscope (SEM, Quanta 200Mk2, FEI) and an optical light microscope (Nikon MM 40 measuring microscope system, Japan), respectively. The HT-XRD patterns were identified using Jade 6.0 software. There was a minor shift in HT-XRD peaks due to the thermal expansion of the samples, which was taken into consideration while identifying the peaks. This shift phenomenon also appeared in the HT-XRD analysis of oxidation of pyrite.^[44]

The pore structure was evaluated by the N₂ gas adsorption method using a TriStar 3000 surface area analyzer. All the samples were degassed at 200 °C for 2 hours. The specific surface area was determined by the Brunauer–Emmett–Teller (BET) method. The

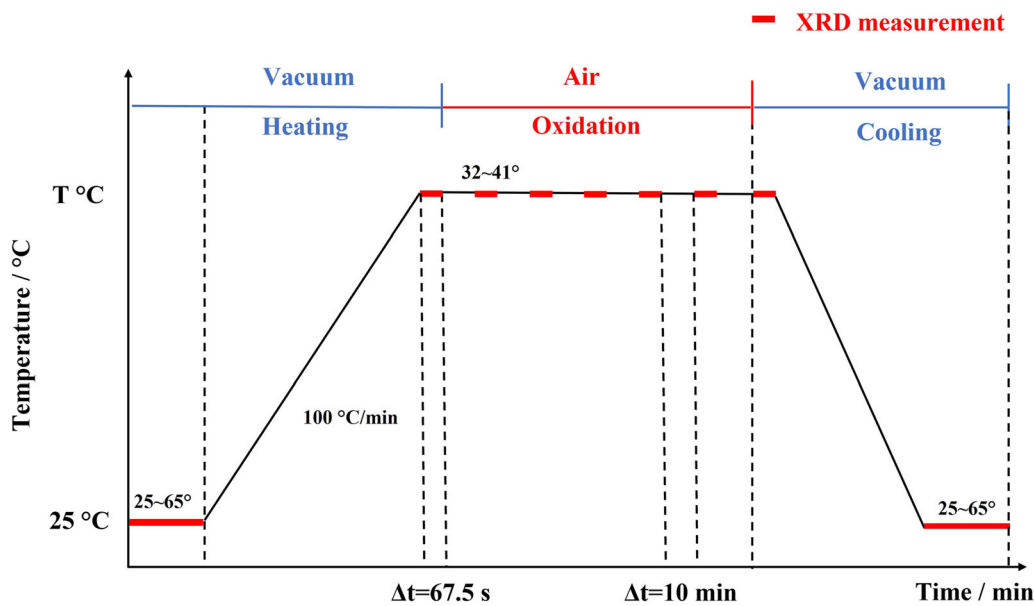


Fig. 1—Schematic diagram of HT-XRD measurements in the defined temperature.

cumulative pore volume, average pore diameter, and pore size distribution were analyzed using the Barrett–Joyner–Halenda (BJH) method.

III. RESULTS AND DISCUSSION

A. Oxidation Behavior by TGA Analysis

Figure 2 shows the oxidation TG-DTG curves of different samples. From Figure 2(a), it is obvious that sample B is the easiest to oxidize among the three samples. Based on the oxidation rate, as shown in Figures 2(b) through (d), the oxidation reaction can be divided into at least three oxidation stages. Peak 1 in all the samples locates at around 330 °C. At the temperature around peak 1, the oxidation mainly occurs at the surface of particles and the oxidation rate is limited by chemical reaction.^[33] The diffusion of Fe^{2+} and Fe^{3+} ions is also limited due to the low oxidation temperature. Therefore, the height of peak 1 is relatively low. The oxidation product is supposed to be $\gamma\text{-Fe}_2\text{O}_3$.^[30,45,46] At the temperature around peak 2 (550 °C), the $\gamma\text{-Fe}_2\text{O}_3$ becomes unstable and transforms

to $\alpha\text{-Fe}_2\text{O}_3$.^[37] From the kinetic point of view, the rate-limiting step for oxidation of magnetite in particle scale is solid-state diffusion. The diffusion rate constant is independent of oxygen partial pressure but increases with the temperature.^[37] The increasing temperature speeds up the diffusion of Fe^{2+} and Fe^{3+} ions and, hence, increases the oxidation rate. However, with the oxidation reaction proceeding, the formed $\alpha\text{-Fe}_2\text{O}_3$ shell blocks the diffusion of the iron and oxygen ions, which results in the decrease of the oxidation rate.^[47] At higher temperatures, the following peaks (peak 3 or 4) of different samples show diversities, which can be explained by the side reactions between impurities and iron oxides. The isomorphous substitution occurs widely in the structure of magnetite-based ores, resulting in an impurity element existing in the lattice of magnetite.^[48]

To comprehensively evaluate the oxidation behavior of different samples, the oxidation capacity index (OCI) is introduced. By analogy with the definition of the comprehensive combustion property index (S)^[49] of coal, the OCI of magnetite-based iron ore is calculated as Eqs. [2] through [7]:

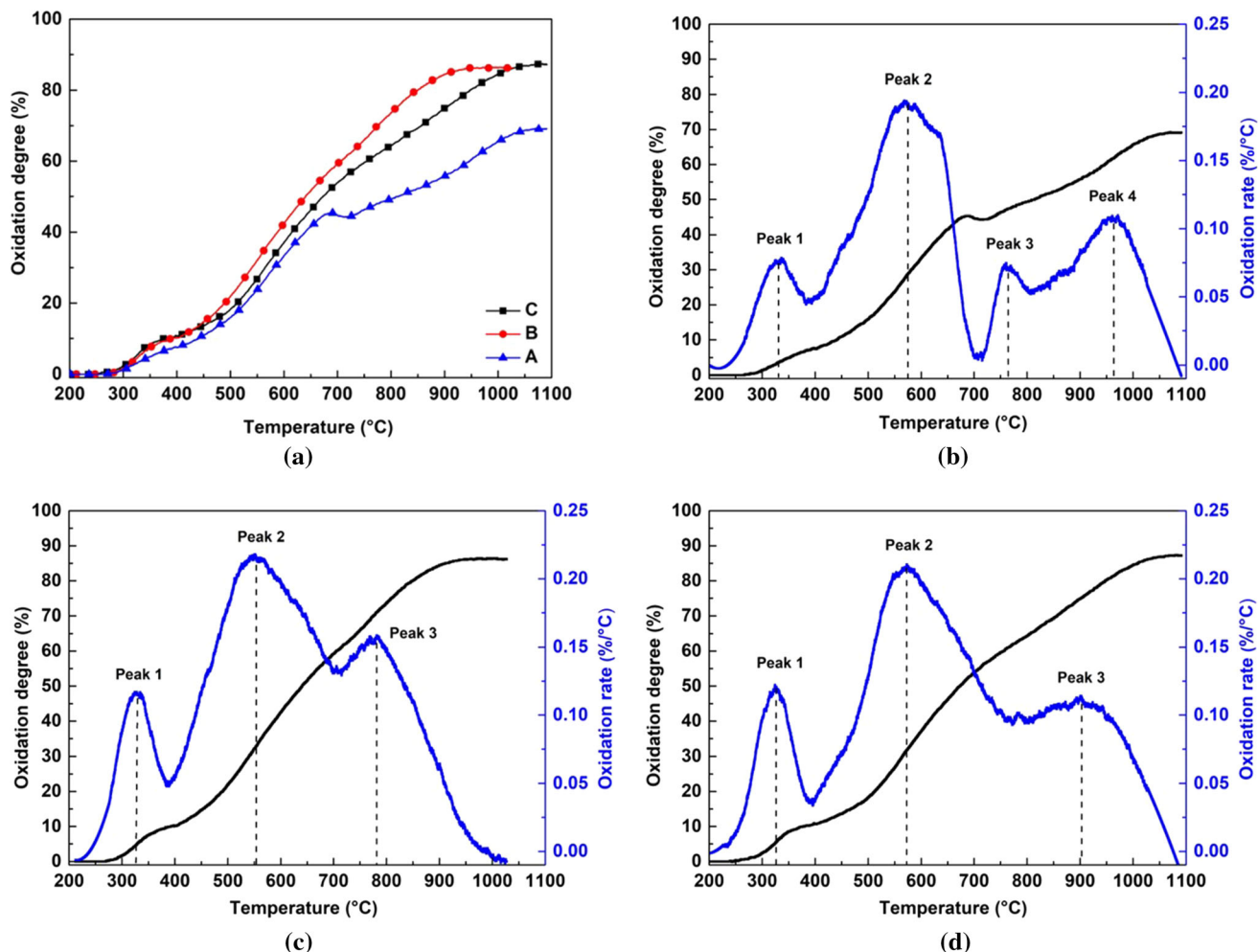


Fig. 2—Oxidation TG-DTG curves of the samples: (a) TG curve of samples, (b) TG-DTG curve of sample A, (c) TG-DTG curve of sample B, and (d) TG-DTG curve of sample C.

$$\frac{dw}{dt} = A \cdot \exp\left(-\frac{E}{RT}\right), \quad [2]$$

$$\frac{d}{dT}\left(\frac{dw}{dt}\right) = A \cdot \exp\left(-\frac{E}{RT}\right) \cdot \frac{E}{RT^2}. \quad [3]$$

Insert Eq. [3] into Eq. [2]:

$$\frac{R}{E} \frac{d}{dT}\left(\frac{dw}{dt}\right) = \left(\frac{dw}{dt}\right) \frac{1}{T^2}. \quad [4]$$

When oxidation starts, $T = T_i$:

$$\frac{R}{E} \frac{d}{dT}\left(\frac{dw}{dt}\right)_{T=T_i} = \left(\frac{dw}{dt}\right)_{T=T_i} \frac{1}{T_i^2} \quad [5]$$

Equation [6] is obtained from Eq. [5]:

$$\begin{aligned} \frac{R}{E} \frac{d}{dT}\left(\frac{dw}{dt}\right)_{T=T_i} &= \frac{(\frac{dw}{dt})_{max} (\frac{dw}{dt})_{mean}}{(\frac{dw}{dt})_{T=T_i} T_e} \\ &= \frac{(\frac{dw}{dt})_{max} (\frac{dw}{dt})_{mean}}{T_i^2 T_e}, \end{aligned} \quad [6]$$

where $\frac{d}{dT}\left(\frac{dw}{dt}\right)_{T=T_i}$ indicates the oxidation rate of the magnetite at the initial oxidation temperature; $\frac{(\frac{dw}{dt})_{max}}{(\frac{dw}{dt})_{T=T_i}}$ is the ratio of the maximum reaction rate and the initial reaction rate; and $\frac{(\frac{dw}{dt})_{mean}}{T_e}$ is the ratio of the mean reaction rate and the reaction finishing temperature T_e , which indicates the overall oxidation rate.

The right side of formula [6] is defined as the OCI:

$$OCI = \frac{(\frac{dw}{dt})_{max} (\frac{dw}{dt})_{mean}}{T_i^2 T_e} \quad [7]$$

The characteristic parameters of the oxidation are listed in Table III. T_i is the temperature when the oxidation starts. The temperature when sample B starts to be oxidized is much lower than that of samples A and C. T_{p-1} , T_{p-2} , T_{p-3} , and T_{p-4} are the temperatures of the peaks in the DTG curves. The highest oxidation rate of these three samples is in the temperature range of 548 °C

to 573 °C. The temperature of the second highest oxidation rate is in the range of 764 °C to 902 °C. The OCI represents the OCI of magnetite-based iron ore. A higher OCI value for a magnetite-based ore indicates that it is easier to oxidize. Sample B shows the highest OCI, followed by samples C and A.

B. Structural Evolution

1. Morphology analysis

The morphologies of the raw samples A, B, and C are shown in Figures 3 through 5, respectively. The surface morphologies of all the samples are similar. They are smooth and compact, with sharp edges. From SEM images, few gangues can be observed in sample A. However, the gangues are widely spread in samples B and C. As shown in Figures 4(c) and (d), the SiO₂ is the main impurity phase in sample B and is intertwined with the magnetite phase. As shown in Figures 5(c) and (d), the SiO₂ is also the main gangue in sample C but dotted with Ca, Al, and Na impurities. The SEM-ESD analysis is coincident with the chemical analysis that is shown in Table I.

Figure 6 shows the oxidation results of the isothermal oxidation tests, which give a similar trend as observed during the TGA tests. Within the same duration time, sample B shows the highest oxidation degree followed by samples C and A. The surface morphologies under different duration times are shown in Figures 7 through 9. As shown in Figures 7(b), 8(b), and 9(b), after only 2 minutes, the dense surface structure becomes rough and presents a nanosized gridlike structure. This phenomenon also occurred during the oxidation of vanadium-titanium magnetite ores.^[43,50,51] The gridlike structures are supposed to be hematite phase and caused by the out-diffusion of Fe²⁺. After 5 minutes, as shown in Figures 7(c), 8(c), and 9(c), the gridlike structures in sample B are much bigger than those in the other two samples. The gridlike structures in sample A are slightly bigger than those in sample C. According to Table I, sample B contains fewer impurity elements, while sample C has the most impurities. The impurity elements might replace the iron ions in the lattice and influence the diffusion of the cations. It can be suggested

Table III. Characteristic Parameters of the Oxidation

Parameters	Sample A	Sample B	Sample C
T_i (°C)	265	214	239
T_{p-1} (°C)	337	325	326
T_{p-2} (°C)	570	548	573
T_{p-3} (°C)	764	778	902
T_{p-4} (°C)	962	—	—
T_e (°C)	1083	1000	1091
$(\frac{dw}{dt})_{max-1}$ (pct/min)	0.5663	0.8719	0.9050
$(\frac{dw}{dt})_{max-2}$ (pct/min)	1.4375	1.6143	1.5784
$(\frac{dw}{dt})_{max-3}$ (pct/min)	0.5318	1.1468	0.8558
$(\frac{dw}{dt})_{max-4}$ (pct/min)	0.7971	—	—
$(\frac{dw}{dt})_{mean}$ (pct/min)	0.4778	0.6470	0.5998
$OCI \times 10^{-8}$ (pct ² min ⁻² °C ⁻³)	0.9031	2.2807	1.5192

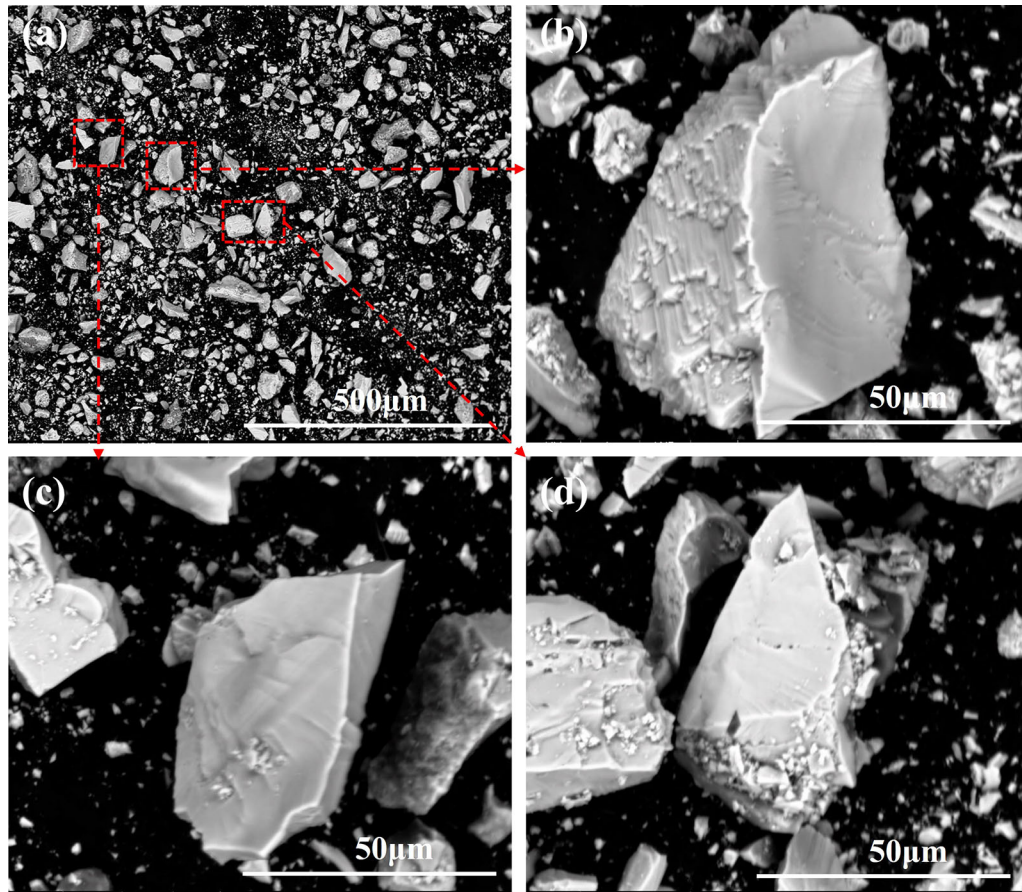


Fig. 3—Surface morphology of raw sample A under SEM: (a) through (d) different magnification times.

that these impurity elements influence the diffusion of the iron ions, resulting in the different growth behavior of the gridlike structures. With the oxidation time, the gridlike structures grow bigger and connect with each other.

2. Internal structure evolution

To investigate the evolution of the internal structure, the samples under different duration times are observed, as shown in Figure 10. All the raw magnetite samples show compact structures. These three samples follow a similar oxidation path: surface oxidation to internal oxidation. As shown in Figures 10(b), (f), and (j), the oxidation first occurs at the surface of the magnetite particle. Then, with increasing oxidation time, as shown in Figures 10(c), (g), and (k), obvious hematite shells are formed. In the final oxidation stage, as shown in Figures 10(d), (h), and (l), the hematite shell does not grow uniformly inward toward the magnetite core. Instead, the needlelike hematite structures originate from the surface hematite shell and grow inside the particle. It should be noted that no pores or cracks can be observed in the boundaries between the hematite and

magnetite phases. The oxidized samples still show compact structures. The oxidation mechanism is introduced in Section II-F.

C. Pore Structure Parameters Based on N_2 Adsorption

1. Specific surface area and pore volume

In this study, BET and BJH methods are used to investigate the pore structures during the oxidation of magnetite-based iron ores. The results of the pore structure parameters are listed in Table IV. The specific areas of the raw samples A, B, and C are 1.63, 0.94, and 0.83 m^2/g , respectively. After 5 minutes of oxidation, the specific surface areas decrease significantly to 0.52, 0.38, and 0.29 m^2/g , which can be explained by the sintering effect at the high temperature. With the oxidation time, the specific areas keep decreasing. The total pore volumes of all the samples show the same trend as their specific areas. However, the average pore sizes of the samples keep increasing with the oxidation. This is due to the closure of the small pores, which is caused by the sintering effect. It should be noted that sample B shows the biggest specific area and pore volume after 60

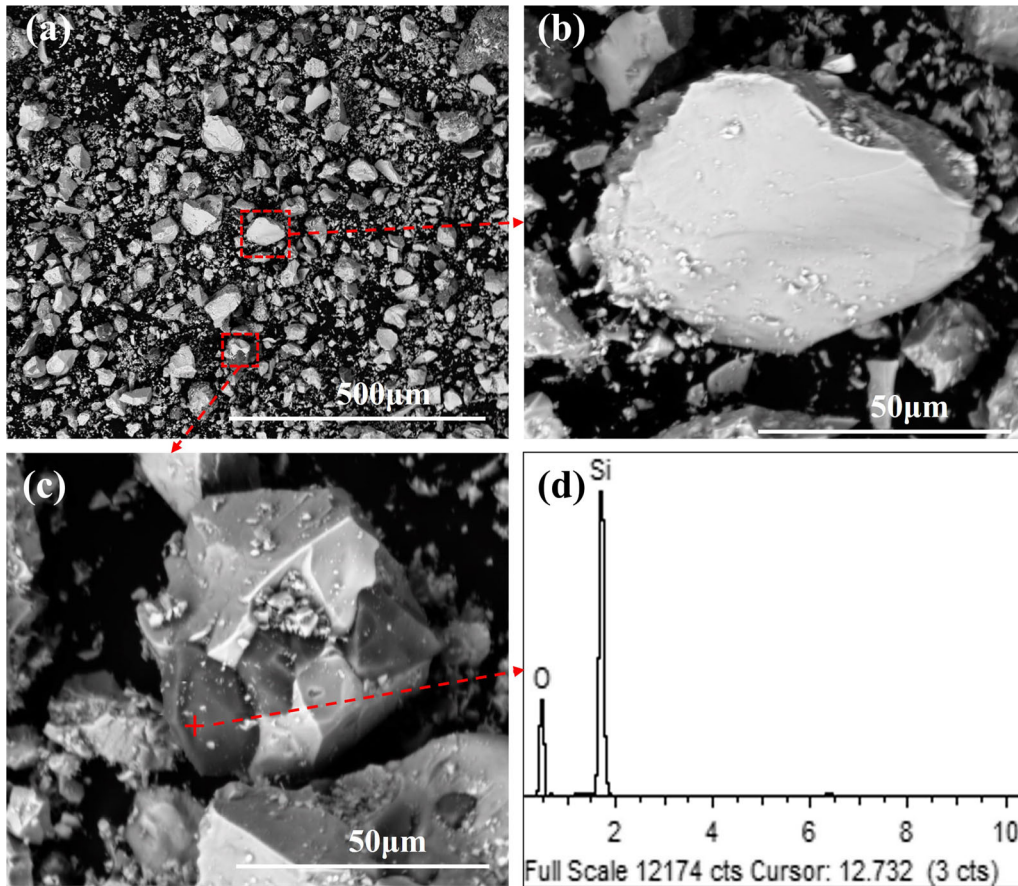


Fig. 4—Surface morphology of raw sample B under SEM: (a) through (c) different magnification times and (d) EDS analysis of the gangue.

minutes of oxidation, which may contribute to its high oxidation rate in the late oxidation process.

2. Pore size distribution

The pore size distributions of the samples within different duration times are shown in Figure 11. For the raw samples, the dominant pore size is between around 2 and 5 nm. For the oxidized samples, the pore size that is smaller than 3 nm decreases significantly. This phenomenon confirms the sintering effect.

D. HT-XRD Analysis

The HT-XRD patterns of the samples present similar characteristics. Therefore, as an example, only the patterns of sample B are shown in Figure 12. The appearance of Pt peaks in Figure 12 is because of the platinum heating strip. The HT-XRD results reveal that the temperature is one of the major factors influencing the oxidation of magnetite. At 400 °C, as shown in Figure 12(a), a small hematite peak appears after 10 minutes. However, the relative intensities of the hematite peaks remain stable afterward, which

illustrates that the amount of the hematite phase does not increase. At 600 °C, as shown in Figure 12(b), the relative intensities of the hematite peaks grow with the duration time. At 800 °C and 1000 °C, the oxidation of the sample proceeds quickly. After 10 minutes, the peaks of the magnetite phase are hardly observed.

Bhargava *et al.*^[44] normalized the relative intensity of the strongest peaks of the magnetite, hematite, and pyrite phases, respectively, to investigate the phase transformation of pyrite at high temperature. It should be noted that the relative peak intensity of each phase is not proportional to its content. In this study, a similar method, named the matrix-flushing method,^[52,53] is used to conduct the quantitative analysis. The intensity of phase j can be expressed as

$$I_j = \frac{C_j \cdot x_j}{\rho_j \cdot \mu_m}, \quad [8]$$

where C_j is the structure factor, x_j is the proportion of phase j in the mixture phases, ρ_j is the density of phase j , and μ_m is the mass absorption coefficient of the mixture phases.

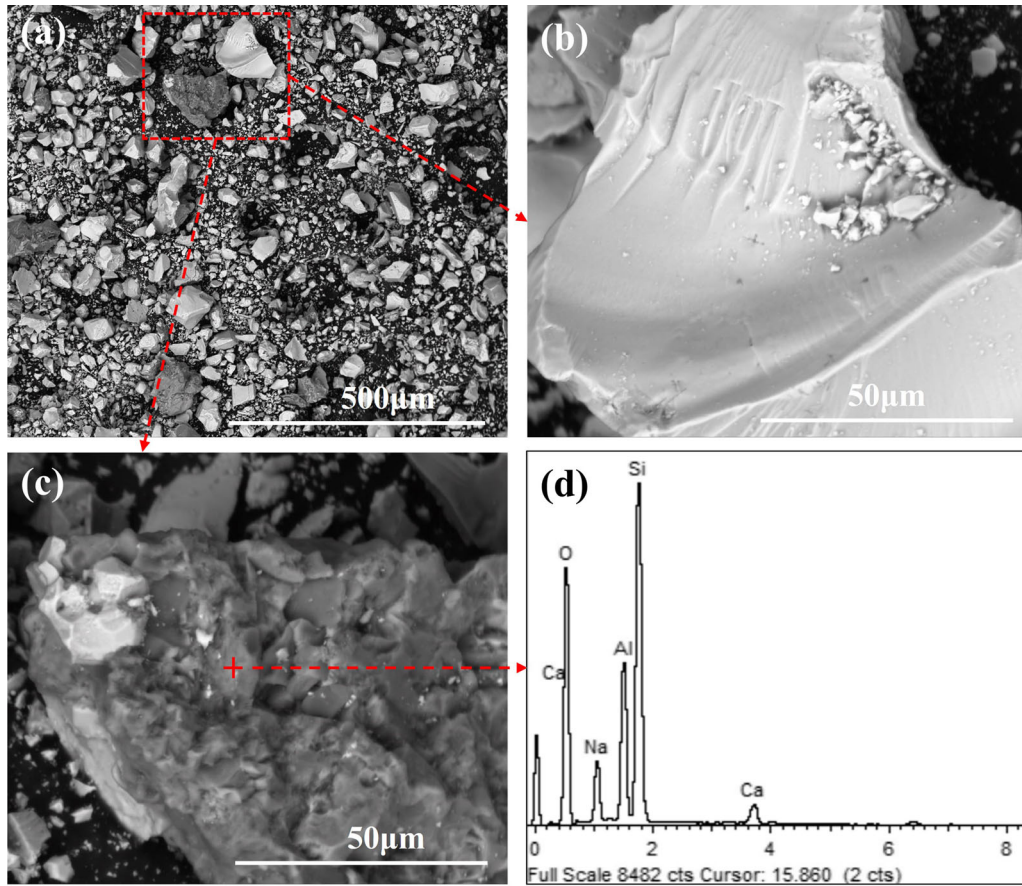


Fig. 5—Surface morphology of raw sample C under SEM: (a) through (c) different magnification times and (d) EDS analysis of the gangue.

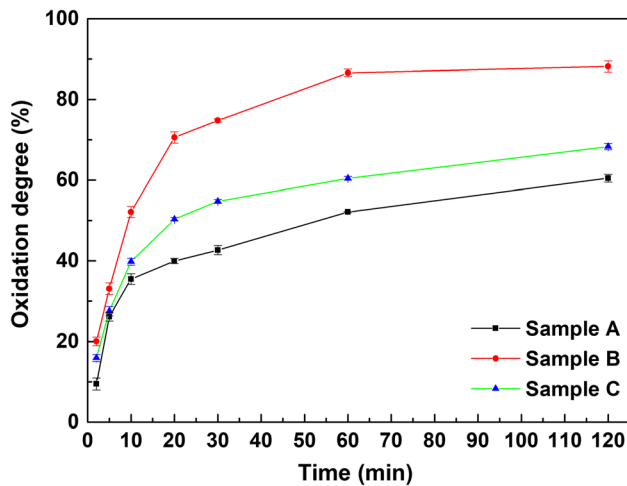


Fig. 6—Oxidation degree within certain duration times.

Assuming that phase j is a certain reference phase, phase i can be calculated.

$$I_j/I_i = \frac{C_j \cdot x_j / \rho_j \cdot \mu_m}{C_i \cdot X_i / \rho_i \cdot \mu_m} \quad [9]$$

Since C_j , C_i , ρ_j , ρ_i , and μ_m are constant, $\frac{C_j}{\rho_j \cdot \mu_m}$ and $\frac{C_i}{\rho_i \cdot \mu_m}$ can be defined as k_j and k_i , respectively. Therefore, the proportion of phases i and j can be calculated based on Eqs. [10] and [11]:

$$x_i/x_j = \frac{I_i}{k_i} / \frac{I_j}{k_j}, \quad [10]$$

$$x_i + x_j = 1, \quad [11]$$

where I_i is the intensity of phase I and k_j is the relative intensity ration (RIR). The RIR of each phase can be found in the PDF card database. The RIRs of the magnetite and hematite phases are 4.9 and 3.2, respectively.

The magnetite and hematite peaks located at around 35 deg overlap each other. To distinguish and split each peak, the XRD pattern is refined by Jade 6.0. Figure 13 shows an example of the XRD patterns after refinement. In this way, the relative content of the magnetite and hematite can be calculated. The results are shown in Figure 14. The result is consistent with the TGA test that demonstrates that sample B is the easiest one to oxidize. The oxidation of magnetite proceeds relatively

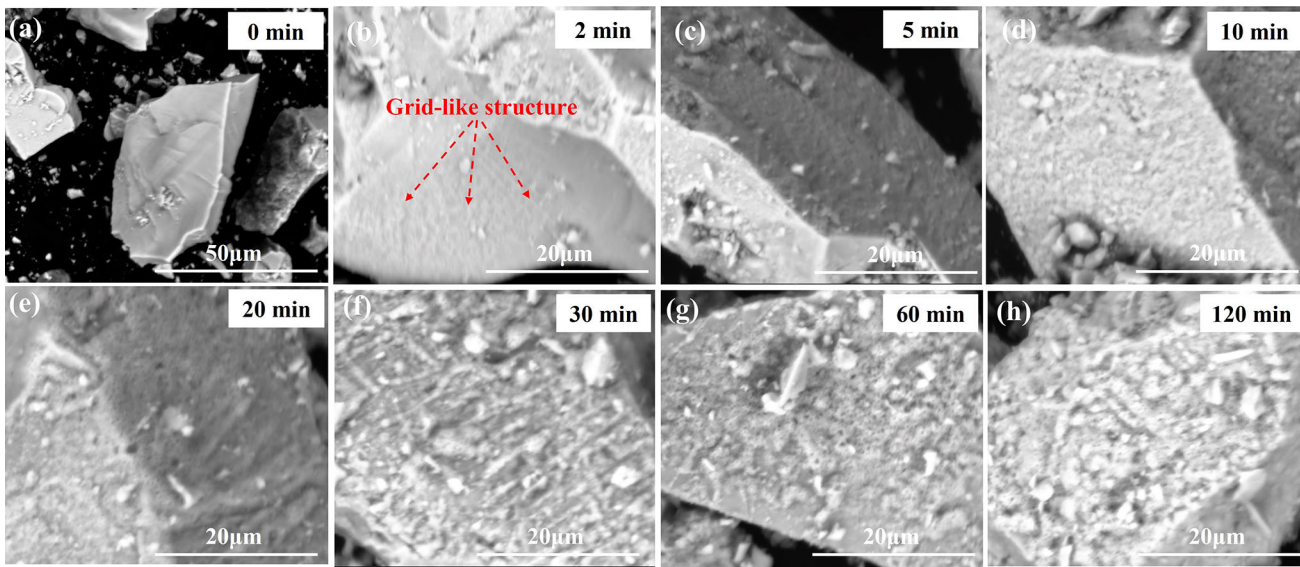


Fig. 7—SEM images of the oxidized products of sample A obtained under different duration times: (a) 0 min, (b) 2 min, (c) 5 min, (d) 10 min, (e) 20 min, (f) 30 min, (g) 60 min, and (h) 120 min.

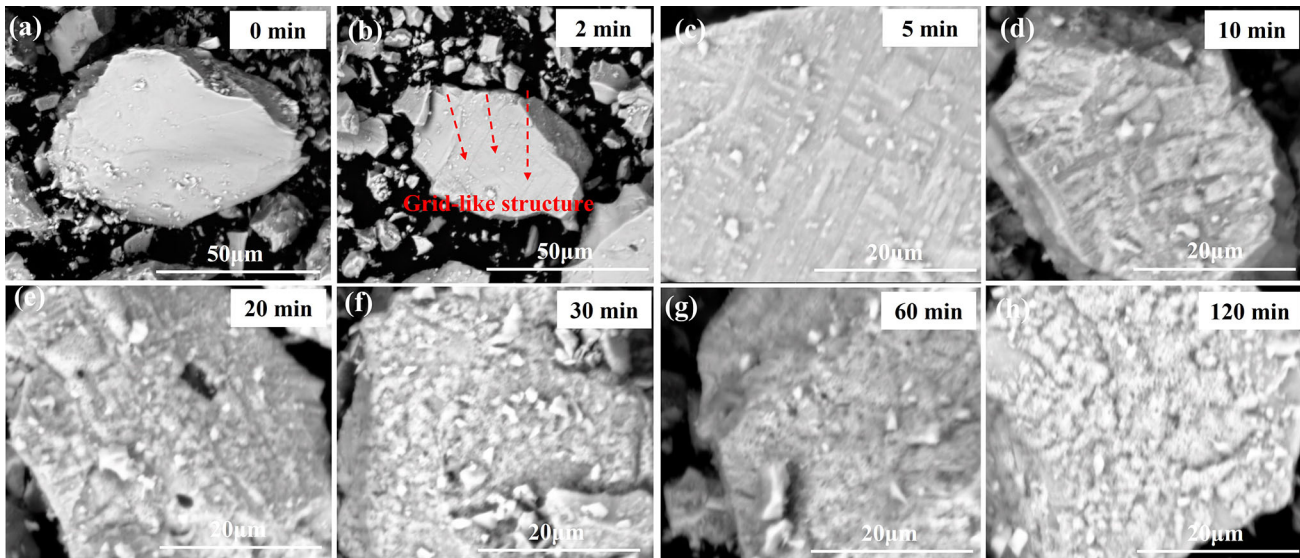


Fig. 8—SEM images of the oxidized products of sample B obtained under different duration times: (a) 0 min, (b) 2 min, (c) 5 min, (d) 10 min, (e) 20 min, (f) 30 min, (g) 60 min, and (h) 120 min.

slowly at 400 °C and 600 °C. When the temperature is increased to 800 °C and above, the oxidation rate increases significantly.

E. First-Principles Calculation

From the observation of the hematite structure, discussed in Section II-B, it seems that the hematite phase shows a certain growth habit. Yang and co-workers^[54,55] studied the effects of SiO₂ and Al₂O₃ on the

growth habit of calcium ferrite based on the surface energy (SE) by the first-principles calculation method. The growth rates of the crystal faces are proportional to their surface energies. Based on our previous studies,^[54,55] the preferred growth orientation of the hematite phase is calculated using the same method and calculation parameters. Figure 15 shows the HT-XRD patterns of sample B under 600 °C and 800 °C without normalization. The hematite crystal face (104) shows quite high intensity after 10 minutes and the

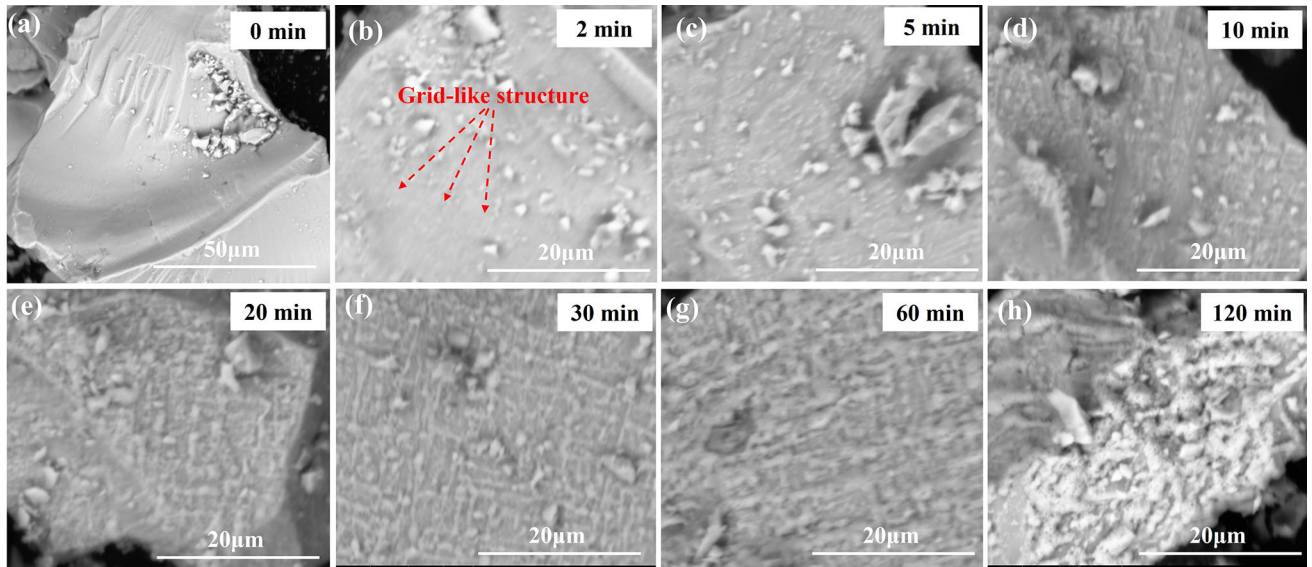


Fig. 9—SEM images of the oxidized products of sample C obtained under different duration times: (a) 0 min, (b) 2 min, (c) 5 min, (d) 10 min, (e) 20 min, (f) 30 min, (g) 60 min, and (h) 120 min.

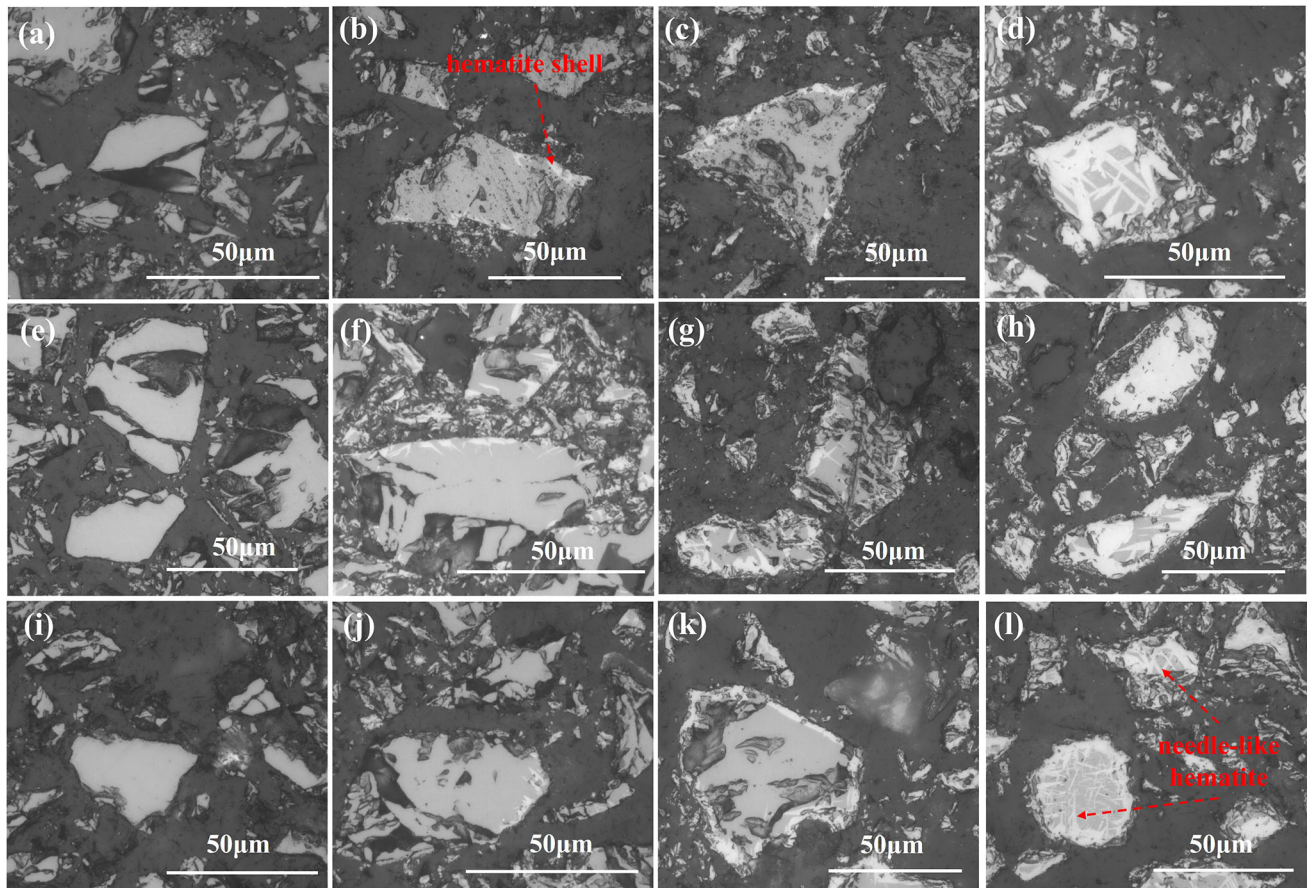


Fig. 10—Polished section images of the oxidized samples obtained under different duration times: (a) through (d) sample A under 0, 2, 5, and 60 min; (e) through (h) sample B under 0, 5, 30, and 120 min; and (i) through (l) sample C under 0, 2, 30, and 120 min.

Table IV. Pore Structure Parameters of Samples Within Different Duration Times

Duration Time (Min)	Sample A			Sample B			Sample C		
	Average Pore Size (nm)	Total Pore Volume ($\times 10^{-4}$ cm ³ /g)	Specific Surface Area (m ² /g)	Average Pore Size (nm)	Total Pore Volume ($\times 10^{-4}$ cm ³ /g)	Specific Surface Area (m ² /g)	Average Pore size (nm)	Total Pore Volume ($\times 10^{-4}$ cm ³ /g)	Specific Surface Area (m ² /g)
0	4.93	16.03	1.63	5.30	9.23	0.94	4.60	7.12	0.83
5	5.94	6.53	0.52	5.60	4.34	0.38	6.80	3.28	0.29
10	5.79	7.50	0.54	5.60	3.16	0.27	6.10	2.62	0.23
20	5.87	7.80	0.55	5.87	3.12	0.27	9.88	1.78	0.18
60	6.13	2.46	0.24	5.70	3.16	0.30	10.61	1.34	0.16

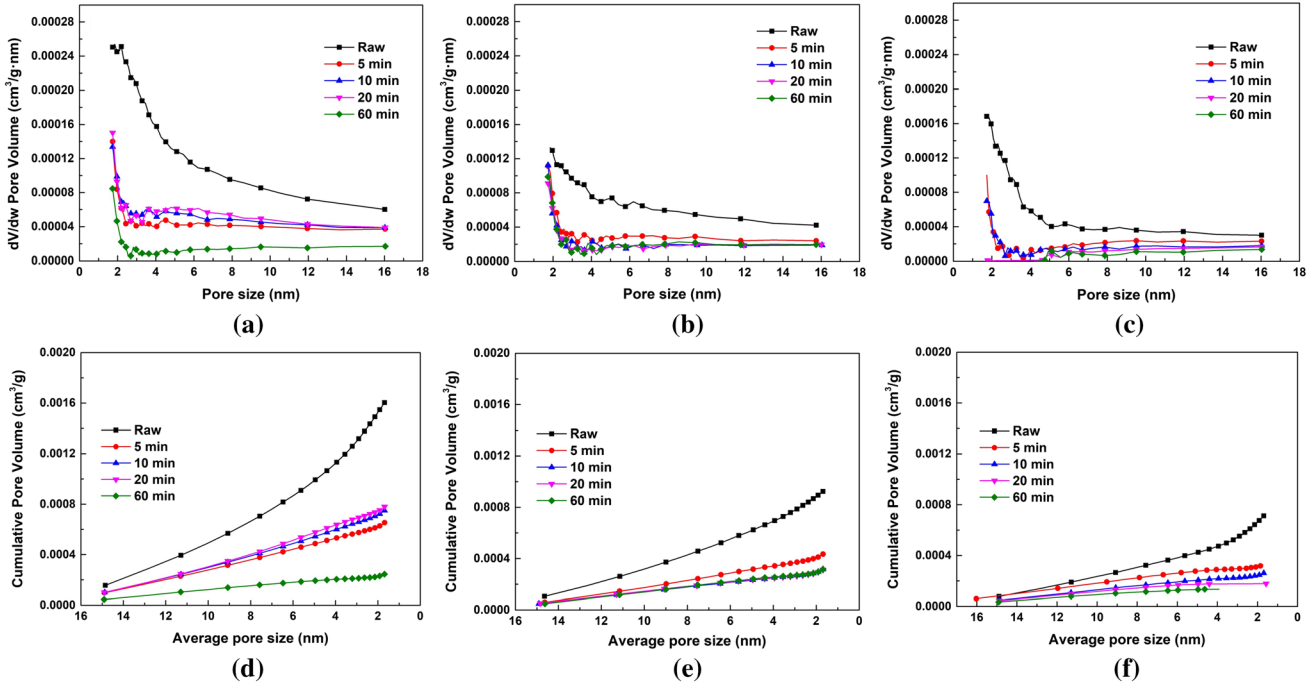


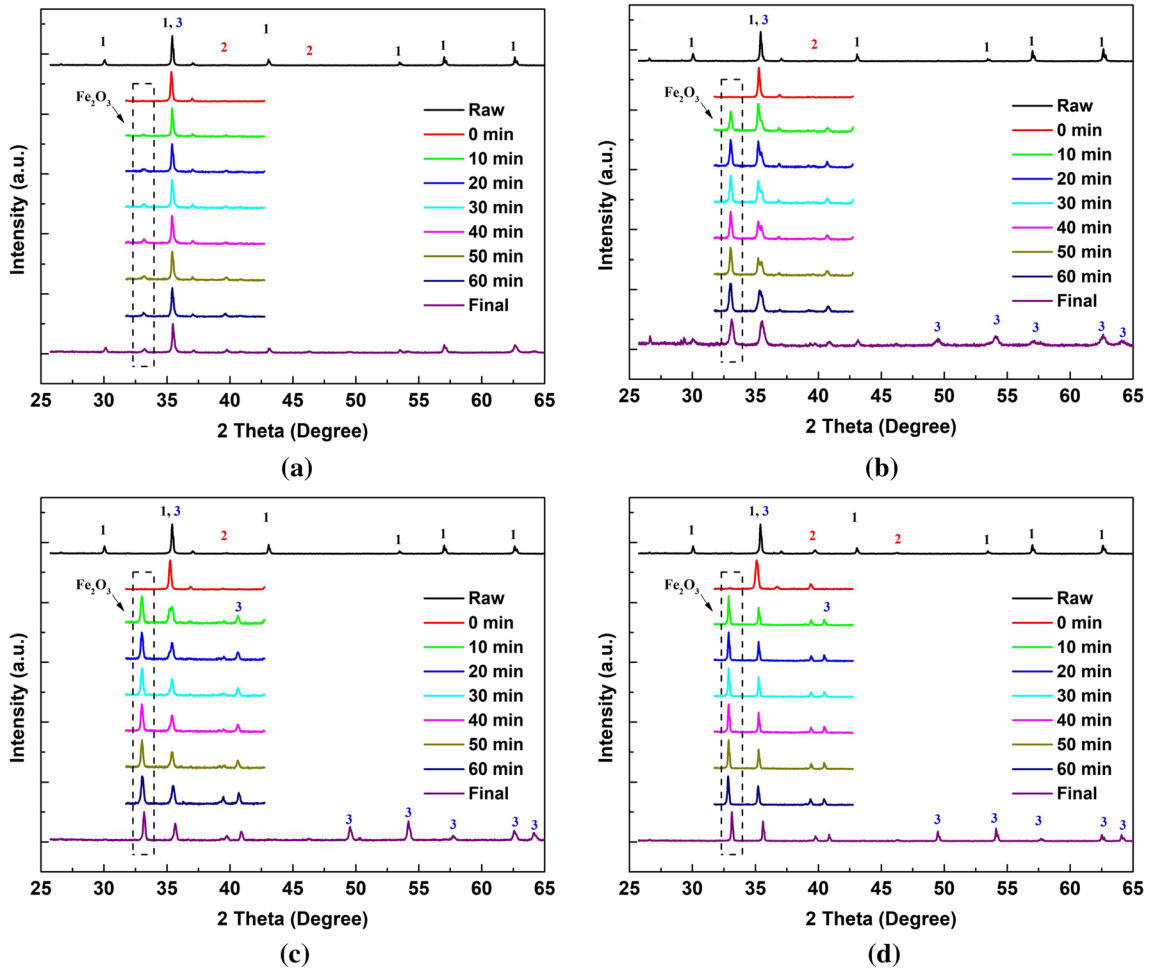
Fig. 11—Pore size distribution of the samples: (a) and (d) sample A, (b) and (e) sample B, and (c) and (f) sample C.

intensity is much larger than that of crystal faces (110) and (113). With the oxidation time, the intensities of (104) and (110) crystal face gradually increase. That is, the hematite phase has a preferred orientation along the (104) or (110) crystal face. The oxidation temperature difference showed no influence on the preferred orientation. The SE is calculated as shown in Eq. [12]:

$$SE = (E_{surface} - n \times E_{bulk}) / (2A), \quad [12]$$

where $E_{surface}$ and E_{bulk} are the total energy of the crystal surface model and the energy of the unit cell, respectively. A and n are the surface area of the crystal plane model and the number of the cells contained in the crystal plane model.

The model used for the calculation is shown in Figure 16. The calculated SE of each crystal face is shown in Figure 17. The SEs of the (104), (110), and (113) are 18.88, 27.37, and 15.59 eV/nm², respectively. The surface energies of the (104) and (110) crystal



1: Fe_3O_4 (PDF card No. 89-0688); 2: Pt (PDF card No. 04-0802); 3: Fe_2O_3 (PDF card No. 89-0597)

Fig. 12—*In-situ* HT-XRD patterns of sample B under different temperatures and duration times: (a) 400 °C, (b) 600 °C, (c) 800 °C, and (d) 1000 °C.

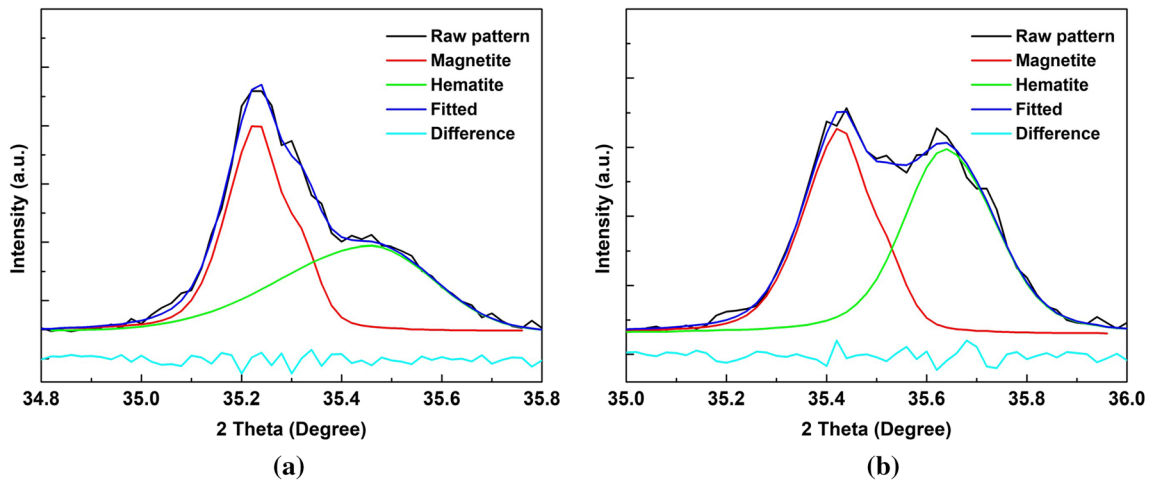


Fig. 13—Rietveld refinement profile of sample B for oxidation at 600 °C: (a) 10 min and (b) final.

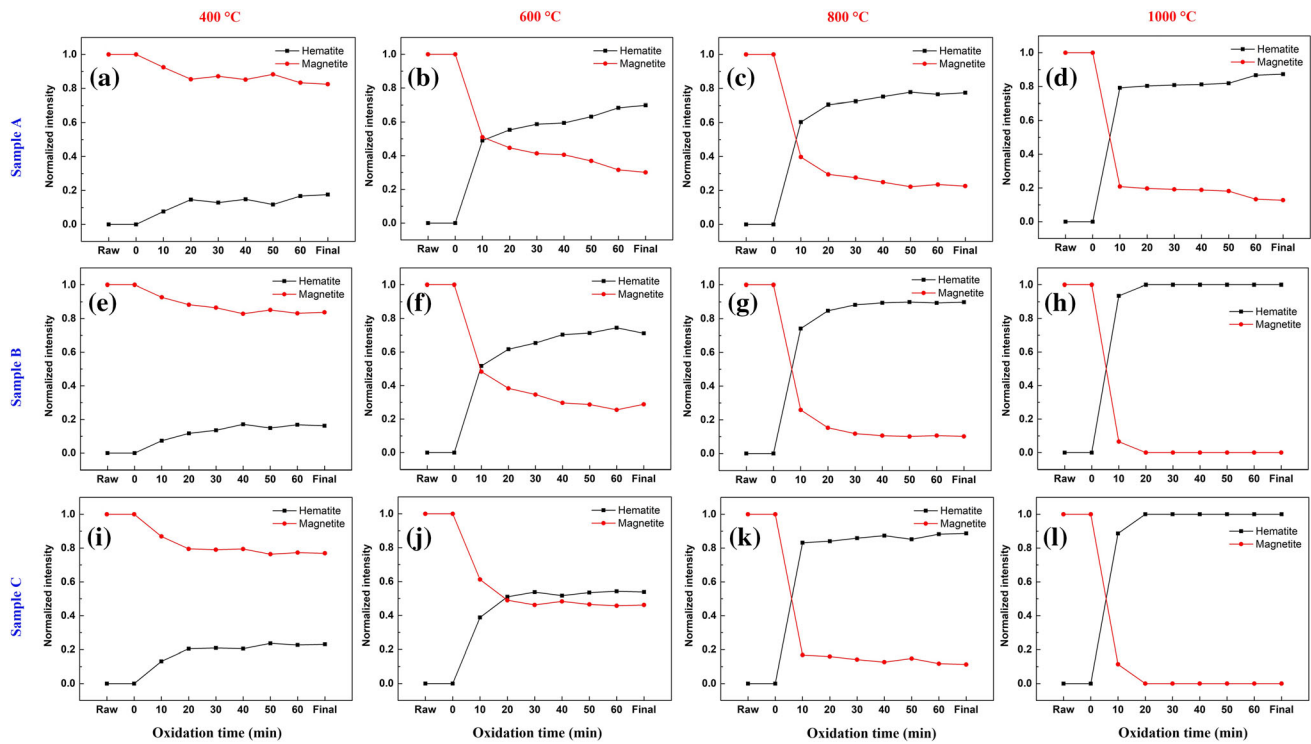


Fig. 14—Normalized intensities of the samples: (a) through (d) sample A under 400 °C, 600 °C, 800 °C, and 1000 °C; (e) through (h) sample B under 400 °C, 600 °C, 800 °C, and 1000 °C; (i) through (l) sample C under 400 °C, 600 °C, 800 °C, and 1000 °C.

surfaces are larger than that of the (113) crystal surface. Hence, the hematite crystals may preferentially orient themselves along the (104) or (110) crystal surface, which shows agreement with the HT-XRD results.

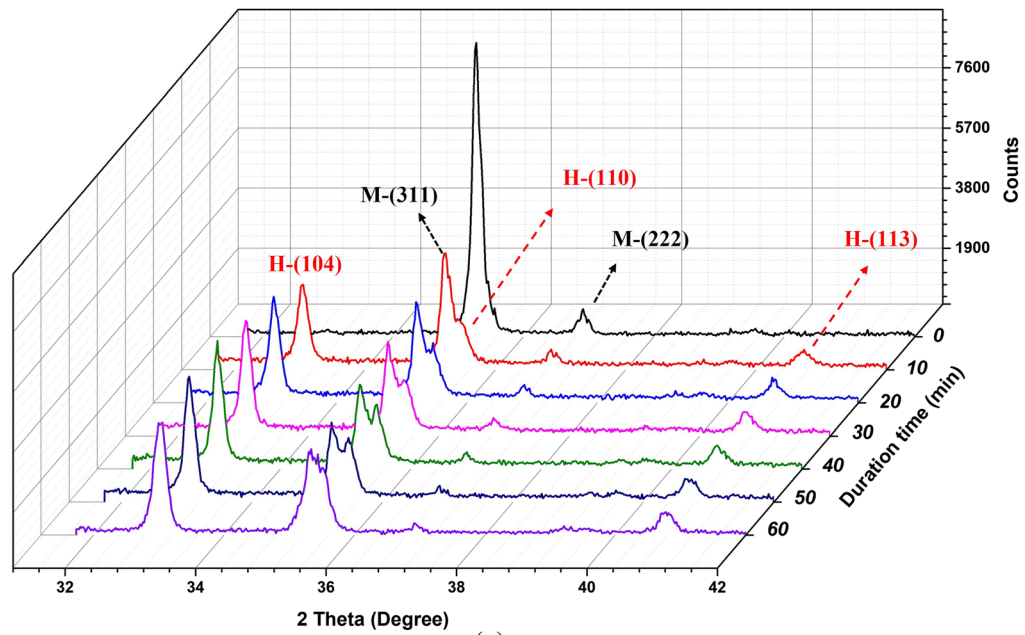
F. Oxidation Mechanism

The magnetite crystal unit has 32 oxygen anions and 24 iron cations (16Fe^{3+} and 8Fe^{2+}). The oxygen anions have a cubic close-packed structure in the magnetite unit. There are 96 interstices between the oxygen anions, of which 64 are tetrahedral interstices and 32 are octahedral interstices. Only eight tetrahedral interstices are occupied by Fe^{3+} cations. Sixteen of 32 octahedral interstices are occupied by 8Fe^{3+} cations and 8Fe^{2+} cations.^[56] As a result of such free interstices, the iron cations move more easily in the crystal lattice than oxygen anions.^[57] The size of an O^{2-} anion (1.26 Å) is much larger than that of an Fe^{2+} cation (0.75 Å) and Fe^{3+} cation (0.69 Å). Thus, the smaller size of the iron cation guarantees its predominant diffusion in the magnetite crystal unit.

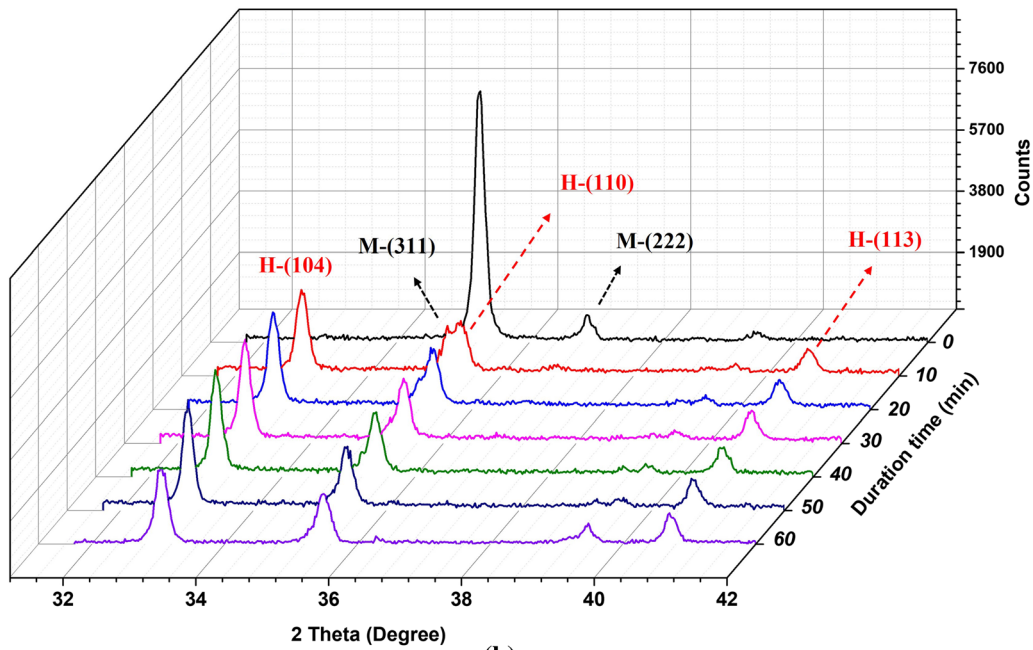
From the aspect of the crystal lattice, during the oxidation of magnetite, when an oxygen atom penetrates the magnetite lattice, two electrons are trapped. The local charges in the crystal must be neutral;

therefore, two positively charged holes, 2h^+ , are generated in the place of the previous electrons.^[58] Figure 18 shows the schematic of the oxidation mechanism. When the Fe^{2+} cation captures the charged hole h^+ , the valence increases and the iron becomes trivalent. However, in the later oxidation period, the charged hole h^+ has a greater opportunity to meet the Fe^{3+} cation. In this case, they are tantamount to an impurity cation with a higher valence ($>3^+$), which forces the lattice to become more compact.^[58] Hence, the mobility of the iron cations decreases significantly, resulting in a very slow oxidation rate of magnetite in the later stage.

From the aspect of a single magnetite particle, the oxidation first occurs at the surface and then extends inside. Figure 19 shows the oxidation process of a single magnetite particle. When the oxygen atoms capture the electrons from the magnetite phase, the oxidation occurs. The first hematite film appears in the interface. The Fe cations prefer to diffuse to the surface of the particle due to the low iron cation contents. The concentration gradient becomes the chemical drive for the outgrowth of the hematite. On the other hand, as discussed in Section II–E, the hematite phase has a preferred orientation along the (104) or (110) crystal face, which results in the formation of the gridlike structure at the surface. With the oxidation, the



(a)



(b)

Fig. 15—HT-XRD patterns of sample B without normalization: (a) under 600 °C and (b) under 800 °C. H and M represent hematite and magnetite, respectively.

hematite becomes the dominant phase at the surface. Then, the Fe^{3+} cations start to diffuse toward the particle center and form the needlelike hematite structures. The needlelike hematite structures grow and merge until the end of the oxidation.

IV. CONCLUSIONS

The purpose of this research is to investigate the oxidation of magnetite-based iron ore fines, which are helpful in optimizing the production of DRI by means of fluidized bed technology. Three magnetite-based iron

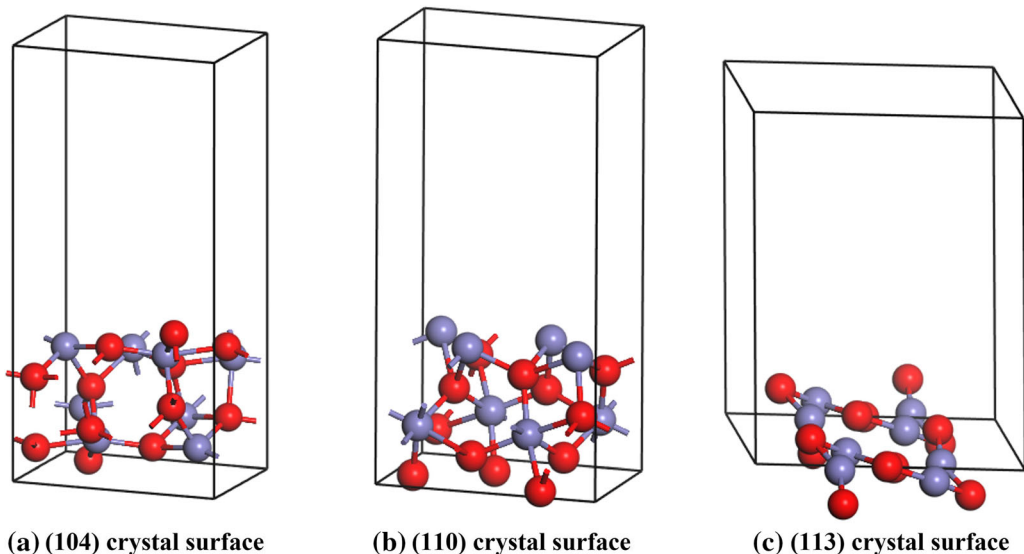


Fig. 16—Model used for the calculation (the red ball represents O ion; the purple ball represents Fe ion): (a) (104) crystal surface, (b) (110) crystal surface, and (c) (113) crystal surface.

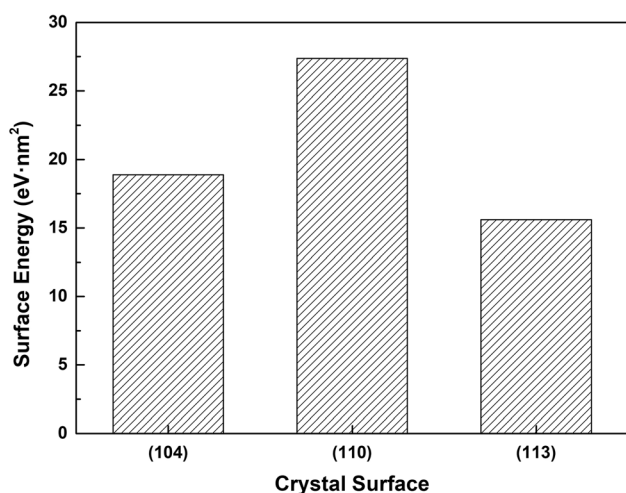


Fig. 17—Surface energies of the (104), (110), and (113) crystal surfaces.

ore brands are analyzed in terms of their oxidation characteristics, surface morphology, and structural evolution. The following conclusions are obtained.

1. According to nonisothermal oxidation DTA analysis, the oxidation reaction can be divided into at least three stages. The first two oxidation rate peaks are observed at around 330 °C and 550 °C, respectively, indicating the formation of γ -Fe₂O₃ and α -Fe₂O₃.

The highest oxidation rate of these three samples is in the temperature range between 548 °C and 573 °C. Sample B shows the highest OCI, followed by samples C and A. The magnetite-based iron ore with a higher OCI value is easier to oxidize.

2. During oxidation, the surface of all of the samples becomes rough and presents nanosized gridlike structure due to the outgrowth of hematite. The gridlike structures of sample B are much bigger than those in the other two samples. Sample B contains fewer impurity elements, while sample C contains the most impurities. It seems that these impurity elements influenced the diffusion of the iron ions, resulting in the different growth behaviors of the gridlike structures. With oxidation time, the gridlike structures grow bigger and connect with each other. At the same time, the hematite phase also grows in the particle, forming the needlelike structures.
3. The specific surface areas of samples A, B, and C decrease significantly after only 5 minutes of oxidation—from 1.63, 0.94, and 0.83 m²/g to 0.52, 0.38, and 0.29 m²/g, respectively. With the oxidation time, the specific areas keep decreasing. The total pore volumes of all the samples show the same trend as their specific areas. Compared with the raw samples, the pore size smaller than 3 nm in the oxidized sample is significantly reduced.
4. The hematite phase shows a certain growth habit. Based on HT-XRD patterns, the hematite crystal

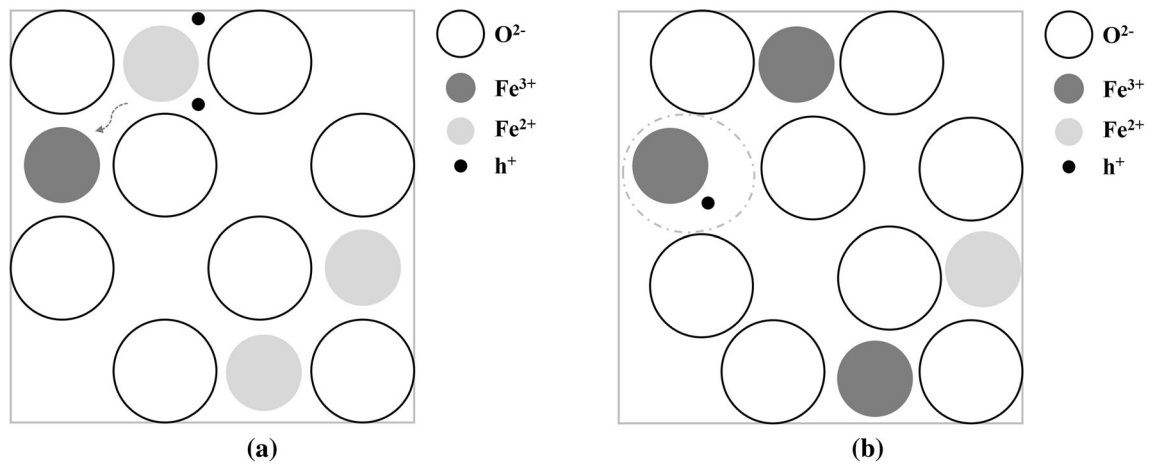


Fig. 18—Schematic of the oxidation mechanism of magnetite: (a) the Fe^{2+} cation turns into the Fe^{3+} cation and (b) later oxidation period.

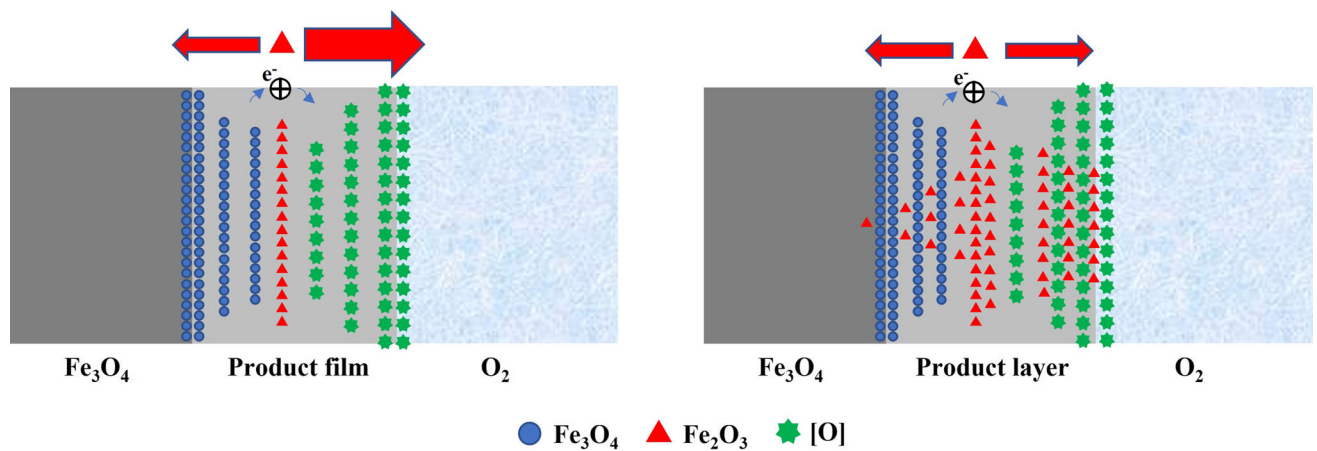


Fig. 19—Oxidation process of a single magnetite particle.

face (104) shows quite high intensity after 10 minutes of oxidation and the intensity is much larger than that of crystal faces (110) and (113). With the oxidation time, the intensities of (104) and (110) crystal faces gradually increase. The first-principles calculation confirms the preferential orientation. Theoretically, the surface energies of the (104) and (110) crystal surfaces are larger than that of the (113) crystal surface. Hence, the hematite crystals may preferentially orient themselves along the (104) or (110) crystal surface.

ACKNOWLEDGMENTS

The authors gratefully acknowledge the funding support of K1-MET GmbH, metallurgical competence center. The research program of the K1-MET competence center is supported by COMET (Competence Center for Excellent Technologies), the Austrian program for competence centers. COMET is funded by the Federal Ministry for Climate Action, Environ-

ment, Energy, Mobility, Innovation and Technology; the Federal Ministry for Digital and Economic Affairs; the provinces of Upper Austria, Tyrol, and Styria; and the Styrian Business Promotion Agency (SFG). In addition, the research work is partially financed by Montanuniversitaet Leoben. One of the authors (ZH) greatly acknowledges the financial support from the China Scholarship Council program (Grant No. 201908420284).

CONFLICT OF INTEREST

On behalf of all of the authors, the corresponding author states that there is no conflict of interest.

FUNDING

Open access funding provided by Montanuniversität Leoben.

OPEN ACCESS

This article is licensed under a Creative Commons Attribution 4.0 International License, which permits use, sharing, adaptation, distribution and reproduction in any medium or format, as long as you give appropriate credit to the original author(s) and the source, provide a link to the Creative Commons licence, and indicate if changes were made. The images or other third party material in this article are included in the article's Creative Commons licence, unless indicated otherwise in a credit line to the material. If material is not included in the article's Creative Commons licence and your intended use is not permitted by statutory regulation or exceeds the permitted use, you will need to obtain permission directly from the copyright holder. To view a copy of this licence, visit <http://creativecommons.org/licenses/by/4.0/>.

REFERENCES

1. B. McNab, A. Jankovis, D. David, and P. Payne: *Proc. Iron Ore Conf.*, The Australasian Institute of Mining and Metallurgy (The AusIMM), Perth, Australia, 2009, pp. 1–12.
2. Department of the Premier and Cabinet: *South Australia's Magnetite Strategy: Making Our State's Magnetite the World's Choice for Steelmaking*, p. 7, <https://sarigbasis.pir.sa.gov.au/WebtopEw/ws/samref/sarigl/image/DDD/BROCH028.pdf>. Accessed September 16, 2021.
3. L. Blaney: *Magnetite (Fe₃O₄): Properties, Synthesis, and Applications*, 2007, pp. 36–39, https://scholar.google.com/scholar?hl=en&as_sdt=0%2C5&q=Magnetite+%28Fe3O4%29%3A+Properties%2C+synthesis%2C+and+applications%2C&btnG=. Accessed September 16, 2021.
4. D. Zhu, J. Pan, L. Lu, and R.J. Holmes: *Iron Ore*, Processing and Environmental Sustainability, Woodhead Publishing, Sawston, England, Mineralogy, 2015, pp. 435–73.
5. H. Han and L. Lu: *Miner. Process. Extr. Metall. Rev.*, 2018, vol. 39, pp. 217–30.
6. S. Purohit, G. Brooks, M.A. Rhamdhani, M.I. Pownceby, and N.A.S. Webster: *Ironmak. Steelmak.*, 2020, vol. 47, pp. 674–85.
7. S. Purohit, G. Brooks, M.A. Rhamdhani, M.I. Pownceby, and N.A.S. Webster: *Ironmak. Steelmak.*, 2020, vol. 47, pp. 852–64.
8. S. Purohit, M.A. Rhamdhani, and G. Brooks: *AISTech Conf.*, Philadelphia, PA, 2018, pp. 1–8.
9. D. Zhu, V. Mendes, T. Chun, J. Pan, Q. Li, J. Li, and G. Qiu: *ISIJ Int.*, 2011, vol. 51, pp. 214–19.
10. X. Jiang, L. Wang, and F.M. Shen: *Adv. Mater. Res.*, 2013, vol. 805–806, pp. 654–59.
11. K. Huitu, M. Helle, H. Helle, M. Kekkonen, and H. Saxén: *Steel Res. Int.*, 2015, vol. 86, pp. 456–65.
12. World Steel Association: *Climate Change Mitigation*, http://www. acero.org.ar/wp-content/uploads/2019/07/fact20sheet_climate20mitigation_2019_vfinal.pdf. Accessed September 16, 2021.
13. European Commission: *2050 Long-Term Strategy—Climate Action—European Commission*, https://ec.europa.eu/clima/policies/strategies/2050_en. Accessed September 16, 2021.
14. A. Toktarova, I. Karlsson, J. Rootzén, L. Göransson, M. Odenberger, and F. Johnsson: *Energies.*, 2020, vol. 13, p. 3840.
15. SALCOS: SALCOS Official webpage, <https://salcos.salzgitter-ag.com/en/>. Accessed September 16, 2021.
16. V. Vogl, M. Åhman, and L.J. Nilsson: *J. Cleaner Prod.*, 2018, vol. 203, pp. 736–45.
17. M. Axelson, I. Robson, T.G. Wyns, and G.A. Khandekar: *Breaking Through—Industrial Low-CO₂ Technologies on the Horizon (2018)*, The Institute for European Studies (IES), p. 52. <https://researchportal.vub.be/en/publications/breaking-through-industrial-low-co2-technologies-on-the-horizon>. Accessed September 16, 2021.
18. Daniel Spreitzer: Ph.D. Thesis, Montanuniversitaet Leoben, Leoben, Austria, unpublished research, 2020.
19. H. Zheng, D. Spreitzer, T. Wolfinger, J. Schenk, and R. Xu: *Metall. Mater. Trans. B.*, 2021, vol. 52B, pp. 1955–71.
20. S. Forsmo, S.-E. Forsmo, P.-O. Samskog, and B. Björkman: *Powder Technol.*, 2008, vol. 183, pp. 247–59.
21. T.K. Sandeep Kumar, N.N. Viswanathan, H.M. Ahmed, C. Andersson, and B. Björkman: *Metall. Mater. Trans. B.*, 2015, vol. 46B, pp. 635–43.
22. R. Liang, S. Yang, F. Yan, and J. He: *J. Iron Steel Res. Int.*, 2013, vol. 20, pp. 16–20.
23. D. Papanastassiou and G. Bitsianes: *Metall. Trans.*, 1973, vol. 4, pp. 487–96.
24. T.K. Sandeep Kumar, N.N. Viswanathan, H. Ahmed, A. Dahlin, C. Andersson, and B. Björkman: *Metall. Mater. Trans. B.*, 2019, vol. 50B, pp. 162–72.
25. H. Zhang, J. Fu, J. Pan, F. Zhang, and Z. Guo: *J. Wuhan Univ. Technol. Mater. Sci. Edit.*, 2018, vol. 33, pp. 1516–23.
26. H. Zhang and J. Fu: *Int. J. Miner. Metall. Mater.*, 2017, vol. 24, pp. 603–10.
27. H. Zhang, M. Lu, and J. Fu: *J. Cent. South Univ.*, 2016, vol. 23, pp. 2999–3005.
28. U. Colombo, F. Gazzarrini, G. Lanzavecchia, and G. Sironi: *Science.*, 1965, vol. 147, p. 1033.
29. U. Colombo, G. Fagherazzi, F. Gazzarrini, G. Lanzavecchia, and G. Sironi: *Nature*, 1964, p. 175.
30. E.Z. Basta: *Econ. Geol.*, 1959, vol. 54, pp. 698–719.
31. H.J. Cho, M. Tang, and P.C. Pistorius: *Metall. Mater. Trans. B.*, 2014, vol. 45B, pp. 1213–20.
32. H.J. Cho and P.C. Pistorius: *AISTech Conf.*, Association for Iron & Steel Technology (AIST), Atlanta, GA, 2012, pp. 503–11.
33. A. Sardari, E.K. Alamdari, M. Noaparast, and S.Z. Shafaei: *Int. J. Miner. Metall. Mater.*, 2017, vol. 24, pp. 486–92.
34. T.K. Sandeep Kumar, N.N. Viswanathan, H. Ahmed, A. Dahlin, C. Andersson, and B. Björkman: *Metall. Mater. Trans. B.*, 2019, vol. 50B, pp. 150–61.
35. E.R. Monazam, R.W. Breault, and R. Siriwardane: *Ind. Eng. Chem. Res.*, 2014, vol. 53, pp. 13320–28.
36. S. Song and P.C. Pistorius: *ISIJ Int.*, 2019, vol. 59, pp. 1765–9.
37. H. Zheng, J. Schenk, D. Spreitzer, T. Wolfinger, and O. Dagha-geleh: *Steel Res. Int.*, 2021, p. 2000687.
38. C.R. van Hise: *A Treatise on Metamorphism*, U.S. Government Printing Office, Washington, DC, 1904, p. 467.
39. J.W. Gruner: *Econ. Geol.*, 1926, vol. 21, pp. 375–93.
40. E. Park and O. Ostrovski: *ISIJ Int.*, 2004, vol. 44, pp. 74–81.
41. E. Park and O. Ostrovski: *ISIJ Int.*, 2004, vol. 44, pp. 999–1005.
42. D. Zhu, C. Yang, J. Pan, and X. Li: *Metall. Mater. Trans. B.*, 2016, vol. 47B, pp. 2919–30.
43. F. Pan, Q. Zhu, Z. Du, and H. Sun: *J. Iron Steel Res. Int.*, 2016, vol. 23, pp. 1160–67.
44. S.K. Bhargava, A. Garg, and N.D. Subasinghe: *Fuel.*, 2009, vol. 88, pp. 988–93.
45. E.R. Schmidt and F.H. Vermaas: *Am. Miner.*, 1955, vol. 40, pp. 422–31.
46. H. Lepp: *Am. Miner.*, 1957, vol. 42, pp. 679–81.
47. B.H. Wang: *National Ironmaking Production Technology Conf.*, Beijing, 2010, pp. 327–31.
48. C. Dupuis and G. Beaudoin: *Miner. Deposita.*, 2011, vol. 46, pp. 319–35.
49. J. Xiumin, Z. Chuguang, Q. Jianrong, L. Jubin, and L. Dechang: *Energy Fuels.*, 2001, vol. 15, pp. 1100–02.
50. J. Zhang, Q. Zhu, Z. Xie, C. Lei, and H. Li: *Metall. Mater. Trans. B.*, 2013, vol. 44B, pp. 897–905.
51. X. Fu, Y. Wang, and F. Wei: *Metall. Mater. Trans. A.*, 2010, vol. 41A, pp. 1338–48.
52. F.H. Chung: *J. Appl. Crystallogr.*, 1974, vol. 7, pp. 519–25.
53. F.H. Chung: *J. Appl. Cryst.*, 1974, vol. 7, pp. 526–31.
54. W. Wang, D. Yang, Z. Ou-Yang, R. Xu, and M. Song: *Metall. Mater. Trans. B.*, 2019, vol. 50B, pp. 678–87.
55. D. Yang, W. Wang, J. Li, R. Xu, X. Wang, and G. Wang: *Metall. Mater. Trans. B.*, 2020, vol. 51B, pp. 776–85.
56. Y. Kapelyushin, Y. Sasaki, J. Zhang, S. Jeong, and O. Ostrovski: *Metall. Mater. Trans. B.*, 2017, vol. 48B, pp. 889–99.
57. A.V. Roshchin and Vasily Roshchin: *Russ. Metall.*, 2003, pp. 1–5.
58. A. V. Roshchin and Vasily Roshchin: *Russ. Metall.*, 2003, pp. 97–102.

Publisher's Note Springer Nature remains neutral with regard to jurisdictional claims in published maps and institutional affiliations.

Phase Transition of Magnetite Ore Fines During Oxidation Probed by *In Situ* High-Temperature X-Ray Diffraction



HENG ZHENG, ODAY DAGHAGHELEH, YAN MA, BERND TAFERNER, JOHANNES SCHENK, and YURY KAPELYUSHIN

The reduction of magnetite-based iron ore fines in a hydrogen-induced fluidized bed becomes an attractive fossil-free ironmaking route. Our previous study showed that a prior oxidation treatment of magnetite was helpful to improve its fluidization and reduction behavior. However, the underlying oxidation mechanisms of magnetite ore fines remained unclear and required further investigations. In this study, two magnetite ore brands were analyzed *via in situ* high-temperature X-ray diffraction (HT-XRD) during oxidation, to investigate the thermal transformation of Fe_3O_4 to $\alpha\text{-Fe}_2\text{O}_3$ at crystal scale. The lattice constants and crystallite sizes of both phases and oxidation degree were evaluated at different temperatures based on the HT-XRD patterns. The lattice constants of Fe_3O_4 and $\alpha\text{-Fe}_2\text{O}_3$ increased with an increase in temperature due to the thermal expansion and can be successfully fitted with temperature by second-order polynomials. With Fe_3O_4 being oxidized into Fe_2O_3 , the Fe_2O_3 crystallite grew and showed a certain growth habit. The Fe_2O_3 crystallite grew faster along the a/b axis than the c axis. The oxidation kinetics followed the parabolic law as shown by the sigmoid-shaped oxidation degree curve, suggesting that the solid diffusion of ions was the rate-limiting step.

<https://doi.org/10.1007/s11663-023-02754-z>
© The Author(s) 2023

I. INTRODUCTION

MAGNETITE ore is one of the important resources for ironmaking plants. The global magnetite ore production is approximately 583 million tons per year accounting for 28 pct of the total iron ore production.^[1] In some countries, such as South Australia, the major iron ore deposit is magnetite.^[2] The current commercial practice of magnetite ore fines usually requires pelletization to produce iron ore pellets with appropriate size and strength.^[3] However, the pelletizing process requires additional energy and cost and generates CO_2 emissions.

One possible concept for future crude steel production is using a hydrogen-based fluidized bed to produce hydrogen direct reduced iron (HDRI), followed by an electric arc furnace (EAF) process.^[4,5] Therefore, the production of HDRI using magnetite ore fines in a hydrogen-induced fluidized bed becomes of great interest. The hydrogen-based fine-ore reduction (HYFOR) process developed by Primetals Technologies is one of the successful examples. The HYFOR process allows for the operation of any type of iron ore fines with particle sizes of 100 pct < 150 μm .^[6] In the case of using magnetite ore fines, prior oxidation occurs in the preheating stage. A series of laboratory-scale experiments showed that the prior oxidation of magnetite was helpful to improve its fluidization and reduction behavior.^[7-9] Thus, it is of great importance to understand the oxidation mechanisms of magnetite ore fines for optimizing the process route.

The exothermic effect, structural evolution, and kinetic analysis regarding the oxidation of magnetite were summarized in our previous work.^[10,11] In general, the oxidation of magnetite experienced two stages, where the magnetite was oxidized into an intermediate phase and further oxidized to $\alpha\text{-Fe}_2\text{O}_3$. During the oxidation, whisker or rough pleated structures of hematite were formed on the surface of magnetite particles. The rate-limiting step for oxidation of

HENG ZHENG, ODAY DAGHAGHELEH, and BERND TAFERNER are with the Montanuniversitaet Leoben, Franz-Josef-Straße 18, 8700 Leoben, Austria. Contact email: heng.zheng@stud.unileoben.ac.at YAN MA is with the Max-Planck-Institut für Eisenforschung, Max-Planck-Straße 1, 40237, Düsseldorf, Germany. JOHANNES SCHENK is with the Montanuniversitaet Leoben and also with the K1-MET GmbH, Stahlstraße 14, 4020 Linz Austria. Contact e-mail: johannes.schenk@unileoben.ac.at YURY KAPELYUSHIN is with the South Ural State University (National Research University), Lenina Avenue 76, Chelyabinsk, Russian Federation 454080.

Manuscript submitted October 20, 2022; accepted February 16, 2023.

magnetite in particle scale was generally solid-state diffusion which can be well described by parabolic law. The diffusion of oxygen into/within the magnetite particles was not the rate-limiting step. There are many kinetic studies on the oxidation of magnetite at the particle scale using thermogravimetric analysis (TGA).^[12–16] In addition, some post-mortem X-ray diffraction (XRD) measurements were conducted to study crystal transformation after the oxidation of magnetite. It was found that magnetite from different mines showed different lattice constants due to various types of gangue elements.^[17] The lattice constant of oxidized magnetite also differed after oxidation at different temperatures.^[18] The strain/stress occurring in the lattice should promote the nucleation of α -Fe₂O₃ and the crystallite size of magnetite governed the formation of γ -Fe₂O₃ and the oxidation kinetics.^[19] The crystallite size of the oxidized magnetite calculated based on the Scherrer equation was comparable to that measured by transmission electron microscopy (TEM), which proved the accuracy of the XRD method for obtaining the crystallite size.^[20] However, little information is available in the literature on the phase transition at the crystal scale during oxidizing magnetite, which limits the understanding of the oxidation mechanisms of magnetite. The objective of the present study is to investigate the thermal transformation of magnetite ore fines at the crystal scale *via in situ* high-temperature XRD (HT-XRD) during oxidation. The findings provide deeper insights into the phase transformation from magnetite to hematite under an oxidation condition.

II. EXPERIMENTAL PROCEDURES

A. Materials

Two commercial magnetite ore brands were investigated in this study and their chemical compositions are listed in Table I. The particle size distributions and apparent densities of the ores were characterized by CILAS 1064 particle size analyzer and Ultrapycnometer 1000 density analyzer, respectively. The results are listed in Table II. The raw ores were dried at 110 °C for 6 h before all the following tests.

Table I. Chemical Analysis of the Raw Magnetite Samples, (Wt Pct)^[11]

	Fe _{tot}	FeO	SiO ₂	Al ₂ O ₃	MgO	CaO	TiO ₂	P	S
Ore A	68.78	27.71	5.60	0.18	0.17	0.17	—	0.017	0.05
Ore B	65.65	27.66	3.33	1.16	1.62	1.62	0.22	0.017	0.10

Table II. Particle Size Distributions and Density of the Raw Magnetite Samples^[11]

	D10 (μ m)	D50 (μ m)	D90 (μ m)	Skeletal Density (g/cm ³)
Ore A	4.81	28.35	62.66	4.94
Ore B	6.10	32.25	70.16	5.09

B. In Situ High-Temperature X-Ray Diffraction (HT-XRD)

The HT-XRD analyses were performed on a Rigaku Ultima IV XRD diffractometer with a Cu target. The K α radiation was filtered as the X-ray source. The measurement step size was 0.02 deg and the sampling time was 0.15 s/step. In each measurement, 300 mg of material was placed on a platinum heating strip and heated in the HTK-16 high-temperature chamber (Anton Paar) to 1000 °C at a heating rate of 100 °C/min. The material was placed in a very thin layer to avoid thermal gradients along the height. It is difficult to determine the thickness of the layer. The layer was composed of a stack of approximately 3 magnetite particles and supposed to be thinner than 150 μ m. The *in situ* HT-XRD measurements were conducted at temperatures of 400 °C, 600 °C, 800 °C, and 1000 °C, as shown in Figure 1. The air could be exchanged between the facility chamber and the outside. Due to the small amount of magnetite, the change of oxygen partial pressure was negligible. The oxygen partial pressure was assumed to be the same as the ambient atmosphere. Before and after the oxidation experiments, the XRD measurements were conducted at room temperature with a scanning angle between 25 and 65 deg. It should be noted that the temperature ramping was halted and the material was kept at a fixed temperature during the *in situ* HT-XRD measurements. The oxidation reaction continued during the HT-XRD scans. To minimize the duration of the HT-XRD measurements and increase the time resolution, the scanning angle was set in a narrow range between 32 and 41 deg, where three hematite peaks and two magnetite peaks could be observed. In this case, each HT-XRD measurement took around 67.5 s.

C. HT-XRD Data Treatment

The Rietveld refinement method was widely used for phase quantification in ironmaking area.^[21–24] At current study, the Jade 6.0 software provided by Materials data Inc. was employed to identify and fit the diffraction peaks in this study. The overlapped peaks of magnetite and hematite at around 35 deg were successfully

separated by refinement in Jade 6.0 software, and the location and profile of individual peaks were obtained, as shown in Figure 2. Besides, the quantitative information of crystal information, such as lattice constants,^[25] crystallite size,^[26] and phase fraction,^[27] can be obtained.

1. Determination of Lattice Constants

Based on our previous TGA tests, the oxidation started at around 200 °C then reached the first peak at around 330 °C and the second peak started at around 400 °C.^[11] The oxidation product was supposed to be γ -Fe₂O₃ between 200 °C and 400 °C. Above 400 °C, γ -Fe₂O₃ transformed into α -Fe₂O₃. In the present study, the oxidation temperature was higher than 400 °C, and thus only α -Fe₂O₃ was expected to be the oxidation product (hereafter, α -Fe₂O₃ is referred to as Fe₂O₃). Therefore, two crystal structures were considered: Fe₃O₄ (cubic close-packed crystal) and Fe₂O₃ (hexagonal close-packed crystal). The relationship between interplanar spacings (d), lattice constants (a), and crystal planes $\{hkl\}$ are expressed in Eqs. [1] and [2].^[28] When a specific plane and corresponding interplanar spacing are known, the lattice constants can be calculated. The interplanar spacing can be obtained by Bragg's law as shown in Eq. [3].

$$\text{Cubic close-packed crystal : } \frac{1}{d^2} = \frac{h^2 + k^2 + l^2}{a^2} \quad [1]$$

Hexagonal close-packed crystal :

$$\frac{1}{d^2} = \frac{4}{3} \frac{(h^2 + k^2 + hk)}{a^2} + \frac{l^2}{c^2} \quad [2]$$

$$\text{Bragg's law : } d = \frac{n\lambda}{2\sin\theta}, \quad [3]$$

where d is the interplanar spacing; a and c are the lattice constants, $\{hkl\}$ is the crystal plane; n is the diffraction order, and here the value is 1.

2. Determination of Crystallite Size

Crystallite size (D) can be calculated using the Scherrer equation, as given in Eq. [4]. It should be noted that the crystallite size refers to the average thickness perpendicular to the (hkl) planes. The (110) and (104) planes of Fe₂O₃ crystal were chosen for quantifying the crystallite size. Because these two peaks exhibit relatively high intensities and have similar instrumental broadening conditions (similar peak position).^[29] As shown in Figure 3, the (110) plane is parallel to the c axis and (104) plane is at a small angle to the a/b axis.^[29] Therefore, the crystallite size along the c axis and a/b axis can be calculated according to Eqs. [5], [6].

$$D = \frac{K\lambda}{\beta \cos\theta} \quad [4]$$

$$D_{a/b} = D_{110} \times \cos\alpha_{110} \quad [5]$$

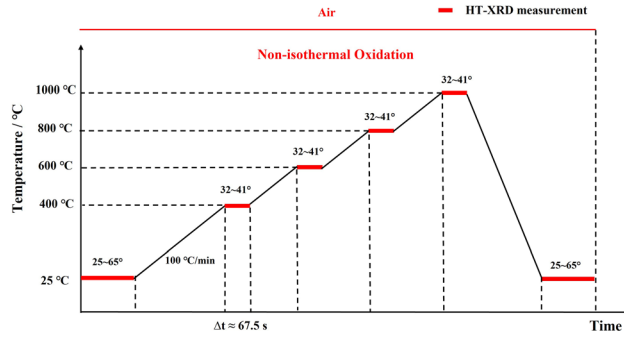


Fig. 1—Temperature profile for HT-XRD measurements.

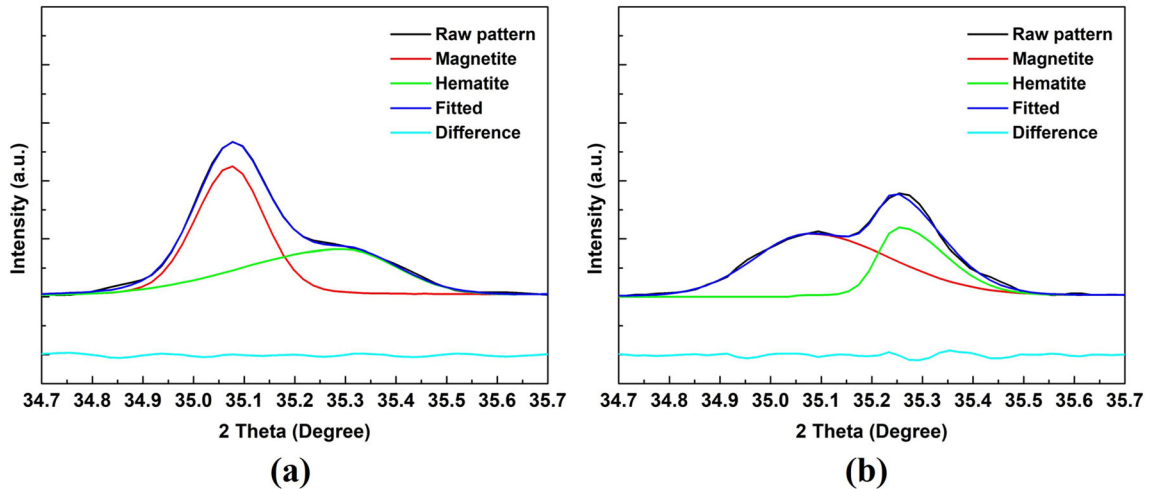


Fig. 2—Rietveld refinement peak profile of Ore A at different temperatures: (a) 600 °C and (b) 800 °C.

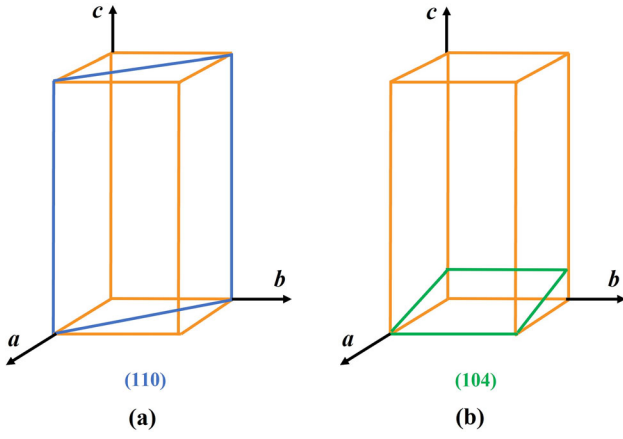


Fig. 3—Schematic of Fe_2O_3 crystal: (a) (110) plane and (b) (104) plane.

$$D_c = D_{104} \times \cos\alpha_{104}, \quad [6]$$

where D is crystallite size, nm; K is 0.94 (Scherrer constant); λ is 0.15406 nm (the wavelength of $K\alpha$ Cu X-ray source); β is full width at half maximum (FWHM), radians; θ is peak position, radians; $D_{a/b}$ and D_c represent the crystallite size calculated based on (110) and (104) peaks; α_{110} is the angle between [110] direction and x - y plane; α_{104} is the angle between the [104] direction and the y - z plane. Here, $\cos\alpha_{110} = 1$ and $\cos\alpha_{104} = 0.6192$.^[29]

3. Determination of Oxidation Degree

The matrix-flushing method^[30,31] was used to obtain the content of Fe_3O_4 and Fe_2O_3 . The relative mass content of each phase is proportional to the ratio between its peak intensity and relative intensity ratio (RIR). The RIR value of each phase can be found in the PDF card database. The RIRs of the Fe_3O_4 and Fe_2O_3 phases are 4.9 and 3.2, respectively. The impurities were not considered in the calculation. The content of Fe_2O_3 and Fe_3O_4 can be calculated based on Eqs. [7], [8].^[11]

$$x_H/x_M = \frac{I_H/k_H}{I_M/k_M} \quad [7]$$

$$x_H + x_M = 1, \quad [8]$$

where x_H and x_M are the relative mass content of Fe_2O_3 and Fe_3O_4 . I_H , I_M , k_H , and k_M are the intensities and RIR values of Fe_2O_3 and Fe_3O_4 , respectively.

Kapelyushin *et al.*^[32] calculated the reduction degree of Fe_3O_4 in the CO-CO₂ atmosphere based on HT-XRD analysis. The oxidation degree of Fe_3O_4 can be obtained by a similar method. The initial mass content of Fe_3O_4 was calculated *via* the mass balance of iron. Hence, the theoretical weight gain can be obtained as given in Eqs. [9], [10]. The actual weight gain was calculated based on the Fe_2O_3 mass content *via* Eq. [11]. Thereafter, the oxidation degree (w) can be obtained by Eq. [12].^[33,34]

$$m_M = x_M + \frac{x_H}{W_H} \times \frac{2}{3} \times W_M \quad [9]$$

$$\Delta m_{\text{theory}} = \frac{m_M}{W_M} \times \frac{W_O}{4} \quad [10]$$

$$\Delta m = \frac{x_H}{W_H} \times \frac{2}{3} \times \frac{W_O}{4} \quad [11]$$

$$w = \frac{\Delta m}{\Delta m_{\text{theory}}} \times 100 \text{ pct}, \quad [12]$$

where W_H , W_M , and W_O are mole masses of Fe_2O_3 , Fe_3O_4 , and O_2 , respectively. m_M , Δm_{theory} , Δm , and w are the initial mass content of Fe_3O_4 , theoretical weight gain, actual weight gain, and oxidation degree.

III. RESULTS AND DISCUSSION

A. Oxidation of Magnetite

Figure 4 shows the oxidation behavior of two ores at different temperatures probed by HT-XRD. Two ores revealed similar oxidation behavior, as suggested by the diffraction patterns. All the peaks shifted to a lower diffraction angle with an increase in temperature due to thermal expansion.^[35–37] The (104) peak of Fe_2O_3 firstly appeared at 400 °C, as shown in Figures 4(a) and (c). With an increase in temperature, the intensity of the (104) peak increased, indicating a higher fraction of Fe_2O_3 . The (311) peak of Fe_3O_4 vanished at 1000 °C, representing deep oxidation of Fe_3O_4 . The width of (104) peak became narrower with increasing temperature, which suggested the growth of Fe_2O_3 crystallite.

B. Oxidation Degree

The oxidation degrees of both ores at different temperatures are shown in Figure 5. Ore A was easier to be oxidized than Ore B, as indicated by its faster kinetics. The oxidation degree was lower than 10 pct at 400 °C in both cases. When the temperature increased to 600 °C, the oxidation degree increased significantly. Above 800 °C, the oxidation rate slowed down. The sigmoid-shaped oxidation degree curve indicated that the kinetics followed the parabolic law, where the solid diffusion of ions was the rate-limiting step. The oxidation mechanism was explained in our previous study.^[11] Each magnetite crystal unit contains eight Fe_3O_4 molecules, i.e., 32 oxygen anions and 24 iron cations (16 Fe^{3+} and 8 Fe^{2+}). The oxygen anions present a cubic close-packed structure, where 96 interstices exist. Only 8 out of 64 tetrahedral interstices are occupied by Fe^{3+} cations. 16 out of 32 octahedral interstices are occupied by 8 Fe^{3+} cations and 8 Fe^{2+} cations.^[11] Due to so many interstices, the iron cations can move easily within the crystal lattice. The

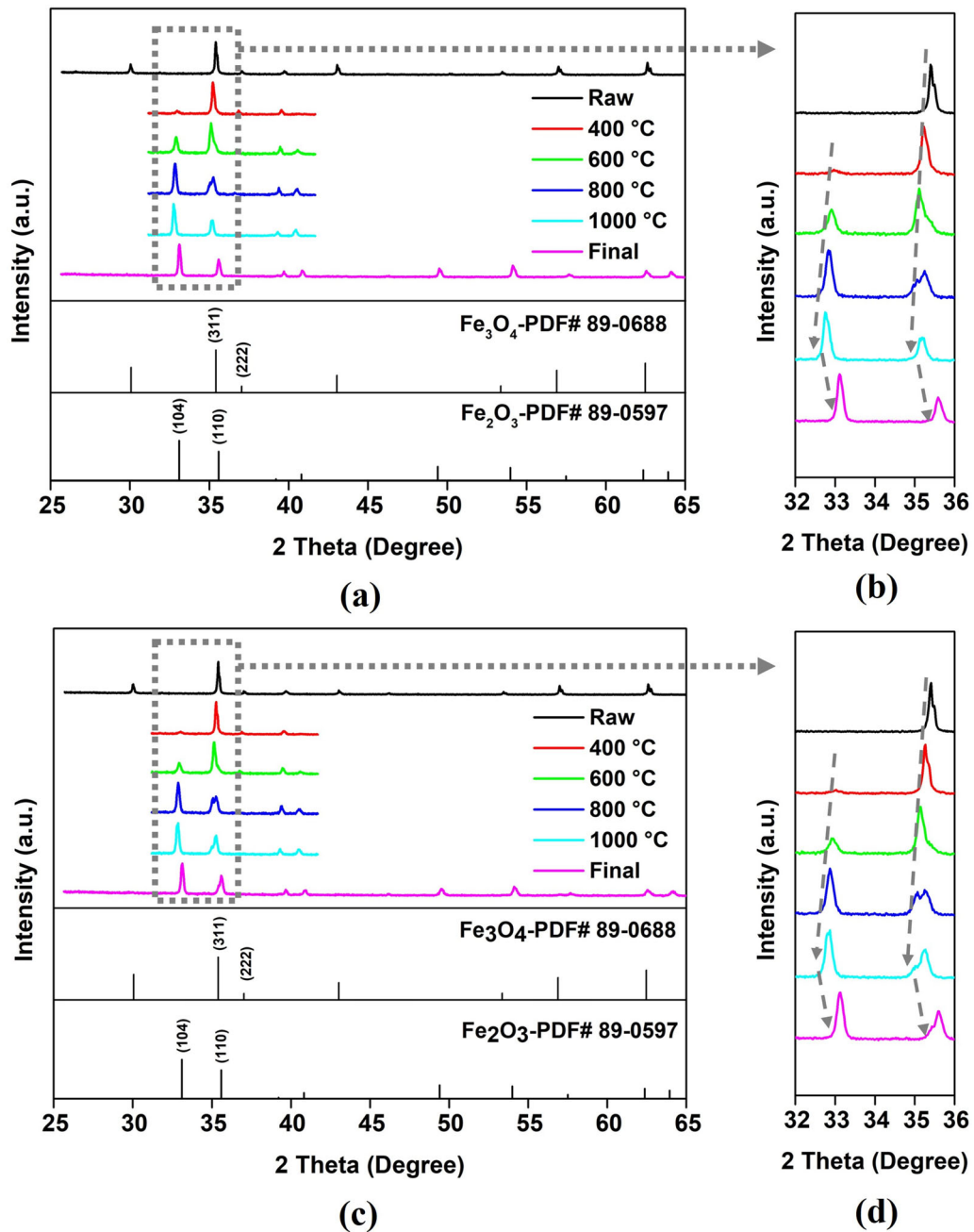


Fig. 4—*in situ* HT-XRD patterns at different temperatures: (a), (b) Ore A; (c), (d) Ore B.

O^{2-} anion can hardly move due to its bigger size. From the crystal scale, when an oxygen atom is trapped by Fe_3O_4 for phase transformation, two electrons are taken from the crystal by the oxygen atom. In the meanwhile, two positively charged holes $2h^+$ are generated in the place of the previous electrons for a neutral local charge in the crystal. Then Fe^{2+} cation may capture the charged hole h^+ and becomes Fe^{3+} cation. In later oxidation stage, due to the high amount of Fe^{3+} cations, the charged hole h^+ has less opportunity to meet Fe^{2+} cations. In the contrast, the charged hole h^+ decreases the mobility of the iron cations and expand the crystal unit.

C. Evolution of Lattice Constants

Table III summarizes the lattice constants of Fe_3O_4 in the ores at different temperatures. The results are comparable to those in the literature. The change in lattice constant with increasing temperature is supposed to be caused by thermal expansion and lattice modification during oxidation.^[18] As shown in Table III, the lattice constant at a specific temperature measured in this study was slightly larger than that in the literature. Such a difference might be due to a much higher oxygen partial pressure in the present study, as the magnetite was oxidized under an air atmosphere. This condition could result in a larger lattice constant of magnetite due

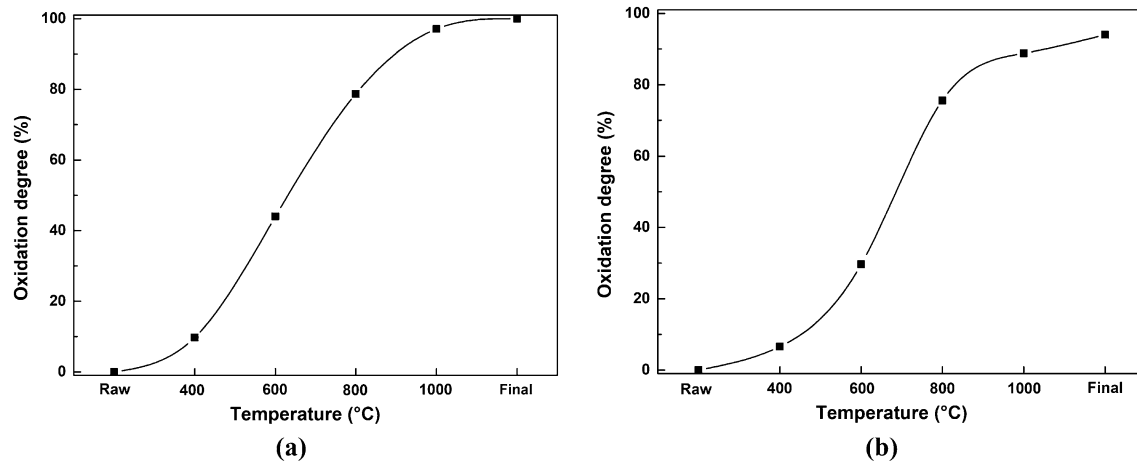


Fig. 5—The oxidation degrees of Ore A and B at different temperatures: (a) Ore A; (b) Ore B.

to partial oxidation^[38] (*i.e.*, a higher oxygen occupancy in the lattice). The temperature dependence of the lattice constant can be represented by polynomials up to the fifth order.^[39] Here, the relation between lattice constant and temperature was successfully fitted with the second-order polynomials (Figure 6), within a temperature range of 25 °C to 800 °C. The temperature-dependent lattice constant of Fe_3O_4 can be described as follows: $a = 2.53 \times 10^{-8} \times T^2 + 8.64 \times 10^{-5} \times T + 8.4132$. At the higher temperature (*e.g.*, 1000 °C), the (222) peak of Fe_3O_4 disappeared, which reduced the accuracy in the assessment of the lattice constant. Thus, the lattice constant at 1000 °C was not considered.

Table IV lists the lattice constants of Fe_2O_3 at different temperatures. Based on Eq. [2], at least two peaks of Fe_2O_3 are required to obtain the lattice constant a and c for a trigonal crystal structure. Therefore, only one set of a and c can be calculated at each temperature in the current study. The lattice parameters of Fe_2O_3 measured in this study were slightly larger than those in the literature, where a was 5.01 to 5.04 Å and c was 13.68 to 13.73 Å in the temperature range of 300 °C to 800 °C.^[41] Stefano *et al.*^[37] studied the phase transformation from goethite ($\alpha\text{-FeOOH}$) to hematite ($\alpha\text{-Fe}_2\text{O}_3$) in the temperature range of 200 °C to 1000 °C by synchrotron powder diffraction. Hematite was formed by the release of the OH^- groups of goethite phase. The hexagonally close-packed arrays of oxygen anions present in the parent goethite still remained in the newly formed hematite. Tatsuo *et al.*^[42] studied the thermal expansion of hematite at high temperatures, where no chemical reaction occurred. In current study, the hematite was formed by the oxidation of magnetite. The oxygen anions are transferred from cubic close-packed arrays to the hexagonally close-packed arrays. The aforementioned three hematite phases were generated through distinct pathways. Figure 7 shows the relative increase in a and c of the three hematite phases. The correlation between lattice constants and temperature can be also fitted with second-order polynomials (Figure 8). The temperature-dependent lattice constant of Fe_2O_3 can be

described as follows: $a = -2.81 \times 10^{-8} \times T^2 + 8.76 \times 10^{-5} \times T + 5.0368$; $c = 3.01 \times 10^{-8} \times T^2 + 1.09 \times 10^{-4} \times T + 13.7621$.

The SiO_2 was the dominant impurity in both ores. At current study, the maximum temperature was 1000 °C, the SiO_2 was considered as inert phase. The size of Mg^{2+} (72 pm) is similar to Fe^{2+} (74 pm). Therefore, the influence of SiO_2 and MgO on the lattice constant was ignored. The ore B contains more gangue minerals than the ore A. The impurities such as Al_2O_3 and CaO should have influence on the crystal cell of Fe_3O_4 and Fe_2O_3 . Due to the smaller size of Al^{3+} (54 pm) than Fe^{3+} (65 pm), the substitution of Fe^{3+} by Al^{3+} in Fe_3O_4 or Fe_2O_3 crystal cell would result in a contraction of the cell volume. The Ca^{2+} cations either displace Fe^{2+} or occupy vacancies in Fe_3O_4 cell, both of which may result in an expansion of the crystal cell due to the larger size of Ca^{2+} (100 pm). In other words, the Al^{3+} and Ca^{2+} show the opposite effect on the crystal size of Fe_3O_4 cell. Figure 9(a) illustrates the expansion of Fe_3O_4 crystal cell at different temperatures. The difference between the Ore A and Ore B was not significant. The Fe_3O_4 crystal cell expansion rate of Ore B was slightly smaller than that of Ore A, which can be explained by the substitution of Fe^{3+} by Al^{3+} . However, the expansion rate at 800 °C was an exception. The Al^{3+} cations had better mobility within the Fe_3O_4 crystal cell than that of Ca^{2+} cations. Only at high temperature, *i.e.*, 800 °C, the effect of Ca^{2+} cations became more dominant than Al^{3+} cations and promoted the expansion of the Fe_3O_4 crystal cell. Figure 9(b) shows the expansion of Fe_2O_3 crystal cell at different temperatures. The Fe_2O_3 crystal cell expansion rate of Ore B was slightly larger than that of Ore A at 600 °C and became more obvious at 800 °C. While at 1000 °C, the expansion rate of Ore B was smaller than that of Ore A. This phenomenon could be also explained by the combined effect of Al^{3+} and Ca^{2+} cations in the Ore B. Based on the stability diagram of $\text{Fe}_3\text{O}_4\text{-FeAl}_2\text{O}_4$ and $\text{Fe}_2\text{O}_3\text{-FeAlO}_3$, Al^{3+} cations prefer to combine with Fe_3O_4 to form magnetite-based solid solution.^[43] At 1000 °C, the

Table III. The Lattice Constant and Volume of the Fe₃O₄ Cell Measured by High-Temperature X-Ray Diffraction During the Oxidation of Fe₃O₄ in Air

Temp	Ore A		Ore B		**Ref. 40	**Ref. 38
	$a = b = c$ (Å)	Volume (Å ³)	$a = b = c$ (Å)	Volume (Å ³)	$a = b = c$ (Å)	$a = b = c$ (Å)
25 °C	8.4156 ± 0.0021	596.0207	8.4165 ± 0.0007	596.2214	8.3778	—
400 °C	8.4476 ± 0.0035	602.8437	8.4473 ± 0.0010	602.7819	8.4203	8.3888
600 °C	8.4796 ± 0.0010	609.7186	8.4797 ± 0.0005	609.7486	8.4547	8.4424
800 °C	8.4953 ± 0.0042	613.1268	8.4974 ± 0.0005	613.5637	8.4761	8.4698
*1000 °C	—	—	—	—	8.4969	8.4987

*The intensity of Fe₃O₄ peaks at 1000 °C is quite low and not suitable for the calculation of lattice constant.

**The lattice constant from Refs. 40 and 38 are the values measured at vacuum conditions.

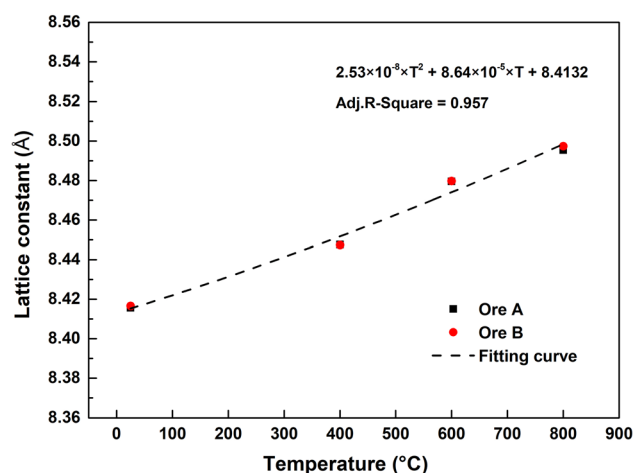


Fig. 6—The lattice constant of Fe₃O₄ as a function of temperature measured by high-temperature X-ray diffraction during oxidation of Fe₃O₄ in air.

oxidation degree of Ore B was 88.8 pct. With the decrease of magnetite phase, the Al³⁺ cations diffused from magnetite to hematite phase, resulting in the lower expansion rate of Ore B.

D. Evolution of Crystallite Size of Fe₂O₃

Figure 10 shows the Fe₂O₃ crystallite sizes of Ore A and B along the *c* axis and the *a/b* axis. With an increase in temperature, more and more Fe₃O₄ was oxidized into Fe₂O₃, and thus the Fe₂O₃ crystallite in both ores grew, as shown in Figure 10. It was also observed in both ores that Fe₂O₃ grew faster along *a/b* axis ($D_{a/b}$ in Figure 10) than *c* axis (D_c in Figure 10) in the crystal unit, especially in the beginning of oxidation. Also, the crystallite size along the *a/b* axis revealed a larger size than that along the *c* axis. Such findings suggested a growth habit of Fe₂O₃ during oxidation. It is worth noting that $D_{a/b}$ and D_c were calculated based on the (110) and (104) peaks, respectively. In our previous study,^[11] it was found that the surface energy of the (110) crystal surface was larger than that of the (104) crystal surface. The growth rates of the crystal faces are proportional to their surface energies, indicating a larger crystallite size along the *a/b* axis, which concurs well with the current study. The growth habit of Fe₂O₃ was

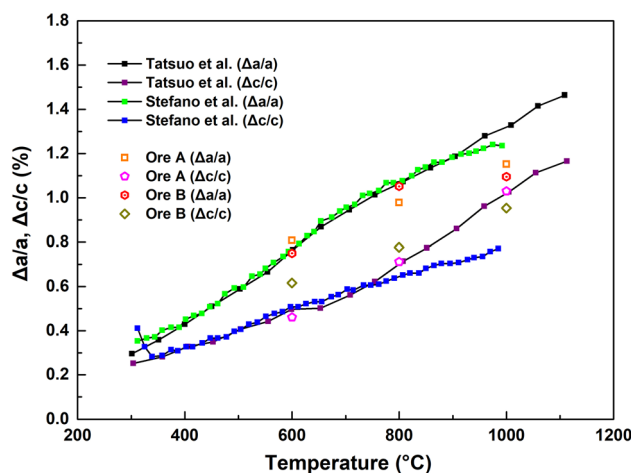


Fig. 7—The relative increase in lattice parameters *a* and *c* of Fe₂O₃ at different temperatures^[37,42]

also observed in TEM micrographs of Fe₂O₃ during the decomposition of goethite, where the Fe₂O₃ phase showed acicular morphology.^[44] In general, it is believed that the Fe₂O₃ phase presents acicular microcrystals due to its crystallographic-dependent properties. Besides, the crystallite sizes of Ore A were slightly larger than that of Ore B at specific temperatures. It cannot be explained with present experimental data. It may be because of the higher contents of Al₂O₃ and MgO in Ore B, which inhibit the diffusion of Fe cations.^[45,46] On the other hand, the crystallite sizes, calculated based on the peak (311), of the parent Fe₃O₄ phase of the Ore A and Ore B are 1027.7 Å and 812.6 Å, respectively. The larger crystallite size of Fe₂O₃ might inherit from the larger parent Fe₃O₄ phase.

IV. CONCLUSIONS

In this study, the thermal transformation of two magnetite ore fines was investigated using *in situ* high-temperature X-ray diffraction (HT-XRD) during oxidation. The following conclusions can be obtained:

- (1) The crystal information, such as lattice constant and crystallite size, can be successfully characterized by HT-XRD. The peaks in HT-XRD patterns shifted to a lower diffraction angle with an increase in

Table IV. The Lattice Constant and Volume of the Fe₂O₃ Cell

Temp	Ore A			Ore B		
	<i>a</i> = <i>b</i> (Å)	<i>c</i> (Å)	Volume (Å ³)	<i>a</i> = <i>b</i> (Å)	<i>c</i> (Å)	Volume (Å ³)
25 °C	5.0391	13.7648	302.6958	5.0391	13.7648	302.6958
*400 °C	—	—	—	—	—	—
600 °C	5.0798	13.8282	309.0220	5.0769	13.8496	309.1470
800 °C	5.0884	13.8628	310.8451	5.0921	13.8717	311.4972
1000 °C	5.0972	13.9066	312.9067	5.0943	13.896	312.3125

*The intensity of Fe₂O₃ peaks at 400 °C is quite low and not suitable for the calculation of lattice constant.

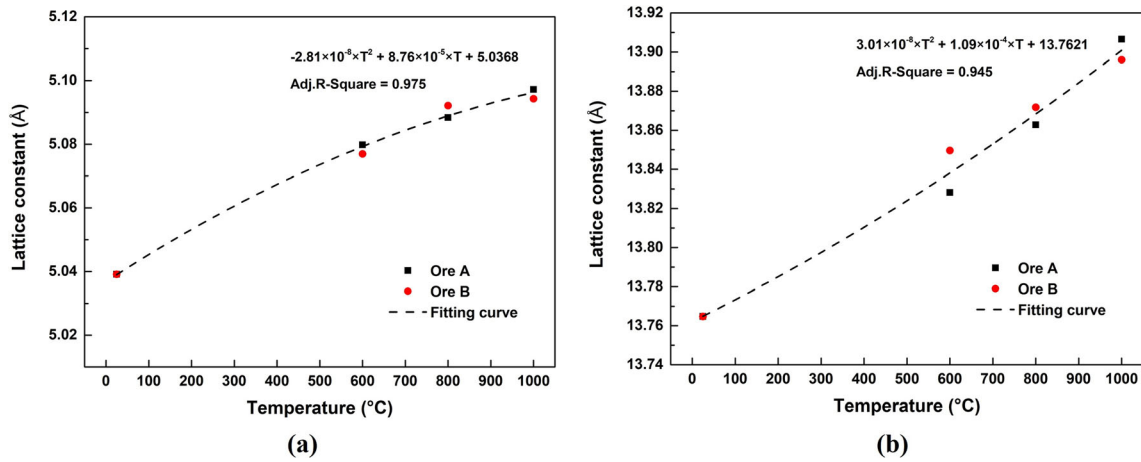


Fig. 8—The lattice constants of Fe₂O₃ as a function of temperature: (a) lattice constant *a*; (b) lattice constant *c*.

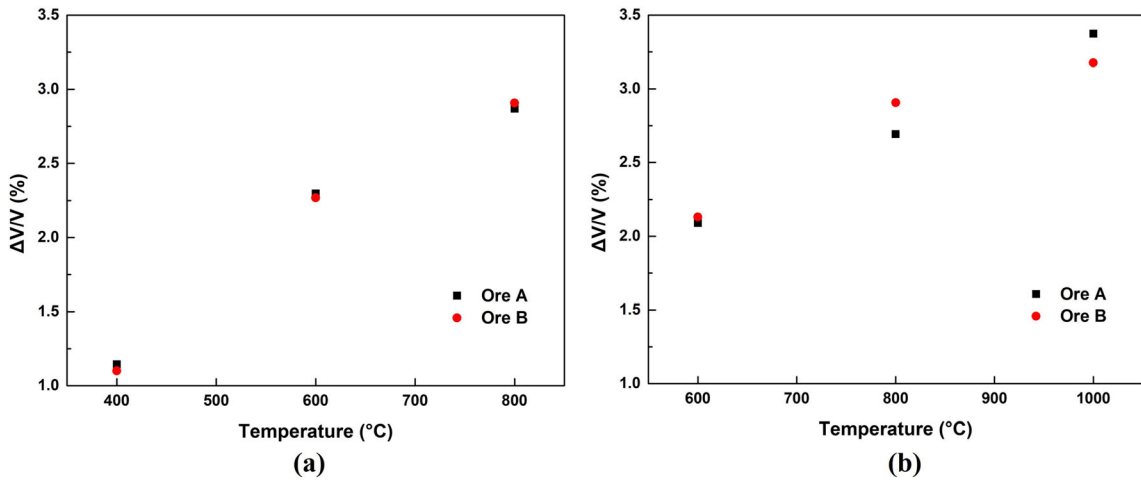


Fig. 9—The expansion of crystal cell volume as a function of temperature: (a) Fe₃O₄; (b) Fe₂O₃.

temperature due to thermal expansion. The intensity of the (104) peak of Fe₂O₃ increased with the increasing temperature, indicating an increase in the fraction of Fe₂O₃. The width of the (104) peak became narrower with the increasing temperature,

suggesting a growing crystallite size of Fe₂O₃ during oxidation.

- (2) The lattice constants of Fe₃O₄ and Fe₂O₃ both increased with the temperature and followed second-order polynomials. The correlation of lattice

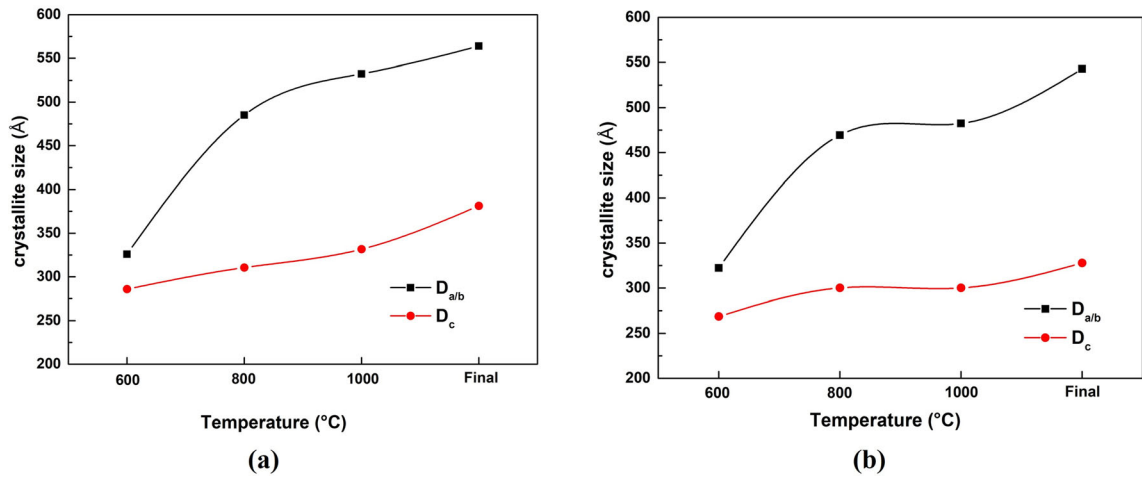


Fig. 10—The crystallite sizes of Ore A and B along the a/b axis and the c axis of a crystal cell at different temperatures: (a) Ore A; (b) Ore B.

constant and temperature can be expressed as follows:

$$\text{Fe}_3\text{O}_4 : a \\ = 2.53 \times 10^{-8} \times T^2 + 8.64 \times 10^{-5} \times T + 8.4132;$$

$$\text{Fe}_2\text{O}_3 : a \\ = -2.81 \times 10^{-8} \times T^2 + 8.76 \times 10^{-5} \times T \\ + 5.0368; c \\ = 3.01 \times 10^{-8} \times T^2 + 1.09 \times 10^{-4} \times T \\ + 13.7621.$$

- (3) During oxidation, Fe_3O_4 transformed into Fe_2O_3 . The growth of Fe_2O_3 revealed a certain growth habit. The growth rates of Fe_2O_3 crystallite along the a/b axis was faster than that in the c axis, thus showing acicular microcrystals. Such a morphology may affect the subsequent reduction, which requires further investigations.

ACKNOWLEDGMENTS

The authors gratefully acknowledge the funding support of K1-MET GmbH, metallurgical competence center. The research program of the K1-MET competence center is supported by COMET (Competence Center for Excellent Technologies), the Austrian program for competence centers. COMET is funded by the Federal Ministry for Climate Action, Environment, Energy, Mobility, Innovation and Technology, the Federal Ministry for Digital and Economic Affairs, the provinces of Upper Austria, Tyrol and Styria and the Styrian Business Promotion Agency (SFG). In addition, the research work is partially financed by Montanuniversität Leoben. Zheng Heng greatly

acknowledges the financial support from the program of the China Scholarship Council (No.201908420284). Y. Ma acknowledges financial support through the Walter Benjamin Programme of the Deutsche Forschungsgemeinschaft (Project No. 468209039). Dr Yury Kapelyushin acknowledges financial support from the Russian Science Foundation Grant No. 21-79-00081, <https://rscf.ru/project/21-79-00081/>.

CONFLICT OF INTEREST

On behalf of all authors, the corresponding author states that there is no conflict of interest.

FUNDING

Open access funding provided by Montanuniversität Leoben.

OPEN ACCESS

This article is licensed under a Creative Commons Attribution 4.0 International License, which permits use, sharing, adaptation, distribution and reproduction in any medium or format, as long as you give appropriate credit to the original author(s) and the source, provide a link to the Creative Commons licence, and indicate if changes were made. The images or other third party material in this article are included in the article's Creative Commons licence, unless indicated otherwise in a credit line to the material. If material is not included in the article's Creative Commons licence and your intended use is not permitted by statutory regulation or exceeds the permitted use, you will need to obtain permission directly from the copyright holder. To view a copy of this licence, visit <http://creativecommons.org/licenses/by/4.0/>.

REFERENCES

- Department of the Premier and Cabinet: South Australia's Magnetite Strategy: Making our state's magnetite the world's choice for steelmaking, p. 7, <https://sarigbasis.pir.sa.gov.au/WebtopEw/ws/samref/sarigl/image/DDD/BROCH028.pdf>. Accessed 6 Aug 2022.
- Government of South Australia: Magnetite: South Australia's potential (2018), <https://www.energymining.sa.gov.au/industry/geological-survey/mesa-journal/previous-feature-articles/magnetite-south-australias-potential>. Accessed 6 Aug 2022.
- D. Zhu, J. Pan, L. Lu, and R. J. Holmes: *Iron Ore*, 2015, pp. 435–73.
- SALCOS®: SALCOS Official webpage (31.01.2021), <https://salcos.salzgitter-ag.com/en/>. Accessed 31 January 2021.
- V. Vogl, M. Ahman, and L.J. Nilsson: *J. Clean. Prod.*, 2018, vol. 203, pp. 736–45.
- S. Daniel, W. Johann, H. Bernhard, R. Norbert, W. Thomas, S. Wolfgang, and F. Alexander: *Mitsubishi Heavy Ind. Tech. Rev.*, 2022, vol. 59, pp. 1–5.
- Daniel Spreitzer: Ph.D. Thesis, Montanuniversitaet Leoben, Leoben, Austria, 2020. <https://pure.unileoben.ac.at/portal/files/6390410/AC16176350.pdf>.
- H. Zheng, D. Spreitzer, T. Wolfinger, J. Schenk, and R. Xu: *Metall. Mater. Trans. B*, 2021, vol. 52B, pp. 1955–71.
- H. Zheng, O. Daghighaleh, T. Wolfinger, B. Taferner, J. Schenk, and R. Xu: *Int. J. Miner. Metall. Mater.*, 2022, vol. 28, pp. 1873–81.
- H. Zheng, J. Schenk, D. Spreitzer, T. Wolfinger, and O. Daghighaleh: *Steel Res. Int.*, 2021, pp. 2000687.
- H. Zheng, J. Schenk, R. Xu, O. Daghighaleh, D. Spreitzer, T. Wolfinger, D. Yang, and Y. Kapelyushin: *Metall. Mater. Trans. B*, 2022, vol. 53B, pp. 1644–60.
- H.J. Cho, M. Tang, and P.C. Pistorius: *Metall. Mater. Trans. B*, 2014, vol. 45B, pp. 1213–20.
- H.J. Cho and P.C. Pistorius: *AISTech Conf.*, Association for Iron & Steel Technology (AIST), Atlanta, GA, 2012, pp. 503–11.
- T. K. Sandeep Kumar, N. N. Viswanathan, H. Ahmed, A. Dahlin, C. Andersson, and B. Bjorkman: *Metall. Mater. Trans. B.*, 2019, vol. 50, pp. 150–61.
- A. Sardari, E.K. Alamdari, M. Noaparast, and S.Z. Shafaei: *Int. J. Miner. Metall. Mater.*, 2017, vol. 24, pp. 486–92.
- E.R. Monazam, R.W. Breault, and R. Siriwardane: *Ind. Eng. Chem. Res.*, 2014, vol. 53, pp. 13320–28.
- E.R. Schmidt and F.H. Vermaas: *Am. Miner.*, 1955, vol. 40, pp. 422–31.
- K.V.G.K. Gokhale: *Econ. Geol.*, 1961, vol. 56, pp. 963–71.
- B. Gillot, A. Rousset, and G. Dupre: *J. Solid State Chem.*, 1978, vol. 25, pp. 263–71.
- A.-F. Lehlooh, S. Mahmood, and I. Abu-Aljarayesh: *J. Magn. Magn. Mater.*, 1994, vol. 136, pp. 143–48.
- B.I. Whittington: *Metall. Mater. Trans. B*, 2000, vol. 31B, pp. 1175–86.
- S. Swanepoel, A.M.G. Craig, and J.P.R. Villiers: *Metall. Mater. Trans. B.*, 2022, vol. 53B, pp. 3805–24.
- V.D.A. Oliveira, R.D.J.T. Lana, H.C.D.S. Coelho, G.J.S. Brigolini, and C.G.D. Santos: *Metall. Mater. Trans. B*, 2020, vol. 51B, pp. 1418–31.
- H.H. Zhu, J. Chen, J.X. Deng, R.B. Yu, and X.R. Xing: *Metall. Mater. Trans. B.*, 2012, vol. 43B, pp. 494–502.
- Z.Y. Wang, J.L. Zhang, X.D. Xing, Z.J. Liu, Y.P. Zhang, X.L. Liu, and Y.R. Liu: *JOM*, 2016, vol. 68, pp. 656–67.
- H. Sun, A.A. Adetoro, F. Pan, Z. Wang, and Q. Zhu: *Metall. Mater. Trans. B.*, 2017, vol. 48B, pp. 1898–1907.
- X. Fu, Y. Wang, and F. Wei: *Metall. Mater. Trans. A.*, 2010, vol. 41A, pp. 1338–48.
- R.J.D. Tilley: *Crystals and Crystal Structures*, Wiley, Chichester, 2006, p. 36.
- E. Eneroeth and C. Bender Koch: *Minerals Engineering*, 2003, vol. 16, pp. 1257–67.
- F.H. Chung: *J. Appl. Crystallogr.*, 1974, vol. 7, pp. 519–25.
- F.H. Chung: *J. Appl. Cryst.*, 1974, vol. 7, pp. 526–31.
- Y. Kapelyushin, Y. Sasaki, J. Zhang, S. Jeong, and O. Ostrovski: *Metall. Mater. Trans. B.*, 2015, vol. 46B, pp. 2564–72.
- D. Zhu, C. Yang, J. Pan, and X. Li: *Metall. Mater. Trans. B.*, 2016, vol. 47B, pp. 2919–30.
- F. Pan, Q. Zhu, Z. Du, and H. Sun: *J. Iron Steel Res. Int.*, 2016, vol. 23, pp. 1160–67.
- L. Kurpaska: *J. Mol. Struct.*, 2018, vol. 1163, pp. 287–93.
- S.K. Bhargava, A. Garg, and N.D. Subasinghe: *Fuel*, 2009, vol. 88, pp. 988–93.
- S. Gialanella, F. Girardi, G. Ischia, I. Lonardelli, M. Mattarelli, and M. Montagna: *J. Therm. Anal. Calorim.*, 2010, vol. 102, pp. 867–73.
- D. Levy, G. Artioli, and M. Dapiaggi: *J. Solid State Chem.*, 2004, vol. 177, pp. 1713–16.
- T. Langreiter and V. Kahlenberg: *Curr. Comput. Aid. Drug Des.*, 2015, vol. 5, pp. 143–53.
- G.R. Holcomb: *Mater. High Temp.*, 2019, vol. 36, pp. 232–39.
- Paolo Venturelli: *Am. Miner.*, 1999, pp. 895–904.
- T. Saito: *Bull. Chem. Soc. Jpn.*, 1965, vol. 38, pp. 2008–009.
- A.C. Turnock and H.P. Eugster: *J. Petrol.*, 1962, vol. 3, pp. 533–65.
- L.A. Pérez-Maqueda, J.M. Criado, C. Real, J. Šubrt, and J. Boháček: *J. Mater. Chem.*, 1999, vol. 9, pp. 1839–46.
- A. V. Roshchin and Vasily Roshchin: *Russ. Metall.*, 2003, pp. 1–5.
- A. V. Roshchin and Vasily Roshchin: *Russ. Metall.*, 2003, pp. 97–102.

Publisher's Note Springer Nature remains neutral with regard to jurisdictional claims in published maps and institutional affiliations.